Interactions of moisture and oxidative ageing mechanisms in paving binders
Towards improving durability of pavements

Ma, L.

DOI
10.4233/uuid:3dd1b05e-8802-41da-b54b-92f610ad6cd5

Publication date
2024

Document Version
Final published version

Citation (APA)
Ma, L. (2024). *Interactions of moisture and oxidative ageing mechanisms in paving binders: Towards improving durability of pavements*. [Dissertation (TU Delft), Delft University of Technology]. https://doi.org/10.4233/uuid:3dd1b05e-8802-41da-b54b-92f610ad6cd5

Important note
To cite this publication, please use the final published version (if applicable).
Please check the document version above.

Interactions of moisture and oxidative ageing mechanisms in paving binders

Interactions of moisture and oxidative ageing mechanisms in paving binders

Towards improving durability of pavements

Dissertation

for the purpose of obtaining the degree of doctor
at Delft University of Technology,
by the authority of the Rector Magnificus, prof. dr. ir. T. H. J. J. van der Hagen,
chair of the Board for Doctorates,
to be defended publicly on
Monday 8, April 2024 at 10:00 o'clock

by

Lili MA

Master of Engineering in Transportation Engineering
Southeast University, China,
born in Huai'an, China.

This dissertation has been approved by the promotors.

Composition of the doctoral committee:

Rector Magnificus,	chairperson
Prof. dr. ir. S. M. J. G. Erkens,	Delft University of Technology, promotor
Dr. A. Varveri,	Delft University of Technology, copromotor
Independent members:	
Prof. dr. ir. E. Schlangen,	Delft University of Technology
Prof. dr. A. Bhasin,	University of Texas at Austin, USA
Prof. dr. ir. W. Van den bergh,	University of Antwerp, Belgium
Prof. dr. B. Hofko,	Vienna University of Technology, Austria
Prof. dr. H. M. Jonkers,	Delft University of Technology, reserve member
Other members:	
Dr. O. A. Moultos,	Delft University of Technology

Keywords: moisture, ageing, bituminous binders, chemo-mechanical relationship

ISBN 978-94-6384-550-2

An electronic version of this dissertation is available at http://repository.tudelft.nl/.

Contents

Summary

Extensive transportation infrastructure is crucial for enabling efficient transportation and fostering economic development. However, the operation of roadways contributes to escalating environmental and societal issues, including noise pollution and carbon emissions. To achieve a balance between economy, environment, and society, growing focus is being placed on enhancing the durability and sustainability of asphalt pavement in all aspects. A pivotal factor contributing to the deterioration of asphalt pavement performance is the degradation of bitumen properties, significantly affected traffic and climate conditions. The latter is primarily related to two key processes: oxidative aging and moisture in bitumen. Extensive studies have been undertaken to investigate the moisture and ageing behavior while large variations have been reported due to the complexity of these behavior, the diversity of bitumen types, and the variability of environmental conditions. Such discrepancies complicate the formulation of bituminous binders and mixtures that mitigates these issues.

The objectives of this thesis are centered on gaining a thorough understanding of the mechanisms behind moisture and ageing behavior in bitumen, working towards a fully coupled moisture and ageing behavior in bitumen and their impact on bituminous materials. To figure out the complex moisture and aging effects in bitumen, it is essential to initiate from a simpler scenario without involving too many variables and then gradually take into consideration more factors affecting the moisture and ageing processes.

Guided by this principle, the moisture diffusion behavior in bitumen and its effects on bitumen properties are initially investigated. To obtain fundamental insights into the moisture mechanisms, both experiments and molecular dynamics simulations are conducted for mutual interpretation and corroboration. Results show that the moisture in bitumen consists of three states: free water characterized by a constant diffusion coefficient and a saturated concentration, immobile water bonded to polar functional groups with a maximum concentration dependent on the number of these available groups, and water clusters, whose diffusion coefficient is significantly lower compared to free water and varies with cluster size.

The effects of ageing on the physicochemical and rheological properties of bitumen derived from diverse crude oil sources are evaluated and the physicochemical-rheological relationship is elucidated. The direct analysis of specific parameters and the chemometric analysis of full curves obtained from various chemical, physical, and rheological tests are combined for more accurate and extensive characterization. Results provide new insights into the chemo-mechanical relationship of bitumen, demonstrate the high capability of comprehensive information embedded in FTIR spectra and GPC curve in characterizing various rheological properties, and guide the selection of key physicochemical and rheological parameters for the evaluation of bitumen degradation.

To characterize the impact of ageing on the moisture diffusion behavior in bitumen including moisture diffusion coefficient and absorption amount, the moisture transport

in aged bitumen is measured through dynamic vapor sorption. The key factors determining moisture diffusion coefficient and moisture absorption are fractional free volume and polarity of bitumen. The changes of these two factors with increasing ageing level integratedly lead to increased activation energy for the diffusion of free water and reduced enthalpy of its adsorption. Simultaneously, the ageing kinetics of bitumen films are affected by the presence of moisture. The presence of moisture can inhibit oxidative reaction through the competitive diffusion between oxygen and moisture while the removal of moisture accelerates it due to additional diffusing pathways created by the diffusion of water molecules, especially water clusters.

In conclusion, this thesis provides in-depth insights into the understanding and evaluation of moisture diffusion and oxidative reaction in bitumen, as well as their respective effects on bitumen properties. The effects of moisture on the ageing process and that of ageing on the moisture behavior elucidated in this thesis establish a robust foundation for the modelling of fully coupled moisture-ageing effects in bituminous binders. These findings provide valuable guidance for the design, construction, and maintenance of porous asphalt pavement aiming at improved pavement durability and sustainability.

Samenvatting

Een uitgebreide transportinfrastructuur is cruciaal voor het mogelijk maken van efficiënt vervoer en het bevorderen van economische ontwikkeling. Echter, de exploitatie van wegen draagt bij aan toenemende milieuproblemen en maatschappelijke kwesties, waaronder geluidsoverlast en koolstofemissies. Om een evenwicht te bereiken tussen economie, milieu en maatschappij, wordt er steeds meer nadruk gelegd op het verbeteren van de duurzaamheid en levensduur van asfaltverharding in alle opzichten. Een cruciale factor die bijdraagt aan de achteruitgang van de prestaties van asfaltverharding is de degradatie van de eigenschappen van bitumen, die aanzienlijk wordt beïnvloed door verkeer- en klimaatomstandigheden. Laatstgenoemde is voornamelijk gerelateerd aan twee sleutelprocessen: oxidatieve veroudering en vocht in bitumen. Er zijn uitgebreide studies uitgevoerd om het vocht- en verouderingsgedrag te onderzoeken, terwijl er grote variaties zijn gerapporteerd vanwege de complexiteit van deze gedragingen, de diversiteit van bitumentypes en de variabiliteit van de milieuomstandigheden. Dergelijke verschillen bemoeilijken de formulering van bitumineuze bindmiddelen en mengsels die deze problemen mitigeren.

De doelstellingen van deze scriptie zijn gericht op het verkrijgen van een grondig begrip van de mechanismen achter het vocht- en verouderingsgedrag in bitumen, werkend naar een volledig gekoppeld vocht- en verouderingsgedrag in bitumen en de impact daarvan op bitumineuze materialen. Om de complexe effecten van vocht en veroudering in bitumen te doorgronden, is het essentieel om te starten vanuit een eenvoudiger scenario zonder te veel variabelen te betrekken en vervolgens geleidelijk meer factoren in overweging te nemen die de vocht- en verouderingsprocessen beïnvloeden.

Geleid door dit principe worden het vochtdiffusiegedrag in bitumen en de effecten ervan op de eigenschappen van bitumen in eerste instantie onderzocht. Om fundamentele inzichten te verkrijgen in de vochtmechanismen, worden zowel experimenten als moleculaire dynamica simulaties uitgevoerd voor wederzijdse interpretatie en bevestiging. Resultaten tonen aan dat het vocht in bitumen bestaat uit drie toestanden: vrij water, gekenmerkt door een constante diffusiecoëfficiënt en een verzadigde concentratie, immobiel water gebonden aan polaire functionele groepen met een maximale concentratie afhankelijk van het aantal van deze beschikbare groepen, en waterclusters, waarvan de diffusiecoëfficiënt aanzienlijk lager is in vergelijking met vrij water en varieert met de grootte van de cluster.

De effecten van veroudering op de fysisch-chemische en reologische eigenschappen van bitumen, afgeleid van diverse soorten ruwe olie, worden geëvalueerd en de relatie tussen fysisch-chemische en reologische eigenschappen wordt verduidelijkt. De directe analyse van specifieke parameters en de chemometrische analyse van volledige curven, verkregen uit verschillende chemische, fysische en reologische tests, worden gecombineerd voor een nauwkeurigere en uitgebreidere karakterisering. Resultaten bieden nieuwe inzichten in de chemo-mechanische relatie van bitumen, demonstreren de hoge capaciteit

van uitgebreide informatie ingebed in FTIR-spectra en GPC-curve bij het karakteriseren van verschillende reologische eigenschappen, en leiden de selectie van sleutel fysisch-chemische en reologische parameters voor de evaluatie van bitumendegradatie.

Om de impact van veroudering op het vochtdiffusiegedrag in bitumen te karakteriseren, inclusief de vochtdiffusiecoëfficiënt en absorptiehoeveelheid, wordt het vochttransport in verouderd bitumen gemeten via dynamische dampadsorptie. De sleutelfactoren die de vochtdiffusiecoëfficiënt en vochtabsorptie bepalen, zijn het fractionele vrije volume en de polariteit van bitumen. De veranderingen van deze twee factoren met toenemende verouderingsniveau leiden geïntegreerd tot een verhoogde activeringsenergie voor de diffusie van vrij water en een verminderde enthalpie van zijn adsorptie. Tegelijkertijd worden de verouderingskinetica van bitumenfilms beïnvloed door de aanwezigheid van vocht. De aanwezigheid van vocht kan de oxidatieve reactie remmen door de competitieve diffusie tussen zuurstof en vocht, terwijl de verwijdering van vocht het versnelt vanwege extra diffusiepaden gecreëerd door de diffusie van watermoleculen, met name waterclusters.

Ter afsluiting biedt deze scriptie diepgaande inzichten in het begrip en de evaluatie van vochtdiffusie en oxidatieve reactie in bitumen, evenals hun respectievelijke effecten op de eigenschappen van bitumen. De effecten van vocht op het verouderingsproces en die van veroudering op het vochtgedrag die in deze scriptie worden toegelicht, leggen een robuuste basis voor de modellering van volledig gekoppelde vocht-verouderingseffecten in bitumineuze bindmiddelen. Deze bevindingen bieden waardevolle richtlijnen voor het ontwerp, de bouw en het onderhoud van poreus asfaltverharding met als doel de duurzaamheid en duurzaamheid van de verharding te verbeteren.

1

Introduction

Moisture and oxidative ageing are two main factors influencing the sustainability of paving binders. This chapter introduces the background of moisture- and oxygen-induced degradation in bituminous materials, the significance of the thesis topic, and the research objectives. Moreover, the outline of the thesis is provided.

1

1.1 Background

Extensive and efficient transport infrastructure networks are of paramount importance in facilitating transportation and economic growth. However, the construction, operation, and maintenance of roads lead to increasing negative impacts on the environment and society such as noise pollution and carbon emissions. In response to the urgent challenges of climate change and the limited non-renewable sources, there is a growing focus on durability and sustainability in all aspects of asphalt pavement (Lesueur et al., 2012; Zhao et al., 2021), aiming to achieve a balance between economy, environment, and society.

The durability of asphalt pavement is mainly influenced by external conditions, such as traffic loading and complex climate conditions (Chaturabong & Bahia, 2017; Mo et al., 2009; Tayfur et al., 2007), but also by other factors related to pavement design, construction and maintenance (Frigio et al., 2013). To develop sustainable materials, construction techniques, and maintenance strategies, an in-depth understanding of how climate conditions or (heavy) traffic loads degrade pavement performance is indispensable, which is crucial for addressing distresses such as ravelling, cracking, and rutting.

In this thesis, the effect of climate conditions on the durability of paving materials is studied. Two of the main causes for pavement degradation are moisture damage and oxidative ageing (Kassem et al., 2009; Zhang & Leng, 2017) caused by climate conditions such as the presence of water (either as vapor or liquid), oxygen (including its reactive derivatives) (Primerano et al., 2022), high temperature, and UV-Visible radiation (Mirwald et al., 2022). Moisture in the environment can enter bitumen, resulting in cohesive degradation of bitumen and mastic, and then reach the mastic-aggregate interface, where it leads to loss of adhesion (Ma et al., 2021). Similarly, oxygen can also diffuse into the bitumen film. The presence of oxygen and its derivatives within bitumen, in combination with high temperature and/or UV-Visible radiation, leads to oxidative ageing and causes an increase in stiffness and brittleness of bitumen, as well as a decrease in adhesion between bitumen and aggregates (Al-Rub et al., 2013). Both moisture- and oxygen-induced damage occur mainly in bitumen or at bitumen-aggregate interface.

The Netherlands has an extensively dense highway network, more than 90% of which are paved with specific types of porous asphalt (PA). Compared to dense-graded asphalt mixtures, the air void content of PA is more than 20% and these pores are highly interconnected (Varveri, 2017). Therefore, PA has superior performance in noise reduction, water drainage, and road safety during rainfall (Zhang & Leng, 2017), which is more sustainable from the perspective of positive social and environmental impacts. However, the higher void content also allows more water and oxygen to penetrate into the bitumen and the bitumen-aggregate interface, thus accelerating moisture damage and oxidative ageing (Jing et al., 2019).

Consequently, it is of vital importance to study the moisture- and oxygen-induced damage in bituminous binders and at the bitumen-aggregate interface, and to incorporate this fundamental knowledge into design, construction and maintenance strategies with the aim to improve pavement durability and sustainability.

1.2 Research statement

Moisture damage in asphalt mixtures is governed by water transport behavior (Apeagyei et al., 2015b). Moisture transport in PA consists of initial convective flow of liquid water or diffusion of vapor in the void network of the mixtures and subsequent diffusion into the bitumen films and bitumen-aggregate interfaces. Moisture diffusion mainly leads to either the loss of cohesive resistance within bitumen or the loss of adhesion between bitumen and mineral aggregates (Nobakht et al., 2020), which are critical factors related to the ravelling of PA. The convective flow in the void network can cause hydraulic scouring effects under the impact of vehicle tires, thereby exacerbating these failures.

Several experimental techniques can be used to quantify the moisture transport rate in bitumen. Gravimetric methods measure the mass change in moisture absorption with time (Cheng et al., 2003; Herrington et al., 2021). Spectroscopic methods, such as infrared and electrochemical impedance spectroscopy, identify changes in water concentration by analyzing chemical information (Apeagyei et al., 2015a; Chen et al., 2022; Vasconcelos et al., 2010). Results from different experimental techniques show considerable deviations in the values of the diffusion coefficients that range from 10^{-17} to 10^{-9} m^2/s (Ma et al., 2021; Varveri, 2017). This may be due to the systematic errors in the measurements resulting from equipment, differences in testing protocols (e.g., temperature, time), and the applications of different theoretical models used to explain the moisture transport behavior.

The challenges in measuring the water transport rate in bitumen and understanding the underlying mechanisms result from the complex chemical properties of bitumen. The chemical components of bitumen can be classified into saturates, aromatics, resins, and asphaltenes, collectively known as SARA fractions (Rudyk, 2018). Bitumen is overall a hydrophobic organic material, indicating a low tendency to absorb water. The low absorption capacity of bitumen makes it difficult to measure moisture uptake accurately. Another complicating factor is the presence of polar functional groups predominantly found in the resins and asphaltenes fractions of bitumen (Petersen, 2009). The polarity of these functional groups and the polarity of water make the interactions between moisture and bitumen rather complex.

Oxygen transport and oxidative ageing in bitumen are also affected by its chemical composition, especially by the concentration of the reactive species within bitumen. Oxygen diffuses from the atmospheric air and through the voids of asphalt mixtures into bitumen films. The active components in bitumen can then react with the diffused oxygen, leading to bitumen hardening and embrittlement. The consumption of oxygen during oxidative reactions changes the oxygen concentration gradient, which in turn causes further oxygen diffusion. Therefore, bitumen ageing is a process with dynamic coupling of the oxygen diffusion and the oxidative reactions (Han et al., 2013; Herrington, 2012).

Many studies have focused on the evaluating ageing kinetics and their effects on bitumen properties (Herrington, 2012; Ma et al., 2021). Various test protocols, parameters, and indices are proposed to describe the chemical changes during the ageing process and the resulting changes in the physical, rheological, and mechanical properties. Ageing effects can be integrated into the analysis of asphalt pavement performance to provide a more accurate evaluation, modeling, and prediction of its long-term performance. This requires correlating the ageing-caused chemical changes to the mechanical degradation

of bitumen, and further to the deterioration of pavement performance (Pipintakos et al., 2022; Redelius & Soenen, 2015; Wang et al., 2022; Weigel & Stephan, 2017a).

A single evaluation index has been demonstrated to be inadequate in evaluating the chemical and mechanical properties of bitumen (Pipintakos et al., 2022), as well as the chemo-mechanical relationship, especially when targeting the generalization of all types of bitumen. Bitumens from different crude oil sources exhibit significant differences in their chemical components and micro-structures (Petersen, 2009). The evolving use of polymer modifiers, rejuvenators, and additives further adds to this complexity. Instead of solely relying on a single index, the combination of multiple indices obtained from various techniques seems to be a promising approach for a more comprehensive study of the chemo-mechanical relationship. Despite all the efforts in chemo-mechanical characterization of aged bitumen (Ma et al., 2021; Redelius & Soenen, 2015; Sun et al., 2020; Tauste et al., 2018; Weigel & Stephan, 2017b), more work is still needed to achieve a test specification that provides an accurate prediction of the mechanical properties of bitumen and pavement performance due to the complicated chemical composition of bitumen from different sources, the viscoelastic properties, the interactions with aggregates, as well as their physico-chemical changes due to environmental factors.

Both moisture and ageing can cause the deterioration of asphalt pavement through a series of processes as shown in Fig. 1.1. All these processes both affect and are affected by the chemical composition and microstructure of bitumen. To fully understand these functioning mechanisms, it is essential to examine the effects of each process separately as well as their mutual interactions in bitumen.

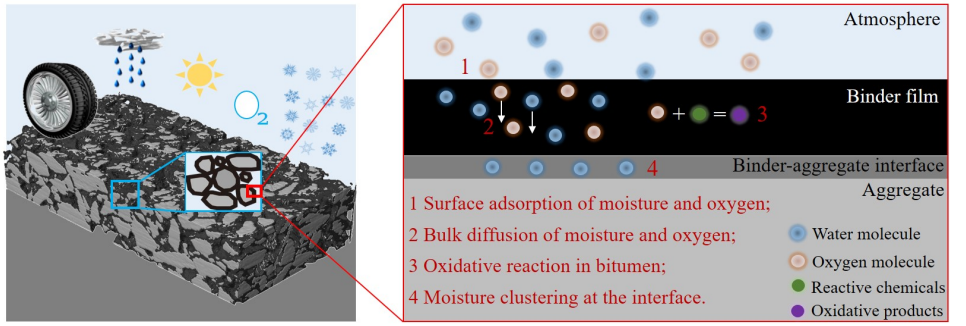

Figure 1.1 Moisture- and oxidative reaction-induced damage mechanisms in asphalt pavements.

It seems reasonable that the moisture transport in bitumen may be influenced by oxidative ageing. The oxidation of bitumen can produce more functional groups with high polarity (Mirwald et al., 2020). Considering the polarity of water, an increased polarity of bitumen indicates stronger interactions between water and bitumen, making it thus more complicated to explain moisture diffusion phenomena. Furthermore, ageing can change the SARA fractions of bitumen, resulting in a different microstructure (Tauste et al., 2018). This microstructure is essentially related to the diffusion path and diffusion rate of moisture (Vasconcelos et al., 2011). Despite these potential effects of ageing on moisture behavior, there is limited literature on the transport behavior in aged bitumen.

Studies about the effect of moisture on bitumen ageing have so far been ambiguous. Some results show that moisture has a small influence on the rheological properties of aged bitumen (Huang et al., 2012). On the other hand, there are findings that water can disrupt the colloidal structure of bitumen and increase the ageing extent (Thomas, 2002). Water may even intervene with the oxygen reaction kinetics via interacting with UV light and bitumen (Azimi Alamdary et al., 2019; He et al., 2018; Qian et al., 2021).

At asphalt mixture level, Ali et al., (2022) reported that long-term aging can increase moisture-induced damage of asphalt mixtures. López-Montero et al., (2016) revealed that ageing leads to a significant increase in the fatigue and cracking of mixtures regardless of the presence or absence of moisture conditions. However, Wu et al., (Wu et al., 2020) demonstrated that the effect of aging does not significantly change the influence of moisture on fatigue and rutting of mixtures, while water can partially hinder the effect of aging due to the depression of oxygen availability and temperature regulation. Although these inconsistencies may be caused by the differences in materials, experimental conditions, and evaluation methods, it indicates to some degree that the direct study of coupled moisture and ageing effects on asphalt mixtures can be challenging. At bitumen level, there is also no consistent understanding on the coupling effects and the underlying mechanisms. To fully understand coupled moisture and ageing behavior, it is recommended to study the phenomena initially at bitumen level. Studying fundamental processes at mixture level, where mineral fillers and mixture structure are considered, would significantly increase the complexity.

1.3 Research objectives

Climate condition is one of the main factors causing deterioration of asphalt pavement performance through the degradation of bitumen properties. Oxidative aging and moisture in bitumen are two important processes contributing to this degradation. Although extreme cases have conclusively highlighted the importance of both processes, detailed studies have revealed widely varying effects of moisture and ageing on bitumen properties, which precludes an accurate understanding and, as such, complicates the design of bituminous binders and mixtures addressing these issues. The variation in outcomes is partially due to the small-scale study, but mostly because these two processes cannot be readily separated and both are influenced by bitumen composition and its microstructure. The interactions between moisture and ageing in bitumen, as well as the underlying mechanisms, are complex. To address this coupling mechanism, separate investigations on moisture and oxygen transport, as well as oxidative ageing, are initially necessary. The impact of these behaviors on bitumen properties needs to be examined. The complete coupling process can be divided into the effects of moisture on ageing and ageing on moisture, both of which require further elucidation. Furthermore, both moisture and ageing are influenced by the chemical composition of bitumen, which can vary significantly depending on the source of crude oil.

The objectives of this thesis were to gain a thorough understanding of the mechanisms underlying the individual moisture and ageing behavior in bitumen and their interdependent relationship, towards a fully coupled moisture and ageing behavior in bitumen and their impact on bituminous materials. To clearly address the moisture and ageing behavior separately and how one affects the other, which is expected to lay solid

groundwork for the full coupling of moisture and ageing effects on bituminous binders and mixtures. This can further be utilized in the design, construction, and maintenance of asphalt pavements with enhanced durability and sustainability. To this end, the following objectives are to be achieved:

- Thoroughly investigating the moisture diffusion behavior in bitumen and its effects on bitumen properties. To obtain fundamental insights into the moisture mechanisms, both experiments and molecular dynamics simulations will be conducted for mutual interpretation and verification.

- Evaluating the effects of ageing on the physicochemical and rheological properties of bitumen derived from diverse crude oil sources and elucidating the physicochemical-rheological relationship. For this purpose, the direct analysis of specific parameters and the chemometric analysis of full curves obtained from various chemical, physical, and rheological tests are combined for a more accurate and extensive characterization of chemo-mechanical relationship of bituminous binders.

- Characterizing the impact of ageing on the moisture diffusion behavior in bitumen including moisture diffusion coefficient and absorption amount, along with the moisture damage in bitumen.

- Studying the ageing kinetics in the presence of moisture and its effects on aged products.

- Exploring the possible coupling approaches for a better prediction of bitumen degradation caused by moisture and ageing behavior.

1.4 Thesis outline

This dissertation, consisting of seven chapters, aims to deliver a thorough exploration of the individual moisture and ageing behavior in bitumen and their mutual interactions. This introductory chapter states the main challenges regarding the study of moisture- and ageing-caused degradation in bitumen and highlights the importance of separately examining moisture and ageing bitumen to the accurate characterization of moisture damage and oxidative ageing in bituminous materials. Additionally, this chapter elucidates the objectives of this work and outlines the thesis contents, as depicted in Fig. 1.2.

Chapter 2 delves into the kinetics and thermodynamics of moisture transport in bitumen utilizing dynamic vapor sorption tests. A detailed description of sample preparation, testing procedures, and sample configurations is presented. A physics-oriented moisture diffusion model is proposed that offers a more precise characterization of moisture diffusion coefficients, equilibrium water absorption, and water clustering mechanisms. Moreover, the chapter demonstrates an efficient optimization method based on finite element simulation, specifically designed for solving the proposed diffusion model, a non-linear inverse problem with multiple unknown parameters.

In Chapter 3, the moisture transport in bitumen is revisited at microscale through molecular dynamics (MD) simulations, with durations up to 600 ns. The water-bitumen systems with water contents ranging from 0 wt% to 1.76 wt% are investigated at temperatures between 298 and 533 K. The selection of force field, the specific setup of water-bitumen configurations, and the MD simulation procedures are presented. The hydrogen bonding and water clustering behavior affected by temperature and water content are evaluated, along with their effects on water self-diffusion coefficient in bitumen. The

impact of water on the density, viscosity, and cohesive energy of bitumen is discussed as well. Eventually, the water states in bitumen, water diffusion coefficients, and impact of water on bitumen properties are elucidated by integrating results from both experiments and MD simulations, targeting a comprehensive understanding of the mechanisms of moisture damage.

Chapter 4 focuses on the effect of ageing on physicochemical and rheological properties of bituminous binders. The chemical composition, molecular weight distribution, thermal behavior, viscoelastic response, fatigue life, stress relaxation, and viscosity of binders at varying ageing states are evaluated utilizing Fourier-transform infrared spectroscopy, gel permeation chromatography, differential scanning calorimetry, and dynamic shear rheometer, for a thorough characterization of the ageing behavior. Specifically, the physicochemical-physicochemical, rheological-rheological, and physicochemical-rheological relationships are explored based on Pearson correlation analysis and canonical correlation analysis, providing insights into the mechanisms underlying ageing-caused degradation of bitumen.

Building on the fundamental knowledge of moisture and ageing behavior in bitumen, Chapter 5 further analyzes how moisture and ageing affect each other. To this end, the moisture transport in aged binders is investigated, focusing on the dependency of mois-

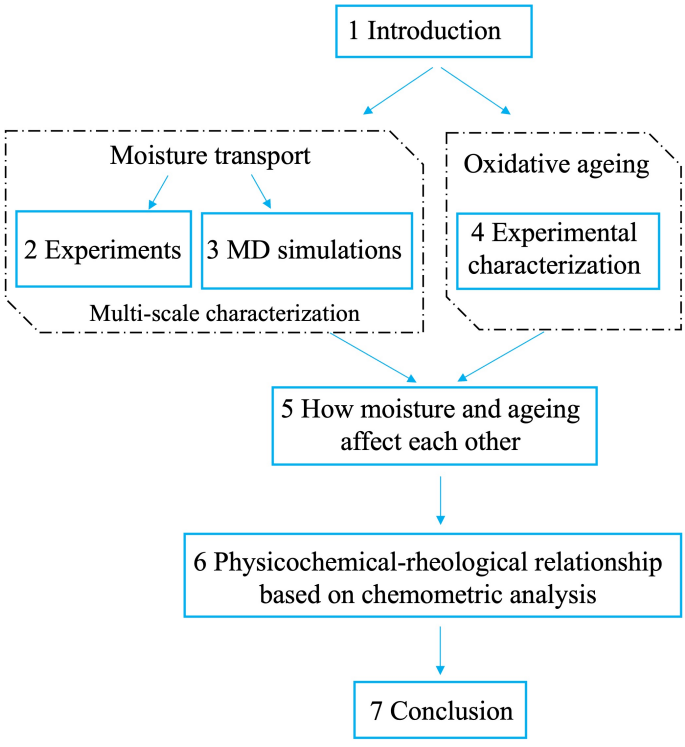

Figure 1.2 Schematic diagram of thesis outline

ture diffusion coefficient and equilibrium absorption on critical bitumen properties of free volume and polarity, aiming for accurate prediction of moisture diffusion coefficient in aged bitumen based on its physicochemical characteristics. The influence of ageing on moisture behavior is further evaluated in terms of the moisture-caused degradation in bitumen rheology. The effect of moisture on ageing behavior is demonstrated through the ageing kinetics in the presence of moisture.

In Chapter 6, chemometric analysis is performed on chemical, structural, and thermal multivariate datasets to classify bitumen originating from different sources and under varying testing conditions and to predict important rheological properties. Various variable selection methods are applied to the classification and regression models for increased model accuracy and efficiency. The analysis on crucial variables that contribute to accurate classification and prediction sheds new light into the mechanisms of ageing and moisture behavior and the physicochemical-rheological relationships in bitumen.

Finally, Chapter 7 presents a summary of the main findings in the thesis and provides recommendations as a continuation of this topic.

References

Ali, S. A., Zaman, M., Ghabchi, R., Rahman, M. A., Ghos, S., & Rani, S. (2022). Effect of additives and aging on moisture-induced damage potential of asphalt mixes using surface free energy and laboratory-based performance tests. *International Journal of Pavement Engineering*, *23*(2), 285–296.

Al-Rub, R. K. A., Darabi, M. K., Kim, S.-M., Little, D. N., & Glover, C. J. (2013). Mechanistic-based constitutive modeling of oxidative aging in aging-susceptible materials and its effect on the damage potential of asphalt concrete. *Construction and Building Materials*, *41*, 439–454.

Apeagyei, A. K., Grenfell, J. R., & Airey, G. D. (2015a). Application of Fickian and non-Fickian diffusion models to study moisture diffusion in asphalt mastics. *Materials and Structures*, *48*(5), 1461–1474.

Apeagyei, A. K., Grenfell, J. R., & Airey, G. D. (2015b). Influence of aggregate absorption and diffusion properties on moisture damage in asphalt mixtures. *Road Materials and Pavement Design*, *16*(sup1), 404–422.

Azimi Alamdary, Y., Singh, S., & Baaj, H. (2019). Laboratory simulation of the impact of solar radiation and moisture on long-term age conditioning of asphalt mixes. *Road Materials and Pavement Design*, *20*(sup1), S521–S532.

Chaturabong, P., & Bahia, H. U. (2017). Mechanisms of asphalt mixture rutting in the dry Hamburg wheel tracking test and the potential to be alternative test in measuring rutting resistance. *Construction and Building Materials*, *146*, 175–182.

Chen, Geng, J., Chen, H., Niu, Y., Wang, R., Wu, W., Zhao, S., & Zhong, Z. (2022). Diffusion of moisture and oxygen in bitumens using electrochemical impedance spectroscopy. *Fuel*, *315*, 123212.

Cheng, Little, D. N., Lytton, R. L., & Holste, J. C. (2003). Moisture damage evaluation of asphalt mixtures by considering both moisture diffusion and repeated-load conditions. *Transportation Research Record*, *1832*(1), 42–49.

Frigio, F., Pasquini, E., Ferrotti, G., & Canestrari, F. (2013). Improved durability of recycled porous asphalt. *Construction and Building Materials*, *48*, 755–763.

Han, R., Jin, X., & Glover, C. (2013). Oxygen diffusivity in asphalts and mastics. *Petroleum Science and Technology*, *31*(15), 1563–1573.

He, X., Hochstein, D., Ge, Q., Ali, A. W., Chen, F., & Yin, H. (2018). Accelerated aging of asphalt by UV photo-oxidation considering moisture and condensation effects. *Journal of Materials in Civil Engineering*, *30*(1), 04017261.

Herrington, P. R. (2012). Diffusion and reaction of oxygen in bitumen films. *Fuel*, *94*, 86–92.

Herrington, P. R., Wu, J. P., van den Kerkhof, L. C., & Bagshaw, S. A. (2021). Water diffusion in bitumen films. *Construction and Building Materials*, *294*, 123530.

Huang, S.-C., Glaser, R., & Turner, F. (2012). Impact of water on asphalt aging: Chemical aging kinetic study. *Transportation research record*, *2293*(1), 63–72.

Jing, R., Varveri, A., Liu, X., Scarpas, A., & Erkens, S. (2019). Laboratory and field aging effect on bitumen chemistry and rheology in porous asphalt mixture. *Transportation Research Record*, *2673*(3), 365–374.

Kassem, E., Masad, E., Lytton, R., & Bulut, R. (2009). Measurements of the moisture diffusion coefficient of asphalt mixtures and its relationship to mixture composition. *International Journal of Pavement Engineering*, *10*(6), 389–399.

Lesueur, D., Petit, J., & Ritter, H. J. (2012). Increasing the durability of asphalt mixtures by hydrated lime addition: What evidence? *European Roads Review*, (20).

López-Montero, T., & Miró, R. (2016). Differences in cracking resistance of asphalt mixtures due to ageing and moisture damage. *Construction and Building Materials*, *112*, 299–306.

Ma, L., Varveri, A., Jing, R., & Erkens, S. (2021). Comprehensive review on the transport and reaction of oxygen and moisture towards coupled oxidative ageing and moisture damage of bitumen. *Construction and Building Materials*, *283*, 122632.

Mirwald, J., Nura, D., Eberhardsteiner, L., & Hofko, B. (2022). Impact of uv–vis light on the oxidation of bitumen in correlation to solar spectral irradiance data. *Construction and Building Materials*, *316*, 125816.

Mirwald, J., Werkovits, S., Camargo, I., Maschauer, D., Hofko, B., & Grothe, H. (2020). Understanding bitumen ageing by investigation of its polarity fractions. *Construction and Building Materials*, *250*, 118809.

Mo, L., Huurman, M., Wu, S., & Molenaar, A. (2009). Ravelling investigation of porous asphalt concrete based on fatigue characteristics of bitumen–stone adhesion and mortar. *Materials & Design*, *30*(1), 170–179.

Nobakht, M., Zhang, D., Sakhaeifar, M. S., & Lytton, R. L. (2020). Characterization of the adhesive and cohesive moisture damage for asphalt concrete. *Construction and Building Materials*, *247*, 118616.

Petersen, J. C. (2009). A review of the fundamentals of asphalt oxidation: Chemical, physicochemical, physical property, and durability relationships. *Transportation Research Circular*, (E-C140).

Pipintakos, G., Lommaert, C., Varveri, A., & Van den Bergh, W. (2022). Do chemistry and rheology follow the same laboratory ageing trends in bitumen? *Materials and Structures*, *55*(5), 146.

Primerano, K., Mirwald, J., Maschauer, D., Grothe, H., & Hofko, B. (2022). Influence of selected reactive oxygen species on the long-term aging of bitumen. *Materials and Structures*, *55*(5), 133.

Qian, G., Yu, H., Jin, D., Bai, X., & Gong, X. (2021). Different water environment coupled with ultraviolet radiation on ageing of asphalt binder. *Road Materials and Pavement Design*, *22*(10), 2410–2423.

Redelius, P., & Soenen, H. (2015). Relation between bitumen chemistry and performance. *Fuel*, *140*, 34–43.

Rudyk, S. (2018). Relationships between SARA fractions of conventional oil, heavy oil, natural bitumen and residues. *Fuel*, *216*, 330–340.

Sun, X., Yuan, H., Song, C., Deng, X., Lv, G., Li, X., & Hu, A. (2020). Rapid and simultaneous determination of physical and chemical properties of asphalt by ATR-FTIR spectroscopy combined with a novel calibration-free method. *Construction and Building Materials*, *230*, 116950.

Tauste, R., Moreno-Navarro, F., Sol-Sánchez, M., & Rubio-Gámez, M. (2018). Understanding the bitumen ageing phenomenon: A review. *Construction and Building Materials*, *192*, 593–609.

Tayfur, S., Ozen, H., & Aksoy, A. (2007). Investigation of rutting performance of asphalt mixtures containing polymer modifiers. *Construction and Building Materials*, *21*(2), 328–337.

Thomas, K. P. (2002). Impact of water during the laboratory aging of asphalt. *Road Materials and Pavement Design*, *3*(3), 299–315.

Varveri, A. K. (2017). *Moisture damage susceptibility of asphalt mixtures: Experimental characterization and modelling* (Doctoral dissertation). Delft University of Technology.

Vasconcelos, K. L., Bhasin, A., & Little, D. N. (2010). Measurement of water diffusion in asphalt binders using Fourier transform infrared–attenuated total reflectance. *Transportation Research Record*, *2179*(1), 29–38.

Vasconcelos, K. L., Bhasin, A., & Little, D. N. (2011). History dependence of water diffusion in asphalt binders. *International Journal of Pavement Engineering*, *12*(5), 497–506.

Wang, Y., Wang, W., & Wang, L. (2022). Understanding the relationships between rheology and chemistry of asphalt binders: A review. *Construction and Building Materials*, *329*, 127161.

Weigel, S., & Stephan, D. (2017a). Modelling of rheological and ageing properties of bitumen based on its chemical structure. *Materials and Structures*, *50*, 1–15.

Weigel, S., & Stephan, D. (2017b). The prediction of bitumen properties based on FTIR and multivariate analysis methods. *Fuel*, *208*, 655–661.

Wu, J., Wang, Y., Liu, Q., Wang, Y., Ago, C., & Oeser, M. (2020). Investigation on mechanical performance of porous asphalt mixtures treated with laboratory aging and moisture actions. *Construction and Building Materials*, *238*, 117694.

Zhang, Y., & Leng, Z. (2017). Quantification of bituminous mortar ageing and its application in ravelling evaluation of porous asphalt wearing courses. *Materials & Design*, *119*, 1–11.

Zhao, Y., Goulias, D., & Peterson, D. (2021). Recycled asphalt pavement materials in transport pavement infrastructure: Sustainability analysis & metrics. *Sustainability*, *13*(14), 8071.

2

Thermodynamics and kinetics of moisture transport in bituminous binders

Moisture transport in bitumen is critical for the moisture-caused damage and the degradation in the durability of asphalt pavements. However, large variations in the measured diffusion coefficient of water in bitumen have been reported. This Chapter aims to investigate the kinetics and thermodynamics of moisture transport in bitumen, as well as to obtain more accurate diffusion coefficients.

For this purpose, sorption dynamics are measured using dynamic vapor sorption (DVS) for different bitumen types at various temperatures and relative humidities. Three transport models are studied and applied to the data obtained from the tests by means of a parameter optimization approach combined with the finite element simulations. An introduction to moisture transport is given in Section 2.1. The details on the test protocol, the three transport models, and the parameter optimization process are explained in Section 2.2, 2.3, and 2.4, respectively. The comparison of the three models and their accuracy in describing the experimental results are discussed in Section 2.5. Section 2.6 presents the analysis of the kinetics and thermodynamics of moisture transport in bitumen on the basis of the best transport model and the experimental results. Section 2.7 summarizes the main results.

Parts of this chapter have been published in Ma, L., Varveri, A., Jing, R., Kasbergen, C., & Erkens, S. (2022). Thermodynamics and kinetics of moisture transport in bitumen. *Materials & Design*, 111028.

2.1 Introduction

The presence of water, either as a vapor or a liquid, has been considered as one of the main causes of various pavement distresses such as raveling, stripping, and cracking (Diab et al., 2014; Kanitpong & Bahia, 2003). The fundamental mechanisms behind these distresses, collectively called moisture damage in the literature, are cohesive and adhesive degradation (Kanitpong & Bahia, 2003). Moisture on and in voids within the asphalt pavement initially diffuses into the bitumen film, resulting in cohesive degradation of bitumen and mastic, and then reaches the mastic-aggregate interface, where it leads to a loss of adhesion (Caro et al., 2008). A distinction is made between cohesive failure and adhesive failure on a basis of macroscopic observations of the failure location.

Research has been conducted to compare the relative importance of adhesive and cohesive failure due to moisture damage. It has been reported that the decrease in adhesive strength is larger than the decrease in cohesive strength as the exposure time to moisture increases. This indicates a change in failure mode from cohesive failure at dry conditions to adhesive failure at wet conditions (Canestrari et al., 2010; Wang et al., 2021), and it suggests that adhesive failure is a more important contributor to moisture damage compared to cohesive failure. In these studies, cohesion is shown to contribute to moisture damage mainly by controlling the rate of moisture diffusion and the subsequent absorption of moisture through mastic and into the mastic-aggregate interface (Cheng et al., 2003). Some prior studies, however, state that cohesive failure is a more common mode of moisture damage (Chaturabong & Bahia, 2018; Moraes et al., 2011). Overall, moisture can soften bitumen and mastic and can weaken the cohesive forces between them. This process is attributed to moisture saturation (Nobakht et al., 2020; Terrel & Al-Swailmi, 1994), but the extent to which cohesion can be affected by moisture is not established yet. The mechanism of how moisture diffusion and saturation decrease cohesion is not experimentally validated.

Moisture transport in bitumen consists of two main processes: moisture adsorption on the bitumen surface and moisture diffusion within the bulk of the bitumen. Surface adsorption kinetics may follow first-order or second-order adsorption rate, depending on the surface characteristics and the interaction between adsorbate and adsorbent (Azizian, 2004). Moisture diffusion behavior can be interpreted as the kinetic transport process characterized by the diffusion coefficient. Moisture diffusion is commonly described by Fick's law or modified diffusion models based on Fick's law (Vasconcelos et al., 2010).

Except for the kinetic surface adsorption and the bulk diffusion process, the adsorption and absorption of moisture are also of significant importance for explaining moisture damage in bituminous materials (Cheng et al., 2003). The Langmuir monolayer isotherm and the Brunauer–Emmet–Teller (BET) multilayer isotherm are commonly utilized to describe the adsorption phenomena. Other models, such as the Guggenheim Anderson de Boer (GAB) model and the Dubinin Radushkevich (DR) model, have been introduced to explain the multilayer adsorption of moisture at high relative humidity (Foo & Hameed, 2010). Moisture absorption or solubility is the thermodynamic equilibrium state resulting from diffusion. The saturated moisture concentration (or moisture solubility) is a function of the relative humidity. At low relative humidity levels, the solubility can be described based on Henry's law, whereas at high relative humidity the Flory-Huggins solubility and other more complex theories can be considered (Metz et al., 2003).

Several spectroscopic and gravimetric techniques have been employed to measure moisture transport kinetics and thermodynamics at the bitumen scale. These techniques include spectroscopic methods such as Fourier transform infrared-attenuated total reflectance (FTIR-ATR) (Vasconcelos et al., 2010, 2011) and electrochemical impedance spectroscopy (EIS) (Chen et al., 2022) and gravimetric measurements (Chen et al., 2022; Cheng et al., 2003; Herrington et al., 2021). FTIR-ATR, in particular, is commonly used to monitor in situ diffusion kinetics in bitumen films (Vasconcelos et al., 2010). In this method, a bitumen sample is cast onto the ATR crystal prism, and then continuous water conditioning is applied on top of it. To monitor the change in spectra over time, all stretching areas ranging from 3000 to 3800 cm^{-1}, which are associated with water, are examined. At each time point, these areas are integrated to determine the absorbed water content over time. It is assumed that the absorbance in the spectra is proportional to the instantaneous increase in mass within the bitumen film (Vasconcelos et al., 2010). In addition to spectroscopic techniques, the gravimetric method is also utilized to directly monitor mass changes. The test sample is placed in a chamber with controlled temperature, pressure, and moisture concentration. Instantaneous data on mass change are collected during the experiment. Mass changes can be accurately measured using a high-resolution balance with a precision of up to 0.1 μg (Chen et al., 2022; Herrington et al., 2021; Ma et al., 2022).

Two factors are crucial for moisture diffusion in bituminous materials: the rate of moisture diffusion and the equilibrium moisture concentration (solubility) (Cheng et al., 2003). Various diffusion models have been used to interpret experimental measurements and to obtain the diffusion coefficient and solubility of water in bitumen. It has been shown that Fick's law fails to properly describe moisture diffusion in bitumen (Vasconcelos et al., 2010). The dual model (Vasconcelos et al., 2010), the Langmuir-diffusion model (Apeagyei et al., 2015; Cheng et al., 2021), and the diffusion-reaction model (Herrington et al., 2021) have been proposed as alternatives. The models used in these studies assume the presence of water molecules in bitumen in two distinct modes: a free mode and a bound mode. The free mode refers to water molecules that can freely diffuse within the bitumen, while the bound mode suggests that water molecules are confined to polar bitumen sites due to hydrogen bonding (Vasconcelos et al., 2010). These two modes exhibit different diffusion dynamics, which are taken into account by the models. In the dual model, the diffusion coefficient of bound water is significantly lower than that of the free mode, indicating that it is partially immobile. On the other hand, the Langmuir and reaction models consider bound water to be completely immobile. When water diffusion coefficients are calculated by applying different models (based on different interpretations of the water-bitumen interaction mechanisms) to the experimental results from different techniques, they span 10^{-17} to 10^{-9} m^2/s (Varveri, 2017).

Experimental measurements have also revealed significant variations in the maximum moisture concentration observed in bitumen. Different studies have reported distinct values for this concentration. In one study, the moisture concentration in bitumen in contact with saturated vapor was found to be approximately 0.02 wt% (Cheng et al., 2003). This measurement reflects the moisture content when bitumen is exposed to saturated vapor conditions. Another study reported a moisture concentration of around 2.5 wt% in bitumen when it is fully immersed in water (Herrington et al., 2021). In a different investigation, the maximum moisture concentration in bitumen under water immer-

sion conditions was found to be approximately 7 wt% (Cheng et al., 2021). This higher value suggests a greater moisture uptake when bitumen is fully submerged in water. It is claimed by Herrington et al., (2021) that the moisture absorption in bitumen films cannot approach a saturated equilibrium value, but instead the rate of absorption became constant, at least within the timeframe of up to 395 days. These significant discrepancies in diffusion coefficient and saturated moisture concentration highlight the sensitivity of bitumen to moisture and the influence of experimental conditions on moisture uptake, suggesting a big challenge in accurately describing water transport behavior in bitumen.

The large variations in moisture diffusion coefficient and solubility, as calculated based on experiments, can be attributed to several factors. These factors include systematic errors in measuring protocols, the utilization of different theoretical transport models, and variations in bitumen originating from different crude oil sources.

The moisture concentration and diffusion coefficient in bitumen depend on its physical and chemical properties, which subsequently depend on the chemical composition (Cheng et al., 2003; Nguyen et al., 1992; Vasconcelos et al., 2011). Bitumen composition further affects the solubility and diffusion coefficient of absorbed water (Cheng et al., 2003). Bitumen is not a single, well-defined material. Instead, the term refers collectively to similar materials whose chemical compositions depend on the crude oil source, additives, processing steps, and aging. The chemical components that comprise a bitumen can be classified on a basis of solubility into saturates, aromatics, resins, and asphaltenes, typically known as SARA fractions (Rudyk, 2018). The saturates fraction in bitumen consists of nonpolar aliphatic hydrocarbons. Aromatics comprise hydrocarbons with saturated and aromatic rings. Resins and asphaltenes contain functional groups with heteroatoms (nitrogen, sulfur, and oxygen), which strongly influence the physicochemical properties of bitumen (Petersen, 2009). The predominantly hydrophobic composition of bitumen leads to it having a low absorption capacity for water (Cheng et al., 2003; Herrington et al., 2021; Ma et al., 2022), whereas the polarity of functional groups makes the interactions between moisture and bitumen rather complex. As described in the aforementioned transport models, it is commonly recognized that water is present in bitumen with different modes. Water molecules in a specific mode act as free with less restrictions from surrounding bitumen molecules. At high water concentration, due to the existence of polar functional groups in bitumen, water molecules not only associate with the hydrophilic sites or polar groups, but bond with water molecules through hydrogen bonds (Lemarchand et al., 2016; Liu et al., 2020; Yang et al., 2020). Both phenomena significantly decrease the diffusion coefficient of moisture in bitumen.

The objective of this chapter is to investigate the diffusion coefficient and solubility of moisture in bitumen under different temperature and relative humidity conditions. To achieve this, various transport models are introduced and compared, aiming to describe both the thermodynamic equilibrium sorption and kinetic transport of moisture on the surface and within the bulk of bitumen. The purpose of these models is to understand the transport mechanisms involved and to make predictions about moisture behavior in bitumen. In order to solve these transport models, a parameter optimization method is employed. This approach helps in finding the optimal values for the model parameters, enhancing the accuracy of the predictions.

This chapter also discusses the moisture sorption isotherms, which provide insights

into the relationship between moisture content and the equilibrium relative humidity at a specific temperature. Furthermore, the transport kinetics of moisture in bitumen are examined, shedding light on the rate at which moisture moves through the material. Additionally, the water clustering mechanism is explored to understand how water molecules interact and cluster together within bitumen. This phenomenon has implications for moisture transport and can influence the overall behavior of moisture in bitumen.

By studying the diffusion coefficient, solubility, sorption isotherms, transport kinetics, and water clustering mechanism, this chapter aims to provide a comprehensive understanding of the thermodynamics and kinetics of moisture transport in bitumen. The findings contribute to our knowledge of moisture behavior in bitumen and its impact on the performance and durability of bituminous materials.

2.2 Dynamic vapor sorption tests

2.2.1 Sample preparation

To investigate moisture transport behavior in bitumen, two fresh 70/100 penetration grade bituminous binders supplied from source V and T, and one styrene butadiene styrene (SBS) modified bitumen were used for performing gravimetric tests. These bitumens are named as V710, T710, and VPMB, respectively. The VPMB was prepared by using V710 as the base binder and adding 4 wt% (by bitumen weight) SBS, which is a linear block copolymer with 28.5% styrene. For the preparation of the samples, first a small amount of bitumen was cut from the stored bitumen and weighed in a high-precision scale to a weight of 40±1 mg; subsequently the bitumen was placed in an aluminum pan with 2.75mm height and 8mm diameter and then heated at 160 °C for approximately 60 seconds to allow bitumen to spread on the bottom of sample pan and create a thin film.

2.2.2 Experimental procedure

The gravimetric tests were conducted using the Dynamic Vapor Sorption (DVS) system from Surface Measurement Systems (SMS) Ltd (Fig. 2.1 (a)). Throughout the experiment, temperature, relative humidity (RH), and mass change were precisely controlled and recorded. The system measures the change of sample mass with a resolution of 0.1 µg (=2.5×10^{-6} of the initial sample weight). Relative humidity is controlled by mixing and adjusting the ratios of saturated water vapor and pure dry carrier gas. A vapor stream at a specified relative humidity is introduced into the sample chamber with a recommended flow rate of 200 sccm (cm^2/min). It is suggested that such flow rate ensures the instantaneous resupply of moisture concentration loss above sample surface due to sorption of bitumen, thus providing a constant boundary condition. In addition, such gas flow rate could accelerate the transport process with little effect on the isotherm results (Arthur et al., 2014; Gritti & Guiochon, 2005). To replicate the actual situation in the atmosphere, dry air was used as carrying gas. The effect of oxidative ageing on the sample mass change and transport behavior was neglected considering the low temperatures (10 °C – 40 °C) and short test periods (8 to 17 days).

To determine when a sample has reached moisture sorption equilibrium, often a dm/dt (change in mass within a unit time) criterion is adopted, in which equilibrium is defined when limited change in mass occurs over a specified time period. However, for the moisture transport tests, the mass change rate in the bitumen samples was smaller than the

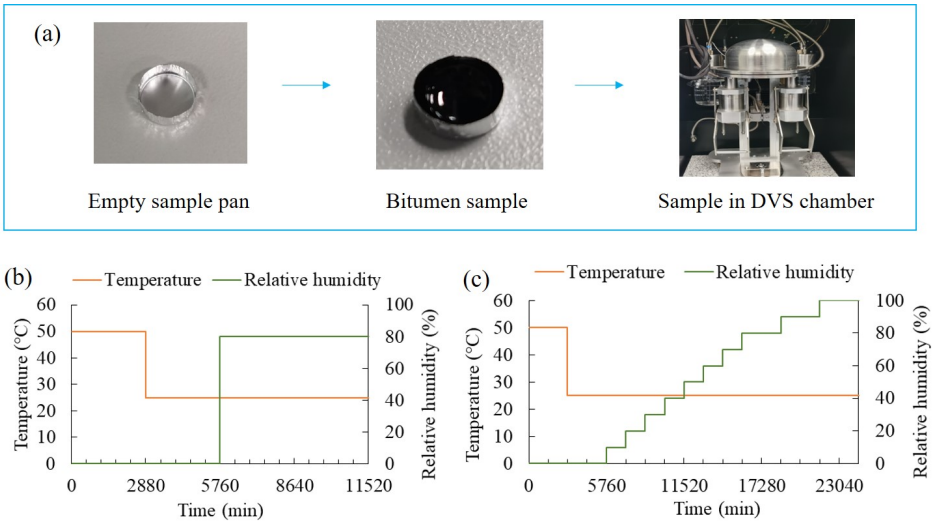

Figure 2.1 (a) Moisture transport measurement procedures and DVS tests for moisture transport via (b) constant RH and (c) multi-step RH methods.

dm/dt value caused by the instrument balance fluctuation in most cases. With the dm/dt method, the test will never be completed due to the dm/dt criterion but because of the achievement of the specified maximum step time. For this reason, a maximum time was set for the moisture transport tests. A series of trial tests were performed to define the duration of the humidity steps so as to ensure that samples would reach equilibrium. On the basis of the trial tests, a drying step of two (2) days at elevated temperature (55 °C) was applied to rapidly remove any pre-existing moisture in the bitumen samples, as well as the subsequent 2 days at the intended test temperature to continue drying and provide a steady temperature environment for further vapor loading.

Two test methods were applied to study the moisture transport behavior, namely the constant RH and the multi-step RH tests (Fig. 2.1 (b) and (c)). The constant RH method consists of two steps i.e. 4-day drying and 4-day RH loading at 80%, which is approximately the average relative humidity in Netherlands (KNMI, 2020). The binders (V710, T710, and VPMB) were tested using constant RH method at the temperatures of 10 °C, 25 °C, 40 °C (and 55 °C exclusively for V710) to investigate the effect of temperature on the moisture transport kinetics of three types of bitumen. For the multi-step RH protocol, after the drying step, RH is applied from 0% to 100% with a step size of 10% (Harley et al., 2012). The moisture transport of V710 at three temperatures (10 °C, 25 °C, 40 °C) was measured following the multi-step RH protocol to measure the moisture sorption isotherms at different temperatures.

2.2.3 Surface area measurement

During sample preparation, due to the high surface energy of aluminum, bitumen in the sample pan tends to flow and adhere to the side walls when heated, forming a upward concave surface when heating as seen in Fig. 2.2. To accurately characterize the dis-

tribution of bitumen in the sample pan, a Digital Microscope VHX-7000 with 100x lens from Keyence was used to determine the surface shape of bitumen. Bitumen, as a black petroleum residue, absorbs most of the lights from LED light source, making it difficult to measure the surface structure. Therefore, some hydrated lime filler (Wigro 60K) was spread on the sample surface to create a thin grey film. The filler has a percentage passing of 83% for the sieve size of 0.063mm, much smaller than the thickness of bitumen film, thus having limited effect on the measured results. The concave surface curve of half a 2D cross section (assuming symmetrical cross section over the center) was fitted using the ellipse equation. Three samples with same preparation procedures were measured to determine the average height of the ellipse (h_e in Fig. 2.2). The bitumen sample surface thus composes of a disc with the height of h_c and a disc with height of h_e subtracted by a ellipsoid having the same height of h_e. Using the symmetry axis in the specimen center, half of a vertical cross section along the specimen diameter, as depicted in Fig. 2.2, was modeled for further modeling.

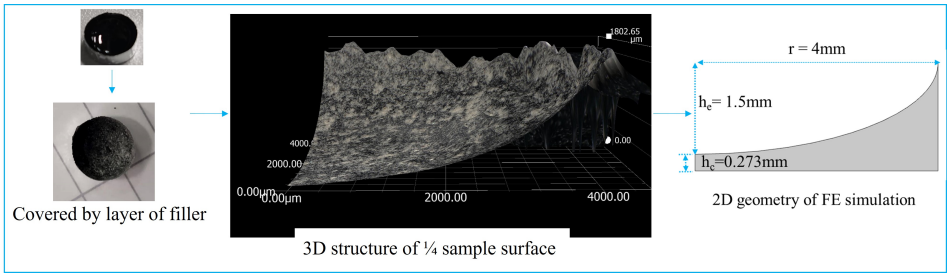

Figure 2.2 Microscopy measurement of bitumen surface and derived 2D geometry.

2.3 Transport kinetics models

The transport of moisture from environment to bitumen is considered to occur in two stages. Specifically, it is assumed that water molecules are first adsorbed on the bitumen surface establishing a constant surface water concentration. These adsorbed molecules then diffuse into bulk bitumen due to the presence of a concentration gradient. Adsorption is theoretically much faster than bulk diffusion, considering that the adsorption is a surface phenomenon with a wider area exposed to the adsorbate while absorption is a bulk behavior facing more resistance of the internal interaction forces (Adamson & Gast, 1997; Bird et al., 2002).

The pseudo-first order (PFO) model proposed by Lagergren is widely used to describe the adsorption kinetics (Ho & Mckay, 1998), suggesting an adsorption rate equation following the first order relationship, which can also be described as the linear driving force model (Sun et al., 2015)

$$\frac{\mathrm{d}s}{\mathrm{d}t} = \alpha\,(S_\mathrm{m} - S) \tag{2.1}$$

, where S denotes the adsorbed moles of gas per gram, S_m is the maximum adsorbed value, and α is the adsorption rate constant. From Eq. 2.1, assuming the initial value of S

is 0, we can get the solution of the PFO model

$$S = S_m\left(1 - e^{-\alpha t}\right) \tag{2.2}$$

Bulk absorption refers to the thermodynamic equilibrium state of diffusion in a bulk with no macro voids. The diffusion process is generally described by Fick's law (Crank & Park, 1968). Fick's first law illustrates that the diffusion flux is proportional to concentration and Fick's second law describes how the concentration changes with time. When diffusion coefficient is independent of the concentration, Fick's second law is defined as

$$\frac{\partial c}{\partial t} = D\nabla^2 c \tag{2.3}$$

where D is the diffusion coefficient, t is the time, and c is the concentration of diffusing species.

Non-Fickian diffusion can occur when the diffusing gas/vapor shows polarity such as water and the absorbent contains polar groups such as bitumen. The dual-phase diffusion model has been proposed to describe the moisture transport behavior in such a situation (Vieth et al., 1976). This model assumes that diffused molecules have two states: one state describes molecules that are free to diffuse and the other state refers to molecules fixed to certain sites or having much slower diffusion rate. Both states still follow Fick's law but with two different diffusion coefficients D_1 and D_2 (Maggana & Pissis, 1999):

$$\frac{\partial c_1}{\partial t} = D_1\nabla^2 c_1 \tag{2.4}$$

$$\frac{\partial c_2}{\partial t} = D_2\nabla^2 c_2 \tag{2.5}$$

$$c_{moi} = c_1 + c_2 \tag{2.6}$$

where c_1 is the free water concentration, c_2 is the bound water concentration, and c_{moi} is the total water concentration.

Besides, in the cluster model developed by Park (Harley et al., 2012; Park, 1986), at lower partial pressure, the water solubility is proportional to its partial pressure as indicated by Henry's law. As the water partial pressure increases, the bulk water concentration is quite high, thus causing the binding of a certain number of water molecules with each other or with functional groups of bitumen through hydrogen bonds:

$$n H_2O \rightleftharpoons (H_2O)_n \tag{2.7}$$

, where n represents the water number in a cluster.

The water concentration in the cluster mode can be described according to

$$c_{cu} = \frac{K_c\,(K_d P)^n}{n} \tag{2.8}$$

, where, K_c is the equilibrium constant for the clustering reaction, K_d is the Henry's law solubility coefficient, P is the water partial pressure, and $K_d P$ is the water concentration in Henry's mode. The equation can be further converted to

$$c_{cu} = \beta\mathscr{H}\left(c_H, c_H^0\right)\left(c_H - c_H^0\right)^n \tag{2.9}$$

, where c_{cu} is the water concentration in clustering mode, c_H is the concentration in Henry's mode, c_H^0 is the threshold of clustering, β is the clustering coefficient, $\mathscr{H}$ is the Heaviside step function, and n is the average number of water molecules in an agglomeration.

The overall bulk concentration is composed of the water concentration in Henry's mode and in clustering mode:

$$\frac{\partial c_b}{\partial t} = \frac{\partial c_H + \partial c_{cu}}{\partial t} = D\frac{\partial^2 c_H}{\partial x^2} \tag{2.10}$$

where c_b is bulk water concentration, D is the Henry's diffusion coefficient. The water in clustering mode is considered not to participate in the diffusion process. According to Eq. 2.9, the time differential of clustering concentration is

$$\frac{\partial c_{cu}}{\partial t} = \beta n \left(c_H - c_H^0\right)^{n-1} \frac{\partial c_H}{\partial t} \tag{2.11}$$

Therefore the diffusion kinetics is defined by

$$\left(1 + \beta n \left(c_H - c_H^0\right)^{n-1}\right) \frac{\partial c_H}{\partial t} = D\frac{\partial^2 c_H}{\partial x^2} \tag{2.12}$$

Based on Eq. 2.10, the pseudo diffusion coefficient can be defined as

$$D_{pse} = \frac{D}{(1 + \beta n (c_H - c_H^0)^{n-1})} \tag{2.13}$$

To study the moisture transport mechanisms and characterize the moisture transport kinetics of bitumen, three models, namely the S-Fick model, the Dual model, and the S-Cluster model were proposed and compared based on their capability to simulate the water transport behavior in bitumen in terms of surface adsorption and bulk absorption. Specifically, in the S-Fick model, surface adsorption is represented by the pseudo first-order equation (Equation 2.2) and the bulk adsorption follows Fick's law of diffusion (Equation 2.3). Four parameters need to be determined, including the maximum surface adsorption mass $s_{m,sf}$, the adsorption rate constant α_{sf}, the saturated bulk absorption concentration $c_{sat,sf}$, and the bulk diffusion coefficient D_{sf}. The Dual model assumes two water transport modes, both following Fick's law with specific diffusion coefficients (Equations 2.4 – 2.6), hence with four unknown parameters, i.e., the saturated moisture concentration c_1 and the diffusion coefficient D_1 of the first transport mode, and the saturated moisture concentration c_2 and the diffusion coefficient D_2 of the second transport mode. The S-Cluster model describes surface adsorption using the pseudo first-order equation (Equation 2.2), whereas bulk absorption is modelled by the water cluster model (Equation 2.12), where the threshold of clustering c_H^0, the clustering coefficient β, the average number of water molecules n in a agglomeration, the maximum surface adsorption mass $s_{m,sc}$, the adsorption rate constant α_{sc}, the saturated bulk absorption concentration $c_{sat,sc}$, and the Henry's bulk diffusion coefficient D_{sc} are the required parameters. These unknown parameters for the three transport models are summarized in Table 2.1.

2.4 Finite element simulation and optimization

The finite element (FE) method was used to simulate the moisture transport behavior in bitumen through COMSOL Multiphysics. Triangular elements were utilized to mesh the 2D bitumen geometry. For the FE simulations, no flux was specified for all boundaries, except for the surface, and the initial water concentration of the bitumen was assumed to be zero. The surface water concentration (namely the adsorbed water concentration) was set to be constant for the bulk diffusion process, considering the much faster equilibrium of surface adsorption. The three transport models were then used in the simulations, respectively. Providing initial guesses for the unknown model parameters, the overall mass change with time was simulated by spatial integration of the moisture concentration in the bitumen film. Subsequently, the unknown parameters were determined by fitting the numerical solution (simulated mass change) to the experimental data obtained from the DVS tests.

Two fundamental parts of an optimization problem are the control variables and the objective functions. Here, the control variables are the unknown parameters in the transport models as summarized in Table 2.1. The objective function is defined by the global least-squares objective function (Q)

$$Q = \sum_{t} \left(s + M \iiint c_{\mathrm{b}} - m_{\mathrm{lab}} \right)^2 \tag{2.14}$$

, where t is the vapor loading time, s represents surface adsorption mass, M is the molar mass of water, c_{b} is the bulk moisture concentration, and m_{lab} indicates the experimental mass change. The overall optimization procedure is displayed in Fig. 2.3 (a).

The optimization process aims to determine the values of the control variables that minimize the objective function, i.e. the difference between simulated and experimental results. The objective function is very sensitive to variations of different parameters. For this reason, prior to the optimization, a scaling transformation is applied to all parameters to ascertain a similar magnitude of values.

Table 2.1 Overview of transport kinetics models parameters

Model	Parameter	Symbol	Unit	MC range
S-Fick	Surface adsorption rate constant	α_{sf}	1/s	0.05 – 0.5
	Equilibrium surface adsorption mass	$s_{\mathrm{m,sf}}$	kg	1E-9 – 1E-8
	Bulk diffusion coefficient of moisture in bitumen	D_{sf}	m^2/s	1E-14 – 1E-11
	Saturated bulk absorption concentration of moisture	$c_{\mathrm{sat,sf}}$	$\mathrm{mol}/\mathrm{m}^3$	40 – 120
Dual	Diffusion coefficient of first transport mode	D_1	m^2/s	1E-12 – 1E-10
	Diffusion coefficient of second transport mode	D_2	m^2/s	1E-14 – 1E-11
	Saturated moisture concentration of first transport mode	c_1	$\mathrm{mol}/\mathrm{m}^3$	20 – 100
	Saturated moisture concentrationof second transport mode	c_2	$\mathrm{mol}/\mathrm{m}^3$	40 – 120
S-Cluster	Surface adsorption rate constant	α_{sc}	1/s	0.001 – 0.1
	Equilibrium surface adsorption mass	$s_{\mathrm{m,sc}}$	kg	1E-9 – 1E-8
	Number of water molecules in a cluster	n	/	1 – 3
	Clustering coefficient	β	/	0.1 – 5
	Threshold moisture concentration when cluster starts	c_{H}^0	$\mathrm{mol}/\mathrm{m}^3$	20 – 100
	Henry's bulk diffusion coefficient of moisture in bitumen	D_{sc}	m^2/s	1E-14 – 1E-11
	Saturated bulk absorption concentration of moisture	$c_{\mathrm{sat,sc}}$	$\mathrm{mol}/\mathrm{m}^3$	40 – 120

For the inverse problem (determining the values of a set of parameters providing simulated data which best match the measured data), in this case a non-linear inverse problem, an optimization method may be trapped in different local minima depending on the initial parameter estimates (seed values), as illustrated in Fig. 2.3 (b). It is therefore indispensable to give good initial guesses for the parameter optimization procedures. For this reason, the Monte Carlo (MC) method, the bound Optimization by Quadratic Approximation (BOBYQA) method (Powell, 2009), and sensitivity analysis were combined to determine the unknown parameters in the moisture transport models. The Monte Carlo Solver searches randomly the data points from the uniform distribution inside the range of values specified by the parameter bounds. The solver can find several local minima inside the specific parameter intervals (if they exist). In order to find all possible local minima with high accuracy, the parameter values should be in a wide range and the density of sampling points should be high, requiring long computation times. The BOBYQA method iteratively approximates the objective function by a quadratic model (Powell, 2009), thus obtaining a faster convergence rate. Therefore, instead of using MC to find more accurate values, BOBYQA method was further applied to optimize the parameter values.

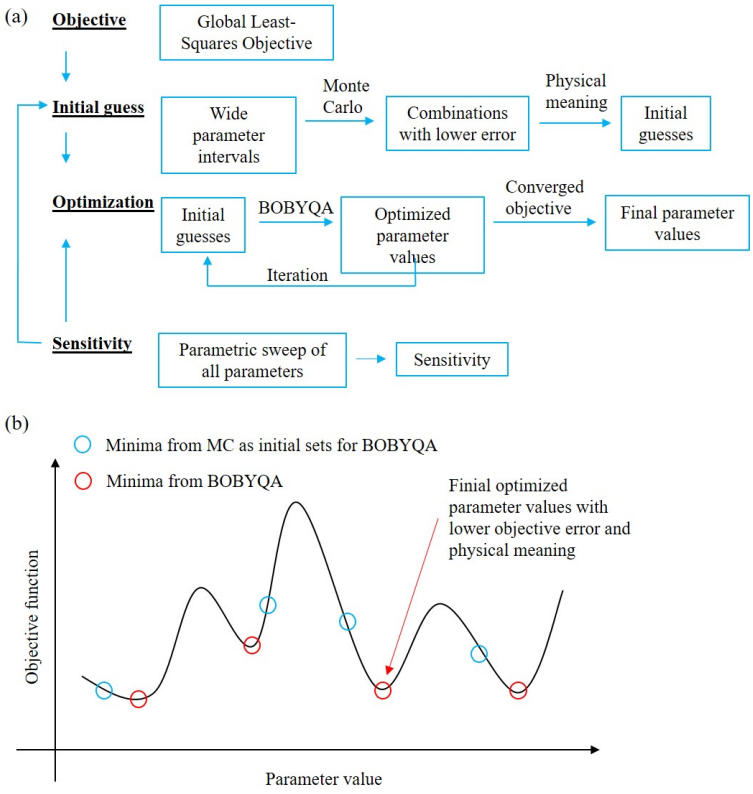

Figure 2.3 Parameter optimization: (a) Flow chart of parameter determination protocol, (b) Parameter optimization results with multiple local minima.

To conduct the parameter optimization, initial parameter values and wide parameter ranges (10 – 100 times of initial value) were determined for MC, as shown in Table 2.1, which had a relatively sparse data point distribution and considered the physical meaning of each parameter on the basis of published data from literature and experimental results (Ma et al., 2021). After obtaining optimized results from the MC process, several parameter sets with lower objective errors and appreciable difference in parameter values were chosen as initial guesses for BOBYQA optimization. The output parameters from BOBYQA optimization were used again as input to perform the BOBYQA optimization. This iteration was executed until a difference of less than 2 % in the objective function and the control variables was observed; then the optimization was assumed to reach convergence and the final optimized parameter values were obtained.

2.5 Solution, sensitivity and uncertainty of transport models

2.5.1 Model optimization

As described in the previous section, to study the moisture transport mechanism and back-calculate the moisture transport parameters including diffusion coefficient, surface adsorption, and bulk solubility, three models have been proposed and solved using a multi-optimization method. The objective function of the undetermined parameter sets in the Dual model and the corresponding objective contours are shown in Fig. 2.4 (a). MC calculates the objective function at mesh points over designated ranges. The darkest green area implies the parameter value ranges with a lower objective error, about 95 – 100 mol/m^3 for c_2 and 5^{-13} – 1.2^{-12} for D_2. The parameter ranges obtained from the MC results are still relatively high even after 10000 points evaluation. The aforementioned BOBYQA method accelerates parameter optimization based on a quadratic approximation model within a trust region with radius of 0.2 (relative to parameter value). The objective function of BOBYQA method shows a rapid convergence in 400 evaluation steps (Fig. 2.4 (b)). In this case, the lowest objective error is acquired after two iterations as an extra iteration shows the same or higher objective error.

The optimized simulation results of the three moisture transport models are illustrated in Fig. 2.5, together with the results of the classic Fick's law model. As expected, Fick's law cannot describe well the moisture transport behavior in bitumen. The proposed three models, i.e., the S-Fick, Dual, and S-Cluster models, show extremely high prediction quality.

To further evaluate the model performance with optimized parameters, three metrics are utilized. The root mean square error ($RMSD$) describes the residual amount of variations in the simulation results compared to experimental results and is defined as

$$RMSD = \sqrt{\frac{\sum_{i=1}^{N} \left(y_{i,\text{test}} - y_{i,\text{model}}\right)^2}{N}} \tag{2.15}$$

, where N is the number of data points, $y_{i,\text{test}}$ is the ith test observation value, $y_{i,\text{model}}$ is the ith model estimated value. The coefficient of determination (R^2) indicates the correlation between modelled results and experiment data:

$$R^2 = 1 - \frac{RSS}{TSS} \tag{2.16}$$

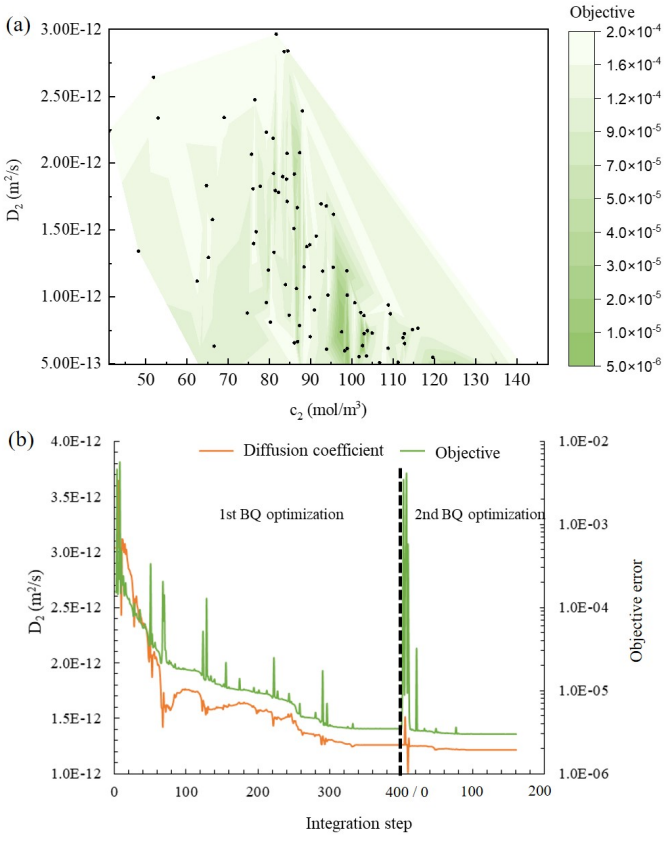

Figure 2.4 Optimization solution procedures of the Dual model for VPMB at 25°C and 80% RH: (a) Objective error contour after 10000 MC model evaluations; black symbols are parameter values with objective smaller than 2×10^{-4}; only c_2 and D_2 are shown. (b) Diffusion coefficient convergence process with two BOBYQA iterations: the 2nd iteration step used the final result from 1st BOBYQA optimization as initial parameter values.

, where TSS = sum of squares of the variation in the test data = $\sum_{i=1}^{N}\left(y_{i,\text{test}}-\overline{y_{i,\text{test}}}\right)^2$ and RSS = the residual sum of squares (the unexplained variation or the variation remaining between model and test data) = $\sum_{i=1}^{N}\left(y_{i,\text{test}}-y_{i,\text{model}}\right)^2$. R^2 is likely to increase with an increasing number of variables in a model. The adjusted R^2, which considers the number of parameters in a model, would allow us to compare models with different numbers of independent variables (Harel, 2009).

$$R^2_{\text{adjusted}} = 1-\frac{(1-R^2)(N-1)}{N-k-1} \tag{2.17}$$

, where k is the number of variables in the model.

These three metrics of the three models are reported in Table 2.2. The R^2 and R^2_{adjusted}, with values close to 1, demonstrate the great experiment-fitting capability of the three

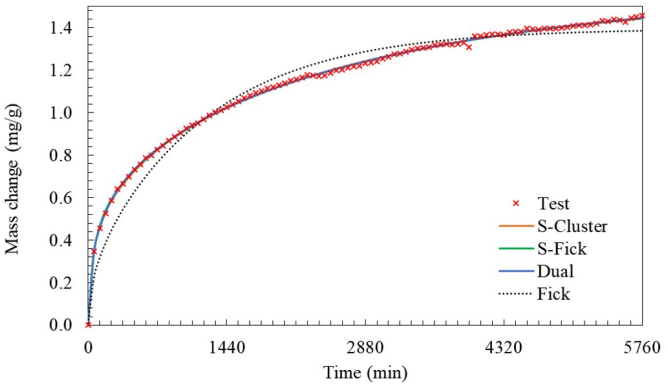

Figure 2.5 Comparison of the proposed moisture transport models results with the classic Fick's law results (denoted as Fick) for V710 at 25°C and 80% RH.

models for bitumen at various temperatures, as illustrated in Fig. 2.6 (a). The Dual model is relatively better than the S-Fick model in simulating water transport kinetics with lower *RMSE* for most cases. The S-Fick and Dual models have slightly lower performance at higher temperatures, especially at the transition point from fast to slow state diffusion, as shown in Fig. 2.6 (b). At 55 °C, the *RMSE* values for the S-Fick, Dual, and S-Cluster models are 1.0×10^{-3}, 9.0×10^{-4}, and 3.1×10^{-4} respectively indicating the superior performance of the S-Cluster model at higher temperatures where increased water sorption occurs.

2.5.2 Sensitivity analysis

Analysis was performed to investigate the sensitivity of the model results with respect to changing parameters of the moisture transport models. The impact of changing values on model outputs were evaluated individually for all parameters and locally for chosen

Table 2.2 Evaluation of moisture transport models.

Metrics		*RMSE*			R^2			$R^2_{adjusted}$		
Temperature	Models	V710	T710	VPMB	V710	T710	VPMB	V710	T710	VPMB
10 °C	S-Fick	4.10E-04	6.80E-04	6.40E-04	0.997	0.989	0.995	0.996	0.988	0.994
	Dual	3.50E-04	6.80E-04	6.50E-04	0.997	0.989	0.995	0.996	0.988	0.994
	S-Cluster	3.90E-04	6.90E-04	6.40E-04	0.996	0.988	0.995	0.995	0.987	0.994
25 °C	S-Fick	3.30E-04	2.70E-04	3.00E-04	0.999	0.999	0.999	0.999	0.999	0.999
	Dual	3.20E-04	2.50E-04	2.30E-04	0.999	1.000	1.000	0.999	0.999	1.000
	S-Cluster	3.10E-04	2.80E-04	2.70E-04	0.999	0.999	1.000	0.999	0.999	0.999
40 °C	S-Fick	4.80E-04	6.30E-04	4.90E-04	0.999	0.996	0.999	0.999	0.996	0.999
	Dual	3.10E-04	4.30E-04	4.30E-04	0.999	0.998	0.999	0.999	0.998	0.999
	S-Cluster	3.60E-04	4.00E-04	4.70E-04	0.999	0.999	0.999	0.999	0.999	0.999
55 °C	S-Fick	1.00E-03	/	/	0.996	/	/	0.996	/	/
	Dual	9.02E-04	/	/	0.997	/	/	0.997	/	/
	S-Cluster	3.06E-04	/	/	1	/	/	1	/	/

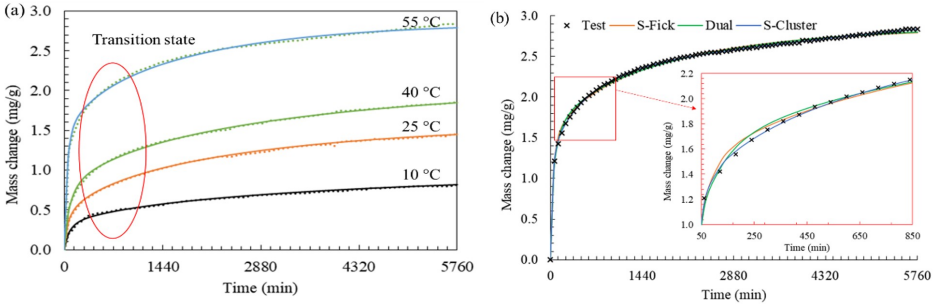

Figure 2.6 (a) Comparison between the experimental results (dotted lines) and the simulated results (solid line) of moisture sorption for V710 at 80% using S-Fick model; (b) Comparison the experiment-fitting performance of three models at 55 °C for V710 at 80%.

points (Cacuci et al., 2005). To evaluate the sensitivity of the target parameter, all other parameters are fixed to reference values, which are selected from the optimized parameter value sets. The local sensitivity behavior is dependent on the choice of the reference parameter values, which should be treated with caution. The target parameter change ranges from 0.1 to 2 or to 10 (dependent on parameters) times the reference value.

The dependence of objective function on parameter changes is shown in Fig. 2.7. In the S-Fick model, D_{sf}, $c_{sat,sf}$, and $s_{m,sf}$ show comparable effects on the objective function, while α has less impact on the model outputs, which indicates more difficulty in determining the optimal value of α. All parameters acquire their minimum objective function at the point of the reference values, suggesting a well-optimized parameter value sets. From the seven parameters in the S-Cluster model, $s_{m,sc}$, n, D_{sc}, $c_{sat,sc}$, and c_H^0 have high sensitivity to variations in the initial values and β, α are less sensitive. The unsymmetrical sensitivity with respect to the minima axis, especially for n, β, α, and c_H^0, highlights extra attention during optimization procedures.

2.5.3 Sources of uncertainty in moisture sorption results

Three main factors were identified that can cause uncertainties in the moisture sorption results, namely the inherent balance drift of DVS, the measurement stability, and the sample properties. The DVS system relies on a micro balance to measure the mass change of samples during moisture sorption tests. However, the balance experiences an inherent drift over time, which can affect the accuracy of the measurements. The drift is observed as an increase or decrease in the measured mass with time when no actual mass change occurs; its direction is independent of temperature and other environmental conditions. This balance drift needs to be accounted for and minimized to obtain reliable and precise results. The balance drift was characterized by measuring the mass change of empty sample pans using the constant RH method at the test temperatures (10 °C, 25 °C, 40 °C). The calibrated balance drift of DVS is ± 0.002 mg/4 days at all test temperatures. The moisture

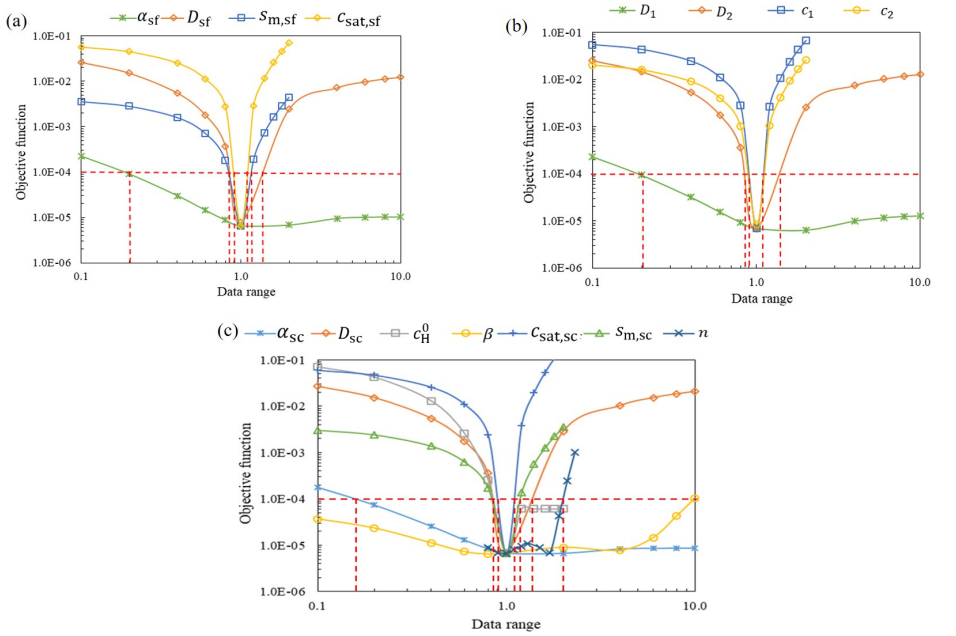

Figure 2.7 Parameter sensitivity analysis of (a) S-Fick model, (b) Dual model, and (c) S-Cluster models using reference parameter values from the optimized results of sample V710 at 25°C and 80% RH. Red dashed lines highlight the variation in each parameter that leads to a objective function value of 1e-4.

sorption mass in the constant RH test results is ca. 0.03 – 0.1 mg (dependent on temperature and bitumen type), suggesting an systematic error limit of 2.0% – 6.3% due to the balance drift. The sample loading process with sample contamination, equipment contact, and the surrounding interference are specified as the measurement stability, which could also affect the measured moisture mass change of the DVS. What's more, bitumen samples have different sample mass and film thickness. Specifically, the bitumen sample mass is controlled in the range of 40 ± 1 mg and the measured h_e height is in the range of 1.3 mm – 1.7 mm.

To examine how the repeatability of moisture sorption tests is affected by measurement stability and sample properties, three V710 samples were measured at 25 °C following the same preparation and testing procedures. Any contaminations such as dust in the sample pan can have a noticeable effect on moisture sorption, especially during the initial state when contamination adsorption occurs. External interference, such as the disturbance of DVS equipment caused by changes in testing temperature or relative humidity can also affect the results. Fig. 2.8 (a) show that initially (mostly surface adsorption), the three samples have large differences in the mass change rate. This rate tends to become more similar at later times until the end of the test. Therefore the surface adsorption is excluded using the S-Cluster model and the repeatability of bulk absorption is then determined (Fig. 2.8 (b)). The relative errors (standard deviation / mean value) of

the measured equilibrium sorption (adsorption and absorption) and the measured equilibrium absorption at 25 °C are approximately 15.3% and 4.3%, respectively. The 4.3% deviation from average sorption generates an objective error of ca. 1.0×10^{-4}. According to Fig. 2.7, for the maximum surface adsorption, bulk solubility, and diffusion coefficient in the three diffusion models, this deviation of measured sorption mass could lead to a parameter uncertainty of ± 15%. The alpha and beta are less sensitive to sorption mass, therefore the uncertainty of the optimized values is much higher.

Except for the uncertainty of experimental sorption mass, the FE geometry could also affect the accuracy of optimized parameter values. Fig. 2.8 (c) depicts the sorption results using two geometries with and without curved surface. The curved surface has a larger area directly exposed to vapor, as a result, faster sorption is seen in the beginning. As shown in Fig. 2.8 (d), the ellipsoid height variation between 1.3 mm and 1.7 mm has a limited effect on the moisture sorption, while the sample of 40 ± 1 mg causes 2.6% sorption difference. To reduce the relative systematic errors, increase the repeatability of moisture sorption tests, and obtain transport parameters with lower uncertainty, it is recommended to increase sample mass and have more replicate tests for future tests.

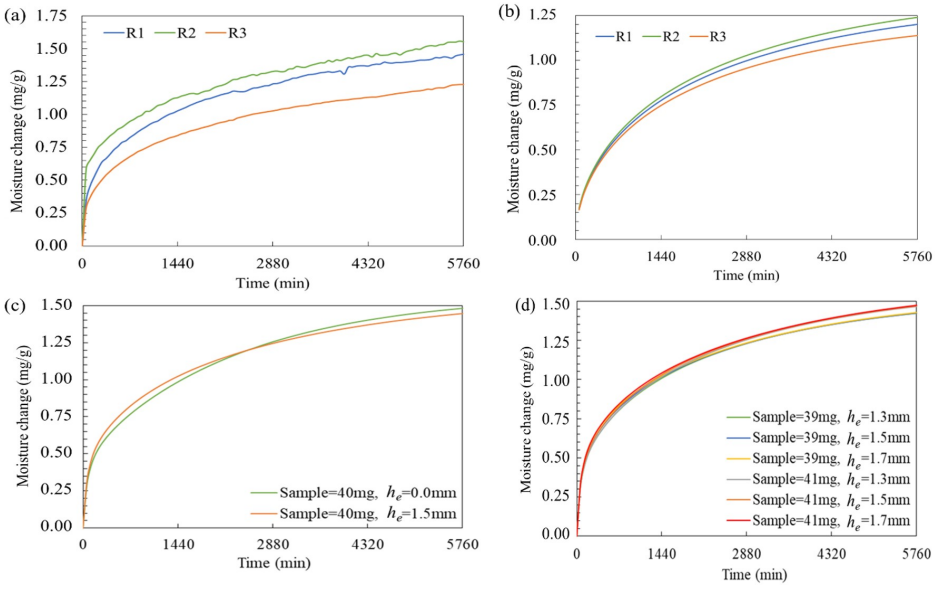

Figure 2.8 (a) Moisture sorption curves for three replicate samples (R1, R2, R3) of bitumen V710 at 25 °C; (b) Moisture bulk absorption curves derived from the total sorption curves using the S-Cluster model for the three replicate samples; (c) Effect of bitumen film shape on moisture sorption for V710 at 25 °C using the S-Cluster model; (d) Effect of sample mass and ellipsoid height on moisture sorption for V710 at 25 °C using the S-Cluster model. The model parameter values are the same for all cases in (c) and (d), except for the sample mass and ellipsoid height.

2.6 Moisture transport in fresh bitumen

2.6.1 Moisture transport behavior

Moisture transport at high relative humidity

Fig. 2.9 shows the experimental moisture sorption of three binders at multiple temperatures and 80% relative humidity. The fast sorption rate is appreciable at the initial stage which is assumed to be combined surface adsorption and bulk absorption. At the slow state, the mass increase rate (the slope at each point) decreases rapidly, where the surface adsorption is close to the equilibrium state and mass increase is mainly due to the bulk diffusion in bitumen. The equilibrium moisture sorption amount and sorption rate increase with temperature for all bitumen types. All three bitumen types display different transport behavior. Apparently, at the same temperature, the SBS-polymer modified bitumen (VPMB) shows much higher sorption amount than the base bitumen (V710 and T710), and T710 has a slightly faster sorption rate compared to V710.

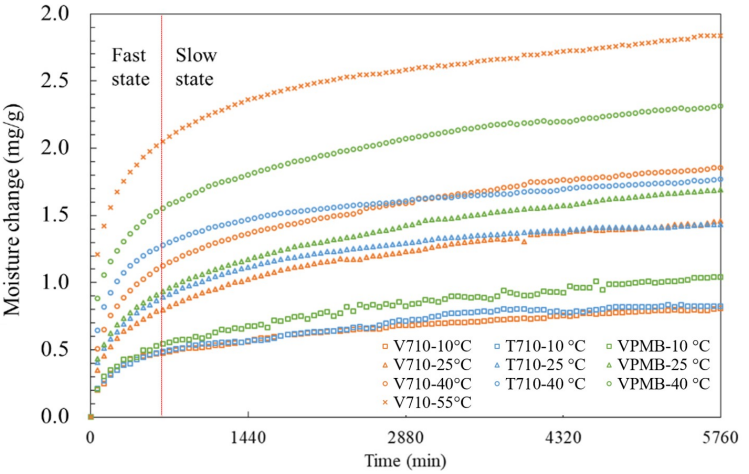

Figure 2.9 Moisture sorption of bituminous binders at different temperatures and 80% relative humidity for four days (data is collected every second; in the graph only one data point for every 60 minutes are plotted).

Table 2.3 and Table 2.4 list the optimized parameter values of the Dual, S-Fick, and S-Cluster models, respectively, for three bitumen types. The Dual model and S-Fick models decompose the overall sorption into two modes; the Dual model assumes both modes following Fick's law with different diffusion coefficients and the S-Fick model assumes one mode belonging to surface adsorption and the other mode to bulk absorption. Both models discern two transport types, one with faster transport rate and the other with slower transport rate as shown in Table 2.3 and 2.4. One challenge here is to identify whether the faster transport mode belongs to surface adsorption as assumed by the S-Fick model or another bulk diffusion type. Many studies have discussed adsorption and absorption processes of water in organic materials (Cheng et al., 2003; Wel & Adan, 1999). Adsorption normally displays faster rate than absorption due to fewer barriers from the surrounding components. Table 2.3 and Table 2.4 indicate that the saturated moisture concentration

Table 2.3 Optimized parameters of the Dual model at 80% RH and different temperatures (T)

Dual	T (°C)	c_1 (mol/m³)	c_2 (mol/m³)	D_1 (m²/s)	D_2 (m²/s)	Objective
V710	10	15.3	40.2	3.00E-11	9.20E-13	8.00E-06
	25	15.0	75.8	4.50E-11	1.60E-12	4.90E-06
	40	34.9	89.9	2.70E-11	1.00E-12	4.80E-06
	55	72.1	92.2	6.60E-11	2.30E-12	3.90E-05
T710	10	12.8	49.4	3.00E-11	7.60E-13	1.70E-05
	25	13.5	69.7	8.40E-11	2.90E-12	2.00E-06
	40	52.9	53.4	3.00E-11	1.60E-12	8.80E-06
VPMB	10	9.6	60.3	4.30E-11	1.10E-12	9.80E-06
	25	21.0	92.4	4.20E-11	1.10E-12	2.70E-06
	40	48.5	91.0	7.70E-11	1.80E-12	8.90E-06

Table 2.4 Optimized parameters of the S-Fick model at 80% RH and different temperatures (T)

S-Fick	T (°C)	D_{sf} (m²/s)	α_{sf} (1/s)	$s_{m,sf}$ (kg)	$c_{sat,sf}$ (mol/m³)	Objective
V710	10	9.50E-13	0.012	9.00E-09	43.2	9.20E-06
	25	1.70E-12	0.015	9.70E-09	76.1	5.20E-06
	40	1.40E-12	0.011	2.10E-08	88.5	1.10E-05
	55	2.60E-12	0.022	4.70E-08	95.3	4.90E-05
T710	10	1.00E-12	0.012	7.80E-09	47.0	2.30E-05
	25	2.80E-12	0.018	1.00E-08	69.1	2.60E-06
	40	2.50E-12	0.013	3.00E-08	58.7	1.90E-05
VPMB	10	1.00E-12	0.012	6.60E-09	60.5	1.20E-05
	25	1.20E-12	0.014	1.40E-08	91.8	4.30E-06
	40	1.90E-12	0.023	3.30E-08	91.9	1.20E-05

of the faster mode in the Dual model is comparable to the surface adsorption of S-Fick model. Consequently, the faster transport mode in the Dual model is assumed to be surface adsorption. In this context, the surface adsorption rate is more than ten times faster than bulk absorption based on the parameter values of the Dual model.

The optimized parameters in the S-cluster model is shown in Table 2.5. For the S-Cluster model, when the Henry's absorption is lower than the cluster threshold c_H^0, the S-Cluster model is the same as the S-Fick model. The bulk absorption in Henry's mode gradually increases with time, along with the generation of water cluster when the Henry's concentration is higher than c_H^0. The V710 and T710 binders display similar cluster size, which is larger than binder VPMB at all temperatures. The smaller water cluster size in the SBS modified bitumen could be due to the internal structure of the bitumen-polymer systems limiting the formation of water clusters (Sengoz et al., 2009).

Moisture transport at multi-step relative humidities

Fig. 2.10 shows the isotherm results of V710 at three temperatures. A linear correlation between relative humidity and moisture content can be observed when relative humidity is below 70% – 80%. At high relative humidities, sorption isotherms deviate from the linear state, indicating a different moisture sorption mechanism. The overall sorption amount increases with temperature at nearly all the RH steps.

To describe the moisture transport kinetics at all humidities (10% – 100%), the S-

Table 2.5 Optimized parameters of the S-Cluster model at 80% RH and different temperatures (T)

S-Cluster	T (°C)	D_{sc} (m²/s)	α_{sc} (1/s)	n	$s_{m,sc}$ (kg)	β	c_H^0 (mol/m³)	$c_{sat,sc}$ (mol/m³)	Objective
V710	10	1.10E-12	0.01	1.13	5.90E-09	0.41	42.9	47.6	8.50E-06
	25	2.10E-12	0.017	1.28	8.80E-09	0.9	67.0	75.2	4.70E-06
	40	3.20E-12	0.017	1.68	1.50E-08	0.92	69.0	80.3	8.20E-06
	55	5.50E-12	0.03	1.9	3.90E-08	1.01	87.0	94.6	4.30E-06
T710	10	1.60E-12	0.01	1.32	8.30E-09	0.4	35.3	41.2	2.40E-05
	25	3.00E-12	0.014	1.42	1.10E-08	0.85	63.4	67.6	3.90E-06
	40	4.60E-12	0.015	1.52	2.60E-08	0.91	53.1	59.0	6.40E-06
VPMB	10	1.80E-12	0.01	1.03	5.40E-09	0.56	39.3	54.2	1.10E-05
	25	2.70E-12	0.016	1.26	1.20E-08	0.42	52.5	74.2	3.50E-06
	40	3.60E-12	0.036	1.31	2.80E-08	1.08	75.0	86.2	9.00E-06

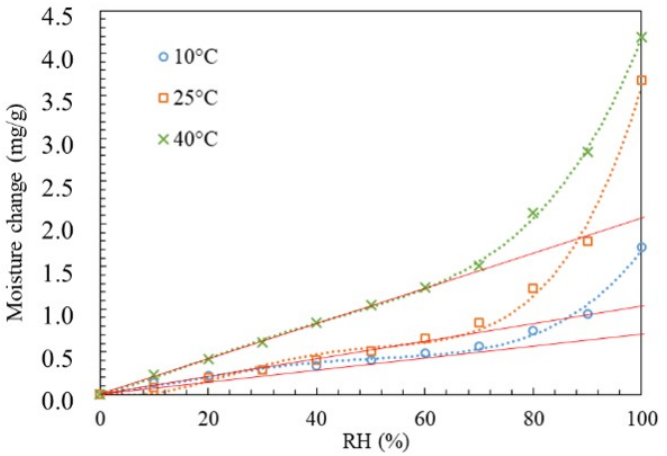

Figure 2.10 Isotherm curves of V710 at different temperatures (i.e. 10 °C, 25 °C, and 40 °C). The dotted lines are fitting results using 4-order polynomial and the red lines indicate the sorption before 70% – 80% RH when moisture content increases linearly with relative humidity.

Cluster model was used due to its better performance at higher sorption amount as illustrated in Fig. 2.6 (b). The S-Cluster model was simplified into the S-Fick model at low RH steps when the Henry's concentration is lower than the cluster threshold. The overall sorption of V710 at three temperatures was then decomposed into surface adsorption, Henry's absorption and clustering as depicted in Fig. 2.11. Both surface adsorption and bulk absorption display approximately linear relationship with relative humidity before ca. 70% RH. At higher relative humidities, bulk water clustering occurs and the moisture soprtion amount increases rapidly with relative humidity, highlighting that cluster formation is the dominant mechanism at this stage.

2.6.2 Moisture diffusion coefficient

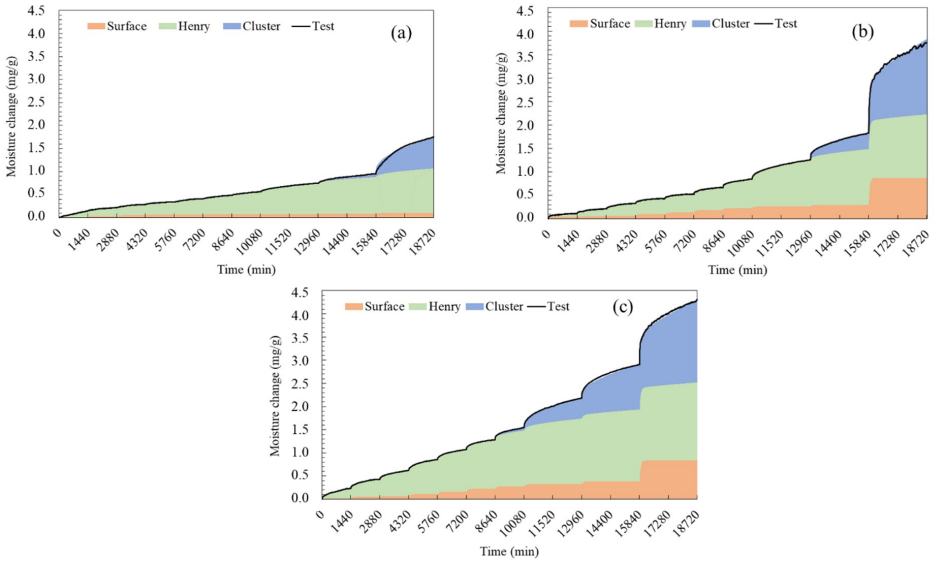

Figure 2.11 Multi-step sorption tests and simulation results using the S-Cluster model of the V710 binder at temperatures of (a) 10 °C, (b) 25 °C, and (c) 40 °C.

Moisture diffusion coefficient at the relative humidity of 80%

Diffusion is an activated process, thus the diffusion coefficient increases with temperature. The dependence of the diffusion coefficient on temperature follows the Arrhenius equation (Neogi, 1996):

$$D = D_0 \mathrm{e}^{\frac{-E_\mathrm{A}}{RT}} \tag{2.18}$$

, where D is the diffusion coefficient, D_0 is the maximum diffusion coefficient, E_A is the activation energy for diffusion, T is the temperature, and R is the universal gas constant. The equation can be modified to a linear expression:

$$\ln D = \ln D_0 - \frac{E_\mathrm{A}}{RT} \tag{2.19}$$

The fitting of the diffusion coefficients in the three models are shown in Fig. 2.12 (a), (b), and (c), respectively. From Fig. 2.12 (a) and (b), it can be observed that the diffusion coefficients obtained from the Dual model and the S-Fick model contradict the assumption of an Arrhenius-type temperature dependence, whereas the diffusion coefficient in the S-Cluster model conforms to the Arrhenius equation (Fig. 2.12 (c)).

Two opposing mechanisms may cause the abnormal change in the bulk diffusion coefficient in the Dual and S-Fick models with temperature: moisture absorption and the formation of water clusters increases with temperature (Table 2.5), leading to a decrease in the real-time diffusion coefficient; higher temperature increases the moisture diffusion coefficient by increasing its kinetic energy. Since the diffusion coefficients obtained from the S-Fick and Dual models represent an average value over the whole testing period, it thus fail in following the Arrhenius equation. In contrast, the S-Cluster model eliminates

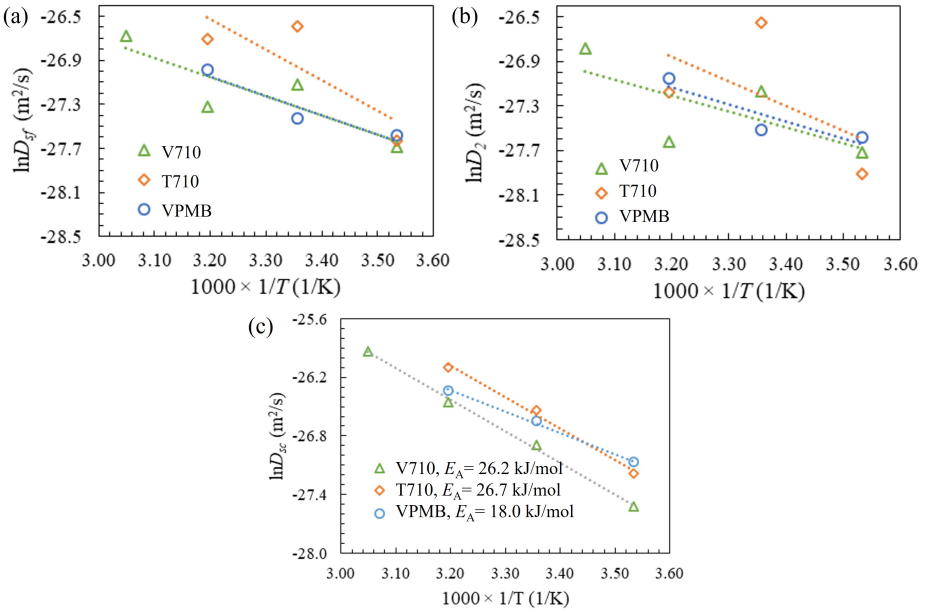

Figure 2.12 Temperature dependence of diffusion coefficients in the (a) S-Fick model, (b) Dual model, and (c) S-Cluster model, where dotted lines are the fitting of the Arrhenius equation.

the effect of clustering and acquires the Henry's diffusion coefficient in bitumen, thus showing the typical increase with temperature.

Fig. 2.12 (c) also shows the activation energy of the three bitumen types. A higher activation energy physically denotes a more difficult diffusion of water molecules within bituminous binders, which can be affected by their physiochemical and structural properties. The V710 and T710 present comparable activation energy, indicating that bitumen with the same penetration grades may demonstrate similar activation energy. Compared to the two unmodified bitumens, the activation energy of VPMB is higher. This increase is attributed to the formation of a polymer network within the bitumen, which may change the hopping barriers for water molecules.

Effects of relative humidity on diffusion coefficient

Fig. 2.13 (a) shows the change in moisture diffusion coefficient in V710 with Henry's concentration at 80% RH based on Eq. 2.13. As expected based on Section 2.3, the diffusion coefficient is shown to decrease with increasing water concentration due to the formation of water clusters and the resulting immobilization of more water molecules through hydrogen bonding.

Fig. 2.13 (b) exhibits the Henry's moisture diffusion coefficient in V710 as a function of RH. For the multi-step RH sorption, the S-Cluster model was utilized to solve the transport kinetics at every RH step with the presence of moisture already absorbed from the previous RH steps. The Henry's diffusion coefficients obtained from the multi-step RH

tests are close to the values calculated from the tests at 80% RH, as indicated in Table 2.5. A general decreasing trend of Henry's diffusion coefficient can be observed as the relative humidity increases (absorption increases), which indicates that the diffusion coefficient of Henry's sorption is not exactly constant as the S-Cluster model assumes. However, this decline is much slower than the effect of clustering behavior (Fig. 2.13 (a)). Therefore, neglecting the decrease with increasing Henry's concentration is considered acceptable.

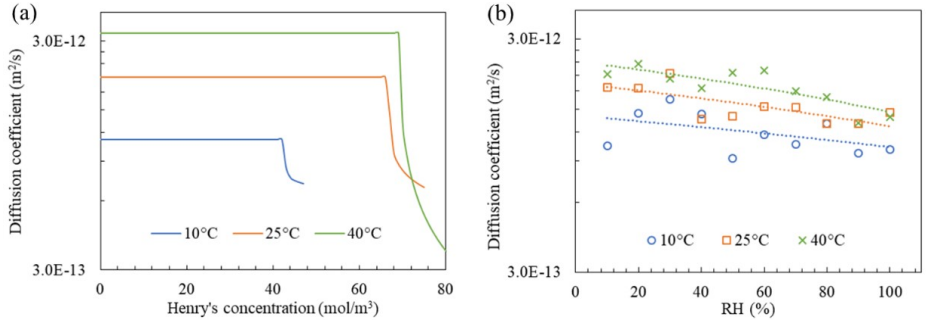

Figure 2.13 (a) Moisture diffusion coefficient change versus Henry's concentration at 80% RH in V710 (using the S-Cluster model); (b) moisture diffusion coefficient (optimized by applying the S-Cluster model to each of the multi-step RH sorption results) in V710 as a function of RH level.

2.6.3 Thermodynamics of moisture transport

Isothermal surface adsorption and bulk absorption

The S-Cluster model decomposes the overall moisture sorption into surface adsorption and bulk absorption, as depicted in Fig. 2.14 (a) and (b), respectively. The pronounced increase in sorption observed at 100% RH and 25 °C in Fig. 2.10 can be assigned to the high surface adsorption of moisture as indicated in Fig. 2.14 (a). The DVS equipment used in this work was calibrated at 25 °C, where almost 100% RH can be actually generated for a target 100% RH. However, at higher temperatures, the actual RH in the sample chamber reaches only 96% – 97% RH when targeting 100% RH. Compared to higher temperatures, the saturated vapor partial pressure (100%) was loaded for the bitumen sample at 25 °C. This means that the capacity for the air to hold additional moisture is at its limit. Therefore, a significant amount of water condensation can be expected, leading to extremely high surface adsorption.

Two factors influence the surface adsorption, namely temperature and vapor partial pressure (with relative humidity being the ratio of vapor partial pressure and saturated vapor partial pressure). Physical adsorption of vapor to the solid surface is accompanied by a decrease in entropy and free energy of the system, and decreases with increasing temperature. However, surface adsorption also increases with vapor partial pressure, which in turn increases with temperature for each RH step. These two contradicting factors are responsible for the changes in adsorption isotherms with varying temperature (Fig. 2.14 (a)).

The Clausius-Clapeyron equation (Poyet & Charles, 2009) was used to describe the

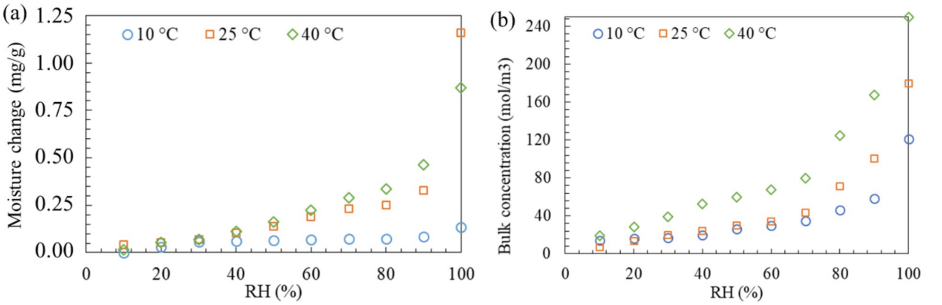

Figure 2.14 Decomposed isotherm curves of V710 using the S-Cluster model: (a) surface adsorption, and (b) bulk absorption.

isosteric heat of sorption Q_{st}:

$$\frac{\partial \ln p}{\partial (1/T)} = \frac{Q_{st}}{R} \tag{2.20}$$

The total isosteric heat of sorption was calculated based on the three sorption isotherms at different temperatures. The computed values range from -42.13 to -35.85 kJ/mol, with the minus indicating an overall exothermic moisture sorption. This heat of sorption results from both the surface adsorption and bulk absorption processes. Surface adsorption process can be divided into two steps: the condensation of vapor and the formation of interactions between water molecules and bitumen components. The energy required for the former, namely, the heat of water condensation, is -43.99 kJ/mol. The latter is expected to further release energy due to formation of the van der Waals and hydrogen bonding interactions between water and surface bitumen molecules. Therefore, the isosteric heat for the water surface adsorption should be lower than -43.99 kJ/mol. The higher heat of sorption (-42.13 – -35.85 kJ/mol) obtained indicates that water absorption within bitumen leads to less energy release compared to the total isosteric heat of sorption or even positive energy intake in order to counterbalance the energy release caused by water adsorption (< -43.99 kJ/mol).

To verify this hypothesis, the enthalpy for water absorption in Henry's mode was calculated through determining the temperature dependence of Henry's constant using the Arrhenius equation, as shown in Fig. 2.15. The enthalpy of dissolution in Henry's mode calculated for the three bitumen types is in the range of -33.9 to -35.9 kJ/mol, which supports the inference that the heat of sorption for bulk absorption is higher than that of the overall sorption calculated using the Clausius-Clapeyron equation.

Moisture solubility at low relative humidity

The Flory-Huggins solution theory is a well-known lattice-based thermodynamic model of polymer solutions which considers the interaction between solvent and solute according to the following equation:

$$\ln \alpha = \ln \phi_1 + \chi (1 - \phi_1)^2 \tag{2.21}$$

, where α is the water activity, ϕ_1 is the water volume fraction, and χ in the interaction parameter. This theory shows good agreement with experimental results in semi dilute

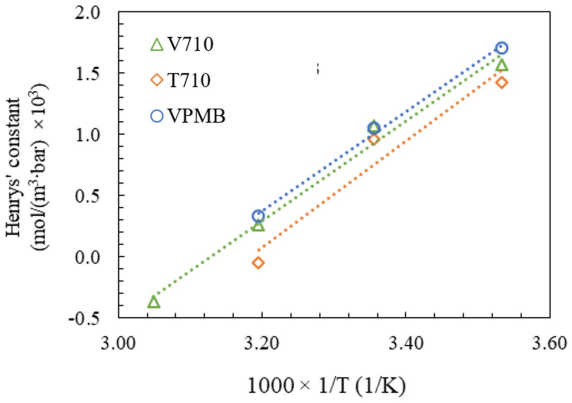

Figure 2.15 The Henry's constant for the Henry's adsorption of moisture in V710 at 80% RH.

concentrations. However, the Flory-Huggins theory fails to describe the moisture absorption behavior at higher water activity (relative humidity) in some materials (Huang et al., 2020) since the water cluster mechanism is not considered. To determine the interaction parameter (χ) between water and bitumen based on the Flory-Huggins theory, the isotherm results at the RH of 0 to 70% were used, since at those conditions no clustering occurs. The isotherm curves fitted by Flurry-Huggins theory are depicted in Fig. 2.16. A water-bitumen interaction parameter of 5.79 at 25 °C is obtained from the fitted results. A higher interaction parameter physically demonstrates a lower immiscibility between water and bitumen. As temperature increases, the interaction parameter decreases (Fig. 2.16), thus enhancing the miscibility of water in bitumen.

Moreover, the interaction parameter (χ) can be derived from the Hansen solubility parameter as

$$\chi = V_{\mathrm{m}} = \frac{(\delta_2 - \delta_1)^2}{RT} \tag{2.22}$$

, where δ_1 and δ_2 are the solubility parameters of water and bitumen, respectively, and V_{m} is the molar volume of water. Regardless of the complex components, the solubility parameter of a Venezuelan bitumen was reported as 19.2 $\mathrm{MPa}^{0.5}$ (Redelius, 2004; Zhu et al., 2019). The solubility parameter of water at 25 °C is 47.8 $\mathrm{MPa}^{0.5}$ (Hansen, 2007). Thus, an interaction parameter of 5.94 for water-bitumen systems is obtained based on the Hansen solubility parameter, which is close to that derived from the Flory-Huggins theory, namely, 5.79. The similarity of the interaction parameter from the isotherm curves and the Hansen solubility parameter signifies a possibility to use water sorption tests as an indirect method to measure the solubility parameter of bituminous binders.

Water clustering at high relative humidity

Zimm and Lundberg (Zimm & Lundberg, 1956) introduced a cluster integral parameter to illustrate the cluster tendency of water molecules in a polymer, which is defined as

$$\frac{G_{11}}{v_1} = -(1-\phi_1)\left[\frac{\partial(\alpha_1/\phi_1)}{\partial\alpha_1}\right]_{P,T} - 1 \tag{2.23}$$

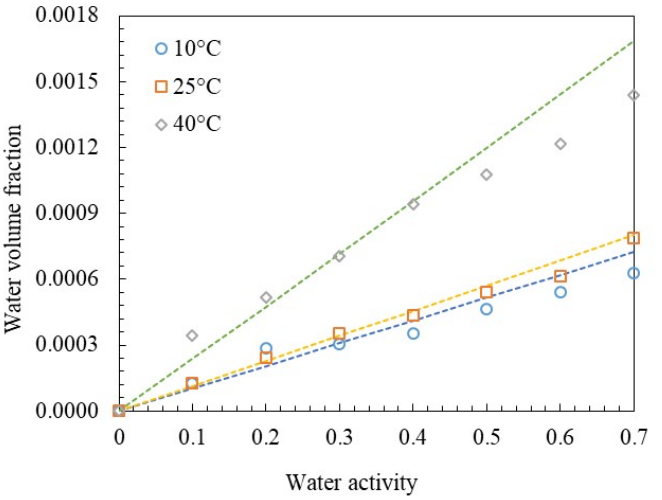

Figure 2.16 Isotherm results (symbols) and Flory-Huggins model regression (dashed lines) of V710 at 10°C, 25°C, and 40°C.

, where $G_{11}$is the cluster integral, v_1 the partial molar volume of diffusing species, α_1 the water activity, and ϕ_1 the water volume fraction. When G_{11}/v_1 < -1, the water activity is linearly proportional to volume fraction, and gas or vapor molecules are more likely to stay isolated. When G_{11}/v_1 > -1, the molecules start to cluster, resulting in a more complex effect on the whole sorption and diffusion process. The average number of water molecules in a cluster, i.e., water cluster size, is described by $1+\phi_1 G_{11}/v_1$ and is shown in Fig. 2.17 (a). When RH is higher than 70%, a water cluster size larger than 2 (molecules) is obtained, which suggests the presence of water clusters.

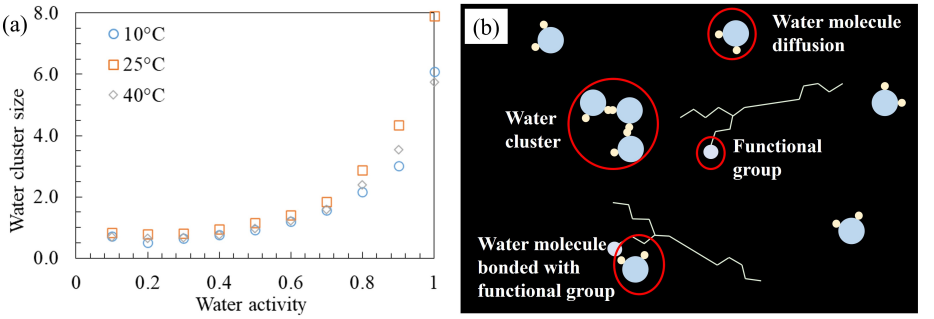

Figure 2.17 (a) Evolution of average water cluster size with water activity for the V710 determined by the Zimm-Lundberg model, (b) water transport and clustering mechanisms in bitumen.

Bitumen, despite containing polar groups from aromatics and asphaltenes, is pre-

dominantly a hydrophobic material. Water molecules in bitumen exist in two states, namely, free state and clustering state. In the case that the affinity between water and bitumen is much lower than the affinity of water molecules themselves, water molecules tend to cluster via hydrogen bonding. Due to the low solubility of free water and the lack of polar sites, water cluster behavior is expected at higher relative humidity. Water clusters may form first among polar sites and grow by using these sites as nuclei, as illustrated in Fig. 2.17 (b).

2.7 Summary

Water transport in bitumen plays a crucial role in causing moisture damage in asphalt pavements. Therefore, understanding the behavior of water transport at different temperatures and relative humidity levels is of utmost importance. In this chapter, three moisture transport models were utilized and compared to study the kinetics and thermodynamics of moisture transport in bitumen. The primary focus was to investigate the impact of bitumen type, temperature, and relative humidity on moisture transport behavior, specifically on diffusion coefficient, solubility, and clustering mechanisms. These parameters were quantified and evaluated to gain insights into the moisture transport process.

The results demonstrated that all three diffusion models were capable of simulating the experimental data with a satisfactory overall quality. However, the S-Cluster model showed particular suitability for higher sorption levels compared to the S-Fick and the Dual models. The S-Cluster model provided a better representation of the moisture transport behavior, especially when considering bulk absorption mechanisms and water clustering. According to the S-Cluster model, moisture transport in bitumen involves Henry's diffusion with a constant diffusion coefficient, following the Arrhenius equation. At high moisture concentration levels, water molecules tend to cluster together, forming larger droplets that significantly decrease the moisture transport rate.

The study examined different types of bitumen and their transport behavior at a relative humidity of 80%. Polymer modified bitumen exhibited smaller water cluster sizes, lower diffusion activation energy, and higher sorption compared to the base bitumen. These differences can be attributed to the structural changes and polymer network formation resulting from the addition of polymers. Furthermore, even though the two base bitumen types shared the same penetration grade, they displayed variations in their diffusion coefficient and solubility. The base bitumen with a faster diffusion coefficient tended to have lower solubility. These distinctions highlight the influence of bitumen composition on its transport properties.

The effect of temperature on moisture sorption was evaluated using the Clausius-Clapeyron equation. The study revealed that both surface adsorption and Henry's solubility are exothermic processes. The overall sorption change with temperature was primarily influenced by the decrease in sorption at specific vapor partial pressures and the increase in vapor partial pressure with rising temperature. At high relative humidity levels (70%-100%), moisture sorption increased significantly faster compared to low relative humidity conditions, indicating the presence of water clusters.

To investigate the interaction between moisture and bitumen, at low relative humidity, the Flurry-Huggins theory was applied. The obtained interaction parameter closely

aligned with the value derived from the Hansen solubility parameter of water and bitumen. The cluster behavior at high relative humidity was interpreted by the Zimm-Lundberg model. Clusters containing more than two water molecules are observed at relative humidity higher than 70%. This cluster size increases significantly with relative humidity, especially at 25 °C. As a summary, moisture in bitumen initially exists in a free state with a constant (or slightly decreasing with Henry's concentration) diffusion coefficient. Subsequently, it becomes bonded to polar sites of bitumen or clusters together to form droplets through hydrogen bonding, resulting in a significant drop in the moisture diffusion coefficient.

References

Adamson, A. W., & Gast, A. P. (1997). *Physical chemistry of surfaces*. John Wiley & Sons, Inc.

Apeagyei, A. K., Grenfell, J. R., & Airey, G. D. (2015). Application of Fickian and non-Fickian diffusion models to study moisture diffusion in asphalt mastics. *Materials and Structures*, *48*(5), 1461–1474.

Arthur, E., Tuller, M., Moldrup, P., & Jonge, L. W. d. (2014). Evaluation of a fully automated analyzer for rapid measurement of water vapor sorption isotherms for applications in soil science. *Soil Science Society of America Journal*, (78), 754–760.

Azizian, S. (2004). Kinetic models of sorption: A theoretical analysis. *Journal of Colloid and Interface Science*, *276*(1), 47–52.

Bird, R. B., Stewart, W. E., & Lightfoot, E. N. (2002). Transport phenomena. *John Wiley and Sons: New York*.

Cacuci, D. G., Ionescu-Bujo, M., & Navon, I. M. (2005). *Sensitivity and uncertainty analysis, volume ii: Applications to large-scale systems*. CRC Press.

Canestrari, F., Cardone, F., Graziani, A., Santagata, F. A., & Bahia, H. U. (2010). Adhesive and cohesive properties of asphalt-aggregate systems subjected to moisture damage. *Road Materials and Pavement Design*, *11*(sup1), 11–32.

Caro, S., Masad, E., Bhasin, A., & Little, D. N. (2008). Moisture susceptibility of asphalt mixtures, part 2: Characterisation and modelling. *International Journal of Pavement Engineering*, *9*(2), 99–114.

Chaturabong, P., & Bahia, H. U. (2018). Effect of moisture on the cohesion of asphalt mastics and bonding with surface of aggregates. *Road Materials and Pavement Design*, *19*(3), 741–753.

Chen, Geng, J., Chen, H., Niu, Y., Wang, R., Wu, W., Zhao, S., & Zhong, Z. (2022). Diffusion of moisture and oxygen in bitumens using electrochemical impedance spectroscopy. *Fuel*, *315*, 123212.

Cheng, Kong, F., & Zhang, X. (2021). Application of the Langmuir-type diffusion model to study moisture diffusion into asphalt films. *Construction and Building Materials*, *268*, 121192.

Cheng, Little, D. N., Lytton, R. L., & Holste, J. C. (2003). Moisture damage evaluation of asphalt mixtures by considering both moisture diffusion and repeated-load conditions. *Transportation Research Record*, *1832*(1), 42–49.

Crank, J., & Park, G. S. (1968). *Diffusion in polymers*. Academic Press.

Diab, A., You, Z., Hossain, Z., & Zaman, M. (2014). Moisture susceptibility evaluation of nanosize hydrated lime-modified asphalt–aggregate systems based on surface free energy concept. *Transportation Research Record, 2446*, 52–59.

Foo, K. Y., & Hameed, B. H. (2010). Insights into the modeling of adsorption isotherm systems. *Chemical Engineering Journal, 156*(1), 2–10.

Gritti, F., & Guiochon, G. (2005). Effect of the flow rate on the measurement of adsorption data by dynamic frontal analysis. *Journal of Chromatography A, 1069*(1), 31–42.

Hansen, C. M. (2007). *Hansen solubility parameters: A user's handbook*. Taylor & Francis.

Harel, O. (2009). The estimation of r2 and adjusted r2 in incomplete data sets using multiple imputation. *Journal of Applied Statistics, 36*(10), 1109–1118.

Harley, S. J., Glascoe, E. A., & Maxwell, R. S. (2012). Thermodynamic study on dynamic water vapor sorption in Sylgard-184. *Journal of Physical Chemistry B, 116*(48), 14183–14190.

Herrington, P. R., Wu, J. P., van den Kerkhof, L. C., & Bagshaw, S. A. (2021). Water diffusion in bitumen films. *Construction and Building Materials, 294*, 123530.

Ho, Y. S., & Mckay, G. (1998). Kinetic models for the sorption of dye from aqueous solution by wood. *Transactions of the Institution of Chemical Engineers, 96*, 183–191.

Huang, J., Derue, I., Le Gac, P. Y., & Richaud, E. (2020). Thermal oxidation of polydicyclopentadiene: Changes in water absorption. *Polymer Degradation and Stability, 180*, 109219.

Kanitpong, K., & Bahia, H. U. (2003). Role of adhesion and thin film tackiness of asphalt binders in moisture damage of HMA (with discussion). *Journal of the Association of Asphalt Paving Technologists, 72*, 502–528.

KNMI. (2020). *Weather data in the netherlands*. https://www.knmi.nl/klimaat-viewer/kaarten/vocht/gemiddelde-relatieve-vochtigheid/jaar/Periode_1991-2020

Lemarchand, C. A., Greenfield, M. L., & Hansen, J. S. (2016). Dynamics and structure of bitumen–water mixtures. *The Journal of Physical Chemistry B, 120*(24), 5470–5480.

Liu, Z., Cao, L., Zhou, T., & Dong, Z. (2020). Multiscale investigation of moisture-induced structural evolution in asphalt–aggregate interfaces and analysis of the relevant chemical relationship using atomic force microscopy and molecular dynamics. *Energy & Fuels, 34*(4), 4006–4016.

Ma, L., Varveri, A., Jing, R., & Erkens, S. (2021). Comprehensive review on the transport and reaction of oxygen and moisture towards coupled oxidative ageing and moisture damage of bitumen. *Construction and Building Materials, 283*, 122632.

Ma, L., Varveri, A., Jing, R., Kasbergen, C., & Erkens, S. (2022). Thermodynamics and kinetics of moisture transport in bitumen. *Materials & Design*, 111028.

Maggana, C., & Pissis, P. (1999). Water sorption and diffusion studies in an epoxy resin system. *Journal of Polymer Science Part B-Polymer Physics, 37*(11), 1165–1182.

Metz, S. J., Vegt, N. F. A. v. d., Mulder, M. H. V., & Wessling, M. (2003). Thermodynamics of water vapor sorption in poly(ethylene oxide) poly(butylene terephthalate) block copolymers. *Journal of Physical Chemistry B, 107*(49), 13629–13635.

Moraes, R., Velasquez, R., & Bahia, H. U. (2011). Measuring the effect of moisture on asphalt–aggregate bond with the bitumen bond strength test. *Transportation Research Record, 2209*(1), 70–81.

Neogi, P. (1996). *Diffusion in polymers*.

Nguyen, T., Byrd, W. E., Bentz, D., & Seiler Jr., J. (1992). *Development of a technique for in situ measurement of water at the asphalt/model siliceous aggregate interface* (tech. rep. SHRP-ID/URF-92-611). Strategic Highway Research Program.

Nobakht, M., Zhang, D., Sakhaeifar, M. S., & Lytton, R. L. (2020). Characterization of the adhesive and cohesive moisture damage for asphalt concrete. *Construction and Building Materials*, *247*, 118616.

Park, G. S. (1986). Transport principles: Solution, diffusion and permeation in polymer membranes. In *Synthetic membranes: Science, engineering and applications* (p. 94).

Petersen, J. C. (2009). A review of the fundamentals of asphalt oxidation: Chemical, physicochemical, physical property, and durability relationships. *Transportation Research Circular*, (E-C140).

Powell, M. J. D. (2009). *The BOBYQA algorithm for bound constrained optimization without derivatives* (Report). University of Cambridge.

Poyet, S., & Charles, S. (2009). Temperature dependence of the sorption isotherms of cement-based materials: Heat of sorption and Clausius–Clapeyron formula. *Cement and Concrete Research*, *39*(11), 1060–1067.

Redelius, P. (2004). Bitumen solubility model using Hansen solubility parameter. *Energy & Fuels*, *18*(4), 1087–1092.

Rudyk, S. (2018). Relationships between SARA fractions of conventional oil, heavy oil, natural bitumen and residues. *Fuel*, *216*, 330–340.

Sengoz, B., Topal, A., & Isikyakar, G. (2009). Morphology and image analysis of polymer modified bitumens. *Construction and Building Materials*, *23*(5), 1986–1992.

Sun, Y., Harley, S. J., & Glascoe, E. A. (2015). Modeling and uncertainty quantification of vapor sorption and diffusion in heterogeneous polymers. *Chemphyschem*, *16*(14), 3072–83.

Terrel, R. L., & Al-Swailmi, S. (1994). *Water sensitivity of asphalt-aggregate mixes: Test selection*.

Varveri, A. K. (2017). *Moisture damage susceptibility of asphalt mixtures: Experimental characterization and modelling* (Doctoral dissertation). Delft University of Technology.

Vasconcelos, K. L., Bhasin, A., & Little, D. N. (2010). Measurement of water diffusion in asphalt binders using Fourier transform infrared–attenuated total reflectance. *Transportation Research Record*, *2179*(1), 29–38.

Vasconcelos, K. L., Bhasin, A., & Little, D. N. (2011). History dependence of water diffusion in asphalt binders. *International Journal of Pavement Engineering*, *12*(5), 497–506.

Vieth, W. R., Howell, J. M., & Hsieh, J. H. (1976). Dual sorption theory. *Journal of Membrane Science*, *1*, 177–220.

Wang, X., Ren, J., Gu, X., Li, N., Tian, Z., & Chen, H. (2021). Investigation of the adhesive and cohesive properties of asphalt, mastic, and mortar in porous asphalt mixtures. *Construction and Building Materials*, *276*, 122255.

Wel, G. K. v. d., & Adan, O. C. G. (1999). Moisture in organic coatings - A review. *Progress in Organic Coatings*, *37*(1-2), 1–14.

Yang, C., Xing, X., Li, Z., & Zhang, S. (2020). A comprehensive review on water diffusion in polymers focusing on the polymer-metal interface combination. *Polymers (Basel)*, *12*(1).

Zhu, J. Q., Balieu, R., & Wang, H. P. (2019). The use of solubility parameters and free energy theory for phase behaviour of polymer-modified bitumen: A review. *Road Materials and Pavement Design*.

Zimm, B. H., & Lundberg, J. L. (1956). Sorption of vapors by high polymers. *The Journal of Physical Chemistry*.

3

Molecular dynamics simulations of moisture transport in bitumen

This chapter builds upon the findings from Chapter 2 and aims to deepen the knowledge of moisture transport in bitumen through the application of molecular dynamics (MD) simulations. The main objective is to investigate the feasibility and accuracy of the assumptions and transport models proposed in Chapter 2 by examining moisture transport behavior at the nanoscale using molecular dynamics (MD) simulations.

To begin, a comprehensive introduction to MD simulations in bitumen research is provided in Section 3.1, highlighting their significance in studying moisture transport phenomena. The force field and simulation procedures utilized in the study are then outlined in detail in Section 3.2, ensuring transparency and reproducibility of the MD simulations. Section 3.3 delves into the core of the investigation, focusing on micro-scale moisture transport in bitumen. Through the MD simulations, the behavior of water molecules within the bitumen matrix is explored, shedding light on their diffusion characteristics and the underlying mechanisms governing moisture transport. Building upon the synergy between the experimental findings from Chapter 2 and the MD simulations, Section 3.4 provides a comprehensive interpretation of the moisture transport behavior in bitumen. By combining the insights gained from both approaches, a deeper understanding of the transport mechanisms and their implications is achieved. The assumptions proposed in the transport models are critically evaluated and validated, allowing for a more accurate characterization of moisture transport in bitumen. Finally, Section 3.5 summarizes the key results and conclusions derived from this chapter.

Parts of this chapter have been published in Ma, L., et al. (2023). Water diffusion mechanisms in bitumen studied through molecular dynamics simulations. *Construction and Building Materials*. 409, 133828.

3.1 Introduction

Water diffusion in bitumen has been investigated by measuring moisture uptake over time via various techniques and interpreting the experimental results using different diffusion models. Large variations of diffusion coefficients have been reported, and several water-bitumen interaction mechanisms have been proposed. These discrepancies among different measurements make it difficult to quantify a single diffusion coefficient of moisture in bitumen and to conclude an exact diffusion mechanism. In this context, Chapter 2 compared the utilization of three diffusion models to describe the moisture diffusion process measured by a gravimetric technique. These models demonstrated good performance in simulating the experimental results, i.e., moisture uptake over time. However, based on their distinct assumptions of moisture diffusion behavior, different diffusion coefficients of moisture in bitumen were derived. Distinguishing among all these diffusion models is therefore important in order to obtain accurate moisture diffusion kinetics and understand the potential for moisture-induced damage in a pavement.

To this end, molecular simulations have the potential to provide useful insight into the underlying mechanisms and to explain why discrepancies in measurements of water diffusion rates occur. In the past two decades, molecular simulation has been used for complementing and interpreting experimental measurements of the physicochemical, structural, and dynamic properties of bitumen. A prerequisite for accurate molecular simulations of bitumen is a well-defined model that represents the chemical composition and physicochemical properties of bitumen (Lemarchand et al., 2016; Li & Greenfield, 2014b). Early models (Jennings et al., 1993) represented bitumens from different crude oil sources by proposing a different "average" molecule to represent the diversity of functional groups in each bitumen. Such a representation cannot exhibit the well-known separation of bitumen into solubility-based SARA fractions, as described in an earlier review (Greenfield, 2011). The three-component models developed by Zhang and Greenfield (Zhang & Greenfield, 2007), referred to as ZG07 in this thesis, represented most solubility classes, yet molecular weights of maltenes were too small, and several polar group functionalities were lacking. A six-component model proposed by Zhang and Greenfield (Zhang & Greenfield, 2008) included those functionalities, yet most molecules were still too small. The four molecule types in the Cooee model created by Hansen et al. (Hansen et al., 2013) used molecule size and shape to distinguish among separate solubility classes but the molecules lacked partial charges. Their use of a united atom model further sped up the computation rate. The twelve-component system proposed by Li and Greenfield (Li & Greenfield, 2014b) (LG14) made better representations of the polarity and molecular weights of each SARA fraction that were aided in part by choosing molecular structures that had been identified by others in geochemistry studies. Many groups have now employed the composition proposed by Li and Greenfield to represent bitumen AAA-1 of the Strategic Highway Research Program (Jones et al., 1993) in molecular simulations. The LG14 composition has been modified by many researchers in order to use either fewer molecule types or a greater range of molecule sizes and functionalities, as documented in a recent review (Ren et al., 2022a).

Molecular dynamics (MD) simulations have been previously performed to gain insights into the mechanisms of water diffusion in bitumen. For example, Lemarchand et al. (Lemarchand et al., 2016) conducted MD simulations of 43 ns duration using the

Cooee model with additions of 0.06 – 4 wt% water and partial charges at sulfur sites in the bitumen. At 377 K and 452 K and almost all concentrations, most water molecules formed a single large droplet. At 377 K, trends over the final 14 ns suggested that water molecules would form a single droplet after a sufficiently long simulation. Analysis of water mean-squared displacement (MSD) over long times (100 ns) showed a decrease in the diffusion rate with increasing water content. This was caused by the formation of water droplets. Radial distribution functions (RDFs) indicated that these droplets were usually located near saturate chain molecules. The cohesive energy density (CED) of the system decreased with increasing water content due to the volume increase exceeding an increase in water interactions (Lemarchand et al., 2016). Xu and Wang (Xu & Wang, 2016) studied a bitumen-aggregate system with 7 – 14 wt% water added to the interface. They sampled interface fluctuations in MD runs of 0.05 ns and found that water molecules at the interface between ZG07 bitumen and a silica or calcite aggregate surface weakened the adsorption of bitumen and decreased the thermodynamic work of adhesion. This resulted in a change that can be interpreted on the macroscopic scale as moisture-induced damage. This was also observed by Liu et al. (Liu et al., 2020), who explained that adhesive failure resulted from the replacement of bitumen–aggregate hydrogen bonds with water–aggregate hydrogen bonds. Du et al. (Du et al., 2021) performed MD simulations of bitumen–water systems using the LG14 model for 1 ns per condition. The water concentrations considered were in the range 1 – 20 wt%. In this study, too, large water clusters formed at most concentrations. The authors reported an increase in the overall water diffusivity in bitumen, which is contrary to experimental observations of a decrease in diffusivity with increasing water content as indicated in Chapter 2 and in Ref. (Lemarchand et al., 2016). For a more extensive list of studies, the reader is referred to a recent review (Ren et al., 2022b).

The vast majority of prior MD simulation studies of water in bitumen have been performed using conditions that fail to achieve a sufficient description of water diffusion as it arises in real-world systems. The main source of this failure is the short sampling time, which is usually limited to a few hundred ps up to 1 ns. Such short MD simulations do not allow for the proper equilibration of the highly viscous bitumen structure, even at elevated temperatures. Although averaged quantities such as density may appear constant with sampling time, this can arise because they have not yet begun to fluctuate significantly, rather than that they have fully converged. Similarly, the short sampling times used for water diffusivity in bitumen in most MD studies do not ensure that proper diffusion behavior (converging to the actual diffusive regime (Jamali et al., 2019) in which mean-squared displacement increases linearly in time) is achieved. These issues are particularly pronounced in simulations at lower temperatures, i.e., close to ambient or colder. Apart from the short runs, some prior simulation studies have considered water concentrations that are much larger than those observed experimentally (Cheng et al., 2021; Cheng et al., 2003). Simulations at smaller water concentrations are required to explain moisture diffusion behavior that is observed in experiments, which are necessarily below the solubility limit. Simulations of bitumen that probe long time scales (Khabaz & Khare, 2018; Lemarchand et al., 2016) reveal effects with much longer relaxation times than can be quantified in simulations of only 0.1 to 1 ns.

This chapter primarily aims to provide useful insights into water transport mecha-

nisms in bitumen by means of molecular dynamics simulations and to perform simulations over time and length scales beyond those of current common practice to ensure reliable and accurate predictions. To mitigate the common simulation drawbacks discussed earlier, MD simulations of water–bitumen are performed using the LG14 model bitumen system and water concentrations closer to levels observed in experiments. To overcome equilibration and convergence problems, simulations of up to 600 ns (0.6 μs) are conducted, which is orders of magnitude longer than most of the available studies to date. To investigate water diffusion mechanisms, hydrogen bonding and water clustering in the water-bitumen systems are evaluated. This guides the subsequent discussion of structural and physicochemical properties of water-bitumen systems, including density, viscosity, and cohesive energy. By combining molecular dynamics simulations and experimental results from Chapter 2, along with findings from published papers, the aim is to provide a micro-scale comparison among diffusion models, a deep insight into the diffusion mechanisms, and a guideline on the meanings of diffusion coefficients at different orders of magnitude obtained from experiments.

3.2 Force field and molecular dynamics simulation methodology

3.2.1 Force field parameters

The Optimized Potential for Liquid Simulations All-Atom (OPLS-AA) force field (Jorgensen et al., 1996; Kaminski et al., 2001) was used to model bitumen throughout this thesis. The force field parameters were obtained from the work of Li and Greenfield (Li & Greenfield, 2014b), who supplemented the OPLS-AA implementation available in Towhee software (Martin, 2013) with additional parameters to address molecular interactions that were missing in prior parameterizations. OPLS-AA has been shown (Li & Greenfield, 2014b; Zhang & Greenfield, 2007) to be successful enough in modeling bituminous materials, for which it is impossible to make a one-to-one connection between experimental data and molecular composition on a molecule-by-molecule basis due to the large number of different molecules involved. The OPLS-AA force field considers the contributions of bonded terms, i.e., bond stretching, angle bending, backbone torsion, and improper torsion to maintain planarity (Li & Greenfield, 2011), and non-bonded terms, i.e., Lennard-Jones (LJ) and Coulombic interactions. The bond stretching energy is described by the harmonic style,

$$E_{\text{bond}} = K_l(l - l_0)^2 \tag{3.1}$$

where l_0 is the equilibrium bond distance and K_l is a force constant. The harmonic angle bending energy is computed by

$$E_{\text{angle}} = K_\theta(\theta - \theta_0)^2 \tag{3.2}$$

where θ is the bond angle, θ_0 is the equilibrium value of the angle, and K_θ is a force constant. Angle differences are computed within LAMMPS in radians. The dihedral energy uses the potential

$$E_{\text{dihedral}} = \frac{1}{2}K_1[1 + \cos(\phi)] + \frac{1}{2}K_2[1 - \cos(2\phi)] + \frac{1}{2}K_3[1 + \cos(3\phi)] \tag{3.3}$$

where K_1, K_2, and K_3 are force constants, and ϕ is the dihedral angle. The improper energy is computed by

$$E_{\text{improper}} = K[1 + d\cos(n\phi)] \tag{3.4}$$

where ϕ is the improper angle, d equals +1 or -1, and K is a force constant. The standard 12/6 Lennard-Jones (LJ) potential energy describes the potential energy of interaction between two non-bonding atoms as

$$E_{\text{LJ}} = 4\epsilon\left[\left(\frac{\sigma}{r}\right)^{12} - \left(\frac{\sigma}{r}\right)^{6}\right] \quad r < r_{\text{c}} \tag{3.5}$$

where r is the distance between atoms, ϵ denotes the depth of the potential well, σ represents the LJ particle radius and r_{c} is the cutoff. Coulombic pairwise interaction energy is given by

$$E_{\text{col}} = \frac{C q_i q_j}{r} \quad r < r_{\text{c}} \tag{3.6}$$

where r_{c} is the cutoff. A cutoff of 10 Å was used for the LJ and Coulombic interactions. Analytic tail corrections of long-range van der Waals were used for energy and pressure. The long-range electrostatic interactions beyond 10 Å were computed via the Particle-Particle Particle-Mesh (PPPM) method with a relative precision of 10^{-5} (Brown et al., 2012). Geometric combining rules were used for the LJ interactions between non-identical atoms, as implemented into OPLS-AA development and parameterization (Jorgensen et al., 1996). A scaling factor of 0.5 was used for all interactions between atom pairs separated by 3 bonds (Jorgensen et al., 1996). The extended simple point-charge (SPC/E) model (Berendsen et al., 1987) was used for water. SPC/E is a rigid three-site water model that shows good agreement with experimentally measured transport (Tsimpanogiannis et al., 2020; Tsimpanogiannis et al., 2019), thermodynamic (Wu et al., 2006), and structural (Mark & Nilsson, 2001) properties of pure water. Hydrogen bonding arises through favorable Lennard-Jones and Coulombic interactions. The RATTLE extension (Andersen, 1983) of the SHAKE algorithm (Ryckaert et al., 1977) was used to fix the bond lengths and bond angle of each water molecule.

3.2.2 Composition and simulation details

The 12-component all-atom LG14 model (Li & Greenfield, 2014b) was used to represent the saturate, aromatic, resin, and asphaltene fractions in bitumen. Its composition was devised to represent the AAA-1 bitumen of the Strategic Highway Research Program (SHRP) (Kennedy et al., 1994). The exact components comprising LG14 are shown in Fig. 3.1 and overall composition of the model bitumen is provided in Table 3.1. As noted in Fig. 3.1, functional groups that contain heteroatoms (sulfur, nitrogen, and oxygen) are present in all five polar aromatics (quinolinohopane, thio-isorenieratane, benzobisbenzothiophene, pyridinohopane, and trimethylbenzene-oxane) and in all three asphaltenes (asphaltene-phenol, asphaltene-pyrrole, and asphaltene-thiophene).

In the MD simulations, the 72 molecules (containing 5572 atoms) from Table 3.1 were used for the bitumen phase (following the mole fractions of the LG14 AAA-1 model). Subsequently, 0, 2, 4, 8, 16, or 32 water molecules were added. These system sizes correspond to water concentrations in bitumen on the macroscale of 0 wt%, 0.11 wt%, 0.22 wt%, 0.44

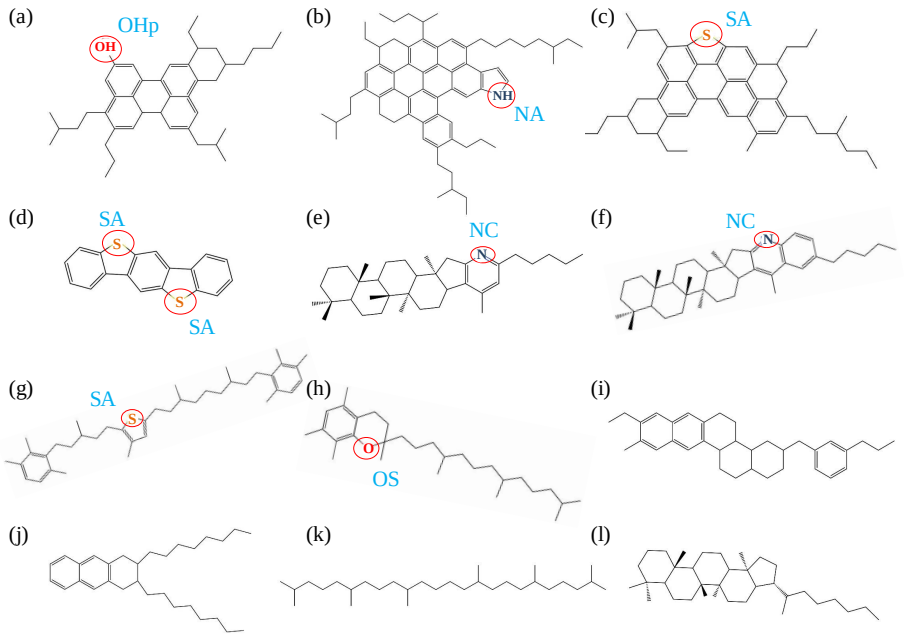

Figure 3.1 Chemical components that comprise the LG14 bitumen model (Li & Greenfield, 2014b). Asphaltene molecules: (a) asphaltene-phenol, (b) asphaltene-pyrrole, and (c) asphaltene-thiophene; resin molecules: (d) benzobisbenzothiophene, (e) pyridinohopane, (f) quinolinohopane, (g) thio-isorenieratane, and (h) trimethylbenzene-oxane; aromatic molecules: (i) perhydrophenanthrene-naphthalene (PHPN), and (j) dioctyl-cyclohexane-naphthalene (DOCHN); saturate molecules: (k) squalane and (l) hopane. Red circles indicate heteroatom-based functional groups; their OPLS-aa atom types are denoted by blue labels.

Table 3.1 Bitumen composition

Molecule	Number in the system	Molar mass (g/mol)
asphaltene-phenol	3	575.0
asphaltene-pyrrole	2	888.5
asphaltene-thiophene	3	707.2
benzobisbenzothiophene	15	290.4
pyridinohopane	4	530.9
quinolinohopane	4	554.0
thio-isorenieratane	4	573.1
trimethylbenzene-oxane	5	414.8
perhydrophenanthrene-naphthalene (PHPN)	11	464.8
dioctyl-cyclohexane-naphthalene (DOCHN)	13	406.8
squalane	4	422.9
hopane	4	483.0

wt%, 0.93 wt%, and 1.76 wt%, respectively. All simulations here were performed at a pressure of 1 atm to mimic atmospheric conditions. Higher pressures can increase the density of bitumen slightly and can impact transport properties such as the viscosity of bitumen and the self-diffusion coefficient of water in bitumen. Such an investigation is outside the scope of this work. Simulations were performed at six temperatures, i.e., 298.15 K, 313.15 K, 353.15 K, 393.15 K, 443.15 K, and 533.15 K. This temperature range spans ambient temperature (often encountered in pavement applications), medium-high temperatures (i.e., 313 K and 353 K) that are the upper limit for experimental measurements of water diffusion behavior (Ma et al., 2022), and very high temperatures (i.e., 443 K and 533 K). Although the high temperatures considered here are not typically observed during the service life or processing of bitumen or of asphalt mixtures, they allow for reaching relatively well-equilibrated configurations without requiring prohibitively long MD simulations, while still being able to provide important physical insight into water transport behavior in bitumen. This is because the physical mechanisms that govern water diffusion in bitumen are fundamentally similar at both low and high temperatures. Performing MD simulations at high temperatures is common practice in molecular simulation studies of bitumen (Khabaz & Khare, 2018; Lemarchand et al., 2016; Li & Greenfield, 2014a). Our simulation results at 533 K can be directly compared to results from these previous studies.

All MD simulations were performed using the open-source LAMMPS software (version 22 August 2018) (Plimpton, 1995; Thompson et al., 2022) according to the procedure described hereafter. Initial configurations of one water-bitumen system per composition were generated in Packmol (Martínez et al., 2009). Energy minimization of each system was performed using the conjugate gradient algorithm. Periodic boundary conditions (PBC) were applied in all directions. To create five independent configurations for each set of conditions, an NPT simulation was performed at 1000 K and 1 atm for 5 ns with a time step of 1.0 fs. Configurations were obtained from the simulation trajectories at 1.0 ns, 2.0 ns, 3.0 ns, 4.0 ns, and 5.0 ns. Next, each of these five water-bitumen systems were quenched to each temperature of interest and were equilibrated in the NPT ensemble at 1 atm to ensure that density and total energy converged to equilibrium fluctuations. The Nosé-Hoover thermostat and barostat with coupling constants of 100 and 1000 fs, respectively, were used to regulate the temperature and pressure (Allen & Tildesley, 2017). Then, equilibration runs in the NVT ensemble were carried out in a simulation box whose volume was set equal to the average volume computed from the NPT runs in the previous step. Finally, production runs in the NVT ensemble were performed to compute transport and structural properties of the water-bitumen systems. The durations of the production runs were determined from the time needed for the transport properties (self-diffusion coefficient and viscosity) to converge. These were indicated by linear increases with time of the mean-squared displacement and the mean-squared stress fluctuations (Jamali et al., 2019). The durations of all equilibration and production simulations for the systems studied here are listed in Table 3.2. The positions of atoms were recorded every 10 ps for the simulations at 533.15 K and every 100 ps for the simulations at all other temperatures. Averages and standard deviations of all simulation results were obtained from the five independent runs at each composition.

Table 3.2 Details of simulation times

Temperature/[K]	NPT equilibration /[ns]	NVT equilibration /[ns]	NVT production /[ns]
533	1	1	10
443	10	2	100
393	20	10	100
353	20	10	300
313	50	10	600
298	80	10	600

3.2.3 Hydrogen bonding and water clusters

Hydrogen bonding and clustering of water molecules were quantified to study the mechanism of water diffusivity in bitumen. Hydrogen bonds were detected based on two criteria: (1) the distance between a hydrogen bond acceptor and a hydrogen bond donor is less than 3.5 Å, and (2) the angle between a hydrogen atom, a hydrogen bond donor, and a hydrogen bond acceptor is less than 30° (Starr et al., 2000). Potential acceptors were considered to be the oxygen atom of water and the heteroatoms of bitumen that are circled in Fig. 3.1. Potential donors are the oxygen of water and the bitumen heteroatoms OHp and NA that are bonded to hydrogen.

Neighboring water molecules were considered to be in a cluster when their oxygen atoms were within the hydrogen bonding distance of 3.5 Å. Water clusters were identified by using the clustering algorithm of Sevick et al. (Sevick et al., 1988): in a system with N water molecules, first all water-water distances (i.e., oxygen-oxygen) are computed. An $N \times N$ symmetric water pair matrix $\boldsymbol{C}$ is then generated, where C_{ij} equals 1 if the distance between water molecules i and j is smaller than 3.5 Å (the molecules i and j are referred to as directly connected pairs) or C_{ij} equals 0 otherwise. The next step is to find water molecules that are indirectly connected. If $C_{ij} = 1$ and $C_{jk} = 1$, then water molecules i and k are also connected, i.e., $C_{ik} = 1$, thus forming a cluster assembly composed of water molecules i, j, and k. To this purpose, one water pair with $C_{\ell m} = 1$ is randomly selected as an initial cluster assembly. All other water pairs with $C_{ij} = 1$ are considered, and the water molecules in these pairs are ascribed to this assembly when these pairs have common water molecules (i or j equals ℓ or m). The process is repeated until no more additions are found, and the total number of water molecules in this assembly is denoted as the cluster size. Then, a new indirect search is repeated by starting with a remaining water pair (not in this cluster) identified as a new initial cluster assembly. These steps are executed repeatedly until all cluster assemblies are identified.

Radial distribution functions (RDFs) were also computed to analyze the positions of hydrogen bonds and water clusters in bitumen. An RDF describes the average distribution of particles around a central reference particle. RDFs were sampled up to a distance of 25 Å with 100 bins by using the LAMMPS `rerun` command.

3.2.4 Transport properties and cohesive energy

The OCTP plugin (Jamali et al., 2019) in LAMMPS was used for an on-the-fly calculation of the self-diffusion coefficient of water according to

$$D_{\text{self}} = \lim_{t\to\infty} \frac{1}{6tN_{\text{w}}} \left\langle \sum_{i=1}^{N_{\text{w}}} \left(\boldsymbol{r}_i(t) - \boldsymbol{r}_i(0)\right)^2 \right\rangle \tag{3.7}$$

where N_{w} is the number of water molecules, t is the correlation time, $\boldsymbol{r}_i$ is the position vector of the i-th water molecule, and the averaged summation provides the MSD. The angle brackets $\langle\ \rangle$ denote an ensemble average. The self-diffusion coefficient has been shown to depend on the system size (Celebi et al., 2021; Yeh & Hummer, 2004). To correct diffusivity for finite-size effects, the Yeh-Hummer (YH) correction term was used (Celebi et al., 2021; Jamali et al., 2020; Jamali, Wolff, Becker, et al., 2018; Yeh & Hummer, 2004):

$$D^{\infty}_{\text{self}} = D_{\text{self}} + \frac{k_{\text{B}} T \xi}{6\pi\eta L} \tag{3.8}$$

where D^{∞}_{self} is the diffusivity of water at the thermodynamic limit, ξ is a constant equal to 2.837297, L is the edge length of the simulation box, k_{B} is the Boltzmann constant, T is the absolute temperature, and η is the shear viscosity. The viscosity was also computed using the OCTP plugin (Jamali et al., 2019) as

$$\eta = \lim_{t\to\infty} \frac{1}{10\cdot 2t} \frac{V}{k_{\text{B}}T} \left\langle \sum_{\alpha\beta} \left(\int_0^t P^{\text{os}}_{\alpha\beta}(t')\,\mathrm{d}t' \right)^2 \right\rangle \tag{3.9}$$

where

$$P^{\text{os}}_{\alpha\beta} = \frac{P_{\alpha\beta} + P_{\beta\alpha}}{2} - \delta_{\alpha\beta} \left(\frac{1}{3} \sum_{k=x,y,z} P_{kk} \right) \tag{3.10}$$

V is the volume of the system, $P^{\text{os}}_{\alpha\beta}$ are the traceless and symmetric pressure tensor components, and $\delta_{\alpha\beta}$ is the Kronecker delta. The computation of η in MD does not depend on the system size (Jamali, Hartkamp, et al., 2018; Jamali, Wolff, Becker, et al., 2018; Moultos et al., 2016).

The cohesive energy (intermolecular energy) among bitumen components was calculated to study cohesion of bitumen in the presence of water. It was defined as the sum of the intermolecular energy among only the bitumen components; interactions of water were omitted in this calculation. The *group/group* compute command in LAMMPS was used to distinguish between intramolecular and intermolecular contributions to van der Waals (i.e., LJ) energies that were computed directly between pairs. This entails an assumption that no molecule interacts directly with a periodic image of itself. Distinguishing between intramolecular and intermolecular contributions to Coulomb energy requires additional nuance. For atoms closer than a transition distance to each other, a direct pairwise computation of Coulomb energy can make this distinction. The long-range contribution to the Coulomb energy (PPPM) (Brown et al., 2012) accounts for interactions that arise over longer distances. By using reciprocal space to compute interactions between an atom and all other atoms beyond the transition distance, it indirectly includes interactions between a molecule and its infinite number of periodic images. Though

these images arise from the same parent molecule, and thus would be categorized as intramolecular, their long-range Coulomb contribution corresponds to interactions between separate molecules within the framework of periodic boundary conditions.

In order to separate intramolecular and intermolecular contributions to the long-range Coulomb energy, the transition distance between a direct Coulomb energy calculation and a long-range (PPPM) calculation was increased to 25 Å in a separate simulation of an LG14 model with three times the number of atoms, which had an equilibrated box length larger than 50 Å. Because all bitumen molecules have a maximum intramolecular atom-atom separation that is less than 25 Å, the entire intramolecular electrostatic energy was calculated by partitioning the direct Coulombic energy. All of the long-range Coulomb energy contribution was thus assumed to be intermolecular. This includes the interactions between a molecule and its periodic images that arise over all length scales that are incorporated into the PPPM long-range Coulomb approach.

3.3 Water diffusion mechanisms in bitumen

3.3.1 Hydrogen bonding in water-bitumen systems

The presence of water hydrogen bonding was evaluated in order to assess how its extent affects diffusion mechanisms. Fig. 3.2 (a) shows a representative MD simulation snapshot of a bitumen system with 0.93 wt% water content, with molecules presented in unwrapped periodic boundary coordinates to enhance visualization clarity. The three distinct types of hydrogen bonds that occur in water-bitumen systems, i.e., bitumen-bitumen, water-bitumen, and water-water hydrogen bonds, are shown in Fig. 3.2(b), (c), and (d), respectively. A water molecule is capable of hydrogen bonding to a molecule of bitumen and simultaneously to another water molecule. Five types of heteroatom-based functional groups (denoted in Fig. 3.1) in the LG14 bitumen model (Li & Greenfield, 2014b) participate in bitumen-bitumen or water-bitumen hydrogen bonds. The simulation box contains 2 pyrrole (NA), 8 pyridine or quinoline (NC), 3 phenol (OHp), 5 ether (OS), and 37 thiophene (SA) of these heteroatom-based groups.

The numbers of hydrogen bonds of each type were counted in each saved configuration and were averaged over the sampling duration and subsequently over all five independent simulations. Fig. 3.3 shows these average numbers of all three types of hydrogen bonds for bitumen containing up to 1.76 wt% water over the temperature range 298–533 K. As can be seen in Fig. 3.3 (a), there are 0.4 – 1.4 hydrogen bonds between bitumen components in a system without water for the considered temperatures. This range decreases to 0.2 – 0.8 bitumen-bitumen hydrogen bonds at 0.11 wt% water and decreases further to 0.1 – 0.6 hydrogen bonds at higher water contents. Few bitumen-bitumen hydrogen bonds occurred during most of the simulations. This indicates that hydrogen bond energy is not strong enough to favor the few bitumen-bitumen configurations that incorporate a hydrogen bond, compared to all other configurations with similar energies yet without the specificity of a hydrogen bonding geometry. The decrease in the number of bitumen-bitumen hydrogen bonds with the presence of water may be due to higher attractive forces between water and bitumen molecules, which causes bitumen-bitumen hydrogen bonds to be replaced by water-bitumen hydrogen bonds. The small size of water enables relative ease for it to achieve hydrogen bonding configurations near bitumen; this can also play a role.

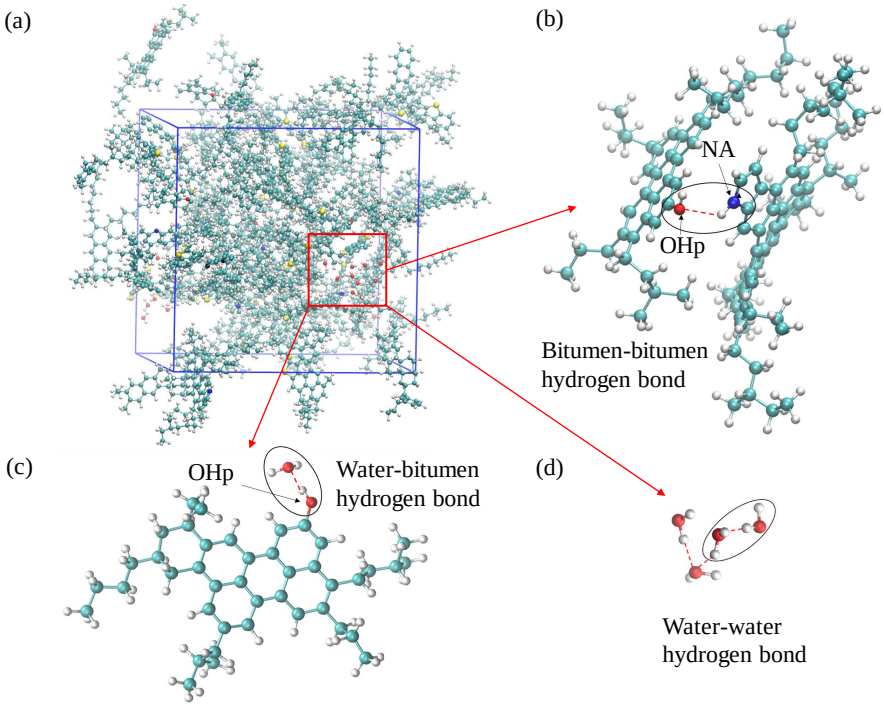

Figure 3.2 Snapshots of (a) a water-bitumen system with 0.93 wt% water content, (b) a bitumen-bitumen hydrogen bond between asphaltene-phenol and asphaltene-pyrrole, (c) a water-bitumen hydrogen bond, and (d) three water-water hydrogen bonds at 313 K. A red dashed line represents a hydrogen bond between two molecules. NA and OHp are heteroatom-based functional groups in bitumen, as shown in Fig. 3.1. Color code for atoms: carbon (cyan), hydrogen (gray), nitrogen (blue), oxygen (red), and sulfur (yellow)

An increasing presence of water leads to a sharp increase in the number of water-bitumen and water-water hydrogen bonds, as shown in Fig. 3.3 (b) and (c), respectively. With 2 water molecules in the box (0.11 wt%), at least one hydrogen bonded to a bitumen molecule at temperatures up to 393 K. At 443 K, the average number of 0.55 corresponds to one hydrogen bond in just under every two configurations. A water-bitumen hydrogen bond occurred approximately once per 5 configurations at 533 K. With 16-fold increases in water content, the number of water-bitumen hydrogen bonds rose by factors of 4.5 times (at 298 K) to 11 times (at 533 K).

In contrast to bitumen-bitumen, the number of hydrogen bonds formed among water molecules is significantly affected by the temperature of the system. Fig. 3.3 (d) shows the average number of hydrogen bonds per water molecule. This was calculated by summing the number of water-bitumen hydrogen bonds and twice the number of water-water hydrogen bonds, and then dividing by the total number of water molecules. At 533 K (the highest temperature), the number of hydrogen bonds per water molecule increases from ca. 0.1 to 0.7 as the water content increases from 0.11 to 1.76 wt%, while at 443 K and 393

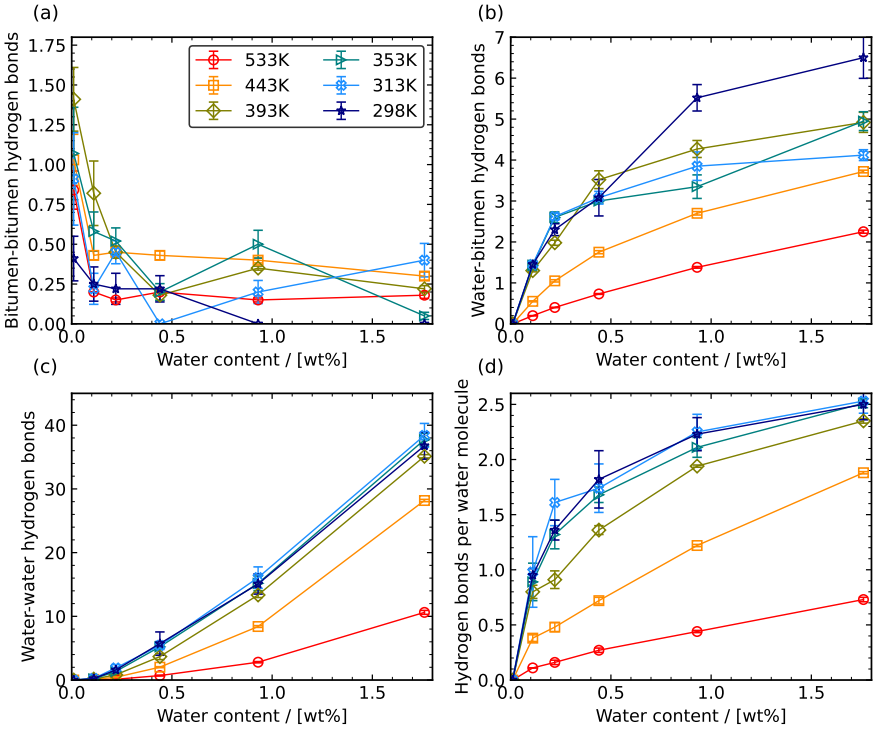

Figure 3.3 Average number of (a) bitumen-bitumen hydrogen bonds, (b) water-bitumen hydrogen bonds, (c) water-water hydrogen bonds, and (d) hydrogen bonds per water molecule as a function of the water content.

K, this normalized number of hydrogen bonds becomes larger. Over temperatures of 298 – 353 K, the number of hydrogen bonds per water molecule increases from ca. 0.9 to 2.5. This clearly shows an increase in hydrogen bonding interactions among water molecules at lower temperature and with higher water content.

Water that forms hydrogen bonds with other water molecules, with bitumen components, or with both is commonly referred to as bound water. Water that does not participate in hydrogen bonding of any kind is referred to as free water (unbound individual water molecules). Fig. 3.4 (a) shows the free water content as a function of the total water content in simulated bitumen at temperatures ranging from 298 K to 533 K.

At lower temperatures (298 – 313 K), increasing the total water content in bitumen has limited influence on free water. As shown in Fig. 3.4 (a), the free water content decreases slightly with increased water content, though the decrease is within the range of the fluctuations. This suggests that the equilibrium free water content is obtained in the bitumen system with 0.11 wt% water, and thus an increase in total water content cannot increase the free water content further. At the system size employed here, this free water content corresponds to fewer than one water molecule per simulation box per snapshot.

At 353 – 443 K, free water content initially increases with increased water content in

the system and reaches maxima of 0.041%, 0.092% and 0.256%. These correspond to approximately 1, 2, and 5 free water molecules, respectively. After the maximum, a slight decrease is observed. At the highest temperature (533 K), free water increases monotonically with the water content in the system. A maximum free water content has not been reached by the highest simulated water content of 1.76 wt%.

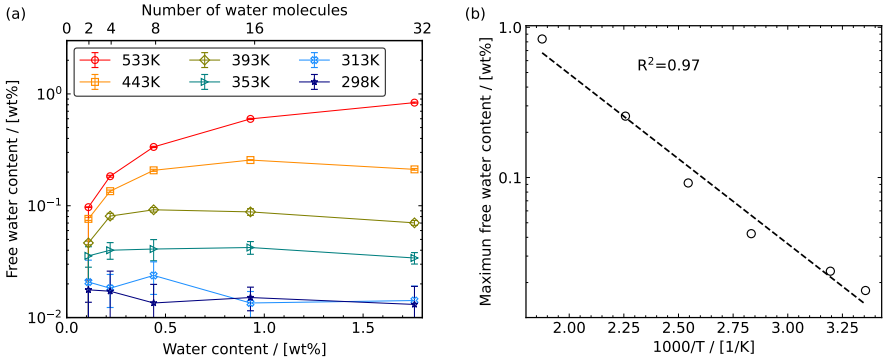

Figure 3.4 (a) Free water content as a function of the water content in bitumen in the temperature range of 298 – 533 K, (b) maximum free water content as a function of temperature.

As a simple model, we consider an energetic cost ΔE for a water molecule to be free rather than hydrogen bonded. At constant temperature, this suggests a probability density proportional to $\exp(-\Delta E/k_B T)$ for free water compared to bound water. Fig. 3.4 (b) shows the maximum free water content at each temperature as an Arrhenius function of temperature. The logarithm of maximum free water content in bitumen varies approximately linearly with the inverse temperature. The slope indicates an energy cost of 9.4 kJ/mol for a water molecule to be free, i.e., to break from a hydrogen bonding network. Hydrogen bonding will be prevalent even at higher pavement temperatures such as 64°C, where thermal energy $RT \sim 2.8$ kJ/mol is much lower than this energy cost for a water molecule to be free.

Functional groups in bitumen have different propensities to hydrogen bond with water. The LG14 bitumen model contains five different types of functional groups, as depicted in Fig. 3.1. The fraction of hydrogen bonds between water and a specific functional group is computed as the ratio of the number of hydrogen bonds between water and this functional group to the total number of water-bitumen hydrogen bonds. Sometimes a single water molecule contributed hydrogen bonds to multiple bitumen functional groups. Each such hydrogen bond contributes separately to these fractions.

Fig. 3.5 distinguishes among the hydrogen bonds between water molecules and different functional groups. Water molecules form hydrogen bonds mainly with the NA, NC, and OHp functional groups. Among all functional groups, OHp and NA provide more of the water-bitumen hydrogen bonding sites, despite their lower concentrations compared to NC and SA. Fig. 3.5 (a) – (d) show that, in most cases, the distribution of hydrogen bonds based on functional groups remains similar regardless of changes in water content.

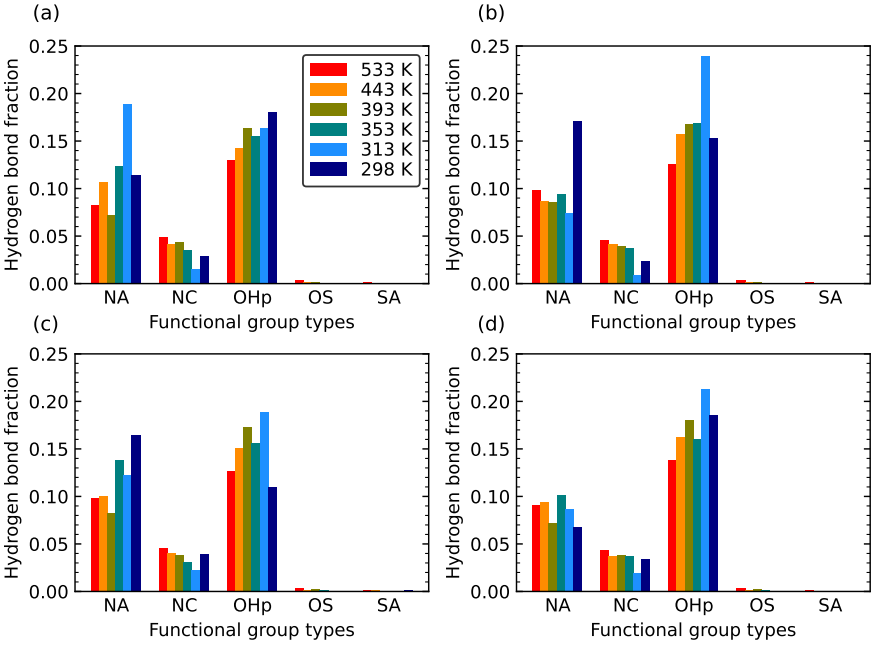

Figure 3.5 Distributions of hydrogen bonds between water and various types of functional groups in bitumen at water contents of (a) 0.11 wt%, (b) 0.22 wt%, (c) 0.44 wt%, and (d) 0.93 wt%. NA, NC, OHp, OS, SA are heteroatom-based functional groups that are shown in Fig. 3.1.

3.3.2 Water clusters

Water clustering describes the aggregation of water molecules via hydrogen bonding. Fig. 3.6 shows the size distributions of water clusters for all water-bitumen systems as a function of temperature. The cluster fraction indicates the ratio of the number of water clusters of one size to the total number of water clusters. Free water is excluded from this calculation, so the smallest cluster size is two water molecules.

Three types of cluster size distributions are revealed in Fig. 3.6, namely monotonically decreasing, bimodal, and multi-modal distributions. At 533 K, the fraction of water clusters shows a monotonic and smooth decrease with increasing cluster size for all water-bitumen systems. At 443 K, the distributions in bitumen systems with water contents of 0.22 – 0.93 wt% also decrease monotonically, while a bimodal distribution is observed for the system containing 1.76 wt% water. After an initial decrease, this distribution has a local peak for a cluster size of about 28 molecules. Water clusters with sizes between 5 and 24 are rare. Similar phenomena are observed for the water-bitumen systems at 393 K and 353 K. The systems with low water content exhibit a monotonically decreasing number fraction of clusters of increasing size, and a bimodal distribution is observed with increasing water content. For the water-bitumen systems with a bimodal distribution, some of the water molecules form water clusters with small sizes up to ca. 5 water molecules, and the rest form large water clusters with sizes as large as the maximum number of water molecules in the systems. The absence of water clusters with intermediate sizes suggests that water molecules either form scattered clusters with small sizes or form one large cluster. Essentially, due to the overall hydrophobicity of bitumen, only a limited number of water molecules are able to dissolve in bitumen, and the additional water molecules tend to form a separate water phase. A particular water content exists that serves as a threshold above which phase separation occurs, as illustrated in Fig. 3.7.

The water content at which the bimodal distribution first occurs is higher at higher temperatures. For the water-bitumen systems at 353 K, 393 K and 443 K, the presence of a bimodal distribution appears by water contents of 0.44 wt%, 0.93 wt%, and 1.76 wt%, respectively. This indicates a higher dissolution of water clusters with small sizes in bitumen at higher temperatures. It is consistent with the increase in free water content that is depicted in Fig. 3.4.

For water-bitumen systems at lower temperatures, i.e., 313 K and 298 K, a multimodal water cluster distribution is obtained in which water clusters form at various sizes that range from two to the maximum number of water molecules in bitumen. The presence of water clusters that contain nearly all water molecules in the systems indicates the same phase separation mechanism as previously described for higher temperatures. However, multiple peaks at low temperatures in Fig. 3.6 imply a more complex water clustering behavior. From another perspective, the larger error bars of cluster fractions at the lowest temperatures can potentially indicate an insufficient sampling time, which leads to different configurations and water cluster distributions among the five independent runs. In this regard, a bimodal water cluster distribution mode similar to the one at higher temperatures could potentially occur for water-bitumen systems at 313 K and 298 K when simulation sampling times even longer than 600 ns are applied.

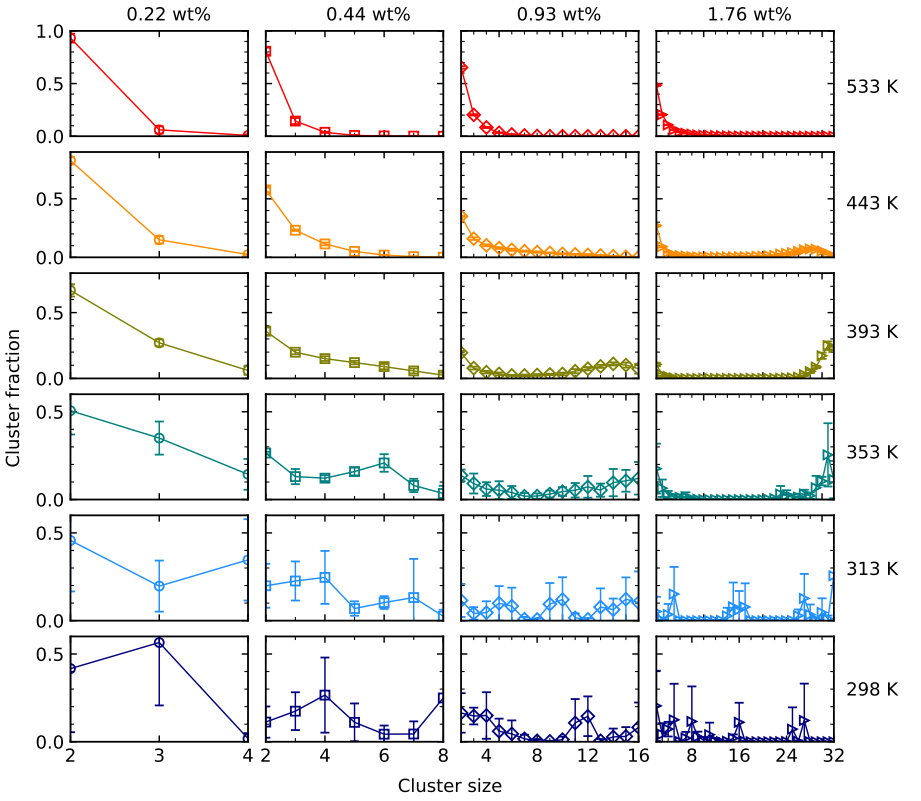

Figure 3.6 Distributions of water cluster sizes for bitumen systems with various water contents (columns) at various temperatures (rows). The maximum cluster size shown equals the number of water molecules in the simulation box.

3.3.3 Water radial distribution function

To investigate the positions of water molecules further, the RDFs for bitumen functional groups and water in the systems with 0.22 wt% and 0.93 wt% water were computed. The position $r = 0$ in Fig. 3.8 corresponds to atom OW, the oxygen atom of water, and $g(r)$ indicates the presence of heteroatoms in polar functional groups, as labeled in Fig. 3.1, or of atom OW, the oxygen atom of water. Because RDF is a tabulation of pair distances and their relative probabilities, this separation can be interpreted equivalently as the distribution of water around heteroatom functional groups.

The location of the first sharp peak is at ca. 2.9 Å for all RDFs, which is consistent with hydrogen bonds between water molecules and these functional groups. The RDF regions of OW-OW exhibit high intensities over ranges from the first peak (2.9 Å) to about 6 Å for the system with 0.22 wt% water and to ca. 10 Å for the system with 0.93 wt% water. This suggests a very high density of water neighbors, namely water clustering. Similar regions of intensities with $g(r) \gg 1$ are found for the RDFs of OHp–OW and NA–OW up to the same concentration-dependent separations, while intensity is less high for NC–OW. At

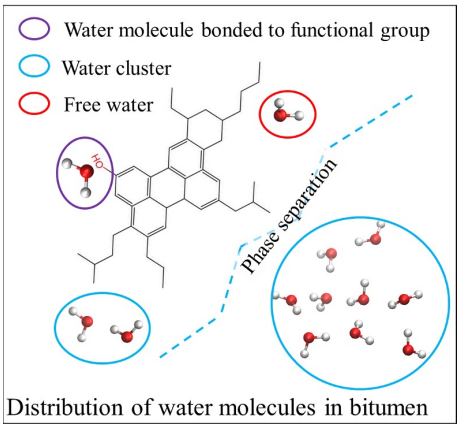

Figure 3.7 Distributions of water molecules in bitumen

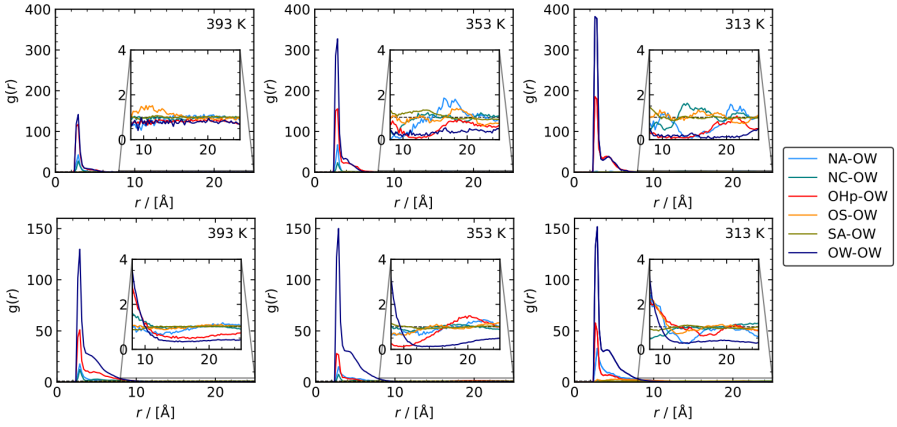

Figure 3.8 Radial distribution functions of water-water and water-bitumen functional groups for systems with water contents of 0.22 wt% (upper row) and 0.93 wt% (lower row) at different temperatures (columns). OW represents the oxygen atom of water and NA, NC, OHp, OS, SA are heteroatom-based functional groups as shown in Fig. 3.1.

larger separations, the local densities of OW–OW separations are suppressed compared to the average density, i.e., $g(r) < 1$ (Fig. 3.8 insets). This provides further support for water clustering because it shows that water molecules are very close to each other or are farther away than the maximum length scale that is probed by the simulations (i.e., half a box length). Findings of $g(r) < 1$ at long separations for OW–OHp, and for OW–NA to some extent, support a description of these clusters as each being in the vicinity of bitumen heteroatoms. The larger RDF peaks for OHp and NA, compared to NC and especially to OS and SA, are consistent with the distributions of hydrogen bonds between water and various types of functional groups depicted in Fig. 3.5.

3.3.4 Water diffusion in bitumen

Interpretations of gravimetric and spectroscopic experimental measurements of water transport in bitumen suggest differences in diffusion rates for water that remains free compared to water that forms hydrogen bonds and water clusters (Cheng et al., 2021; Herrington et al., 2021; Vasconcelos et al., 2010). To analyze this effect in the MD results, MSDs of water molecules for all water-bitumen systems were computed for correlation times (also known as time differences) of 0.1 ps to over 100 ns. Results presented in Fig. 3.9 indicate three regimes. The first represents the ballistic regime in which molecules move freely without having a collision, and MSD $\sim t^2$. The second regime shows anomalous diffusion in which MSD $\sim t^n$ with slope $n < 1$ on a log-log plot. The third regime describes the diffusive mode in which molecules escape this trapped domain and perform a random walk with MSD $\sim t$. These regimes exhibit different trends with increasing water content as denoted by arrows in the figure.

Fig. 3.9 shows that water molecules in bitumen systems with lower water content move through the first regime more rapidly. MSDs are higher at the initial time separation, and the diffusion exponent has already begun to decrease from its short-time $n = 2$ asymptote (inset, dashed line), particularly for lower water content. Lemarchand et al. (Lemarchand et al., 2016) found the same trends in their simulations of water in Cooee model bitumen. As shown in Fig. 3.3 (d), the number of hydrogen bonds per water molecule increases with higher water content, which indicates an increase in hydrogen bonding interactions among water molecules. This increased interaction leads to a slower ballistic motion of water molecules.

An anomalous second regime is found over time spans of ca. 10^{-3} to at least 10^{-1} ns in the water-bitumen systems, with the endpoint occurring at longer times for lower temperatures. Anomalous diffusion indicates motion within kinetically constrained regions (Greenfield, 2004), which means a molecule is blocked from diffusing further until a rare event opens a new path. A higher water MSD in the anomalous regime is observed for the systems with higher water content. This trend can be explained by micro-phase separation between water and bitumen. Water molecules that are surrounded by bitumen molecules move within a small region before being blocked. Water molecules within a water cluster are able to diffuse through the entire cluster before being blocked by the surrounding bitumen.

Higher water content leads to larger water cluster size as already discussed in section 3.2. For water molecules in larger clusters, a longer time is required to escape a cluster and to show diffusive motion. A later initiation of the third regime (MSD $\sim t$) is thus observed for systems with higher water content. As a result, the larger cluster size leads to a lower diffusion coefficient of water. It is important to note that this initiation time increases significantly at lower temperatures, such as from 1 to 10 to over 100 ns at 313 K for 0.11, 0.44, and 0.93 wt%, respectively. Simulations (Du et al., 2021; Luo et al., 2021) that span only shorter times than this crossover can therefore only capture the anomalous and ballistic dynamics. True diffusion is not yet in effect even if a plot with linear axes of MSD vs. correlation time can be fit with a straight line over a limited time domain.

The logarithmic axes of Fig. 3.9 facilitate illustrating how imposing a linear fit, $\log \mathrm{MSD} = \log 6D + \log t$, at too short of a correlation time will suggest a shift of the $n = 1$ line (dashed) to earlier times. This "left shift" of the fit leads to a higher MSD at $t = 1$, which implies

an artificially high diffusion coefficient. Long enough simulations are required in order to have confidence in a reported diffusion coefficient. Prior simulations of water that reached the diffusive regime in bitumen (Lemarchand et al., 2016) also showed a decrease in the diffusion coefficient of water as water content increased.

To illustrate the effects of hydrogen bonding and water clustering on water diffusion dynamics, examples of distinct MSD patterns in a simulation at 313 K are shown in Fig. 3.10. The MSDs of all water molecules (16 water molecules labeled as 1 – 16 in a bitumen system with 0.93 wt% water content) are plotted individually. MSDs between distinct time points $\Delta t = (t_j - t_i) > 0$ evolve in four patterns.

Many water molecules remain in the same cluster through most of the simulation. Water molecules 3, 5, 6, 9, 12, 13, 14, and 15 experience similar MSDs and show similar diffusion dynamics. The upper snapshot inset in Fig. 3.10 visualizes that these water molecules belong to the same water cluster (group 1). Another MSD pattern is shared by water molecules 1, 2, 7, and 16 (group 2). To verify that water molecules with similar MSDs are in the same water cluster throughout the simulation, the probabilities of water molecules being in the same water cluster group were calculated. These are defined as the ratio of the number of snapshots in which water molecules belong to the same cluster group to the total number of snapshots. Molecules 3, 5, 6, 9, 12, 13, 14, and 15 are in group 1 for 97.6% of all snapshots. This probability is 92.5% for water molecules 1, 2, 7, and 16 in group 2. The probabilities that water molecules in Fig. 3.10 are free or have certain types of hydrogen bonds (water-bitumen, water-water, or both) were also calculated as time

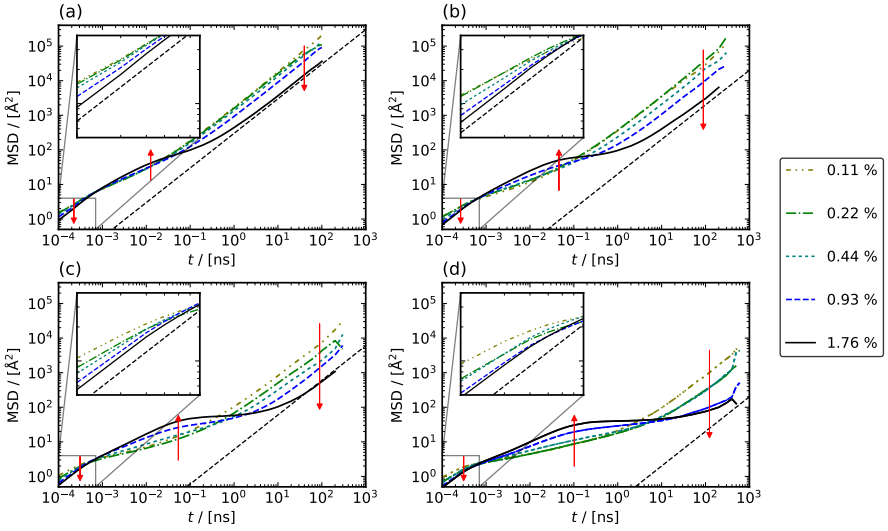

Figure 3.9 Mean-squared displacements of water molecules for bitumen systems with water contents from 0.11 wt% to 1.76 wt% at temperatures of (a) 443 K, (b) 393 K, (c) 353 K and (d) 313 K. Black dashed lines in each panel (inset) have a slope of one (two). Arrows indicate trends of MSDs with increasing water content at different time scales.

averages and are presented in Table 3.3. The probabilities of being free, experiencing water-bitumen, and experiencing water-water hydrogen bonding are similar for water molecules in the same cluster group.

Another pattern involves diffusing water molecules belonging to a distinct water cluster less frequently. Molecule 10 was found to be part of group 1 in 95.4% of the simulation snapshots, lower by 2.2% than other molecules in the same cluster. A representative series of consecutive simulation snapshots corresponding to ca. 600 ps are shown in Fig. 3.11. During this short simulation period, molecule 10 moves away from group 1 and later rejoins this same group. Visualization of the full trajectory shows that this pattern recurs. The similar MSDs of molecule 10 and group 1 for $\Delta t < 1$ ns correspond to their shared dynamics as a group. The greater MSD of molecule 10 at longer correlation times compared to the MSD of molecules in group 1 is a result of its higher mobility when it is outside of the cluster.

Some water molecules depart from a water cluster and diffuse elsewhere. The faster diffusion of molecule 4, compared to group 2, can also be explained by its higher probability of being free and its lower probability of remaining in group 2 (87.7%). Visualization of the full trajectory indicates that molecule 4 diffuses far away from group 2 in some snapshots. Later, it encounters and joins a periodic image of the same group. The probabilities for molecule 11 to form water-bitumen and water-water hydrogen bonds are between the probabilities that are found for molecules in group 1 and group 2. Molecule 11 is in group 1 and group 2 for 37.0 % and 56.6 % snapshots, respectively. Its higher MSD compared to

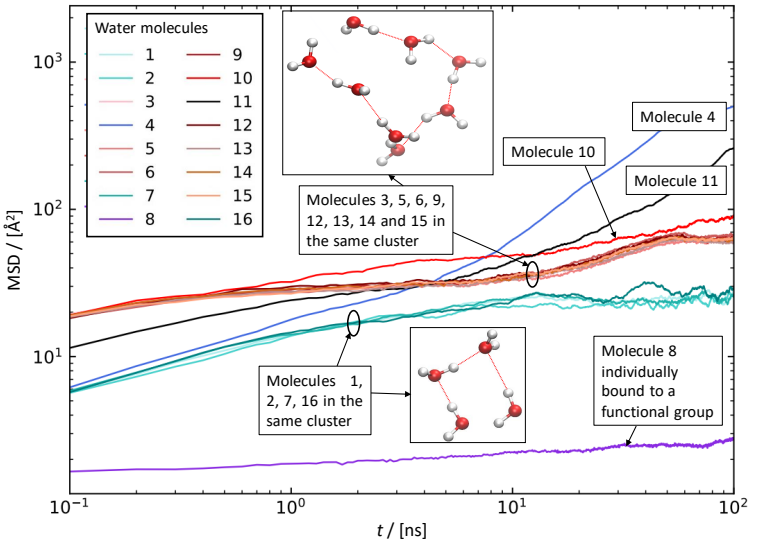

Figure 3.10 MSDs as a function of correlation time for all individual water molecules in a bitumen system with 16 water molecules (0.93 wt% water content) at 313 K. Insets depict water clusters within a representative simulation snapshot at the elapsed time indicated (gray atoms denote hydrogen, red atoms denote oxygen).

Table 3.3 Probabilities for water molecules to stay as free or to form water-bitumen (bit-wat) or water-water (wat-wat) hydrogen bonds in the water-bitumen system with 16 water molecules (0.93 wt% water content) at 313 K. Water molecules hydrogen bonded to both water and bitumen were defined as the bit-wat-wat group.

Water Molecule	Group-1								10	Group-2				4	11	8
	3	5	6	9	12	13	14	15		1	2	7	16			
Free	0.01	0.01	0.01	0.01	0.01	0.01	0.01	0.01	0.03	0.01	0.00	0.01	0.01	0.03	0.01	0.03
Bit-wat	0.00	0.00	0.00	0.00	0.00	0.00	0.00	0.00	0.00	0.04	0.04	0.05	0.05	0.06	0.03	0.97
Bit-wat-wat	0.12	0.12	0.15	0.12	0.12	0.11	0.13	0.13	0.12	0.47	0.40	0.48	0.51	0.44	0.34	0.00
Wat-wat	0.87	0.87	0.84	0.87	0.87	0.87	0.86	0.85	0.84	0.48	0.56	0.46	0.43	0.47	0.62	0.00

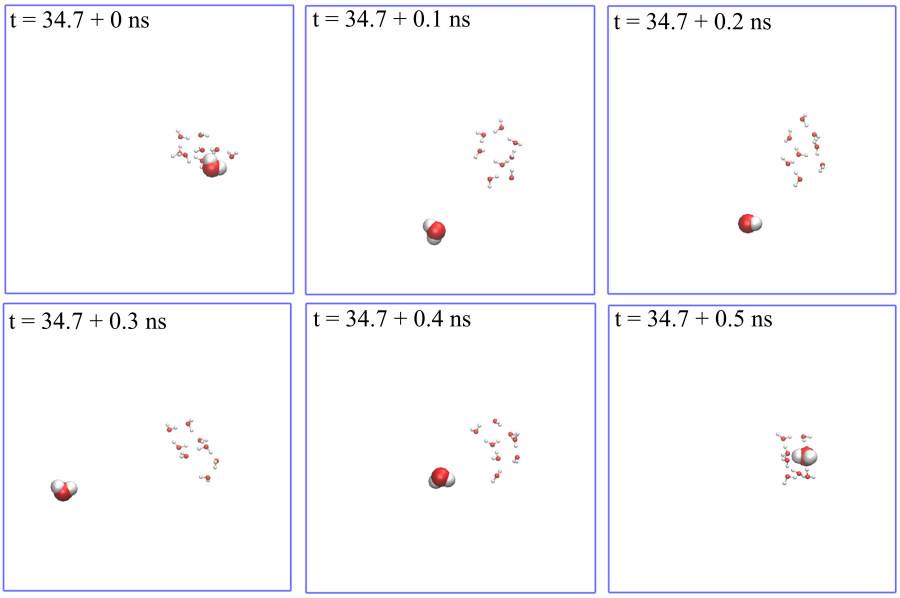

Figure 3.11 Continuous trajectory snapshots (with an interval of 100 ps) of molecule 10 and cluster group 1 in the bitumen system with 16 water molecules (0.93 wt% water content) at 313 K. Molecules with smaller radii represent water cluster group 1 while molecule 10 is depicted with a larger radius.

group 1 and group 2 is a consequence of its higher mobility.

The final pattern is the slow diffusion experienced by molecule 8. In 97% of snapshots, this molecule is hydrogen bonded to functional groups of bitumen. Due to the slower diffusion of bitumen components compared to water, this water molecule diffuses more slowly.

In terms of the three diffusion regimes, Fig. 3.10 shows that water molecules that are in water clusters and or that are hydrogen bonded to bitumen exhibit only anomalous diffusion over the correlation times shown. Only the water molecules that manage to escape

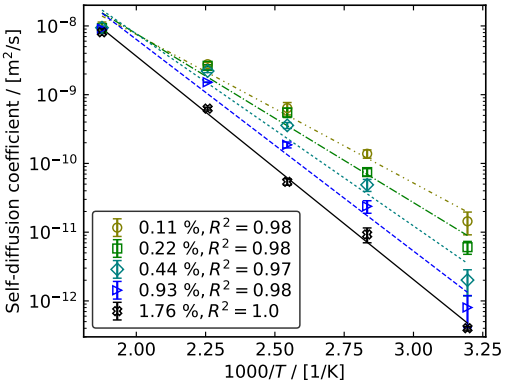

Figure 3.12 Self-diffusion coefficients of water in water-bitumen systems with various water contents as a function of temperature. Lines indicate Arrhenius fits.

Table 3.4 Concentration-dependent self-diffusion coefficient and corresponding Arrhenius parameters for water in bitumen

Water content / [wt%]	0.11	0.22	0.44	0.93	1.76
D^{∞}_{self} at 313 K / [m^2/s]	1.43×10^{-11}	6.05×10^{-12}	2.01×10^{-12}	8.02×10^{-13}	4.01×10^{-13}
D_0 / [m^2/s]	1.58×10^{-4}	6.29×10^{-4}	2.96×10^{-3}	9.15×10^{-3}	1.15×10^{-2}
E_A / [kJ/mol]	41.4	47.0	53.5	58.9	62.2

water clusters and diffuse elsewhere (molecules 4 and 11 in this example) exhibit true diffusive motions. Even molecule 10 exhibits a root-mean-squared displacement smaller than 10 Å over $\Delta t \sim 200$ ns at 313 K.

The self-diffusion coefficients of water in the bitumen systems with various water contents and at different temperatures are shown in Fig. 3.12. They are fit to the Arrhenius equation

$$\ln D^{\infty}_{\text{self}} = \ln D_0 - \frac{E_A}{RT} \tag{3.11}$$

where D^{∞}_{self} is calculated from MSD and corrected for finite-size effects according to Equations 3.7 and 3.8, D_0 is a constant, E_A is the activation energy of self diffusion, R denotes the universal gas constant, and T is the temperature. The fitted parameters are shown in Table 3.4. In Fig. 3.12, it can be seen that increasing water content reduces the self-diffusion coefficient of water. As discussed earlier, lower temperature and higher water content in the system cause increases in the numbers of hydrogen bonds and of water clusters, which result in a slower diffusion rate and a higher activation energy. In all cases, the activation energy for diffusion is significantly greater than the energetic cost for a water molecule to become free of a water cluster.

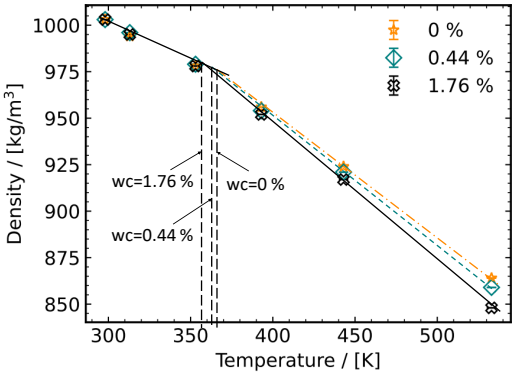

Figure 3.13 Densities of simulated water-bitumen systems with various water contents as a function of temperature. Sloped lines are linear fits of density vs temperature. Vertical dashed lines indicate the intersections of density linefits.

3.3.5 Bitumen properties in the presence of water

So far, we have shown that water molecules in bitumen can be free, hydrogen bonded to bitumen, or hydrogen bonded to other water molecules, and the diffusion coefficient varies significantly for these water states. In this section, density, viscosity, and cohesive energy of water-bitumen systems are computed to evaluate the effects of hydrogen bonding and water clustering on bitumen properties.

The densities of the water-bitumen systems are shown in Fig. 3.13. The bitumen density computed at 298 K without water is 1004 kg/m^3, which is close to the density of 1000 kg/m^3 reported by Li and Greenfield (Li & Greenfield, 2014b) from shorter simulations (same bitumen model as in this work) and 997 kg/m^3 reported by Khabaz and Khare (Khabaz & Khare, 2015) for the same model composition simulated with the general AMBER force field (Wang et al., 2004). The interpolated simulated density is 3.5% smaller than the experimental value of 1030 g/cm^3 at 333 K (Robertson et al., 2001). The thermal expansion coefficient $\alpha = -\frac{1}{\rho}\left(\frac{\partial \rho}{\partial T}\right)_P = 5.5 \times 10^{-4}$ K^{-1} from simulation is slightly smaller than the 5.9×10^{-4} reported from experiments (Robertson et al., 2001).

The density of the simulated water-bitumen systems depends on water content and temperature. The density of water at 1 atm is 972 – 997 kg/m^3 at temperatures from 353 K to 298 K, which is similar to that of bitumen. Therefore, no significant changes are expected for bitumen density upon ideal mixing with water at lower temperatures. At temperatures higher than 353 K, the addition of water decreases the water-bitumen density.

A glass transition is indicated by a change in slope of density as a function of temperature. The transition temperature (T_g) is determined by the intersection of linear fits that represent glassy and rubbery regimes. The computed T_g of ca. 360 K is significantly higher than the experimental value of ca. 250 K (Turner & Branthaver, 1997). A T_g of 350 K was identified in previous MD simulations (Khabaz & Khare, 2015) of the LG14 bitumen model that computed densities at temperatures from 600 to 80 K with a step of 20K. One possible reason for the divergence of computed T_g from experimental values is the much

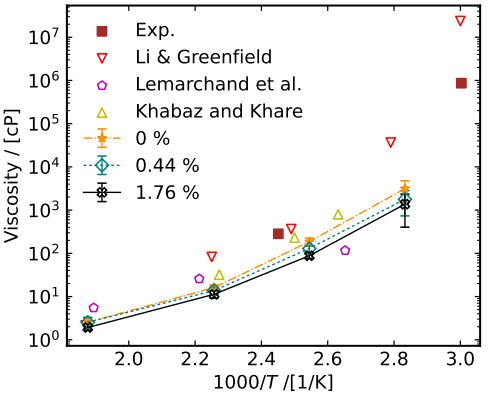

Figure 3.14 Viscosities of water-bitumen and bitumen systems computed in this work and from the MD simulations reported by Li and Greenfield (AAA-1) (Li & Greenfield, 2014a), Lemarchand et al. (Cooee) (Lemarchand et al., 2015), Khabaz and Khare (AAM-1) (Khabaz & Khare, 2018), and from experiments on SHRP AAA-1 bitumen (Jones et al., 1993).

higher cooling rate of MD simulations compared to experimental tests (Khabaz & Khare, 2015). For polymeric materials, a higher experimental cooling rate results in a higher glass transition temperature (T_g) and a lower density because of insufficient time for structural relaxation (Angell et al., 2000). Consequently, the higher cooling rate used in molecular simulations yields a higher T_g than what is typically observed in experimental settings. Furthermore, a decrease in T_g with higher water content demonstrates a plasticization effect of water (Oba & Björk, 1993), which influences the relaxation and viscosity of bitumen systems, as discussed in the following section.

The viscosities of bitumen and water-bitumen systems are shown in Fig. 3.14. A decrease in viscosity with increasing water content is observed, which is consistent with plasticization, i.e., increasing water content can facilitate bitumen mobility, thus resulting in a lower viscosity. Also, the long correlation times that are required until the eventual attainment of a log-scale slope of 1 indicate the long stress relaxation time scales that are required for the viscosity calculation to converge. The relaxation time scale already exceeds hundreds of nanoseconds at 393 K and is even longer at lower temperatures.

Fig. 3.14 also shows the viscosities obtained from experiments (Jones et al., 1993) and from MD simulations reported by Li and Greenfield (Li & Greenfield, 2014a), Lemarchand et al. (Lemarchand et al., 2015), as well as Khabaz and Khare (Khabaz & Khare, 2018). Li and Greenfield (Li & Greenfield, 2014a) calculated viscosity directly at 533 K for the same bitumen model as used in the present work; those at other temperatures were scaled based on the rotational relaxation times computed from MD simulations. Lemarchand et al. (Lemarchand et al., 2015) used the Cooee bitumen model and non-equilibrium MD (NEMD) simulations to compute shear viscosity. The viscosities reported by Khabaz and Khare (Khabaz & Khare, 2018) were computed using the NEMD method, the SHRP AAM-1 version of the LG14 bitumen model (Li & Greenfield, 2014b), and the general AMBER

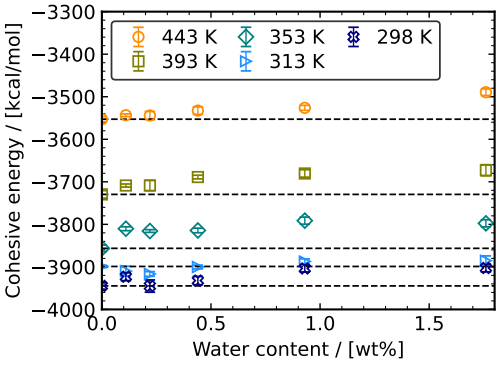

Figure 3.15 Cohesive energy of bitumen components as a function of water contents at various temperatures.

force field (Wang et al., 2004). The computed viscosity at 533 K in this work agrees well with the value provided by Li and Greenfield (Li & Greenfield, 2014a). Other viscosities directly obtained from the present MD simulations are lower than the inferred viscosities in Ref. (Li & Greenfield, 2014a). Compared to the results of the present work, viscosities by Lemarchand et al. (Lemarchand et al., 2015) are slightly higher at higher temperatures and are lower at lower temperatures. The viscosities computed in the present work are slightly lower than those computed by Khabaz and Khare (Khabaz & Khare, 2018) for simulated SHRP AAM-1. All the viscosities shown in Fig. 3.14 that are computed directly by molecular simulation are lower than typical experimental results. This could be due to limitations of the LG14 model in simulating bitumen. This 12-component bitumen model cannot incorporate the full range of molecule polarities and sizes that are present in real bitumen. The benzobisbenzothiophene that supplies much of the sulfur has a low molecular weight compared to most molecules in real bitumen, for example.

Fig. 3.15 shows the variation of bitumen cohesive energy as a function of water content at different temperatures. Adding water molecules in bitumen slightly decreases the cohesive energy of bitumen (negative cohesive energy is more favorable). This may be explained by water molecules replacing the initial bitumen-bitumen hydrogen bonds by forming water-bitumen hydrogen bonds (Fig. 3.3). Furthermore, nearest-neighbor bitumen-bitumen nonbonded interactions other than hydrogen bonding can be replaced by water-bitumen interactions, especially for the locations where water clusters occur (Fig. 3.8). This further weakens the interactions between bitumen components. The variation of cohesive energy with respect to water content does not show a clear dependence on temperature. Differences among the five independent simulations were smaller at higher temperatures; there, the relaxations are faster and the results are better converged.

3.4 Coupling of experimental results and MD simulations

Macro-scale water diffusion models invoke assumptions that absorbed water is present in both free and bound modes (Apeagyei et al., 2015; Cheng et al., 2021; Herrington et al., 2021; Vasconcelos et al., 2010). Results in the prior sections describe the distributions of

free water and water clusters via hydrogen bonding in bitumen, as well as their diffusion dynamics. This section is intended to interpret these simulation results and to provide in-depth insights into the micro-scale diffusion mechanisms and assumptions involved in diffusion models that are used to infer diffusion coefficients from experimental gravimetric and spectroscopic data, as discussed in Chapter 2 and other relevant studies.

3.4.1 Water states in bitumen

Three water hydrogen bonding states are revealed from the MD simulations by quantifying the types of hydrogen bonds: free water, water hydrogen bonded to bitumen, and water hydrogen bonded to water. The extent that water molecules experience each hydrogen bonding state and the ways that their diffusion dynamics can be interpreted via free and bound modes depend on both temperature and water content. To characterize the water hydrogen bonding environment in bitumen further, the relative fractions of each state were calculated at all temperatures. Water molecules hydrogen bonded both to water and to bitumen are included in the category of water–bitumen hydrogen bonds. Results are depicted in Fig. 3.16.

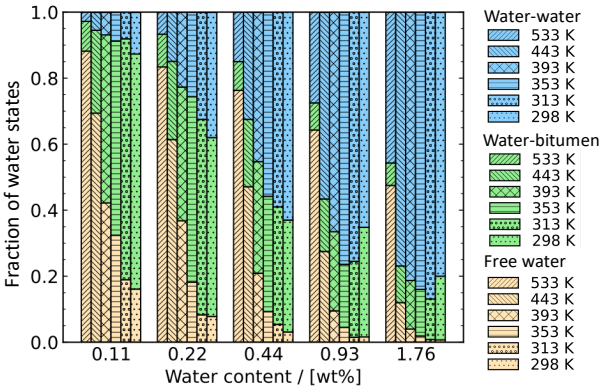

Figure 3.16 Distribution of water hydrogen bonding states in bitumen: free water, water with water-bitumen hydrogen bonds, and water with water-water hydrogen bonds. Within each water content, temperature decreases from left to right.

The structures formed by absorbed water molecules relate qualitatively to the temperature-dependent extent that bitumen molecules can fluctuate in orientation and shape. These affect the accessibility of hydrogen bonding sites. Fig. 3.3, Fig. 3.4, and Fig. 3.16 show that the distribution of hydrogen bonding configurations in bitumen is affected by both temperature and water content. For bitumen systems at lower temperatures, only small absolute differences in the numbers of hydrogen bond types (Fig. 3.3) and in the free water content (Fig. 3.4) are observed with increasing water content. In water-bitumen systems at higher temperatures, a rise of the amount of free water with temperature is more apparent (Fig. 3.4). Simultaneously, a significant decrease is observed in all types of hydrogen bonds with increasing temperature. Combining these trends, there are fewer hydrogen bonds and more free water molecules with increasing temperature. In the lower

temperature regime, changes in temperature have smaller effects on hydrogen bonds and free water contents. Together, these results indicate a higher solubility of water in bitumen and a lower probability to form large water clusters at higher temperatures (Fig. 3.6).

The overall number of hydrogen bonds increases with water content (Fig. 3.3), which results in more water clusters with larger cluster sizes, as shown in Fig. 3.6. Participating in hydrogen bonds is more energetically favorable for water (Fig. 3.4 (b)), so very little water is required before a droplet forms. The cluster size distribution reveals that large water droplets, with sizes as large as the maximum number of water molecules in the systems, form in the simulated bitumen at water concentrations higher than 0.93 wt%, 0.44 wt%, and 0.22 wt% at temperatures of 443 K, 393 K, and 353 K, respectively. Increasing further the water concentration, additional water molecules mostly contribute to the growth of this large droplet (Lemarchand et al., 2016). This growth in water clusters may account for the observed constant rate of absorption, not approaching saturation over 395-day testing period as indicted by Herrington et al. (2021). However, the maximum size to which this droplet grows is still unknown. Overall, at any given temperature, there exists a maximum amount of free and bitumen-bonded water in bitumen. Beyond this threshold, additional water molecules predominantly form clusters.

The three water states and water clustering behavior in bitumen revealed by MD simulations corroborates the assumption of water states in the S-Cluster model proposed in Chapter 2, i.e., water molecules in bitumen exist in three states: free water, water bound to polar sites, and water clustering. The sizes of water clusters derived based on the Zimm-Lundberg model in section 2.6.3 align closely with the simulated water cluster sizes shown in Fig. 3.6. For example, experimental results indicate an approximate cluster size of 2 – 3 for bitumen with a water concentration of 124 mol/m^3 at 313 K, and the simulated mean cluster size at a water content of 0.22 wt% (equivalent to 129 mol/m^3) is also between 2 and 3 (Fig. 3.6).

3.4.2 Diffusion coefficients of water in bitumen

The different diffusion dynamics of the water states revealed by simulations offer insights into the assumptions in the diffusion models used for interpreting experimental data as well as into the physical meanings of different diffusion coefficients as listed in Table 3.5. The diffusion rate of water is influenced by the extent to which it engages in hydrogen bonding and forms water clusters with other water molecules. Free water has the fastest diffusion rate, while water in clusters exhibits much slower diffusion dynamics. Water molecules hydrogen bonded to bitumen may be considered as completely immobile because their large-scale motions are confined to the diffusion of functional groups of bitumen.

MD simulation results for the self-diffusion coefficient of water in systems with low water mass fractions can be compared to the diffusion rate of the free water mode in diffusion models that are fit to data from experiments conducted close to the infinite dilution limit (Cheng et al., 2021; Herrington et al., 2021; Vasconcelos et al., 2010). The self-diffusion coefficients of water in the systems with 0.11 wt% and 0.22 wt% water contents at 313 K are 1.43×10^{-11} m^2/s and 6.05×10^{-12} m^2/s, respectively. The computed self-diffusion coefficients are close to the experimental values of 3.2×10^{-12} m^2/s – 4.6×10^{-12} m^2/s that provided in Chapter 2, in which the water concentration is ca. 0.15 wt%. Other

Table 3.5 Diffusion coefficients of moisture in bitumen, mastics and bituminous mixtures obtained from experiments.

Method	Model	Moisture	Bitumen	Diffusivity (m^2/s)	Absorption	Ref.
FTIR-MIR	Fick's law	Liquid	AAC-1	1.4E-14	6%	(Nguyen et al., 1992)
			AAD-1	2.5E-14	6%	
			AAK-1	3.3E-14	6%	
FTIR-ATR	Dual	Liquid	AAB	1.5E-17	/	(Vasconcelos et al., 2011)
			AAD	1.6E-17	/	
			ABD	5.2E-17	/	
FTIR-ATR	Langmuir	Liquid	Bitumen	**1.1–1.5E-17**	/	(X. Chen et al., 2022)
EIS	Continuous	Vapor	Bitumen	2.2–2.8E-14	/	(X. Chen et al., 2022)
Gravimetric	/	Vapor	AAD-1	1.3E-9	0.021%	(Cheng et al., 2003)
			AAM-1	**4.8E-9**	**0.016 %**	
Gravimetric	Langmuir	Liquid	Bitumen	2.6–6.5E-15	**1.2–7.0%**	(Cheng et al., 2021)
Gravimetric	Reaction	Liquid	Bitumen	0.5–15.2E-14	0.65–2.4%	(Herrington et al., 2021)
Gravimetric	Clustering	80% RH	Bitumen	2.1–3.0E-12	0.12%	In Chapter 2
Gravimetric	Fick's law	85% RH	Mastic (<1mm)	1.3–4.8E-12	0.07–0.14%	(Apeagyei et al., 2015)
Gravimetric	Fick's law	Vapor	FAM (<4.75mm)	2.5E-10	/	(Arambula et al., 2010)

experimental studies (Cheng et al., 2021; Herrington et al., 2021) have reported a much lower diffusion coefficient of the free mode i.e., in the range of 10^{-15} – 10^{-13} m^2/s. In (Cheng et al., 2021), the free water fraction is reported as ca. 0.4 – 0.9 wt% (the total water absorption is ca. 1.2 – 6.5 wt%), which is much higher than the free water fraction in the simulations, as shown in Fig. 3.16. The free and bound phases revealed in (Cheng et al., 2021) may be considered as water molecules belonging to water clusters and hydrogen-bonded to polar sites of bitumen, respectively. Therefore, the lower diffusion coefficients obtained from these experiments could represent the diffusion rate of water clusters instead of the free water molecules, as assumed in the diffusion models.

Structure and diffusion results from MD simulations suggest that the "bound mode" in diffusion models (Cheng et al., 2021; Herrington et al., 2021; Vasconcelos et al., 2010) corresponds to water molecules that are hydrogen bonded to polar sites of bitumen or are clustered together via water-water hydrogen bonding. At temperatures commonly used in experiments (298 K and 313 K), and for lower water contents, the water molecules that form water-bitumen hydrogen bonds dominate the bound phase, which can be assumed as completely immobile. As the water content increases, additional water molecules mainly form water clusters with water-water hydrogen bonds. At this water concentration, the "bound phase" should be considered as diffusing with a much lower diffusion coefficient, which decreases with cluster sizes. However, in the S-Cluster model proposed in Chapter 2, the clustering water fraction is assumed as immobile. Consequently, this model may capture well the diffusion coefficients of water in free mode and hydrogen bonded to polar sites at low water concentration (< 0.11 – 0.22 wt%), but may not adequately describe the diffusion dynamics of water clusters at higher water concentrations.

To summarize, at low water concentrations (such as 0.11 wt%), water molecules either freely diffuse in bitumen with a diffusion coefficient of ca. 10^{-12} m^2/s or are hydrogen bonded to polar sites, which can be assumed as immobile. As water concentration

increases, water clusters occur and their sizes and fractions gradually increase until they become the dominant water phase at water concentrations greater than ca. 0.5 wt%. The diffusion coefficients of these clusters depend on the cluster size and are in the range of 10^{-15} – 10^{-13} m^2/s, or even lower. At this stage, the fraction of free water is small, and the remaining water outside clusters is hydrogen bonded to bitumen and is immobile.

Additionally, Table 3.5 lists considerably lower diffusion coefficients of order 10^{-17} m^2/s measured by FTIR-ATR. During a spectroscopic measurement, particularly with long-time water immersion, the water content in a bitumen film could be high, resulting in a much lower free water fraction and a predominance of water clusters. Therefore, obtained spectral signals might be more representative of the diffusion rate of clusters (with a much lower diffusion rate) than of the diffusion of isolated water molecules within bitumen. Furthermore, diffusion coefficients measured using alternative spectroscopic methods in (Chen et al., 2022; Nguyen et al., 1992) are in the order of 10^{-14} m^2/s, closer to the simulated results as presented in this chapter. This indicates a possibility of technical errors in the results measured by FTIR-ATR. A diffusion coefficient of moisture in bitumen exceeding 10^{-10} m^2 is also mentioned in Table 3.5, which is higher than the simulated diffusion coefficient at lowest water concentration. This high diffusion rate may be attributed to surface diffusion rather than bulk diffusion as indicated in Chapter 2.

3.4.3 Effects of water on bitumen properties

Results from the distributions of hydrogen bonds between water and various types of functional groups (Fig. 3.5) and the radial distribution functions (Fig. 3.8) provide additional information about where hydrogen bonds and water droplets were located within the simulated bitumen. These results show that the positions of hydrogen bonds and water clusters depend on the functional groups in bitumen. Among all types of functional groups in simulated LG14 model, water clusters are mostly next to a pyrrole (NA) or phenol (OHp) group, as indicated by $g(r) < 1$ at large separations for these atom pairs, while some water clusters are near a pyridine (NC) group. From the perspective of the heteroatom, water molecules tend to be nearby rather than randomly distributed. Consequently, the type and fraction of heteroatom-based functional groups in bitumen are crucial factors that affect water clusters. These functional groups act like nuclei for the growth of clusters at high water contents.

In addition to polar functional groups (content of ca. 0.5–5 wt%), inorganic salts and metals (content in the range of 1-1000 ppm) (Read & Whiteoak, 2003) may also act as water clustering sites (Herrington et al., 2021; Nguyen et al., 2005). Salts and metals were not incorporated here. This is due in part to their low concentration; a single NaCl molecule added to the LG14 bitumen model would have a mass concentration of 1800 ppm. These trace elements in bitumen, along with functional groups at a bitumen-aggregate interface, may also act as nuclei for the formation of water clusters.

In experiments, saturated moisture content varies with bitumen types (Cheng et al., 2021; Herrington et al., 2021; Vasconcelos et al., 2010), which vary in heteroatom content and thus in heteroatom bonding chemistry as consequences of the bitumen crude oil source and the production method employed. Cheng et al. (2021) reported a positive relationship between water absorption and asphaltene fraction, which contains more heteroatom components than other SARA fractions. Within the LG14 model for bitumen,

the polar sites that attract water are in distinct fractions. NA and OHp are exclusively in the asphaltene fraction and NC is exclusively in the resin fraction. Sulfide sulfur that can oxidize to sulfoxide is absent in the model. This discrete distinction between asphaltene and resin is a consequence of the relatively small number of distinct molecule types in the LG14 system rather than an accurate depiction of bitumen chemistry in general. Presence of NA and OHp among asphaltenes is consistent with an increased asphaltene fraction providing an increased opportunity for probable water–bitumen hydrogen bonding and water clustering sites. An increased number of these sites may lead to a higher water absorption in bitumens that differ in their distribution of SARA fractions.

The physical properties of water-bitumen systems show that the presence of water in bitumen decreases its viscosity. As noted in sections 3.3.1 and 3.3.2, the soluble water concentration in bitumen (i.e., free water molecules and water molecules with small cluster sizes) is low, especially at lower temperatures. For the water-bitumen systems with high water contents, there are large water clusters (water droplets), which indicate a separated water phase. These clusters can increase the flexibility of bitumen and decrease its viscosity. The presence of water clusters also suppresses interactions between bitumen components and therefore weakens bitumen cohesion.

At macroscopic scales, it can be expected that the majority of water would form large water droplets that accumulate around polar sites in bitumen. In this case, the macroscale cohesion of bitumen could be seriously weakened. Furthermore, the polarity of aggregates is generally higher than that of bitumen (Baldi-Sevilla et al., 2017). Providing a higher concentration of polar sites on the aggregate surface makes water molecules more likely to form clusters at the bitumen-aggregate interface, which can lead to the degradation of adhesion between bitumen and aggregates. By forming water droplets inside bitumen and at the bitumen-aggregate interface, water transport can result in cohesive and adhesive failure.

3.5 Summary

To gain a molecular-level insight into the assumptions of water diffusion models for experimental analysis, and to provide an atomistic explanation of water-induced damage mechanisms in bituminous materials, water-bitumen systems with water contents ranging from 0 wt% to 1.76 wt% at various temperatures were investigated using MD simulations with durations up to 600 ns.

The analysis reveals the presence of three types of hydrogen bonds within the water-bitumen systems: bitumen-bitumen, water-bitumen, and water-water hydrogen bonds. Based on hydrogen bond types, three water molecular states are revealed: free water, water with water-bitumen hydrogen bonds, and water with water-water hydrogen bonds (water clusters). Some water molecules form hydrogen bonds with both bitumen and other water molecules. At lower water contents (compared to a solubility limit that increases with increasing temperature), water molecules are scattered inside the bitumen structure as free molecules or are hydrogen-bonded to bitumen. At higher water contents, most of the water molecules cluster together into large droplets via water-water hydrogen bonding, resulting in a phase separation between water and bitumen. The large water clusters tend to form at positions close to the pyrrole and phenol functional groups in bitumen. The type and content of functional groups are highly related to the absorption of

water in bitumen.

Water diffusion in bitumen is primarily influenced by hydrogen bond interactions between water and bitumen, as well as water clustering behavior. The formation of hydrogen bonds and water clusters substantially reduces the diffusion rate of water in bitumen. The diffusion coefficient of free water in diluted water-bitumen systems is ca. 4.7×10^{-12} m^2/s to 1.4×10^{-11} m^2/s at 313 K. With increasing water cluster size, its diffusion coefficient decreases and could be 1 – 2 orders of magnitude smaller than that of free water. Water molecules hydrogen-bonded to functional groups of bitumen can be assumed as completely immobile compared to bitumen.

The density, glass transition temperature, viscosity, and cohesive energy were computed. In most cases, all these parameters decrease with increasing water content in bitumen, which coincides with the formation of hydrogen bonds and water clusters. When adding water molecules to bitumen, existing bitumen-bitumen hydrogen bonds can be replaced by water-bitumen hydrogen bonds. At high water contents, large water droplets with sizes close to the number of water molecules in the simulation box are formed, which further hinders the interactions between bitumen components. As a result, the cohesion of bitumen is weakened. The presence of these water droplets also reduces the glass transition temperature and viscosity of water-bitumen systems.

References

Allen, M. P., & Tildesley, D. J. (2017). *Computer simulation of liquids*. Oxford university press.

Andersen, H. C. (1983). Rattle: A "velocity" version of the shake algorithm for molecular dynamics calculations. *Journal of Computational Physics*, *52*(1), 24–34.

Angell, C. A., Ngai, K. L., McKenna, G. B., McMillan, P. F., & Martin, S. W. (2000). Relaxation in glassforming liquids and amorphous solids. *Journal of Applied Physics*, *88*(6), 3113–3157.

Apeagyei, A. K., Grenfell, J. R., & Airey, G. D. (2015). Application of Fickian and non-Fickian diffusion models to study moisture diffusion in asphalt mastics. *Materials and Structures*, *48*(5), 1461–1474.

Arambula, E., Caro, S., & Masad, E. (2010). Experimental measurement and numerical simulation of water vapor diffusion through asphalt pavement materials. *Journal of Materials in Civil Engineering*, *22*(6), 588–598.

Baldi-Sevilla, A., Montero, M. L., Aguiar-Moya, J. P., Loria-Salazar, L. G., & Bhasin, A. (2017). Influence of bitumen and aggregate polarity on interfacial adhesion. *Road Materials and Pavement Design*, *18*(sup2), 304–317.

Berendsen, H., Grigera, J., & Straatsma, T. (1987). The missing term in effective pair potentials. *Journal of Physical Chemistry*, *91*(24), 6269–6271.

Brown, W. M., Kohlmeyer, A., Plimpton, S. J., & Tharrington, A. N. (2012). Implementing molecular dynamics on hybrid high performance computers–particle–particle particle-mesh. *Computer Physics Communications*, *183*(3), 449–459.

Celebi, A. T., Jamali, S. H., Bardow, A., Vlugt, T. J. H., & Moultos, O. A. (2021). Finite-size effects of diffusion coefficients computed from molecular dynamics: A review of what we have learned so far. *Molecular Simulation*, *47*(10-11), 831–845.

Chen, Geng, J., Chen, H., Niu, Y., Wang, R., Wu, W., Zhao, S., & Zhong, Z. (2022). Diffusion of moisture and oxygen in bitumens using electrochemical impedance spectroscopy. *Fuel*, *315*, 123212.

Chen, X., Xiao, H., Cao, C., Yan, C., Ren, D., & Ai, C. (2022). Study on moisture diffusion behavior in asphalt binder based on static and dynamic pore water conditions. *Journal of Materials in Civil Engineering*, *34*(8), 04022183.

Cheng, Kong, F., & Zhang, X. (2021). Application of the Langmuir-type diffusion model to study moisture diffusion into asphalt films. *Construction and Building Materials*, *268*, 121192.

Cheng, Little, D. N., Lytton, R. L., & Holste, J. C. (2003). Moisture damage evaluation of asphalt mixtures by considering both moisture diffusion and repeated-load conditions. *Transportation Research Record*, *1832*(1), 42–49.

Du, Z., Zhu, X., & Zhang, Y. (2021). Diffusive dynamics and structural organization of moisture in asphaltic materials based on molecular dynamics simulation. *Journal of Materials in Civil Engineering*, *33*(1), 04020403.

Greenfield, M. L. (2004). Simulation of small molecule diffusion using continuous space disordered networks. *Molecular Physics*, *102*, 421–430.

Greenfield, M. L. (2011). Molecular modelling and simulation of asphaltenes and bituminous materials. *International Journal of Pavement Engineering*, *12*, 325–341.

Hansen, J. S., Lemarchand, C. A., Nielsen, E., Dyre, J. C., & Schrøder, T. (2013). Four-component united-atom model of bitumen. *The Journal of Chemical Physics*, *138*(9), 094508.

Herrington, P. R., Wu, J. P., van den Kerkhof, L. C., & Bagshaw, S. A. (2021). Water diffusion in bitumen films. *Construction and Building Materials*, *294*, 123530.

Jamali, S. H., Bardow, A., Vlugt, T. J., & Moultos, O. A. (2020). Generalized form for finite-size corrections in mutual diffusion coefficients of multicomponent mixtures obtained from equilibrium molecular dynamics simulation. *Journal of Chemical Theory and Computation*, *16*(6), 3799–3806.

Jamali, S. H., Hartkamp, R., Bardas, C., Söhl, J., Vlugt, T. J. H., & Moultos, O. A. (2018). Shear viscosity computed from the finite-size effects of self-diffusivity in equilibrium molecular dynamics. *Journal of Chemical Theory and Computation*, *14*(11), 5959–5968.

Jamali, S. H., Wolff, L., Becker, T. M., Bardow, A., Vlugt, T. J. H., & Moultos, O. A. (2018). Finite-size effects of binary mutual diffusion coefficients from molecular dynamics. *Journal of Chemical Theory and Computation*, *14*(5), 2667–2677.

Jamali, S. H., Wolff, L., Becker, T. M., De Groen, M., Ramdin, M., Hartkamp, R., Bardow, A., Vlugt, T. J. H., & Moultos, O. A. (2019). OCTP: A tool for on-the-fly calculation of transport properties of fluids with the order-n algorithm in LAMMPS. *Journal of Chemical Information and Modeling*, *59*(4), 1290–1294.

Jennings, P. W., Pribanic, J. A., Desando, M. A., Raub, M. F., Stewart, F., Hoberg, J., Moats, R., Smith, J. A., Mendes, T. M., McGrane, M., Fanconi, B., VanderHart, D. L., & Manders, W. F. (1993). *Binder characterization and evaluation by nuclear magnetic resonance spectroscopy* (tech. rep. SHRP-A-335). Strategic Highway Research Program, National Research Council. Washington, D.C.

Jones, D. R., et al. (1993). *SHRP materials reference library: Asphalt cements: A concise data compilation. shrp-a-645* (Vol. 1). Strategic Highway Research Program, National Research Council Washington, DC.

Jorgensen, W. L., Maxwell, D. S., & Tirado-Rives, J. (1996). Development and testing of the OPLS all-atom force field on conformational energetics and properties of organic liquids. *Journal of the American Chemical Society*, *118*(45), 11225–11236.

Kaminski, G. A., Friesner, R. A., Tirado-Rives, J., & Jorgensen, W. L. (2001). Evaluation and reparametrization of the OPLS-AA force field for proteins via comparison with accurate quantum chemical calculations on peptides. *The Journal of Physical Chemistry B*, *105*(28), 6474–6487.

Kennedy, T. W., Huber, G. A., Harrigan, E. T., Cominsky, R. J., Hughes, C. S., Von Quintus, H., & Moulthrop, J. S. (1994). *Superior performing asphalt pavements (Superpave): The product of the SHRP asphalt research program* (tech. rep. SHRP-A-410) [Available on-line from http://www.trb.org/publications/shrp/SHRP-A-410.pdf]. Strategic Highway Research Program.

Khabaz, F., & Khare, R. (2015). Glass transition and molecular mobility in styrene–butadiene rubber modified asphalt. *The Journal of Physical Chemistry B*, *119*(44), 14261–14269.

Khabaz, F., & Khare, R. (2018). Molecular simulations of asphalt rheology: Application of time–temperature superposition principle. *Journal of Rheology*, *62*(4), 941–954.

Lemarchand, C. A., Bailey, N. P., Todd, B. D., Daivis, P. J., & Hansen, J. S. (2015). Non-Newtonian behavior and molecular structure of Cooee bitumen under shear flow: A non-equilibrium molecular dynamics study. *The Journal of Chemical Physics*, *142*(24), 244501.

Lemarchand, C. A., Greenfield, M. L., & Hansen, J. S. (2016). Dynamics and structure of bitumen–water mixtures. *The Journal of Physical Chemistry B*, *120*(24), 5470–5480.

Li, D. D., & Greenfield, M. L. (2014a). Viscosity, relaxation time, and dynamics within a model asphalt of larger molecules. *The Journal of Chemical Physics*, *140*(3), 034507.

Li, D. D., & Greenfield, M. L. (2011). High internal energies of proposed asphaltene structures. *Energy Fuels*, *25*, 3698–3705.

Li, D. D., & Greenfield, M. L. (2014b). Chemical compositions of improved model asphalt systems for molecular simulations. *Fuel*, *115*, 347–356.

Liu, Z., Cao, L., Zhou, T., & Dong, Z. (2020). Multiscale investigation of moisture-induced structural evolution in asphalt–aggregate interfaces and analysis of the relevant chemical relationship using atomic force microscopy and molecular dynamics. *Energy & Fuels*, *34*(4), 4006–4016.

Luo, L., Chu, L., & Fwa, T. (2021). Molecular dynamics analysis of oxidative aging effects on thermodynamic and interfacial bonding properties of asphalt mixtures. *Construction and Building Materials*, *269*, 121299.

Ma, L., Varveri, A., Jing, R., Kasbergen, C., & Erkens, S. (2022). Thermodynamics and kinetics of moisture transport in bitumen. *Materials & Design*, 111028.

Mark, P., & Nilsson, L. (2001). Structure and dynamics of the TIP3P, SPC, and SPC/E water models at 298 K. *The Journal of Physical Chemistry A*, *105*(43), 9954–9960.

Martin, M. G. (2013). MCCCS Towhee: a tool for Monte Carlo molecular simulation. *Molecular Simulation*, *39*, 1212–1222.

Martínez, L., Andrade, R., Birgin, E. G., & Martínez, J. M. (2009). Packmol: A package for building initial configurations for molecular dynamics simulations. *Journal of Computational Chemistry*, *30*(13), 2157–2164.

Moultos, O. A., Zhang, Y., Tsimpanogiannis, I. N., Economou, I. G., & Maginn, E. J. (2016). System-size corrections for self-diffusion coefficients calculated from molecular dynamics simulations: The case of CO_2, n-alkanes, and poly(ethylene glycol) dimethyl ethers. *The Journal of Chemical Physics*, *145*(7), 074109.

Nguyen, T., Byrd, E. W., Bentz, D., & Martin, J. (2005). In situ spectroscopic study of water at the asphalt/siliceous substrate interface and its implication in stripping. *The Journal of Adhesion*, *81*(1), 1–28.

Nguyen, T., Byrd, W. E., Bentz, D., & Seiler Jr., J. (1992). *Development of a technique for in situ measurement of water at the asphalt/model siliceous aggregate interface* (tech. rep. SHRP-ID/URF-92-611). Strategic Highway Research Program.

Oba, K., & Björk, F. (1993). Dynamic mechanical properties of single-ply roof coverings for low-slope roofs and the influence of water. *Polymer Testing*, *12*(1), 35–56.

Plimpton, S. (1995). Fast parallel algorithms for short-range molecular dynamics. *Journal of Computational Physics*, *117*(1), 1–19.

Read, J., & Whiteoak, D. (2003). *Shell bitumen handbook*. Thomas Telford.

Ren, S., Liu, X., Lin, P., Gao, Y., & Erkens, S. (2022a). Molecular dynamics simulation on bulk bitumen systems and its potential connections to macroscale performance: Review and discussion. *Fuel*, *328*, 125382.

Ren, S., Liu, X., Lin, P., Gao, Y., & Erkens, S. (2022b). Review on the diffusive and interfacial performance of bituminous materials: From a perspective of molecular dynamics simulation. *Journal of Molecular Liquids*, *366*, 120363.

Robertson, R. E., Branthaver, J. F., Harnsberger, P. M., Peterson, J., Dorrence, S. M., McKay, J. F., Turner, F., Pauli, T., Huang, S.-C., Huh, J.-D., et al. (2001). *Fundamental properties of asphalts and modified asphalts, volume 1; interpretive report. No. FHWA-RD-99-212* (tech. rep.). United States. Federal Highway Administration.

Ryckaert, J.-P., Ciccotti, G., & Berendsen, H. J. (1977). Numerical integration of the cartesian equations of motion of a system with constraints: Molecular dynamics of n-alkanes. *Journal of Computational Physics*, *23*(3), 327–341.

Sevick, E., Monson, P., & Ottino, J. (1988). Monte Carlo calculations of cluster statistics in continuum models of composite morphology. *The Journal of Chemical Physics*, *88*(2), 1198–1206.

Starr, F. W., Nielsen, J. K., & Stanley, H. E. (2000). Hydrogen-bond dynamics for the extended simple point-charge model of water. *Physical Review E*, *62*(1), 579.

Thompson, A. P., Aktulga, H. M., Berger, R., Bolintineanu, D. S., Brown, W. M., Crozier, P. S., in't Veld, P. J., Kohlmeyer, A., Moore, S. G., Nguyen, T. D., et al. (2022). LAMMPS-a flexible simulation tool for particle-based materials modeling at the atomic, meso, and continuum scales. *Computer Physics Communications*, *271*, 108171.

Tsimpanogiannis, I. N., Jamali, S. H., Economou, I. G., Vlugt, T. J., & Moultos, O. A. (2020). On the validity of the Stokes–Einstein relation for various water force fields. *Molecular Physics*, *118*(9-10), e1702729.

Tsimpanogiannis, I. N., Moultos, O. A., Franco, L. F., Spera, M. B. d. M., Erdős, M., & Economou, I. G. (2019). Self-diffusion coefficient of bulk and confined water: A critical review of classical molecular simulation studies. *Molecular Simulation*, *45*(4-5), 425–453.

Turner, T. P., & Branthaver, J. F. (1997). DSC studies of asphalts and asphalt components. In A. M. Usmani (Ed.), *Asphalt science and technology* (pp. 59–101). Marcel Dekker.

Vasconcelos, K. L., Bhasin, A., Little, D. N., & Lytton, R. L. (2011). Experimental measurement of water diffusion through fine aggregate mixtures. *Journal of Materials in Civil Engineering*, *23*(4), 445–452.

Vasconcelos, K. L., Bhasin, A., & Little, D. N. (2010). Measurement of water diffusion in asphalt binders using Fourier transform infrared–attenuated total reflectance. *Transportation Research Record*, *2179*(1), 29–38.

Wang, J., Wolf, R. M., Caldwell, J. W., Kollman, P. A., & Case, D. A. (2004). Development and testing of a general Amber force field. *J. Comput. Chem.*, *25*, 1157–1174.

Wu, Y., Tepper, H. L., & Voth, G. A. (2006). Flexible simple point-charge water model with improved liquid-state properties. *The Journal of Chemical Physics*, *124*(2), 024503.

Xu, G., & Wang, H. (2016). Study of cohesion and adhesion properties of asphalt concrete with molecular dynamics simulation. *Computational Materials Science*, *112*, 161–169.

Yeh, I.-C., & Hummer, G. (2004). System-size dependence of diffusion coefficients and viscosities from molecular dynamics simulations with periodic boundary conditions. *The Journal of Physical Chemistry B*, *108*(40), 15873–15879.

Zhang, L., & Greenfield, M. L. (2007). Analyzing properties of model asphalts using molecular simulation. *Energy & Fuels*, *21*(3), 1712–1716.

Zhang, L., & Greenfield, M. L. (2008). Effects of polymer modification on properties and microstructure of model asphalt systems. *Energy & Fuels*, *22*(5), 3363–3375.

4

Ageing impact on bitumen chemo-mechanical properties and correlations

This chapter explores how ageing affects the physicochemical and rheological properties of bituminous binders. The objective is to investigate the relationships between the properties obtained from these tests, to uncover the mechanisms responsible for the deterioration of binders due to ageing. This study also lays the groundwork for subsequent exploration into the combined effects of ageing and moisture. The correlation analysis, in practical terms, aims to substantiate the idea that various tests share significant commonalities and that one test can adequately represent another.

Section 4.1 provides a review of various tests used to evaluate the impact of ageing on bitumen, highlighting the relationships between different bitumen properties. Section 4.2 describes in detail the binder types and the applied ageing protocols. The chemical, physical, and rheological test techniques are introduced in Section 4.3, as well as the methods and models used for data analysis. Sections 4.4 and 4.5 investigate the effects of ageing on chemical, structural, and thermal properties, along with the changes in rheological properties like stiffness, fatigue, relaxation, and viscosity as bitumen ages. Section 4.6 discusses the relationships between physicochemical and rheological properties, explaining how different combinations of bitumen properties correlate with each other. Furthermore, key chemical and structural properties that influence various rheological properties are identified among all the properties considered. Additionally, the correlations between sets of variables obtained from different tests are explored, assessing the extent of shared information among these tests. Finally, Section 4.7 summarizes the significant findings obtained from this chapter.

4.1 Introduction

Bitumen ageing plays a crucial role in the degradation of pavement performance. It involves processes such as oxidative ageing, evaporation of light components, and physical (steric) hardening (Tauste et al., 2018), with oxidative ageing being the predominant process.

As a mixture of hydrocarbons with polar functional groups, bitumen is susceptible to chemical reactions with ambient oxygen and its reactive derivatives (Lau et al., 1992), leading to oxidative ageing. The chemical process of bitumen oxidation depends on the reactive chemical components and typically involves dehydrogenation, production of new functional groups, and an increase in aromaticity (aromatic condensation) (Nivitha et al., 2016; Polo-Mendoza et al., 2022; Tauste et al., 2018). Ageing causes a significant reduction in the aromatic fraction and a growth in the content of resins and asphaltenes, resulting in increased polarity, acidity, viscosity, and stiffness of bitumen (Mirwald et al., 2020b). These changes ultimately lead to bitumen hardening and brittleness (Eberhardsteiner et al., 2015b), which are manifested in the field by the increased propensity of cracking and pavement failures (Lesueur, 2009; López-Montero & Miró, 2016; Tauste et al., 2018).

Understanding the intricate bitumen ageing process and characterizing the mechanical properties affected by ageing are crucial for evaluating asphalt pavement performance. In this context, a variety of tests have been employed to evaluate bitumen properties during ageing, aiming to gain a thorough understanding of the fundamental mechanisms of the ageing process. Important chemical and physical methodologies used to evaluate bitumen properties include saturate, aromatic, resin, asphaltene (SARA) fractions, Fourier transform infrared spectroscopy (FTIR) (Lamontagne et al., 2001), gel permeation chromatography (GPC), and differential scanning calorimetry (DSC) (Frolov et al., 2020; Redelius & Soenen, 2015). To characterize the mechanical properties of bitumen, instruments such as viscometer, dynamic shear rheometer (DSR), dynamic mechanical analysis (DMA), and bending beam rheometer (BBR) have been applied (Eberhardsteiner et al., 2015b). Based on these tests, various physicochemical and rheological parameters and indices have been proposed over the years to characterize the effects of oxidative ageing on bitumen.

Fourier transform infrared (FTIR) spectroscopy is a rapid and powerful technique in characterizing the chemical composition of bitumen (Mirwald et al., 2020a; Pipintakos et al., 2021). To evaluate the chemical changes in bitumen samples during the ageing process, characteristic peaks and regions of FTIR spectra such as sulfoxides, carbonyls, aliphaticity, and aromaticity are usually determined (Hofko et al., 2017). Among them, the sulfoxide (1030 cm^{-1}) and carbonyl (1700 cm^{-1}) peaks have been successfully used to describe the degree of ageing and are linked to the physical and rheological properties of bitumen (Herrington, 2012; Pipintakos et al., 2022). Other functional groups with lower intensities in FTIR spectra are attracting increasing attention. For example, a change from 2-quinolones (1655 cm^{-1}) and carboxylic acids (1730 cm^{-1}) towards ketones (1700 cm^{-1}) is reported (Mirwald et al., 2020a), which describes the chemical process involved in the formation of ketones.

SARA fractionation has been universally used to examine the chemical composition and microstructure of bitumen. Corbett (1969) separated the SARA fractions based on the

elution-adsorption liquid chromatography on active alumina with solvents of increasing polarity and aromaticity. Later, thin-layer chromatography with flame ionization detection (TLC-FID) emerged as a rapid and economical alternative to measure SARA fractions. Among SARA fractions, asphaltene is a heterogeneous macromolecular fraction, soluble in toluene but insoluble in alkanes. A small fraction of asphaltenes in bitumen can significantly increase the stiffness and mechanical properties (Eberhardsteiner et al., 2015a). Oxidative ageing generally results in lower aromatics content and higher asphaltenes content, therefore it appears that aromatics generate resins and subsequently resins become asphaltenes (Mirwald et al., 2020a; Siddiqui & Ali, 1999). The saturates normally remain stable with the ageing process except in the case of volatile evaporation. The modern colloidal structure of bitumen depicts the asphaltenes as micelles distributed in the aromatics fraction with resins as a surfactant to prevent the precipitation of asphaltenes (Creek, 2005; Lesueur, 2009). The saturates, aromatics, and resins in SARA fractions are collectively termed maltenes. Microscopic and rheological testing conducted separately on asphaltenes and maltenes, as well as on their blended matrix, indicates that oxidative ageing has a relatively minor effect on the creep recovery of individual maltenes and asphaltenes. Instead, it significantly affects the microstructure of bitumen (particularly interaction between asphaltenes and maltenes), which is a dominant factor in the change of bitumen properties due to ageing (Hofko et al., 2015).

Another test method to characterize molecular structures of bitumen affected by ageing is GPC. This method captures the overall molecular weight distribution of bitumen, indicating the complex composition of hydrocarbons with continuous sizes and structures. GPC can be used in cooperation with SARA fractionation to provide a more detailed picture of molecular structure of bitumen. It is widely accepted that during oxidative ageing process, reactive molecules react with oxygen, leading to the production of larger molecules. Therefore, the fraction of molecules within a specific size range can be linked to the properties affected by ageing, especially the rheological properties including penetration, viscosity, and complex modulus (Redelius & Soenen, 2015; Themeli et al., 2015).

DSC has been commonly used to study the thermal sensitivity of bitumen, revealing its structural phase transition. There are two main protocols for conducting DSC tests: conventional DSC, which employs linear temperature loading, and temperature-modulated DSC, which can differentiate changes in heat capacity (reversing heat flow) from kinetic processes (non-reversing heat flow) like crystallization or chemical reactions. DSC can be used to determine the glass transition temperature of bitumen (Apeagyei et al., 2014; Apostolidis et al., 2021; dos Santos et al., 2015) and to evaluate its crystalline and amorphous structures (Frolov et al., 2020; Soenen et al., 2014). Generally, an increase in glass transition temperature with ageing level is reported (Wang et al., 2021) owing to the evaporation of saturates and increased polarity of bitumen. The analysis of wax crystallization based on DSC is complex. The commonly observed double-peak endothermic patterns are attributed to the polydispersity and polymorphism of wax crystallization (Ding & Hesp, 2021) while others disagree and explain it as a hybrid result of melting, recrystallization and dual crystal populations (Frolov et al., 2020).

The rheological properties of bitumen are key indicators of pavement performance under various conditions. Properties such as temperature sensitivity, frequency depen-

dence, fatigue resistance, relaxation, and viscosity, especially their evolution with ageing, are critical for evaluating the performance of bituminous binders. Rheological testing using DSR provides several useful parameters for bitumen evaluation, including crossover frequency (frequency at phase angle of 45°), crossover modulus (complex modulus at phase angle of 45°), the G-R parameter (indicative of fatigue cracking resistance), fatigue life, and relaxation. Additionally, the creep stiffness, the relaxation parameter, and the critical temperature, which are essential for understanding binder performance at low temperatures, can be obtained from the BBR test (Wang et al., 2019). Ageing generally leads to a decrease in crossover frequency, crossover modulus, fatigue life and an increase in G-R value and relaxation time. These changes suggest the degradation of bitumen over time due to ageing processes (Pipintakos et al., 2022; Weigel & Stephan, 2017). Oxidative reactions increase the content of polar groups and the condensed aromatics, which agglomerate and evolve into the asphaltenes fraction, thus increasing the viscosity of bitumen (Herrington, 2012; Petersen, 2009).

Individual parameters each characterize specific bitumen properties and their changes with ageing. Relying only on one parameter to accurately evaluate the ageing process and to quantitatively compare various bitumen types can be challenging due to the complex and distinct compositions of various binders. Arising from the heterogeneity of crude oil worldwide, bitumen derived from different crude oil sources shows varying physical, chemical and mechanical properties (Petersen, 2000). Even bitumen with identical specifications, such as penetration grade, can reveal a wide range of properties, including distinct SARA fractions and diverse ageing kinetics (Juristyarini et al., 2011). Furthermore, bitumen can be blended with other materials to improve its properties, including polymer modifiers, additives, and rejuvenators. The complex composition of the hybrid materials makes it more challenging to understand the ageing process and evaluate the ageing-caused degradation of bitumen. To address this issue, different parameters can be holistically utilized to estimate the bitumen properties, thereby enhancing the reliability of the results. Such an approach requires an accurate interpretation of the essential correlations among various parameters and indices.

In this context, comprehensive analyses combining chemical and rheological properties have been performed to deepen the understanding of bitumen behavior (Morian et al., 2015; Petersen, 2009; Pipintakos et al., 2022; Redelius & Soenen, 2015; Yut & Zofka, 2014). Emphasis is placed on the chemo-mechanical relationship of bitumen, aiming to predict its rheological properties and long-term degradation based on its chemical characteristics. The mechanical properties of bitumen have been demonstrated to be dependent on the distribution of molecules with a continuum in molecular weight, aromaticity, and polarity instead of a single value (Redelius & Soenen, 2015). Nonetheless, certain characteristics of bitumen are found to have a stronger correlation with specific physicomechanical properties. The viscosity of bitumen can be roughly estimated based on a combination of molecular weight and aromaticity (Redelius & Soenen, 2015). The complex shear modulus or phase angle may be related to the extent of polarity. In particular, the polar interaction between molecules is more responsible for the elastic behavior of bitumen (Redelius, 2004). The molecular weight distribution in bitumen also correlates well with its relaxation spectra, as indicated by the rheological index (Gundla & Underwood, 2020). Effective prediction of rheological parameters of bitumen is achieved based

on the linear regression of combined SARA fractions and their molecular weights (Weigel & Stephan, 2017). Within these SARA fractions, a higher content of saturates and aromatics indicates lower stiffness and more viscous deformation while an increased content of resins and asphaltenes leads to a stiffer and more elastic bitumen. Moreover, the microstructure of bitumen, influenced by the complex chemical components and its molecular interactions, is well correlated with the thermal and mechanical properties of bitumen (Yu et al., 2019). In general, for basic rheological properties, such as viscosity, few chemical parameters are sufficient for an acceptable prediction, whereas more fundamental chemical or structural parameters are required to estimate advanced rheological values, such as Glover–Rowe parameter (Pipintakos et al., 2022). It is important to note that the correlations among various bitumen properties depend on the binder types, ageing processes, and measuring conditions. The global application of these correlations should be approached with caution and preceded by rigorous validation tests.

Many physicochemical and mechanical tests have been used to evaluate bitumen properties, which generates a plethora of parameters and indices. This abundance of parameters provides a more enriched understanding of the ageing process and the chemo-mechanical relationships. However, when selecting bitumen during the design stage, or assessing degradation and formulating appropriate maintenance strategies, it can be laborious to measure all these properties and too complicated to identify the most crucial and reliable indices. In this chapter, we aim to test the hypothesis that various chemical and mechanical tests reflect the intrinsic characteristics of bituminous binders from multiple perspectives. We will demonstrate that, with comprehensive and precise analysis, these tests share similar variances, as shown in Fig. 4.1. As a result, a limited number of tests can accurately describe bitumen properties and their variation with ageing.

To this end, multiple physicochemical and mechanical properties are measured and analyzed using different models and methods to derive informative parameters and indices. The relationships between these parameters are then analyzed through the Pearson correlation, to quantify their similarities and differences. Furthermore, relationships between different tests, each characterized by a combination of all calculated parameters, are evaluated using the Canonical Correlation Analysis (CCA). This method identifies and determines the common variances between a pair of variable sets from two tests. Therefore, CCA can be used to determine whether various chemical and mechanical tests share substantial common information and whether the results of one test can explain those of another. The chemo-mechanical relationship is expected to facilitate the understanding of ageing mechanisms, reveal the evolution of stiffness, fatigue, viscosity, and relaxation with ageing, and guide the selection of appropriate tests and analysis approaches for evaluating bitumen quality.

The contents of this chapter are organized as follows. Section 4.2 provides the details about materials used and sample preparation procedures, including binders from various sources, with different penetration grades, and those modified with polymers. The chemophysical and rheological tests employed for evaluating bitumen properties are described in Section 4.3. Sections 4.4 and 4.5 delve into the impact of ageing on binders, examining chemical composition, molecular structure, thermal behavior, and rheological properties including stiffness, fatigue, viscosity, and relaxation. The relationships between these properties are also discussed. The main findings are summarized in Section

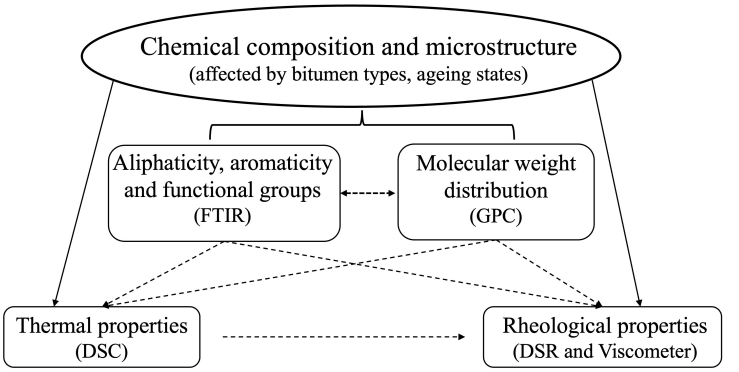

Figure 4.1 Schematics of the relationship between chemophysical and rheological properties.

4.7.

4.2 Materials and sample preparation

4.2.1 Materials

To study the chemical and rheological properties of bitumen derived from diverse crude oil origins, possessing different penetration grades, and subject to the influence of polymer modifiers (specifically, Styrene–butadiene–styrene (SBS)), a total of 39 binder samples were prepared. These samples include eight distinct binder types, each examined at four ageing stages, as described below:

- Bitumen obtained from source Q, with penetration grades 40/60, 70/100, and SBS modified bitumen (commercial product), denoted as Q460, Q710, and QPMB, respectively;

- Bitumen obtained from source T, with penetration grades 70/100, 100/150, and 160/220, denoted as T710, T1015, and T1622, respectively;

- Bitumen obtained from source V, with penetration grades 70/100 and SBS modified bitumen (i.e., 70/100 base bitumen mixed with 4 wt% SBS, which is a linear block copolymer with 28.5% styrene), denoted as V710 and VPMB, respectively.

4.2.2 Ageing protocol

For each bitumen type, a can of fresh binder was heated up to 140 °C for 5 min and poured into four containers with a diameter of 140 mm, each containing 50.0 ± 0.5 g of bitumen. These containers were then placed in an oven at 140 °C for 5 min to obtain a thin bitumen film of 3.2 mm. Four containers were aged at four states comprising one short-term ageing protocol and one long-term ageing protocol with three different ageing times. Short-term ageing was simulated by the thin film oven test (TFOT) at 163 °C for five hours, which is referred to as Oven. Long-term aged samples were prepared using a combination of the TFOT protocol followed by ageing in the Pressure Ageing Vessel (PAV) at 2.1 MPa and 100 °C for 20 h (1P), 40 h (2P), and 80 h (4P). For QPMB, the oven ageing was not conducted.

4.3 Experimental methods and analysis techniques

To evaluate the ageing performance of all binder samples, a series of tests were conducted, including FTIR, DSC, GPC, DSR, and viscosity tests. The Pearson correlation and canonical correlation analysis (CCA) methods were utilized to analyze the relationships between different bitumen properties, as summarized in Fig. 4.2.

Samples	Properties	Tests	Indices	Correlations
Types: Q460, Q710, QPMB, V710, VPMB, T710, T1015, T1622 **Ageing**: Fresh, short-term, 1PAV, 2PAV, and 4PAV	Chemical properties	FTIR	Peak indices at 3600, 3340, 3014, 2955, 2910, 2870, 2850, 1700, 1600, 1460, 1376, 1305, 1160, 1030, 864, 814, 743, 724, 965, 910, 695 cm^{-1}	Chemo-rheological relationship **Method**: Pearson, CCA
		DSC	T_g, ΔC_p, H_{decry1} , H_{decry2}, H_{cry}, T_{cry}	
		GPC		
	Rheological properties	Frequency sweep (DSR)	f_c, G_g, C_1 , C_2, G_c^*, $G-R$, R_{rhe}	
		LAS (DSR)	τ_{max}, G^*_{LVE}, C_{D1}, C_{D2}, D_f, k_D, A_D, B_D, N_{f25}, N_{f50}	
		Relaxation (DSR)	G_0, G_1, G_2, G_3, G_4, γ_1, γ_2, γ_3, γ_4	
		Viscosity (DSR+Viscometer)	m_η, k_η, ZSV, A_{arr}, B_{arr}, A_{vft}, B_{vft}, C_{vft}	

Figure 4.2 Overview of methodology

4.3.1 Fourier-transform infrared spectroscopy

To measure the chemical composition and structure of bitumen, FTIR spectroscopy was carried out using the Attenuated Total Reflection (ATR) mode. The FTIR tests were performed over a wavenumber range of 4000 to 600 cm^{-1}, with a resolution of 1 cm^{-1}. Each measurement involved 32 scans, and three independent measurements were performed for each sample.

The chemical characteristics of the FTIR spectra are shown in Fig. 4.3. The mid-infrared FTIR spectral region of 4000 – 600 cm^{-1} is informative of the aliphaticity, aromaticity, heteroatom-based functionality, and oxygenation of bitumen components. Most of the absorption peaks are assigned to different types of C-H vibrations. The band between 3080 and 3020 cm^{-1} is assigned to the C-H stretching of cis double bonds and aromatics. The bands ranging from 2965 to 2946 cm^{-1} and from 2876 to 2864 cm^{-1} are representative of the asymmetric and symmetric C-H stretching vibrations of CH_3 groups, respectively. For CH_2 groups, the asymmetric and symmetric vibrations are revealed around 2946 – 2880 cm^{-1} and 2864 – 2825 cm^{-1}, respectively. The aliphatic -CH_2 and -CH_3 bending vibrations are shown at band areas of 1485 – 1400 cm^{-1} and 1400 – 1357 cm^{-1}. The band ranges of 900 – 838 cm^{-1}, 838 – 783 cm^{-1}, and 783 – 732 cm^{-1} are attributed to various aromatic C-H in-plane and out-of-plane bending vibrations. The peak at 722 cm^{-1} indicates the presence of long alkyl chain groups in saturates, i.e. $(CH2)_n$, where n is larger than 4. Moreover, the multiple C=C stretching vibrations are at 1600 cm^{-1} (Castro & Vazquez, 2009).

The peaks indicative of heteroatom-based functional groups are observable in FTIR spectra. The absorption bands at 3650 – 3500 cm^{-1} denote the free -OH stretching. The bands between 3500 and 3200 cm^{-1} represent hydrogen bonded -OH and -NH stretching

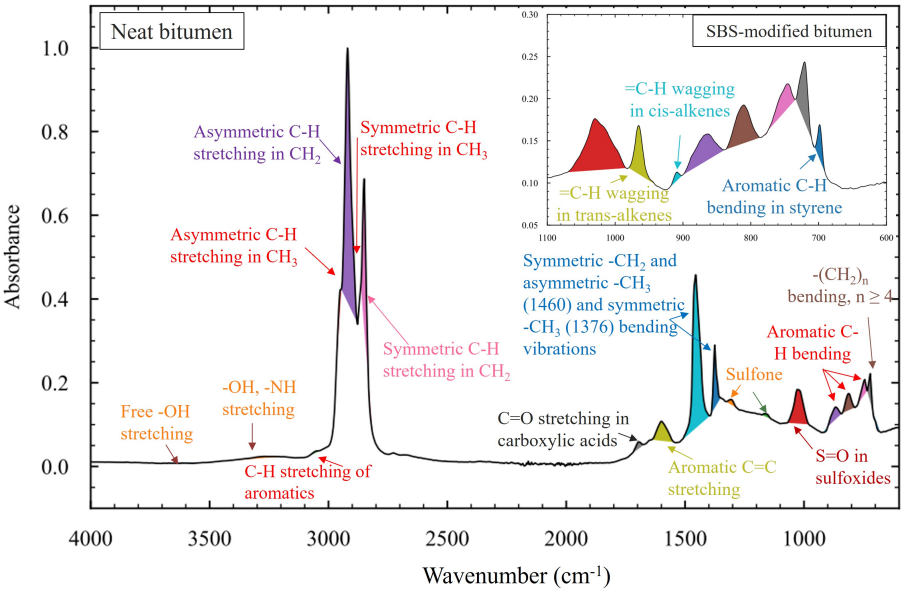

Figure 4.3 FTIR spectra of neat bitumen (4000 – 600 cm^{-1}) and SBS-modified bitumen (1100 – 600 cm^{-1}).

in phenolic, alcoholic, carboxylic acids, and amines, with broad overlapping occurring in the range 3500 – 3100 cm^{-1}. The region between 1750 and 1650 cm^{-1} is attributed to the stretching vibrations of carbonyl functional groups (including esters, ketones, aldehydes, carboxylic acids, and amides) (Asemani & Rabbani, 2020; Smith, 2018). Peaks at 1310 cm^{-1}, 1260 cm^{-1}, 1160 cm^{-1}, 1080 cm^{-1}, 1030 cm^{-1}, and 810 cm^{-1} are associated with sulfur-based functional groups, such as sulfoxides, sulfones, and sulfate ester (Mirwald et al., 2020a). Both the carbonyl- and sulfur-based functional groups are crucial for the chemical changes of binders due to ageing (Buenrostro-Gonzalez et al., 2002; Petersen, 2009). Nitrogen-based functional groups are found at ca. 3239 cm^{-1} (N-H stretching in amides), 1575 cm^{-1} (N-H bending in amides), and 1310 cm^{-1} (C-N bending in pyridine, pyrrole, and amides) (Asemani & Rabbani, 2020; Gabrienko et al., 2015). The peaks and regions denoting these functional groups can overlap with other chemicals and have low intensity in FTIR spectra (Asemani & Rabbani, 2020; Zojaji et al., 2021). Therefore, they are less discussed in the literature than the carbon- and sulfur-related ones.

The SBS modifier consists of a polybutadiene (PB) segment with polystyrene (PS) blocks at each end. The representative FTIR peaks of the SBS in binders include the out-of-plane wagging of =C-H in cis- and trans-alkenes at 910 cm^{-1} and 966 cm^{-1}, respectively, the aromatic C-H bending in styrene at 699 cm^{-1}, the aliphatic $–CH_2$ at 1450 cm^{-1}, and the aromatic rings C=C at ca. 1490 cm^{-1}. The last two peaks overlap with those of neat bitumen (Kumar et al., 2020). During the ageing process, polystyrene remains stable while polybutadiene shows a reduction in peak intensities, indicating polymer degradation due to chain scission.

4.3.2 Gel permeation chromatography

Gel permeation chromatography (GPC) tests were conducted to evaluate the molecular weight distribution of various binders. For each sample, a designated amount of bitumen was dissolved in tetrahydrofuran (THF) to achieve a concentration of 20 mg/mL. The obtained solution was then filtered using Teflon filters with a pore size of 0.45 μm, vigorously agitated, and left to stand in the dark for 24 hours to ensure homogeneity. Subsequently, 50 μL of the prepared solution was injected into organic gel columns for separation. During elution, larger molecules elute first, followed by smaller ones. Calibration was performed using standard polystyrene with known molecular weights. Two replicates were obtained for each binder.

The obtained weight distribution curves were used to compute the peak molecular weight (M_p), the number average molecular weight (M_n), the weight average molecular weight (M_w), Z average (M_z), Z+1 average (M_{z+1}) and polydispersity index (PDI), M_w/M_n.

$$M_n = \frac{\sum_{i=1}^{n} N_i M_i}{\sum_{i=1}^{n} N_i} \tag{4.1}$$

$$M_w = \frac{\sum_{i=1}^{n} N_i M_i^2}{\sum_{i=1}^{n} N_i M_i} \tag{4.2}$$

$$M_z = \frac{\sum_{i=1}^{n} N_i M_i^3}{\sum_{i=1}^{n} N_i M_i^2} \tag{4.3}$$

$$M_{z+1} = \frac{\sum_{i=1}^{n} N_i M_i^4}{\sum_{i=1}^{n} N_i M_i^3} \tag{4.4}$$

where M_i is the molecular weight of a molecule and N_i denotes the number of molecules with the molecular weight of M_i.

Furthermore, fractional analysis was used to interpret the GPC test results for binders. The chromatogram in the range of 12 – 20 min was divided into 13 slices. These slices were then categorized into three sections, as described in Fig. 4.4, including large molecular size (LMS) comprising slices 1-5, medium molecular size (MMS) covering slices 6-9, and small molecular size (SMS) including slices 10-13 (Jennings et al., 1980; Kim et al., 2006), . The area percentages of these sections were calculated and denoted as S_{LMS}, S_{MMS}, and S_{SMS}. For SBS-modified binders, the initial peak at elution times between 9 and 12 min was related to SBS and was not included in the 13 slices for LMS, MMS, and SMS. Instead, it was separately calculated and referred to as S_{SBS}.

4.3.3 Thermal analysis using differential scanning calorimetry

Differential scanning calorimetry (DSC) was used to measure the thermal behavior of bitumen using conventional linear temperature ramp method. The mass of DSC samples ranged from 15 to 20 mg. Bitumen samples were initially cooled from 25 °C to -50 °C and held at -50 °C for 5 min. After that, temperature was increased to 200 °C and maintained there for 5 min to remove any thermal history. The samples were then cooled back to -50 °C and held there for another 5 min. Finally, samples were reheated from -50 °C to 200 °C. Both heating rate and cooling rate were set at 10°C/min, with a nitrogen flow rate

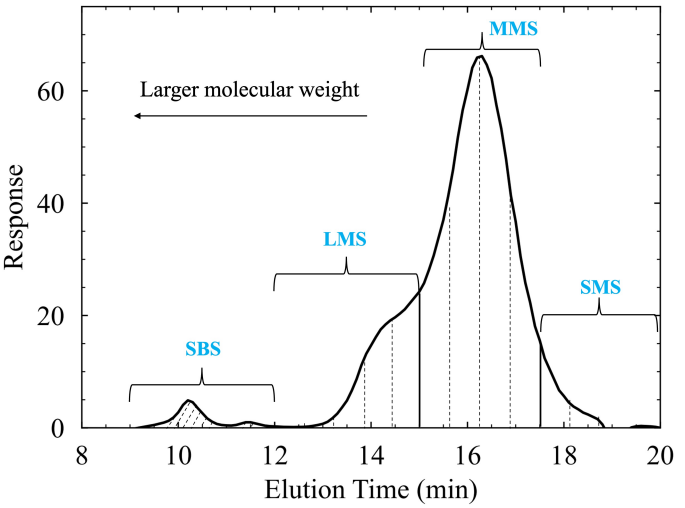

Figure 4.4 GPC chromatogram of bitumen.

of 19.8 ml/min. The heat flow data (measured in mW) during the heating and cooling procedures were recorded.

The DSC test quantifies the amount of heat absorbed or released by a sample when it is heated, cooled, or held at a constant temperature. The heat flow in DSC is expressed as

$$\frac{\mathrm{d}Q}{\mathrm{d}t} = mC_\mathrm{p}\frac{\mathrm{d}T}{\mathrm{d}t} \tag{4.5}$$

where Q denotes the amount of heat, C_p is defined as the heat capacity, m is the sample mass, and $\mathrm{d}T/\mathrm{d}t$ is the heating rate β. C_p is therefore defined as

$$C_\mathrm{p} = \frac{1}{m}\frac{1}{\beta}\frac{\mathrm{d}Q}{\mathrm{d}t} \tag{4.6}$$

The main thermal information provided by DSC includes glass transition temperature, crystalline structure, and melting temperature, as shown in Fig. 4.5. The glass transition temperature T_g characterizes the phase behavior of amorphous materials or the amorphous portion of semi-crystalline materials. Below T_g, molecular chains in bitumen are "frozen", and bitumen is in a brittle and glassy state. As temperature increases, bitumen gradually transitions to a viscous state. T_g obtained from the heating scans during DSC testing is more repeatable and easier to calculate compared to the cooling scans (Soenen et al., 2014). Therefore the last heating scan was used to calculate T_g. T_g is observed over a temperature range that includes an onset, an endpoint and a midpoint. The onset temperature marks the beginning of the glass transition and is defined as the point when heat flow starts to deviate from the baseline, which is the range showing a linear relationship between temperature and heat flow. The endpoint temperature indicates the completion of glass transition, identified as the point when heat flow starts to show a new baseline after the transition. The midpoint temperature, considered as T_g, corresponds

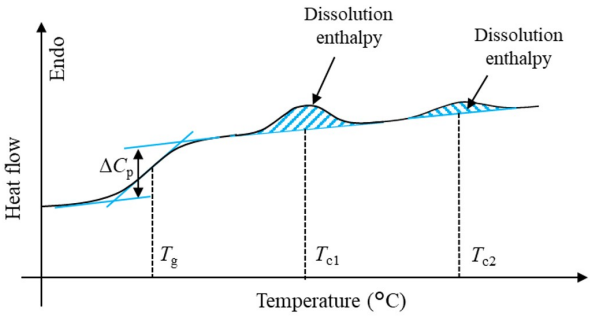

Figure 4.5 Determination of glass transition temperature, crystallization temperature, and crystallization-related enthalpy based on heat flow obtained from DSC tests.

to the middle of the heat flow difference between onset and endpoint. The difference in heat capacity (ΔC_p) between onset and endpoint represents the varying energy required to facilitate molecular motion in glassy and viscous states.

Crystallization and dissolution processes occur in the crystalline fraction of bitumen. During the heating scan, endothermic peaks at temperatures close to 0 – 80 °C can be related to the dissolution of crystalline components. The enthalpy of decrystallization, representing the heat absorbed for the dissolution of crystalline fractions, can be quantified as the integrated area between the endothermic peak and baseline, as illustrated in Fig. 4.5. For the cooling scan, an exothermic peak in the cooling curve corresponds to the crystallization of the crystalline phase. The enthalpy of crystallization can be calculated using the same method as for decrystallization.

4.3.4 Rheological tests using dynamic shear rheometer

Frequency sweep tests

To evaluate the viscoelastic response of binders at varying aging states, the strain-controlled frequency sweep tests on all bitumen samples were performed at temperatures ranging from 0 °C to 80 °C, with an interval of 10 °C. For temperatures of 0 – 30 or 0 – 40 °C (depending on the penetration grade of the sample and its ageing levels), an 8 mm plate with a 2 mm gap was used; for temperatures from 40/50-80 °C, a 25 mm plate with a 1 mm gap was selected. Prior to the frequency sweep, strain amplitude sweep tests were conducted at 0 °C and 40 °C to determine the maximum strain within linear viscoelastic (LVE) range. The selected strain amplitudes were 0.1% for temperatures of 0-30/40 °C and 0.5% for 40/50-80 °C. During the tests, the frequency ranged from 0.01 to 30 Hz at a logarithmic scale, summing up to 21 data points for each temperature.

Based on the results of frequency sweep tests, master curves of the binders were derived utilizing the Williams-Landel-Ferry (WLF) time-temperature superposition principle (TTSP) (Olard et al., 2003) and the Christensen-Anderson-Marasteanu (CAM) model (Marasteanu & Anderson, 1999). The WLF equation determines the shift factor α_T for each temperature as:

$$\log \alpha_T = \frac{-C_1(T - T_0)}{C_2 + (T - T_0)} \tag{4.7}$$

where C_1 and C_2 are material constants, T is the testing temperature, and T_0 is the reference temperature of 20 °C. The CAM model is developed based on Christensen-Anderson (CA) Model (Christensen & Anderson, 1992) to characterize the viscoelastic properties of bitumen:

$$G^*(f_r) = G_g\left(1+\frac{f_c}{f_r}^{v}\right)^{-w/v} \tag{4.8}$$

where G^* is the complex shear modulus, G_g is the glassy modulus, f_c is the crossover frequency, f_r denotes the reduced frequency, and w, v are fitting parameters. Similar to complex modulus, the phase angle δ is defined as:

$$\delta = \frac{90w}{1+(f_c/f_r)^v} \tag{4.9}$$

The storage modulus $G^{'}$ and loss modulus $G^{"}$ can be calculated as

$$G^* = G^{'} + iG^{"},\ \ G^{"} = |G^*|\sin\delta,\ \ G^{'} = |G^*|\cos\delta \tag{4.10}$$

From the master curves of binders, crossover frequency (f_c) and crossover modulus (G_c^*) at the phase angle of 45° were calculated. Furthermore, the rheological index was determined as $R_{rhe} = \log 2/v$, which indicates the transition from elastic behavior to steady flow state. The R_{rhe} can also be linked to complex modulus as $R_{rhe} = \log G_g - \log G_c^*$. The Glover-Rowe (G-R) parameter was derived using the CAM-based master curves at a reference temperature of 15 °C (Glover et al., 2005; G. Rowe et al., 2014):

$$\text{G}-\text{R} = \frac{G^*(\cos\delta)^2}{\sin\delta} \tag{4.11}$$

where G^* and δ are the values at the frequency of 0.005 rad/s. The G-R parameter has been used to evaluate the fatigue cracking of bituminous materials related to ageing (Mensching et al., 2015). An increase in the G-R value with the ageing level suggests a greater susceptibility to fatigue cracking (Zhang et al., 2019).

Fatigue tests

Ageing significantly affects the fatigue life of bituminous binders and mixtures. The fatigue life exhibits a strong power-law relationship with the applied stress or strain. The strain-controlled fatigue life (N_f) is defined as

$$N_f = A_D(\gamma_p)^{-B_D} \tag{4.12}$$

where γ_p is the applied shear strain, and A_D and B_D are fitting parameters.

To evaluate the fatigue characteristics of binders, the linear amplitude sweep (LAS) test, in combination with the simplified viscoelastic continuum damage (S-VECD) model, was applied to determine the key parameters (A_D and B_D) related to fatigue (Hintz & Bahia, 2013; Hintz et al., 2011; Underwood et al., 2012). The LAS test, utilizing an 8 mm parallel plate and a 2 mm gap at 20 °C, consisted of two steps. For the first step, a frequency sweep was performed at frequencies of 0.2, 0.4, 0.6, 0.8, 1, 2, 4, 6, 8, 10, 20, and

30 Hz, along with a constant shear strain of 0.1%. This step aimed to obtain the rheological properties within the LVE range. The second step involved an amplitude sweep of oscillatory shear strain, increasing from zero to 30% in 5 min, at a frequency of 10 Hz.

The VECD model, based on Schapery's work potential theory, characterizes damage evolution over time as

$$\frac{dD}{dt} = \left(-\frac{\partial W}{\partial D}\right)^{\alpha_D} \tag{4.13}$$

where D is the damage intensity, t is time, W is the work input characterized by the dissipated energy density W^D, and α_D is the inverse of the slope of the storage modulus versus frequency at a log-log plot obtained from the first test step. The dissipated energy density W^D is defined as

$$W^D = \pi \cdot \tau_p \cdot \gamma_p \cdot \sin\delta = \pi \cdot \gamma_p^2 \cdot |G^*| \cdot \sin\delta \tag{4.14}$$

where τ_p is the measured shear stress. The W^D can be normalized as

$$W_n^D = \pi \cdot \gamma_p^2 \cdot \frac{|G^*| \cdot \sin\delta}{|G^*|_{LVE} \cdot \sin\delta_{LVE}} \tag{4.15}$$

where $\frac{|G^*| \cdot \sin\delta}{|G^*|_{LVE} \cdot \sin\delta_{LVE}}$ is the material integrity, i.e., the pseudo stiffness C_D. By substituting W in Equation 4.13 with W_n^D, the damage intensity can be obtained as

$$D(t) = \sum_{i=1}^{N} \left(\pi \gamma_t^2 (C_{i-1} - C_i)\right)^{\frac{\alpha_D}{1+\alpha_D}} (t_i - t_{i+1})^{\frac{1}{1+\alpha_D}} \tag{4.16}$$

The material integrity C_D can then be related to the damage intensity D through the power law:

$$C_D(t) = C_{D0} - C_{D1}(D)^{C_{D2}} \tag{4.17}$$

where $C_{D0} = 1$, C_{D1} and C_{D2} are fitting parameters. Therefore, the damage intensity at failure point C_f is defined as

$$D_f = \left(\frac{C_{D0} - C_f}{C_{D1}}\right)^{\frac{1}{C_{D2}}} \tag{4.18}$$

where C_f is the material integrity at peak stress where failure occurs. Based on this, two parameters in Equation 4.12 are derived as

$$A_D = \frac{f(D_f)^{k_D}}{k_D(\pi C_{D1} C_{D2})^{\alpha_D}}, \quad B_D = 2\alpha_D \tag{4.19}$$

where f is the loading frequency, and $k_D = 1 + \alpha_D(1 - C_{D2})$.

Relaxation tests

Stress relaxation tests were performed to assess the relaxation of bituminous binders at 0 °C, using an 8 mm parallel plate and a 2 mm gap. Initially, a shear strain was applied which increased from 0 to 1% within 1 second. The strain was then kept at 1% for 100 seconds to observe the relaxation behavior of binder samples. The relaxation strength of bituminous binders can be described by the generalized Maxwell model (GMM) (Behzadfar &

Hatzikiriakos, 2013). The GMM, consisting of multiple springs and dashpots arranged in parallel, is defined as

$$G(t) = \sum_{i=1}^{N} G_i \exp(\frac{-t}{\lambda_i}) \approx G_0 + \sum_{i=1}^{N-1} G_i \exp(\frac{-t}{\lambda_i}) \tag{4.20}$$

where G_i and λ_i represent the relaxation strength and relaxation time of the ith relaxation mode, respectively. G_0 indicates the relaxation strength of the dashpot with a nearly infinite relaxation time. Based on this equation, the specific characteristics of each relaxation mode were derived.

4.3.5 Viscosity tests

The rotational (Brookfield) Viscometer was utilized to measure the viscosity of binders. Tests were conducted at 0.1, 1, 10, 20, and 50 rpm, with temperatures ranging from 80 to 160 °C. Viscosity was determined by monitoring the torque caused by the continuous rotation of the spindle, which was immersed in a sample chamber filled with 8-10 g of bitumen.

4.3.6 Correlation analysis techniques

To analyze the relationships between various parameters from these chemical, structural, thermal, and rheological tests, Pearson correlation analysis and canonical correlation analysis (CCA) were employed. The former measures the linear correlation between two individual variables, whereas CCA examines the relationship between sets of variables derived from different tests, identifying common information revealed by two different tests (Hardoon et al., 2004; Tenenhaus & Tenenhaus, 2014).

Pearson correlation analysis

The Pearson correlation coefficient r between variables x and y is computed as

$$r_{xy} = \frac{\sum_{i=1}^{n}(x_i - \bar{x})(y_i - \bar{y})}{\sqrt{\sum_{i=1}^{n}(x_i - \bar{x})^2 \sum_{i=1}^{n}(y_i - \bar{y})^2}} \tag{4.21}$$

where n is the number of observations, $\bar{x}$ is the mean of x, and $\bar{y}$ is the mean of y. The r is in the range of -1 – 1, with the r_{xy}=0 denoting no correlation between variable x and y. The r approaching 1 suggests a strong positive correlation, and the r close to -1 reveals a high negative correlation. Additionally, a significance level of $P < 0.05$ suggests statistically significant correlation.

Canonical correlation analysis

CCA is a robust statistical method designed to evaluate the relationship between two sets of variables, denoted as $\boldsymbol{X}_{N\times p}$ and $\boldsymbol{Y}_{N\times q}$, where rows correspond to observations and columns to variables. Prior to analysis, both matrices should be standardized to obtain values on the same scale. In CCA, a predetermined number of independent canonical functions is established, which are used to generate an equivalent number of pairs of canonical variables from the original variable sets, as illustrated in Fig. 4.6. These pairs are selected based on their level of correlation, quantified by their Pearson correlation

coefficient. The CCA process begins by calculating the first canonical function and maximizing Pearson correlation between the first pair of canonical variables. The second pair is then determined to capture as much of the remaining correlated variance as possible, namely, the residual variance left by the first function, which is also known as the deflation of **X** and **Y**. This process is iteratively continued until the designated number of canonical functions is reached. Each pair of canonical variables is orthogonal to others, essentially representing linear combinations of the original variables. The maximum number of canonical functions is limited by the smaller number of variables in either set.

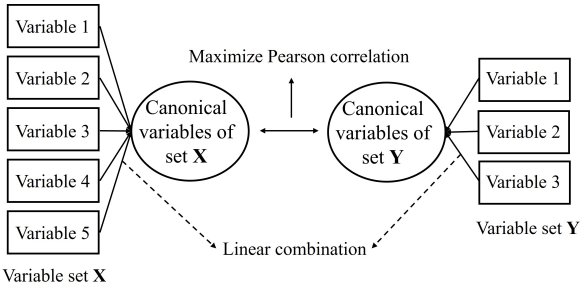

Figure 4.6 Diagram of CCA method.

The CCA method assumes linear correlations between variables. However, it is not recommended to apply CCA for datasets with high multicollinearity, namely, many variables within the dataset are highly correlated. To address this, the Pearson correlations between all variables were calculated before applying CCA, and variables with high correlations ($r > 0.9$) were excluded to ensure minimal multicollinearity. Additionally, considering that the CCA can be significantly affected by outliers, the input data were manually examined for possible outliers. The CCA involves computing the inverses of $\mathbf{X}^T\mathbf{X}$ and $\mathbf{Y}^T\mathbf{Y}$. For a stable solution, it is advisable to have fewer variables than observations in each set.

CCA results can be interpreted using several metrics including canonical correlation, canonical weight coefficient, structure coefficient, canonical cross loading, and redundancy index (Sherry & Henson, 2005). The canonical correlation, R_c, represents the Pearson correlation coefficient between a pair canonical variables derived from **X** and **Y**. The canonical weight, w_c, describes the coefficients used in the linear combination of variables within a set to form a canonical variable. The structure coefficient, or canonical loading, r_s, reflects the Pearson correlation between a canonical variable and an original variable, indicating the direct contribution of an individual variable to the canonical variables, independent of other variables. Canonical cross loading is the Pearson correlation between original variables from **X**(**Y**) and canonical variables of **Y**(**X**), which is denoted as

$$\Lambda = R_c \times r_s \tag{4.22}$$

The redundancy index (R_d) is the amount of variance in one set that is explained by the canonical components of the other set, expressed as

$$R_d = R_c^2 \times \bar{r}_s^2 \tag{4.23}$$

where $\bar{r}_s^2$ is the mean of squared canonical loadings. Among these metrics, the structure coefficient, cross-loading, and redundancy index are particularly recommended. Cross-loading is helpful for assessing the relative importance of the entire set of variables. Meanwhile, the redundancy index facilitates the selection of the canonical variables containing a substantial amount of variance (Dos Santos & Brandi, 2014).

4.4 Physico-chemical properties of aged binders

4.4.1 Changes in chemical composition with ageing

As shown in Fig. 4.3, most informative peaks occur in the spectral ranges of 3100 – 2700 cm^{-1} and 1800 – 600 cm^{-1}. Fig. 4.7 depicts these two spectral ranges for all bitumen types. The V710 and VPMB samples show similar spectra since VPMB uses V710 as its base bitumen. However, distinct differences are observed at the wavenumbers of approximately 965 cm^{-1}, 910 cm^{-1}, and 695 cm^{-1}, which indicate the presence of SBS modifiers. Similar peak positions and shapes are also observed in the spectra of T710, T1015, and T1622, all originating from the same crude oil source. The intensity of sulfoxide peak at 1030 cm^{-1} in the spectra of T1622 is lower than that in T1015 and T710, suggesting fewer sulfur-based functional groups for T1622. Compared to the binders from source T, Q-sourced binders display less similarity, as indicated by the lower degree of parallelism in their FTIR spectra.

The spectra of V710 and VPMB samples at various ageing states are shown in Fig. 4.8 . For both binders, the carbonyl and sulfoxide peaks reveal the largest changes with ageing, highlighting the main chemical reactions during the ageing process. The peak intensity of 966 cm^{-1} and 910 cm^{-1} varies as ageing progresses, indicating the degradation of polybutadiene segment in SBS.

The ageing indices for all peaks indicated in Fig. 4.3 were calculated using the tangential integration, with normalization based on the sum of all peaks (Hofko et al., 2017). Fig. 4.9 (a) and (b) display the sulfoxide and carbonyl indices of various binders. An increase in sulfoxide index is observed during the oven and PAV ageing states, with the rate of increase decelerating with longer ageing time. This is due to the oxidative reactions related to formation of sulfoxide groups, predominantly occurring at short-term and early

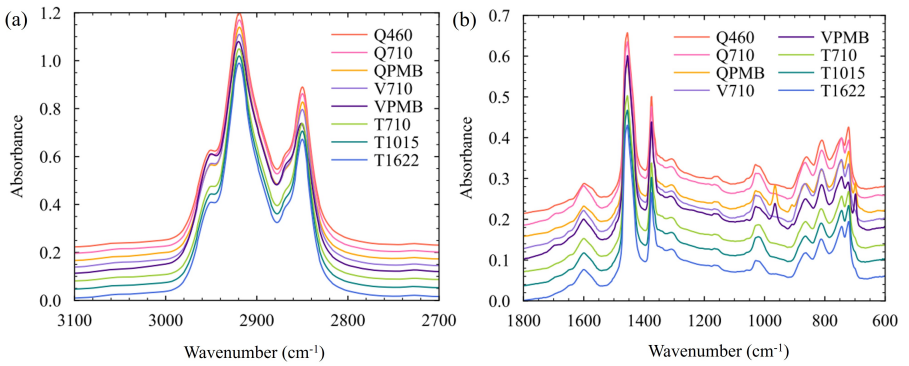

Figure 4.7 FTIR spectra of fresh bitumen in the range of (a) 3100 – 2700 cm^{-1} and (b) 1800 – 600 cm^{-1}.

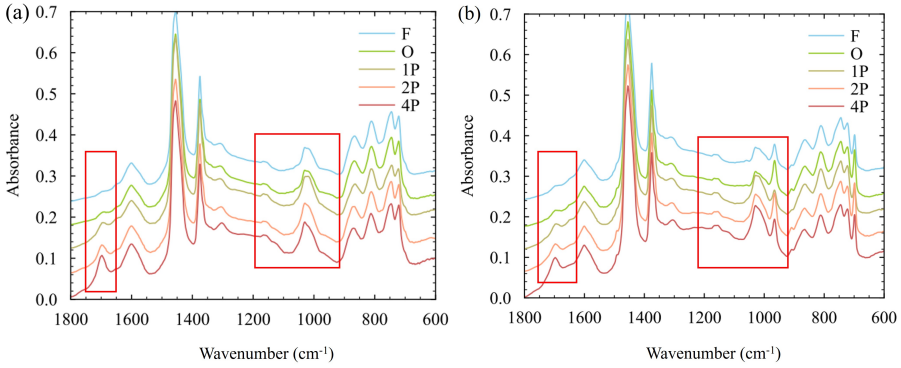

Figure 4.8 FTIR spectra (averages of three replicates for each sample) of bitumen at different ageing states: (a) V710, and (b) VPMB samples

long-term ageing states (Petersen, 2009). Carbonyl index, on the other hand, primarily reflects oxidative ageing during the long-term ageing state, showing a significant increase with longer time of PAV ageing. Compared with binders from source T, aged binders from source Q and V show a lower sulfoxide index but a higher carbonyl index. This indicates a superior long-term ageing resistance of binders obtained from source T. After 80 hours of PAV ageing, comparable sulfoxide and carbonyl indices are observed for the three binders from source T (T710, T1015, and T1622), revealing their similar contents of reactive products. For the polymer-modified binders (PMBs), the carbonyl index is lower than that of their respective base bitumens for up to 40 hours of PAV ageing. Beyond this point, similar ageing indices are reached regardless of SBS modification. SBS degradation, which mainly occurs during the short-term and initial long-term ageing stages, compensates for the ageing in bitumen. As a result, less ageing is observed in the bitumen phase of PMBs (Kaya et al., 2020). With prolonged ageing, SBS is completely degraded, resulting in the bitumen phase being fully exposed to oxidative ageing, thus reaching high ageing levels similar to pure bitumen (Yan et al., 2019).

Among all the peaks described in Fig. 4.3, aside from the carbonyl and sulfoxide indices, the indices at 1600 cm^{-1} (aromatic C=C stretching) and 1160 cm^{-1} (sulfone stretching) increase with ageing. In contrast, the indices of peaks at 2955 cm^{-1} (asymmetric C-H stretching in CH_2), 2910 cm^{-1} (asymmetric C-H stretching in CH_3), 2850 cm^{-1} (symmetric C-H stretching in CH_2), 864 cm^{-1} (aromatic C-H bending), and 814 cm^{-1} (aromatic C-H bending) decrease with higher ageing levels. Four of these additional indices are presented in Fig. 4.9 (c)–(f), namely peaks 1600, 1160, 2910, and 864 cm^{-1}. These trends indicate the aromatic condensation and an increase in polar functional groups of bitumen during the oxidative ageing process (Siddiqui & Ali, 1999). Comparing the data in Fig. 4.9 (c) to (f), three T-sourced bitumens have a higher fraction of asymmetric CH_2, a lower fraction of aromatic C-H in isolated adjacent hydrogen aromatic rings (Asemani & Rabbani, 2020), a lower amount of aromatic rings, and a lower amount of sulfone-based functional groups compared to V710. This indicates their distinct chemical composition and microstructure.

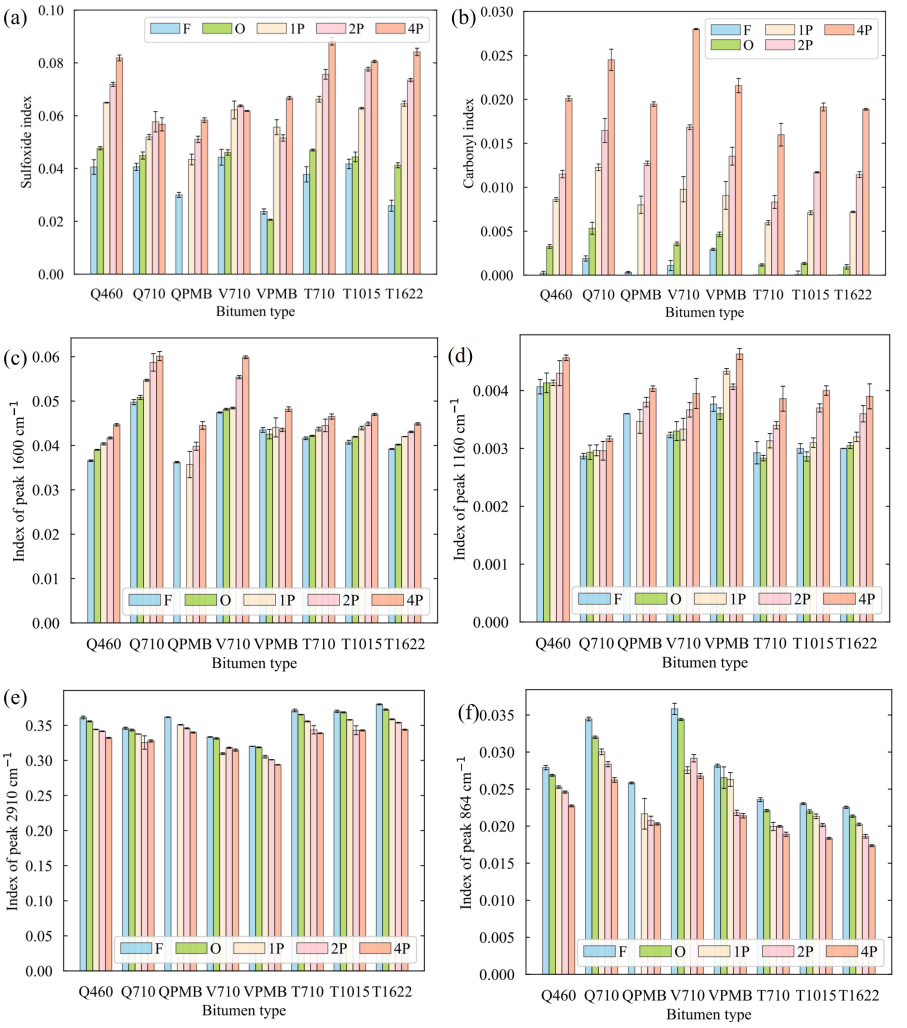

Figure 4.9 Ageing indices of (a) Sulfoxide, (b) carbonyl, (c) peak 1600 cm^{-1} indicating aromatic C=C stretching, (d) peak 1160 cm^{-1} denoting sulfone stretching, (e) peak 2910 cm^{-1} denoting asymmetric C-H stretching in CH_3, and (f) peak 864 cm^{-1} representing aromatic C-H bending.

4.4.2 Evolution of molecular weight distribution with ageing

The chromatograms of eight fresh bitumen samples are shown in Fig. 4.10 (a). For T710, T1015, and T1622, the largest difference is obtained in the range of 15 – 17 min, which is probably related to resins and aromatics fractions. Despite this, the three binders from source T generally present similar response intensities with elution time, indicating their consistent crude oil sources. In contrast, Q460 and Q710 display markedly different chromatograms. For SBS-modified binders, a distinct peak is observed in the range of 9 – 12 min. The peak positions of SBS modifiers in QPMB and VPMB differ slightly, indicating

different SBS structures used in these two binders. Compared to V710, the intensity of VPMB within 18 – 20 min is lower. This reduction could be attributed to the evaporation of light components during the preparation of SBS-modified bitumen at elevated temperatures up to 190 °C. Moreover, in SBS-bitumen systems, the SBS component may absorb light fractions from the base bitumen and form cross-linked network structure (Ma et al., 2021), a phenomenon possibly persisting during sample preparation for the GPC test. As a result, the response intensity around 18–20 min in VPMB is lower than in V710. QPMB is a commercial product with an undisclosed chemical composition of base bitumen. Comparing QPMB with Q710 and Q460, a lower intensity at ranges with small molecular sizes (SMS) is still obtained.

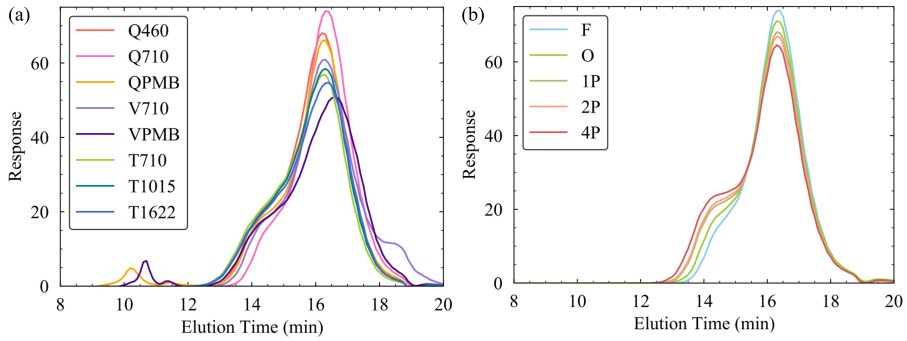

Figure 4.10 GPC chromatograms for (a) fresh binders and (b) Q710 at various ageing states.

Fig. 4.10 (b) shows how the chromatograms of Q710 evolve with ageing, showcasing the impact of ageing on molecular weight distribution of binders. As ageing level increases, the response intensity between approximately 12.5 and 15.5 min increases and that in the range of 16 – 17.5 min decreases. There is no significant variation in the chromatogram between 17.5 and 20 min. In chromatograms, shorter elution times correspond to larger molecular weights of the eluted molecules. During the ageing process, saturates mostly remain unchanged, while aromatics tend to decrease by 12-24 wt%. Resins can be generated from aromatics but may also further transform into asphaltenes, thereby exhibiting complex increasing or decreasing effects depending on the binder type. The content of asphaltenes, in particular, can increase up to 24 wt% (Mirwald et al., 2020a; Petersen, 2009; Redelius & Soenen, 2015). Combining the evolution in SARA fractions and the changes in chromatograms with ageing, it can be inferred that the elution time between 17.5 and 20 min is linked to saturates in bitumen. The range of roughly 14.5 – 17.5 min corresponds to aromatics and resins, while the time spanning 12 – 14.5 min indicates the molecular weight of asphaltenes. These chromatographic changes align well with the varying SARA fractions observed during the ageing process.

Based on the chromatograms, fractional parameters of S_{LMS}, S_{MMS}, and S_{SMS} and structural parameters including peak molecular weight (M_p), the number average molecular weight (M_n), the weight average molecular weight (M_w), Z average (M_z), and polydispersity index (PDI), were computed. Among them, S_{LMS}, S_{MMS}, S_{SMS}, and PDI of all samples are presented in Fig. 4.11. The LMS, MMS, and SMS fractions mainly corre-

spond to asphaltenes, resins and aromatics, and saturates, respectively. As ageing proceeds, the S_{LMS} increases while S_{MMS} decreases. The S_{SMS} is less affected by ageing level. In most cases, ageing results in an increase in M_w, M_n, M_z, and PDI values, although SBS-modified binders present decreased PDI and M_n due to SBS degradation.

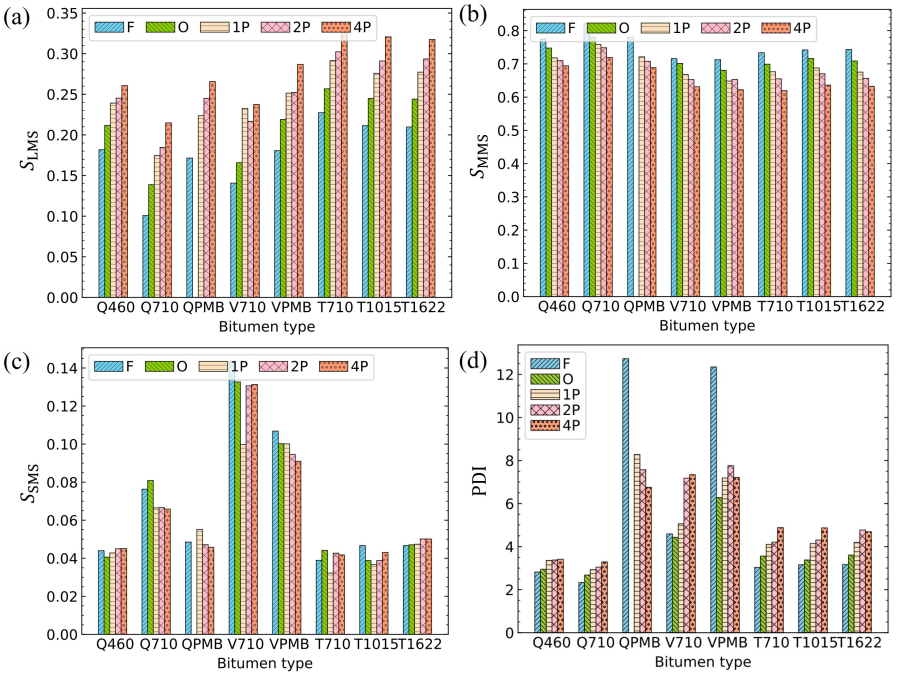

Figure 4.11 Fractional areas for (a) LMS, (b) MMS, and (c) SMS, along with (d) polydispersity.

For T710, T1015, and T1622 derived from source T, as well as the Q460 and Q710 from source Q, a higher penetration grade corresponds to a larger S_{LMS} and a smaller S_{SMS}. This trend aligns with the understanding that softer bitumen typically contains more light components while stiffer bitumen often exhibits higher aromaticity and polarity. Comparable PDI is observed for bitumen from the same source, indicating that they have similar distribution molecular weights.

4.4.3 Thermal properties evolution with ageing

Fig. 4.12 (a) and (b) depict the heat flows of all bitumen types at fresh state, obtained from the last cooling and heating scans, respectively. During the cooling scans, an exothermic peak is first revealed for most bitumen types, which may be attributed to the crystallization of crystalline fractions. Subsequently, a significant decrease in the exothermic heat flow is shown for all bitumen types. This is due to the glass transition of the bitumen samples. The heating curve of most binders typically consists of a glass transition, an exothermic cold crystallization, and one or two successive endothermic peaks (Claudy et al., 1991; Frolov et al., 2020). The gradual increase in endothermic heat flow above ca. 100

°C corresponds to the vaporization of the volatile components in bitumen (Claudy et al., 1991).

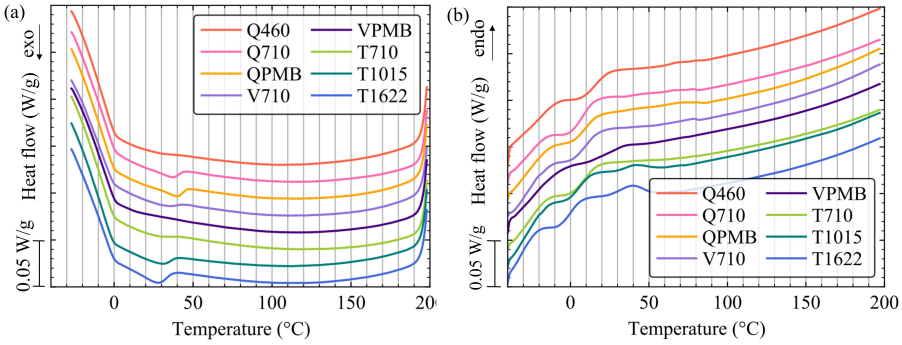

Figure 4.12 (a) Cooling and (b) heating curves for fresh bitumen types.

Glass transition describes the change from a brittle and glassy state to a viscous or rubbery state in amorphous materials. During the glass transition towards a viscous state, there is a continuous increase in both heat capacity and free volume. A broad glass transition range from -40 to -10 °C is obtained for bituminous binders due to their wide distribution of molecular weights and structures. For bitumen with crystalline phases, which upon previous fast cooling could not crystallize completely due to the high viscosity of bitumen, cold crystallization may occur during subsequent heating scan (Apostolidis et al., 2021; Elkashef et al., 2020; Michon et al., 1999). The observed endothermic peaks are related to the dissolution of the crystallized fractions in bitumen (Claudy et al., 1991; Frolov et al., 2020). Different bitumen types present distinct cooling and heating curves, reflecting their unique thermal characteristics.

Fig. 4.13 (a) and (b) show the cooling and heating curves of T710 at different ageing states, respectively. Variations are observed in both the glass transition region and the crystallization-related region for the cooling and heating curves. This indicates that oxidative ageing causes the changes in the chemical components or microstructure related to glass transition and crystalline components.

To quantify the effects of ageing on the thermal properties of binders, several thermal parameters were calculated based on the DSC results. Fig. 4.14 (a) and (b) show the T_g and ΔC_p of various binders at different ageing states. The T_g is commonly reported to increase with ageing due to the increased asphaltene concentration, polarity, and viscosity (Liu et al., 2017). However, as shown in Fig. 4.14 (a), minimal changes or even a slight decrease in T_g are observed with increasing ageing. This unexpected trend may be caused by the exothermic cold crystallization, which partially overlaps with the glass transition region (Kriz et al., 2008).

A higher T_g is observed for binders with lower penetration (Kriz et al., 2008). The T_g depends significantly on the fraction of saturates and aromatics (Claudy et al., 1991), which have much lower T_g values compared to resins and asphaltenes. Consequently, binders with lower penetrations, having a larger fraction of resins and asphaltenes, demonstrate higher T_g values. A slight decrease in ΔC_p due to glass transition is revealed with

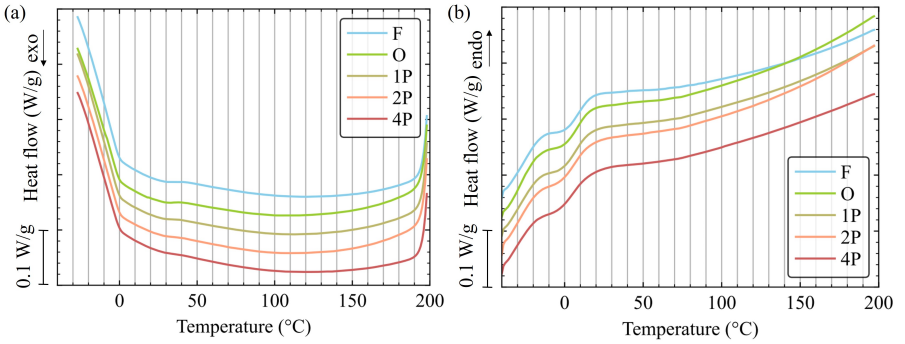

Figure 4.13 (a) Cooling and (b) heating curves for T710 at different ageing states.

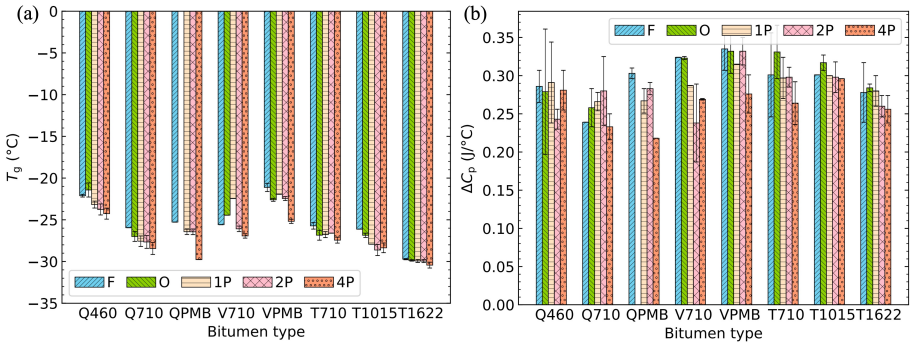

Figure 4.14 (a) Glass transition temperature and (b) heat capacity change.

increasing penetration grade. Compared to base bitumen, the T_g of PMB is higher. The SBS added to the bitumen can absorb saturates and aromatic components (which significantly affect the glass transition temperature) and swell to form polymeric network, leading to an increased T_g.

The interpretation of crystallization and decrystallizaion behavior in bitumen is varied and no consensus has been reached (Claudy et al., 1991; Ding & Hesp, 2021; Frolov et al., 2020; Lesueur, 2009). According to Frolov et al. (Frolov et al., 2020), the two endothermic peaks observed in heating curves result from the combination of the broad endothermic background of primary wax crystals and the recrystallization exotherm followed by the dissolution endotherm of secondary crystals. To accurately calculate the crystalline fraction, which is widely accepted as being proportional to the enthalpy of crystallization or dissolution, only the area of the broad endothermic background should be considered. In this study, both the crystallization area in the cooling curve and the two endothermic areas in the heating curve were calculated.

Fig. 4.15 (a) and (b) depict the enthalpy of crystallization H_{cry} during cooling and the summed enthalpy of dissolution H_{dis1}+H_{dis2} related to the two endothermic peaks during the heating scans. The crystalline components primarily consist of n-alkanes and

branched paraffins, which are mainly found in saturates and aromatics (Claudy et al., 1991). The crystallization- and dissolution-related enthalpies show similar relative values among different bitumen types. For binders from the same source, the softer one tends to have a higher enthalpy. At the same penetration grade, the crystallization enthalpy of bitumen from source T is lower than that from source V and Q. The addition of the SBS modifier reduces the crystalline enthalpy (Schaur et al., 2017). Additionally, the enthalpy of crystallization obtained from the cooling scan is smaller compared to the decrystallization enthalpy derived from the heating scan. A slight decrease in enthalpy is observed with increasing ageing level for binders from source T.

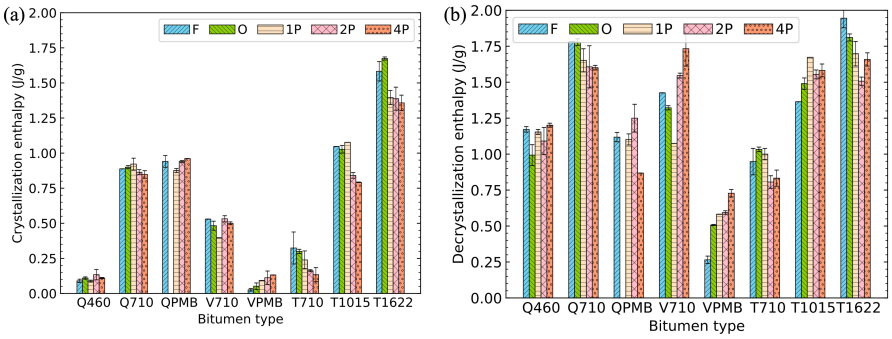

Figure 4.15 (a) Crystallization enthalpy based on cooling scans and (b) dissolution enthalpy obtained from heating curves for bitumen types at various ageing states.

4.4.4 Linking chemical and physical characteristics of aged binders

To analyze the relationships among various spectral peak indices, the Pearson correlation coefficients (r) were calculated and are presented in Table 4.1. An r value of 0.71 between peak indices of 3340 and 1600 cm^{-1} signifies a positive relationship between polar functional groups, typically found in phenolic, alcoholic, carboxylic acids, and amides, and aromatic compounds. Strong correlations are observed among peaks representing aliphatic stretching and bending in CH_2 and CH_3, namely peak indices of 2955, 2910, 2870, 2850, 1460, and 1376 cm^{-1}. This highlights their comparable effectiveness in describing the aliphatic structures of bitumen. The peak denoting -$(CH_2)_n$ bending is also highly related to these aliphatic peaks. In contrast, the correlations between the peak representing aromatic C=C stretching (1600 cm^{-1}) and those for aromatic C-H bending (as represented by 864, 814, and 743 cm^{-1}) are relatively low. This reflect different types of aromatic compounds or varying degrees of substitution. Additionally, the high correlations between peaks related to SBS indicate their association with the presence of SBS polymer. Notably, three SBS-related peaks exhibit strong negative correlations with the peak at 3055 cm^{-1}. This observation could indicate that many of the chemical components in bitumen are substituted polynuclear aromatic compounds. A higher concentration of SBS corresponds to a lower bitumen fraction, and thus a lower intensity of the peak 3055 cm^{-1} is observed.

Parameters obtained from GPC tests also demonstrate specific correlations. Accord-

Table 4.1 Pearson correlation coefficients between indices of various peaks (cm^{-1}) . This table only lists the correlation coefficients smaller than -0.6 or larger than 0.6 and p < 0.05.

Peak (cm^{-1})	3340 -OH	3055 -CH	2955 CH_3	2910 CH_2	2870 CH_3	2850 CH_2	1700 -C=O	1600 C=C	1460 $CH_{3/2}$	1376 CH_3	1305 -S	1160 -S	1030 -S=O	864 -CH	814 -CH	743 -CH	724 $-CH_2$	965 SBS	910 SBS	695 SBS
3340	1.00																			
3055		1.00																		
2955			1.00																	
2910				1.00																
2870		-0.61	0.74	-0.81	1.00															
2850		0.62	-0.69	0.89	-0.90	1.00														
1700				-0.60			1.00													
1600	0.71						0.62	1.00												
1460			0.94		0.64	-0.72			1.00											
1376			0.90	-0.67	0.84	-0.87			0.92	1.00										
1305											1.00									
1160					0.73						0.61	1.00								
1030							0.67						1.00							
864														1.00						
814														0.88	1.00					
743														0.62		1.00				
724			-0.67	0.80	-0.76	0.95			-0.78	-0.85						-0.72	1.00			
965		-0.83																1.00		
910		-0.84																0.96	1.00	
695		-0.92			0.61	-0.65											-0.66	0.93	0.86	1.00

ing to the Pearson correlation analysis, there is a negative correlation of -0.81 between S_{LMS} and S_{MMS}. The absolute r values between S_{LMS} and S_{SMS}, as well as between S_{MMS} and S_{SMS}, are less than 0.7. These r values suggest that the changes in asphaltene content with ageing are affected by molecules with medium molecular weight, primarily by resins and aromatics. Neither S_{LMS} nor S_{MMS} is strongly correlated with S_{SMS}, consistent with the ageing mechanism that saturates undergo limited changes during the ageing process (Mirwald et al., 2020a). The r between S_{SMS} and M_w is -0.96, suggesting a strong negative correlation between them.

Furthermore, the Pearson correlation coefficients for different thermal properties were calculated. The r between H_{cry} and T_g is -0.81, and the one between H_{cry} and H_{dis2} (second endothermic peak) is 0.85. For other thermal properties analyzed in this study, the correlation coefficients were observed to fall within the range of -0.6 to 0.6.

To analyze the relationships between chemical and structural properties, the Pearson correlation analyses were conducted for parameters obtained from FTIR and GPC tests, and results are listed in Table 4.2. The S_{LMS} is positively related to peak 1030 (denoting sulfoxide functional group) by a r of 0.72, suggesting the common presence of sulfur-based polar functional groups in large molecules. In contrast, S_{LMS} exhibits negative associations with peaks 864 and 814 by r values of -0.9 and -0.76, respectively. These peaks correspond to -CH in penta- and tetra-substituted aromatic rings, respectively. The negative correlations indicate that larger molecular structures are less likely to contain aromatic rings with a high degree of substitution. In the case of S_{SMS}, a strong positive correlation of 0.92 is observed with peak 743, while the r between S_{SMS} and peak 724 is -0.71. The peak at 743 cm^{-1} indicates the C-H out-of-plane bending in di-substituted aromatic rings, and the peak 724 reveals the -$(CH_2)_n$ (n >4) bending in alkyl side chains. Their r value is -0.72, as listed in Table 4.1, suggesting that the di-substitutions of aromatic rings

are mostly alkyl chains shorter than four carbons or non-alkyl chains. These findings indicate that molecules with small molecular sizes are more likely to involve aromatics with multiple alkyl side substitutions and less straight-chain alkanes with more than four carbons. Moreover, the peak molecular weight M_p is linked to the -CH_2 and -CH_3 groups in bitumen. M_w correlates negatively to the peak at 864 and 743 cm^{-1}. M_{z+1} is highly correlated to peaks at 965 and 910 cm^{-1}, which represent the =C-H wagging in SBS, indicating a good characterization of SBS content in bitumen by Z+1 average molecular weight.

Table 4.2 Pearson correlation coefficients between parameters derived from FTIR and GPC tests.

Peak (cm^{-1})	M_w	M_n	M_p	M_z	M_{z+1}	PDI	S_{SBS}	S_{LMS}	S_{MMS}	S_{SMS}
2955			-0.76							
2870			-0.70							
2850			0.83							
1460			-0.80							
1376			-0.78							
1030								0.72		
864	-0.75							-0.90		
814								-0.76		
743	-0.87									0.92
724			0.87							-0.71
965		0.72		0.79	0.90	0.73	0.83			
910		0.80		0.81	0.92	0.70	0.80			
695					0.76		0.74			

The Pearson correlation coefficients between characteristic peaks identified by FTIR and the thermal properties measured using DSC tests were computed. The results show that all these coefficients fall within the range of -0.7 to 0.7. This indicates that the thermal properties of bitumen are not predominantly influenced by specific chemical groups. Rather, they depend on the SARA fractions which may be represented by the combinations of several specific peaks (Melendez et al., 2012). Furthermore, the absolute values of all Pearson correlation coefficients between parameters obtained from GPC and DSC tests are below 0.7, suggesting a limited correlation between two sets of parameters.

The Pearson analysis reveals the specific correlation between two parameters obtained from FTIR, GPC, and DSC tests. To further explore the relationships between sets of parameters obtained from these tests, the Canonical Correlation Analysis (CCA) was performed, which is particularly useful in understanding the complex interdependencies between different types of data. During this analysis, certain FTIR peaks, GPC parameters, and DSC variables were excluded if the r between any two parameters within a dataset are larger than 0.9, in order to mitigate multicollinearity within theses datasets.

Table 4.3 shows the squared canonical correlation coefficients (R_c^2), mean of squared structure coefficients $\bar{r}_{sx}^2$ and $\bar{r}_{sy}^2$ for independent (**X**) and dependent datasets (**Y**), and redundancy indices of the first four canonical functions (R_{dx} and R_{dy}) derived from pairs of FTIR-GPC, FTIR-DSC, and GPC-DSC datasets.

The R_c^2 values quantify the shared variance between each pair of canonical variables derived from two datasets. For FTIR and GPC datasets, the first three R_c^2 values are larger than 0.90, indicating the strong correlations between these two datasets.The redundancy index evaluates the amount of variance of a variable set explained by the other variable

Table 4.3 Indices to evaluate the canonical variables obtained from CCA analysis.

Function	FTIR-GPC				FTIR-DSC				GPC-DSC			
	CC_1	CC_2	CC_3	CC_4	CC_1	CC_2	CC_3	CC_4	CC_1	CC_2	CC_3	CC_4
R_c^2	0.99	0.95	0.91	0.81	0.95	0.90	0.82	0.68	0.87	0.76	0.69	0.21
$\tilde{r}_{sx}^2$	0.18	0.33	0.11	0.05	0.11	0.14	0.08	0.21	0.22	0.22	0.24	0.12
R_{dx}	0.18	0.31	0.10	0.04	0.11	0.13	0.06	0.15	0.19	0.16	0.17	0.03
$\tilde{r}_{sy}^2$	0.32	0.30	0.09	0.16	0.29	0.28	0.05	0.09	0.23	0.07	0.10	0.51
R_{dy}	0.32	0.28	0.08	0.13	0.28	0.25	0.04	0.06	0.20	0.06	0.07	0.11

set in a given canonical function. The first two canonical variables for both FTIR and GPC display much higher redundancy indices than the third and fourth ones, indicating a substantial amount of variance captured within them. Therefore, only the first two canonical variables are analyzed.

In the case of the FTIR-DSC pair, the high R_c^2 of 0.95 for the first canonical function and of 0.90 for the second function between the two sets imply the statistical significance of the first two canonical functions. Four canonical variables for FTIR demonstrate comparable R_{dx}. However, for DSC, the first two canonical variables reveal considerably larger R_{dy} compared to the latter two variables, indicating that the latter two variables contain no significant variance. For FTIR, it may be that the selected peaks are mutually related to a certain degree, and thus there is still useful information left even after two to three rounds of deflation. In contrast, limited variance is left for DSC results after two rounds of deflation.

The correlations between the canonical variables derived from GPC and DSC datasets are lower compared to the other two pairs of datasets. GPC measures the molecular weight distribution of binders without revealing their specific microstructure, therefore, cannot accurately describe the thermal behavior such as glass transition and crystallization.

The structure coefficients and cross loadings for the first two canonical variables of all three pairs of datasets are listed in Table 4.4. For each variable in the two sets (**X** and **Y**), the r_s and Λ_s show similar values, indicating that these variables are related to canonical variables of both sets to a similar extent. This is consistent with the strong correlation between the canonical variables of **X** and **Y**.

According to the cross loadings of variables between FTIR and GPC datasets, the peaks 3014 (C-H stretching in aromatic rings), 2955 (asymmetric C-H stretching in CH_3), 2850 (symmetric C-H stretching in CH_2), 846 (-CH in penta-substituted aromatic rings), 814 (-CH in tetra-substituted aromatic rings), and 724 (-$(CH_2)_n$ bending, $n \geq 4$) cm^{-1} are correlated to CCY_1 of GPC with $\Lambda_{s,x1}$ of 0.63, -0.43, 0.53, 0.68, 0.57, and 0.45, respectively. The structure coefficients of M_p, S_{LMS}, and S_{MMS} with respect to CCY_1 are 0.65, -0.62, and 0.92. Combining $\Lambda_{s,x1}$ and $r_{s,y1}$ together, it can be inferred that aromatic rings with various numbers of substitutions constitute most molecules with medium molecular weight, which also relate to M_p since it occurs in MMS area. Second canonical variable mainly depends on the chemical groups -CH_2, -CH_3, and -CH in partly substituted aromatic rings, as well as alkyl chains, which is strongly linked to weight average molecular weight (M_w).

According to the CCA analysis between FTIR and DSC datasets, the cross loadings

Table 4.4 Structure coefficients and cross loadings for the first two pairs of canonical variables obtained from the CCA analysis of FTIR, GPC, and DSC results.

FTIR-GPC					FTIR-DSC					GPC-DSC				
X	$r_{s,x1}$	$r_{s,x2}$	$\Lambda_{s,x1}$	$\Lambda_{s,x2}$	X	$r_{s,x1}$	$r_{s,x2}$	$\Lambda_{s,x1}$	$\Lambda_{s,x2}$	X	$r_{s,x1}$	$r_{s,x2}$	$\Lambda_{s,x1}$	$\Lambda_{s,x2}$
3340	-0.18	-0.21	-0.18	-0.21	3340	0.12	0.28	0.12	0.26	M_w	0.11	0.27	0.10	0.24
3014	0.63	0.16	0.62	0.16	3014	0.34	0.33	0.33	0.32	M_n	0.27	-0.53	0.25	-0.46
2955	-0.43	-0.62	-0.43	-0.60	2955	-0.73	-0.56	-0.71	-0.54	M_p	-0.74	0.35	-0.69	0.31
2910	0.30	0.62	0.30	0.60	2910	0.03	0.26	0.02	0.25	PDI	0.26	-0.57	0.25	-0.49
2850	0.53	0.71	0.52	0.69	2850	0.43	0.27	0.42	0.26	S_{LMS}	0.13	0.67	0.12	0.58
1700	-0.28	0.04	-0.28	0.04	1700	0.31	0.31	0.30	0.30	S_{MMS}	-0.76	-0.26	-0.71	-0.23
1600	0.14	-0.38	0.14	-0.37	1600	0.33	0.44	0.32	0.41					
1030	-0.32	0.47	-0.31	0.46	1030	0.22	0.46	0.22	0.44					
864	0.68	-0.63	0.68	-0.62	864	0.25	-0.37	0.25	-0.35					
814	0.57	-0.54	0.56	-0.52	814	0.10	-0.63	0.10	-0.60					
743	0.08	-0.95	0.08	-0.92	743	-0.12	-0.08	-0.11	-0.08					
724	0.45	0.81	0.44	0.79	724	0.42	0.20	0.41	0.19					
Y	$r_{s,y1}$	$r_{s,y2}$	$\Lambda_{s,y1}$	$\Lambda_{s,y2}$	Y	$r_{s,y1}$	$r_{s,y2}$	$\Lambda_{s,y1}$	$\Lambda_{s,y2}$	Y	$r_{s,y1}$	$r_{s,y2}$	$\Lambda_{s,y1}$	$\Lambda_{s,y2}$
M_w	-0.28	0.92	-0.28	0.89	T_g	-0.23	-0.85	-0.22	-0.81	T_g	0.01	-0.32	0.01	-0.28
M_n	-0.36	0.05	-0.36	0.05	H_{dis1}	0.65	0.46	0.63	0.44	H_{dis1}	-0.69	0.18	-0.64	0.16
M_p	0.65	0.62	0.64	0.61	H_{dis2}	-0.27	0.43	-0.26	0.41	H_{dis2}	0.29	0.17	0.27	0.15
PDI	-0.26	-0.42	-0.26	-0.41	H_{cry}	-0.14	-0.52	-0.14	-0.49	H_{cry}	-0.06	0.08	-0.05	0.07
S_{LMS}	-0.62	0.60	-0.61	0.58	T_{cry}	0.95	-0.08	0.93	-0.07	T_{cry}	-0.78	-0.45	-0.73	-0.39
S_{MMS}	0.92	0.21	0.91	0.21										

of the FTIR variables show that peaks at 3014 (C-H stretching in aromatic rings), 2955 (asymmetric C-H stretching in CH_3), 2850 (symmetric C-H stretching in CH_2), and 724 (-$(CH_2)_n$ bending, $n \geq 4$) cm^{-1} are substantially related to the first canonical variable of DSC, among which the peak at 2955 cm^{-1} has a higher correlation of -0.73 compared to other variables. The CCY_1 has a structure coefficient of 0.95 with the crystallization peak in the cooling curves and of 0.65 with the decrystallization enthalpy derived from the first endothermic peak. This indicates that crystallization primarily depends on the aliphatic groups in bitumen, supportive of the understanding that crystalline materials in bitumen are macrocrystalline waxes with *n*-alkanes and microcrystalline waxes dominated by iso- and cycloalkanes (Edwards & Redelius, 2003). It is worthy noting that CCY_1 is negatively related to indices at peak 2955 cm^{-1} but positively related to indices of 2850 and 724 cm^{-1}. The former describes the fraction of CH_3 and the latter denotes the presence of CH_2. The carbon atoms in paraffin waxes are between 20 and 40. A higher content of CH_2 suggests a higher content of waxes.

The cross loadings of CCX_2 show that FTIR variables that relate to CCY_2 are primarily peaks at 2955 (asymmetric C-H stretching in CH_3), 1600 (aromatic C=C stretching), 1030 (S=O stretching), and 814 (two isolated adjacent hydrogens in aromatic rings). The peak at 814 cm^{-1} has the largest negative correlation with CCY_2 while the peak at 1030 cm^{-1} shows the most substantial positive correlation. The structure coefficient between CCY_2 and T_g is the highest (-0.85). SARA fractions, i.e., saturates, aromatics, resins, and asphaltenes, have their distinct T_g. The T_g of bitumen is influenced by their fractions, functional groups, micro structures (Frolov et al., 2018; Kriz et al., 2008), etc. The peak

variables that contribute the most to the CCY_2, which correlates considerably with T_g, include aliphatics, aromatics, and polar groups. These variables align with the factors that affects T_g of bitumen.

The first canonical variable from the CCA analysis of GPC and DSC datasets shows that combined H_{dis1}, H_{dis2} and T_{dis2} are positively related to the M_p and S_{MMS}. Although the crystal-related thermal properties are theoretically dependent on the fraction of wax alkanes, it may be that crystal components are positively linked to molecules with MMS based on studied samples. Furthermore, it should be noted that a high correlation coefficient between two variables indicates a strong linear relationship, but it does not imply dependency.

4.5 Rheology of aged binders

4.5.1 Viscoelastic response to ageing

To evaluate the rheological properties of different bitumen types and their response to oxidative ageing, the frequency sweep tests were conducted, and the CAM model was utilized to create the master curves of complex modulus and phase angle. Fig. 4.16 depicts the master curves for all bitumen types. The master curves of complex modulus reveal overall higher fitting quality compared to those of the phase angle. This is due to the higher uncertainty in phase angle measurements caused by the damage-induced distortion of the stress waveform during experiments (Cao et al., 2018). For binders from the same sources, the complex modulus decreases and the phase angle increases with a higher penetration grade. T710 and V710 exhibit a lower complex modulus and a higher phase angle compared to Q710. This indicates that different bitumen types, even from the same source, can exhibit varied rheological responses.

Compared to base bitumen, the addition of SBS modifier increases the complex modulus and reduces the phase angle. However, at high frequencies, the effect of SBS on complex modulus and phase angle is not noticeable due to the high stiffness of bitumen

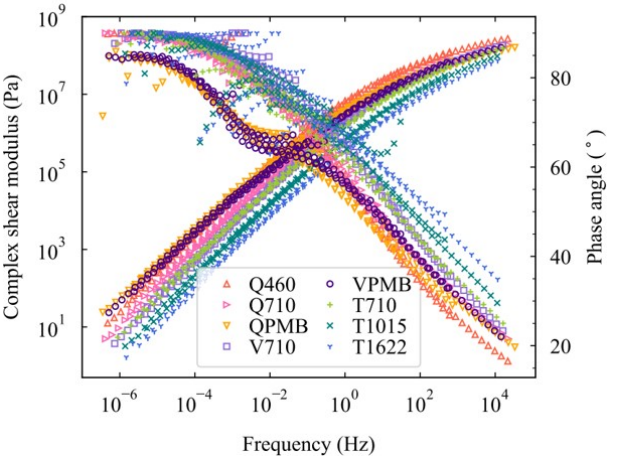

Figure 4.16 Master curves of all types of fresh bitumen

phase, which predominantly contributes to the rheological response. In the frequency range of 10^{-1} – 10^{-3} Hz, the phase angle of SBS-modified bitumen diverges in behavior from that of base bitumen, exhibiting a distinct plateau. This plateau is attributed to the influence of the polymeric network structure within the binder (Airey, 2003). This network, created by the entangled polystyrene and polybutadiene blocks, is indicative of a broad distribution of relaxation times, therefore providing a balance between elastic and viscous behavior over a wide frequency range. At frequencies lower than 10^{-3} Hz (or higher temperatures), the PMB with a high SBS content (> 4 – 6 wt%) demonstrates a rapid decrease in phase angle with increasing frequency. This behavior is linked to the dissolution of polymers in bitumen and the formation of continuous polymeric network. At lower frequencies or higher temperatures, bitumen becomes more viscous and polymers gradually take over, resulting in a lower phase angle. However for the two PMBs examined in this work, the phase angle increases again at lower frequencies, eventually reaching the viscous state (δ=90°). This observation indicates that an SBS content of 4 wt% in V710 and Q710 is not high enough to form the continuous SBS network. Therefore, the polymeric network is fully relaxed at low frequencies.

Fig. 4.17 shows the master curves of V710 and VPMB at various ageing states. For both V710 and VPMB, the complex modulus increases and the phase angle decreases with increasing ageing, demonstrating the hardening of bitumen due to the oxidative ageing process. Specifically, in SBS-modified bitumen, the plateau in the master curves of phase angle observed for fresh bitumen diminishes considerably after short-term ageing. This change is related to the degradation of SBS during the ageing process. The ageing-caused hardening, i.e., the increase in the complex modulus of SBS modified bitumen is less pronounced compared to base bitumen. This may be explained by two factors: the presence of SBS appears to slow down the ageing process in the base bitumen; the degradation of the SBS modifier during ageing process counterbalances the increased stiffness (Cappello et al., 2021).

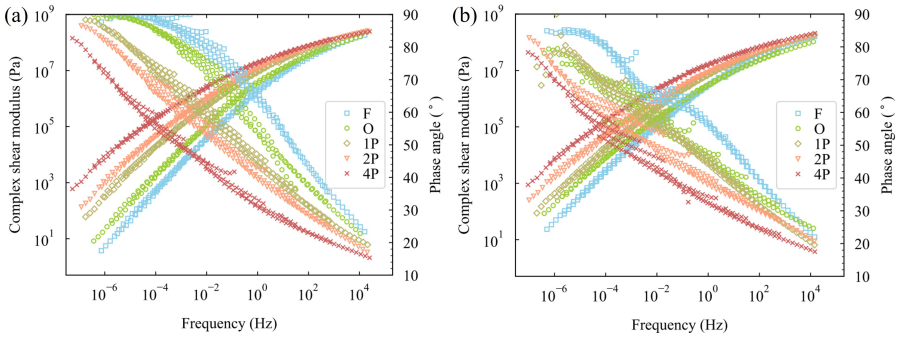

Figure 4.17 Master curves of (a) V710 and (b) VPMB at various ageing states.

It is widely recognized that the ageing process leads to stiffer and more brittle bituminous binders. To evaluate the effects of ageing on the rheological properties of all bitumen types, several key parameters were calculated, including the crossover frequency (f_c), crossover modulus (G_c^*), rheological index (R_{rhe}), and Glove-Rowe parameter ($G-R$).

The results are shown in Fig. 4.18. The crossover frequency is the frequency at which the viscous and elastic components of the complex modulus are equal (where δ=45 °). Generally, higher ageing levels correlate with a lower crossover frequency due to increased stiffness of bitumen caused by the substantial chemical and structural changes during the ageing process (Qin et al., 2014). The complex modulus at the crossover frequency is known as the crossover modulus, which also decreases with increasing ageing time. The crossover frequency and crossover modulus are significantly related to each other (Farrar et al., 2013). Oxidative ageing of bitumen increases its polarity and molecular interactions, leading to a more dense and viscous structure. An overall increase in complex modulus is therefore revealed as shown in Fig. 4.17. However, due to the higher stiffness of aged bitumen, the crossover frequency shifts to a lower value, and thus the corresponding crossover modulus decreases.

Binders with a higher penetration grade are softer and less viscous, exhibiting a higher crossover frequency along with a reduced crossover modulus. The SBS modification decreases the crossover frequency and crossover modulus of binders. An appropriate amount of SBS can create a polymeric network within bitumen. This presence of network improves the elasticity at higher frequencies (or lower temperatures), causing a shift in the crossover frequency to a lower value, which in turn lowers the crossover modulus.

The R_{rhe}, indicative of the shape of master curve and the skewness of relaxation spectrum (Christensen et al., 2017), is larger for bitumen at higher ageing level. Bitumen with larger R exhibits a wider relaxation spectrum and potentially a longer fatigue life due to increased energy dissipation. However, a higher R_{rhe} also indicates a stiffer and more brittle binder, leading to reduced crack resistance. At high strain levels, such bitumen might be more susceptible to fatigue. Compared to crossover frequency and crossover modulus, R_{rhe} displays less variations for binders from the same bitumen sources.

Fig. 4.18 (d) presents increased $G-R$ values with ageing. The $G-R$ parameter effectively characterizes the stiffness and embrittlement of bituminous binders, serving as an indicator of their ductility and cracking resistance at intermediate temperature (Glover et al., 2005). Two thresholds with respect to damage levels are defined, a warning threshold at 180 kPa signaling damage onset and a critical threshold at 600 kPa indicating significant cracking (G. M. Rowe & Sharrock, 2016). Softer bitumen exhibits a lower $G-R$ value, indicating a higher resistance to fatigue cracking. However the ageing process tends to mitigate this advantage, resulting in similar levels of cracking after 80 hours of PAV ageing. After 40 hours of PAV ageing, the $G-R$ values of all binders from source Q and V are larger than 180 kPa. These values further surpass 600 kPa after 80 hours of PAV ageing, suggesting extensive cracking. In contrast, the lower $G-R$ values of binders from source T demonstrate their superior crack resistance compared to those from other sources.

4.5.2 Fatigue properties of aged binders

To evaluate the fatigue life of bituminous binders, linear amplitude sweep tests were performed, and the S-VECD model was applied to interpret the test results. Compared to other fatigue testing methods such as the time sweep (TS), this methodology has a relatively short testing duration and demonstrates high efficiency in evaluating the fatigue life of bituminous binders and mixtures (Ameri et al., 2016). All parameters derived from the LAS tests and the S-VECD model are listed in Table 4.5.

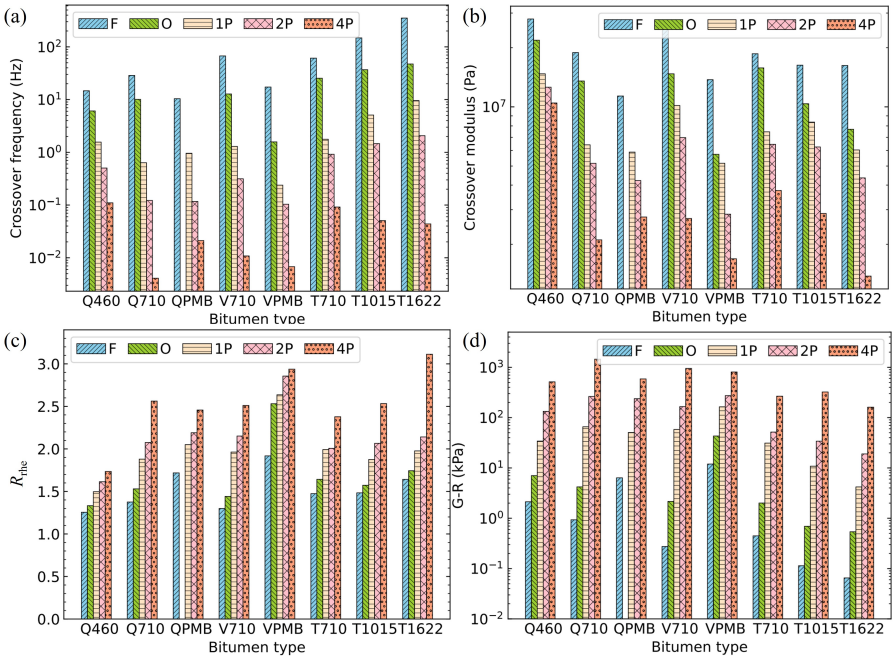

Figure 4.18 (a) Crossover frequency, (b) crossover modulus, (c) R_{rhe}, and (d) Glove-Rowe of all bitumen samples.

Table 4.5 Parameters in the S-VECD model and fatigue life of all binders. Parameters with a superscript of "L" represent values in the logarithmic scale.

Samples	τ^{L}_{max}	C_{D1}	C_{D2}	A^{L}_{D}	B_{D}	N^{L}_{f25}	N^{L}_{f50}	Samples	τ^{L}_{max}	C_{D1}	C_{D2}	A^{L}_{D}	B_{D}	N^{L}_{f25}	N^{L}_{f50}
Q460_F	5.78	0.12	0.44	4.44	-2.75	3.34	2.51	VPMB_F	5.58	0.13	0.38	5.10	-2.94	3.93	3.04
Q460_O	5.86	0.14	0.42	4.75	-3.33	3.43	2.43	VPMB_O	5.65	0.22	0.29	5.52	-3.73	4.03	2.91
Q460_1P	5.96	0.16	0.38	4.83	-3.87	3.29	2.13	VPMB_1P	5.68	0.24	0.28	5.57	-4.28	3.86	2.58
Q460_2P	6.04	0.18	0.36	5.07	-4.51	3.27	1.91	VPMB_2P	5.78	0.24	0.28	5.95	-4.63	4.11	2.71
Q460_4P	6.11	0.20	0.34	5.15	-5.24	3.07	1.49	VPMB_4P	5.88	0.27	0.28	5.93	-5.94	3.57	1.78
Q710_F	5.53	0.12	0.43	4.80	-2.78	3.69	2.86	T710_F	5.48	0.07	0.49	4.86	-2.60	3.83	3.04
Q710_O	5.59	0.15	0.37	5.29	-3.26	3.99	3.01	T710_O	5.58	0.09	0.45	5.14	-2.86	4.00	3.14
Q710_1P	5.76	0.20	0.32	5.45	-4.33	3.72	2.42	T710_1P	5.79	0.14	0.39	5.45	-3.71	3.97	2.86
Q710_2P	5.87	0.22	0.30	5.98	-5.04	3.97	2.45	T710_2P	5.83	0.15	0.37	5.03	-3.96	3.45	2.26
Q710_4P	5.92	0.23	0.30	6.32	-6.10	3.89	2.06	T710_4P	5.87	0.18	0.34	5.72	-4.71	3.85	2.43
QPMB_F	5.60	0.15	0.35	5.28	-3.11	4.04	3.11	T1015_F	5.21	0.06	0.50	4.77	-2.42	3.80	3.07
QPMB_1P	5.63	0.24	0.27	6.05	-3.94	4.48	3.30	T1015_O	5.47	0.10	0.43	5.27	-3.00	4.08	3.18
QPMB_2P	5.73	0.28	0.24	6.42	-4.82	4.50	3.05	T1015_1P	5.62	0.13	0.39	5.71	-3.60	4.28	3.19
QPMB_4P	5.80	0.28	0.24	6.92	-5.46	4.74	3.10	T1015_2P	5.70	0.15	0.36	5.88	-3.90	4.33	3.16
V710_F	5.47	0.10	0.45	4.56	-2.46	3.58	2.84	T1015_4P	5.85	0.18	0.33	6.25	-4.94	4.29	2.80
V710_O	5.61	0.11	0.43	5.13	-3.05	3.91	3.00	T1622_F	5.09	0.06	0.51	4.92	-2.54	3.91	3.15
V710_1P	5.81	0.17	0.34	4.93	-3.90	3.38	2.20	T1622_O	5.31	0.09	0.44	5.35	-2.94	4.18	3.29
V710_2P	5.86	0.19	0.33	5.67	-4.41	3.91	2.58	T1622_1P	5.43	0.10	0.41	5.77	-3.36	4.43	3.42
V710_4P	5.97	0.23	0.30	5.73	-5.45	3.56	1.92	T1622_2P	5.53	0.14	0.37	5.97	-3.89	4.42	3.25
								T1622_4P	5.68	0.17	0.35	5.72	-4.95	3.76	2.27

Fig. 4.19 shows how shear stress of various binders varies with shear strain. With

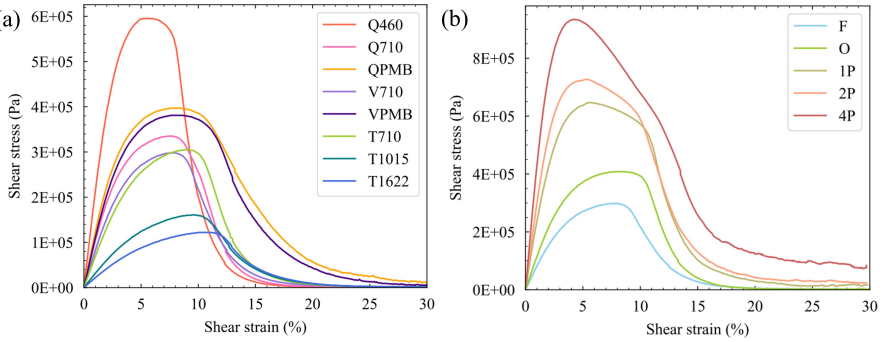

Figure 4.19 Linear amplitude sweep results of (a) fresh bitumen and (b) V710 at various ageing states.

increasing shear strain, the shear stress initially increases and reaches a peak (τ_{max}). After this peak, the shear stress decreases dramatically, signaling the failure of the binders. As depicted in Fig. 4.19 (a), binders with lower penetration grades result in an increased maximum shear stress and a narrower peak width. The entire curves also skew towards lower strains, signifying their higher stiffness and increased sensitivity to strain loading. The τ_{max} listed in Table 4.5 also reveals a lower value for binders with higher penetration grade. Compared to V710 and Q710, the peak stress of T710 occurs at a higher shear strain, suggesting the better resistance to shear strain. The modification of bitumen by SBS leads to both higher peak stress and wider peak width. This results in an increase in stiffness and a reduced susceptibility to shear strain, enhancing the bitumen performance under strain.

Fig. 4.19 (b) shows the plots of stress vs. strain for V710 at different ageing levels. Ageing induces changes in the stress-strain relationship similar to the effects of higher penetration, namely, increased peak stress, narrower peak width, and skewing towards lower strain levels. During the ageing process, binders become stiffer and more brittle, which leads to a higher sensitivity to shear strain. This holds for all types of binders as indicated by the increased τ_{max} value with ageing (Table 4.5).

The damage characteristic curve describes the deterioration in material integrity due to damage accumulation (Cao et al., 2018). Fig. 4.20 (a) displays the $C(D)$ function for all fresh binders. There is a decrease in material integrity as damage intensity increases, which can be approximately described by the power law containing two parameters C_{D1} and C_{D2}, as defined by Equation 4.17. For softer binders, the damage curves appear flatter and lie above stiffer binders, suggesting a slower damage evolution under stress loading. Among Q710, T710, and V710, with the same penetration grade but from different sources, Q710 shows the steepest $C(D)$ curve, followed by V710 and T710. In the power function describing $C-D$ relationship, parameter C_{D1} indicates the basic scale of damage while C_{D2} defines the curve shape and the sensitivity of material integrity to damage. Table 4.5 shows relatively consistent values of C_{D1} and C_{D2} for binders from the same sources, indicating that crude oil source determines fundamental fatigue behavior of binders including the basic scales of damage and the sensitivity of material integrity

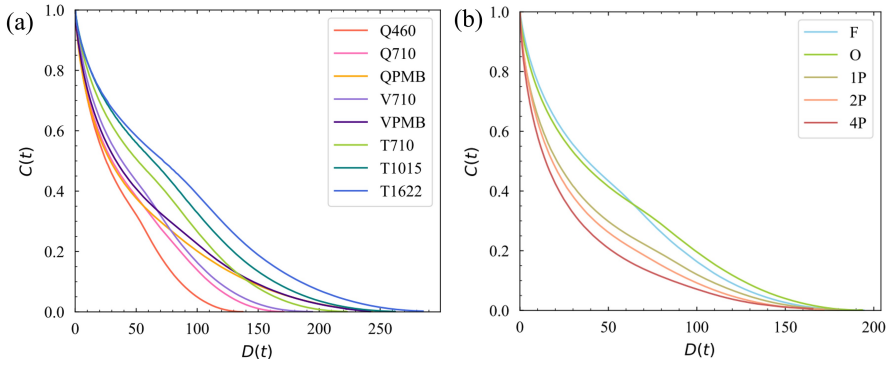

Figure 4.20 Damage curves for binders at (a) fresh state and (b) V710 at various ageing states based on S-VECD model.

to damage. Additionally, Fig. 4.20 (a) shows that adding SBS to bitumen leads to a flatter damage characteristic curve, indicating enhanced resistance to damage. This is reflected in the larger C_{D1} and smaller C_{D2} for PMB compared to pure bitumen.

The damage evolution with ageing is shown in Fig. 4.20 (b). As ageing time increases, the $C(D)$ curve shifts towards the lower left, leading to a larger C_{D1} and a smaller C_{D2}. This suggests that bitumen becomes more brittle and susceptible to fatigue with ageing.

The fatigue life of bituminous binders was analyzed using the S-VECD model, with parameters A_D, B_D, N_{f25} and N_{f50} presented in Table 4.20. The coefficient A_D in the fatigue equation is indicative of the inherent fatigue resistance of binders, while B_D describes the rate of damage under varying strain levels, which depends on the energy release rate upon an external load (Johnson, 2010). A higher A_D value and a lower $|B_D|$ value indicate a better fatigue resistance for bituminous binders. N_{f25} and N_{f50} denote the fatigue life of binders at strain levels of 2.5% and 5.0%, respectively, which have been shown to correlate with in-field fatigue cracking performance (Yang et al., 2022).

A higher fatigue life is observed for softer binders due to their greater deformation capacity. Binders from source T reveal better fatigue resistance compared to other sources regardless of ageing states, especially at higher strain levels. This reflects the strong adaptability to high loading strain for T-sourced binders, as demonstrated by their lower values of $|B_D|$. The addition of SBS modifiers enhances the fatigue life of binders.

Ageing slightly increases the fatigue life of pure bitumen and largely enhances it for PMB at a 2.5% strain level. However, at the strain level of 5.0%, the fatigue life of pure binders gradually decreases with ageing while SBS-modified binders exhibit minimal changes in fatigue life. At low strain levels, ageing enhances the fatigue resistance of binders due to the increased elastic components, which results in less energy loss during loading. With increasing strain level, ageing gradually leads to decreased fatigue life due to increased brittleness, namely the decreased ability to deform without cracking. The improved fatigue life of SBS-modified binders at both 2.5% and 5.0% levels could be attributed to the increased flexibility and polymeric network formed by SBS, and its potential to decelerate the ageing process of bitumen phase.

4.5.3 Relaxation behavior changes with ageing

Relaxation tests were conducted to evaluate the relaxation behavior of bituminous binders at low temperatures, with results for various binders and Q710 at different ageing states depicted in Fig. 4.21. With increasing relaxation time, the shear stress (relaxation strength) decreases because of the rearrangement of the structure to adapt to the strain. The noise observed at longer relaxation times may be caused by the diminished accuracy in measuring low shear stress for the configuration of 8 mm, which is more suited for higher stiffness. The relaxation rate decreases as bitumen undergoes the ageing process. Ageing leads to the formation of larger molecules of higher polarity within bitumen, primarily through oxidative reactions. These larger molecules exhibit a tendency to relax at a slower pace. Binders with a higher penetration grade are found to relax faster due to their lower viscosity, facilitating easier flow and molecular rearrangement under strain. The relaxation rate of SBS-modified binders is slightly lower compared to their base bitumens.

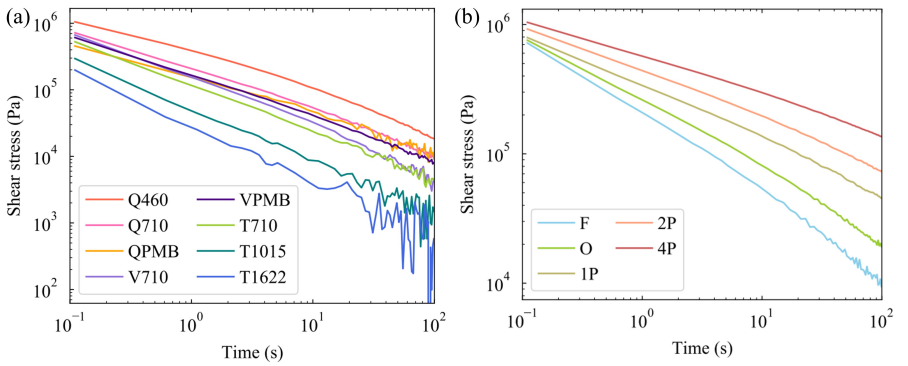

Figure 4.21 Relaxation for (a) all bitumen types at fresh state and (b) Q710 at different ageing states.

The relaxation strengths and relaxation times for various relaxation modes in the GMM model (Equation 4.20) were determined through a linear regression procedure. Theoretically, bitumen exhibits a continuous relaxation spectrum due to its complex chemical components and microstructure. This implies that capturing a greater number of relaxation times can more accurately represent its relaxation behavior. However, including too many regression parameters increases the difficulties in obtaining converged results. To find a balance, trial regressions were performed with 7, 9, and 13 unknown parameters. Considering the trade-off between the fitting accuracy and the model complexity, a total of nine undetermined parameters were eventually used to describe the relaxation process, including G_0 and four pairs of relaxation strength and relaxation time. The fitted parameters are listed in Table 4.6.

As shown in Table 4.6, Maxwell elements characterized by longer relaxation times typically exhibit lower relaxation strengths. As aging levels rise, both the relaxation time and relaxation strength increase, due to the accumulation of condensed aromatic components and increased polarity (Mirwald et al., 2020b; Tauste et al., 2018). For higher penetration grade, both the relaxation strength and relaxation time of each relaxation mode decrease in most cases. Additionally, when SBS polymer is introduced, it tends to prolong

Table 4.6 Parameters in the generalized Maxwell model.

Samples	G_0	G_1	G_2	G_3	G_4	γ_1	γ_2	γ_3	γ_4
Q460_F	1.6E+04	8.2E+05	3.1E+05	1.7E+05	8.7E+04	0.22	1.24	5.61	31.35
Q710_F	9.1E+03	7.1E+05	2.0E+05	1.0E+05	4.6E+04	0.18	0.93	4.69	28.51
QPMB_F	8.2E+03	4.0E+05	1.2E+05	6.3E+04	3.5E+04	0.22	1.24	6.20	34.52
V710_F	3.9E+03	7.7E+05	1.8E+05	7.0E+04	2.7E+04	0.17	0.99	5.01	27.24
VPMB_F	1.0E+04	6.4E+05	1.7E+05	9.0E+04	4.4E+04	0.21	1.19	5.55	34.01
T710_F	3.9E+03	6.3E+05	1.6E+05	8.1E+04	2.4E+04	0.14	0.60	3.11	24.77
T1015_F	1.5E+03	3.9E+05	6.3E+04	3.3E+04	1.1E+04	0.16	0.61	2.84	18.87
T1622_F	8.3E+02	3.4E+05	5.1E+04	2.0E+04	6.0E+03	0.12	0.51	2.32	16.70
Q710_O	1.5E+04	6.7E+05	2.0E+05	1.1E+05	6.0E+04	0.20	1.23	6.16	37.05
Q710_1P	4.0E+04	5.8E+05	2.1E+05	1.2E+05	9.7E+04	0.21	1.23	6.14	35.93
Q710_2P	5.8E+04	6.0E+05	2.5E+05	1.2E+05	1.5E+05	0.22	1.37	7.40	47.76
Q710_4P	1.1E+05	5.6E+05	2.6E+05	1.7E+05	1.7E+05	0.23	1.45	7.55	48.40

the relaxation time of each Maxwell element because of the polymeric network formed by SBS. It is important to note that during relaxation tests, the shortest data interval recorded is 0.01 s, and the longest test duration is 100 s. Therefore, Maxwell elements with relaxation times falling outside this range may not be accurately characterized. Furthermore, on a logarithmic scale, the initial test data points are less densely distributed, indicating a reduced accuracy for the results with shorter relaxation times. This aspect should be noted in interpreting the relaxation behavior, especially for the elements with fast relaxation responses.

4.5.4 Ageing-induced changes in binder viscosity

The viscosity of bitumen at 120–160 °C has been widely used to evaluate the workability of asphalt mixtures during mixing and compaction stages. The viscosity measured at ca. 60 °C is strongly related to the rutting performance of asphalt pavement (De Visscher et al., 2004; Morea et al., 2010; Zeiada et al., 2022). Viscosity is shown to be associated with the ageing of bitumen (Herrington, 2012). During the ageing process, larger molecules with increased polarity are formed within bitumen through oxidative reactions, which cause an increase in viscosity. To investigate the viscosity of different bitumen types at distinct ageing states, the complex viscosity (η^*) was determined using oscillatory shearing in a DSR (Dynamic Shear Rheometer) and calculated as

$$|\eta^*(f)| = \frac{|G^*|}{2\pi f} \tag{4.24}$$

. Moreover, the steady-flow apparent viscosity was measured with a Brookfield Viscometer.

The complex viscosities of various fresh binder types at 60 °C are displayed in Fig. 4.22. For binders obtained from the same source, a higher penetration grade is associated with a lower viscosity. The complex viscosity of V710 is smaller than that of Q710 and T710. Compared to base bitumen, a higher viscosity is observed for SBS-modified binders. At lower frequencies, the viscosity of neat binders reaches a plateau. The fluctuations at low frequencies could be attributed to a reduced measuring accuracy at extremely low loading frequencies. However, for SBS-modified bitumen, the viscosity continues to rise as the frequency decreases.

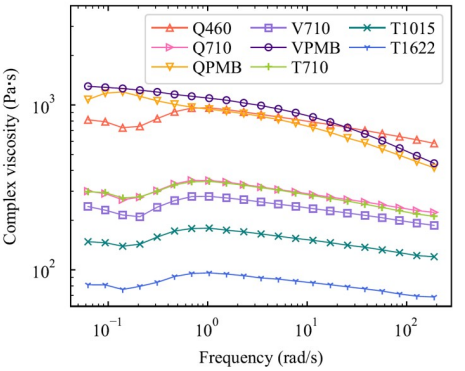

Figure 4.22 Complex viscosity as a function of frequency for all bitumen types at fresh state at 60 °C.

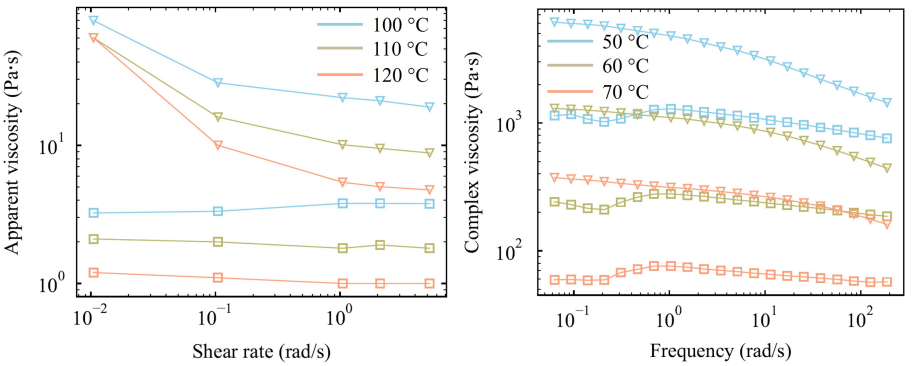

Figure 4.23 (a) Apparent viscosity of fresh V710 and VPMB as a function of shear rate at temperatures of 100, 110, and 120 °C and (b) complex viscosity of fresh V710 and VPMB with increasing frequency at temperatures of 50, 60, and 70 °C. Viscosity of VPMB is represented by downward triangle and that of V710 is denoted by square marker.

To further investigate the dependence of viscosity on frequency for pure and modified binders, the apparent and complex viscosities of V710 and VPMB as a function of shear rate at various temperatures are presented in Fig. 4.23 (a) and (b). At high temperatures, V710 behaves like a Newtonian fluid, with its viscosity exhibiting minimal variation with shear rate. However, the viscosity of VPMB decreases significantly with increasing shear rate, demonstrating its non-Newtonian, shear-thinning characteristic (pseudo plastic region). At lower temperatures as shown in Fig. 4.23 (b), both V710 and VPMB show a lower viscosity with increasing frequency. The non-Newtonian behavior of binders is attributed to their elasticity (Cox & Merz, 1958). When applying a shear stress, the entangled molecular chains within binders align conforming to the shear direction, leading to decreased viscosity. The SBS modifiers added to bitumen form a physical network within it, enhancing the tendency of shear-thinning for SBS-modified binders. The high elasticity of SBS and the established SBS network within bitumen also contribute to a higher viscosity of

modified binders compared to pure ones.

Fig. 4.24 presents the dependence of viscosity on shear rate or frequency for V710 and VPMB at different ageing levels. For V710, a gradual transition from Newtonian to non-Newtonian fluid behavior is observed with increased ageing level. Ageing of bitumen results in increased molecular weights, the formation of functional groups, and a more complex bitumen micro-structure, all of which increase its non-Newtonian characteristic. The complex viscosity of VPMB at fresh state is higher than that of its corresponding base bitumen, V710. As ageing proceeds, the viscosity of VPMB gradually approaches that of V710, and a plateau at low frequencies like that in base bitumen occurs. This trend is largely due to the gradual degradation of SBS during the ageing process. At higher ageing levels when SBS is completely aged, the viscosity of SBS-modified bitumen is comparable to that of unmodified bitumen.

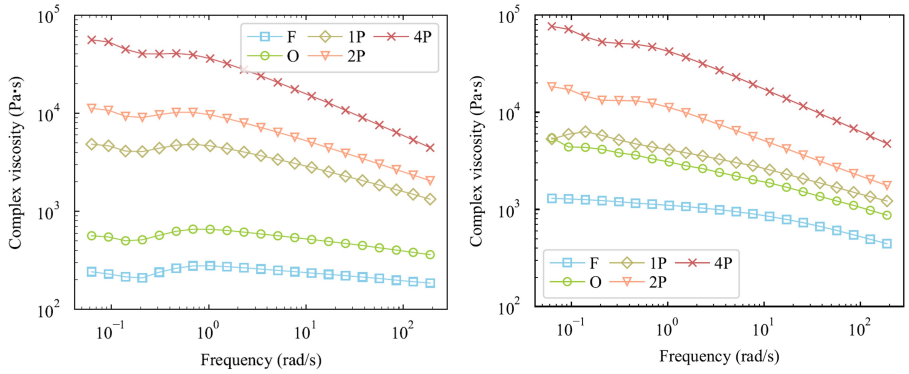

Figure 4.24 (a) Complex viscosity of V710 at different ageing states and at temperatures of 60 °C and (b) complex viscosity of VPMB changing with ageing levels at 60 °C.

The viscosity plateau observed at low frequencies is referred to as the zero shear viscosity (ZSV), a key indicator of the rutting resistance of bituminous materials (Cardone et al., 2014; Zeiada et al., 2022). To analyze the dependence of viscosity on shear rate and to determine ZSV values, viscosity models such as Cross, Carreau, and Carreau-Yasuda (Zeiada et al., 2022) are commonly used. These models demonstrate effective fitting of viscosity as a function of frequency and accurate estimation of ZSV values for unmodified binders, which typically show observable initial plateau followed by a shear-thinning stage in the plot of complex viscosity vs. frequency. However SBS-modified binders do not exhibit the plateau due to the shear-thinning behavior at very low frequencies, resulting from the elasticity of SBS and the formation of polymer network within bitumen. As a result, the prediction of ZSV values of modified binders based on frequency sweep tests can be inaccurate (Zeiada et al., 2022). In this work, the Cross model (Cross, 1965; Morea et al., 2010; Zeiada et al., 2022) was utilized to fit the dependence of viscosity on frequency considering its simplicity and high fitting quality. The model is expressed by the equation

$$|\eta^*(f)| = \frac{\eta_0 - \eta_\infty}{1 + (k_\eta f)^{m_\eta}} + \eta_\infty \tag{4.25}$$

where f is the frequency, $|\eta|^*$ is the complex viscosity, η_0 indicates ZSV, η_∞ represents

the limiting viscosity at infinite shear rate, which can be neglected at test temperatures due to its much smaller value compared to η_0, and k_η and m_η are fitting parameters. The fitting results at 60 °C are shown in Fig. 4.25. Specifically, it is important to interpret the ZSV values of two SBS-modified binders, particularly at their fresh state, with caution.

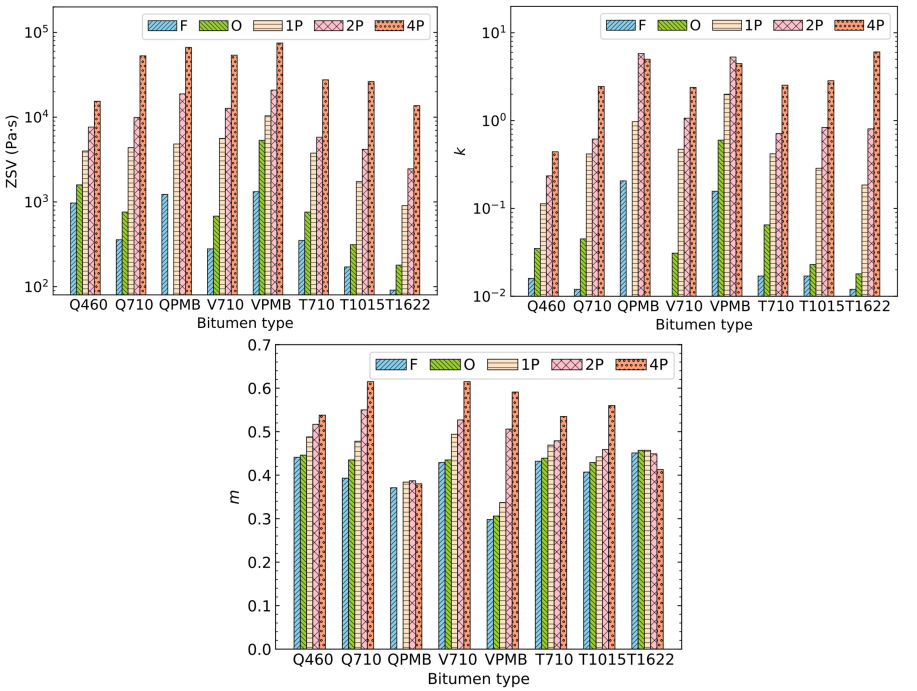

Figure 4.25 Parameters in the Cross model for all binder samples at 60 °C

As shown in Fig. 4.25, a higher penetration grade correlates with a lower zero shear viscosity, and SBS modification increases the viscosity, aligning with the general behavior of viscosity. Ageing increases the ZSV values through increasing the concentration of molecules with high molecular weights, as well as their polarity. The parameter k_η reveals a similar trend to ZSV concerning penetration grade and ageing level. This parameter, which can be interpreted as the longest rotational relaxation time in bituminous binders (Lemarchand et al., 2015), aligns with the Debye-Stokes-Einstein relationship, where viscosity is proportional to the rotational relaxation time. Therefore, a matching increasing trend between k_η and ZSV is observed. An exception is observed for the SBS-modified binders due to the presence of the polymeric network within binders. Additionally, in most cases, parameter m_η also increases with ageing.

The dependence of viscosity on temperature was then analyzed to gain a further understanding of viscosity behavior. Both apparent viscosity and complex viscosity were utilized to evaluate this relationship over a broader temperature range. According to the empirical Cox-Merz relationship (Cardone et al., 2014; Cox & Merz, 1958), it can be assumed that apparent viscosity is analogous to the complex dynamic viscosity at the frequency

equal to the specified shear rate used for measuring apparent viscosity, since both characterize the elastic and viscous response to shearing stress. By combining these two types of viscosity, the viscosity at temperatures ranging from 0 to 140 °C is plotted in Fig. 4.26. The apparent and complex viscosity exhibit comparable values at the same temperatures for both the neat and modified binders, in line with the Cox-Merz relationship. However, it is important to note that the Cox-Merz is inapplicable for SBS-modified binders with an SBS content larger than 4 wt%, due to the increased complexity of the micro-structure (Cardone et al., 2014; Partal et al., 1999). The viscosity trends of various binder types at temperatures ranging from 0 to 140 °C align with those observed at 60 °C, as displayed in Fig. 4.22. Notably, three bitumens from source T and two SBS-modified binders, compared to other types, exhibit a lower viscosity at lower temperatures and a higher viscosity at elevated temperatures. Furthermore, ageing results in increased viscosity at a wide range of temperatures.

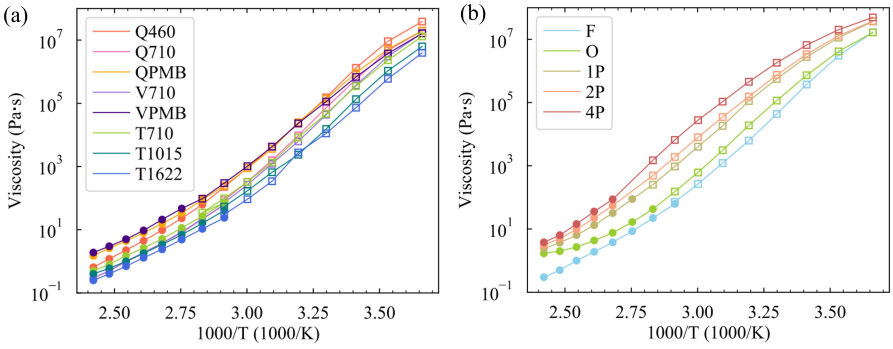

Figure 4.26 Viscosity as a function of the inverse of temperature for (a) all fresh binder types and (b) V710 at various ageing states. All viscosities were measured at a frequency or shear rate of 2.09 rad/s. Filled circles denote the apparent viscosity measured by Viscometer and open squares represent the complex viscosity determined using DSR.

To describe the dependence of viscosity on temperature, the Arrhenius equation can be utilized when the temperature is much higher than the glass transition temperature T_g:

$$\eta(T) = A_{\text{arr}} \exp\left(\frac{B_{\text{arr}}}{T}\right) \tag{4.26}$$

where T is the temperature, $A_{\text{arr}} = \eta_\infty$, namely, the viscosity at infinite temperature, and $B_{\text{arr}} = E_\eta / R$ with E_η denoting the activation energy of self viscosity and R indicating the universal gas constant. However, studies have shown that the viscosity of bitumen fails to follow precisely the Arrhenius equation, particularly at low temperatures and with the presence of polymer modifiers (Cardone et al., 2014; D. D. Li & Greenfield, 2014; Zhai & Salomon, 2005). Instead, the Vogel-Fulcher-Tammann (VFT), a modified form of the Arrhenius equation (Ferry, 1980), is widely used for materials that exhibit glass transition phenomena. The VFT equation is expressed as

$$\eta(T) = A_{\text{vft}} \exp\left(\frac{B_{\text{vft}}}{T - C_{\text{vft}}}\right) \tag{4.27}$$

where A_{vft} is the viscosity at infinite high temperature, B_{vft} is related to the activation energy of viscosity, and C_{vft} is the temperature at which the viscosity diverges. The B_{vft} is proportional to C_{vft} through the constant D_{vft}, which is known as the fragility index. By applying logarithmic scaling to both sides, the equation can be transformed into

$$\ln[\eta(T)] = A'_{vft} + \frac{B_{vft}}{T - C_{vft}} \tag{4.28}$$

. The VFT equation is suitable for the temperatures close to or higher than T_g (Garca-Coln et al., 1989). When T is much larger than C_{vft}, the VFT equation can be reduced to the Arrhenius equation. Both the Arrhenius equation and the VFT model were employed to evaluate the relationship between viscosity and temperature. The Arrhenius equation was applied at temperatures of 60 – 130 °C, and the VFT model was utilized for temperatures ranging from 20 to 130 °C. Only the viscosity measured at the frequency of 2.09 rad/s was used. The effect of shear rate on viscosity is described by the Cross model, as described in the previous section. All parameters in the Arrhenius equation and the VFT model are listed in Table 4.7.

The E_{arr} describes the activation energy required for molecules to escape from a "cage" into an adjoining "hole" (Bird et al., 2002), which depends on the molecular chain structure. Materials characterized by larger molecular size, more complex chain structure, and stronger intermolecular forces tend to exhibit a higher activation energy. As shown in Table 4.7, the E_{arr} values of softer bitumen are lower. The E_{arr} of various binders overall increases with ageing due to increased polarity and more complex structural configurations.

Table 4.7 shows an increase in D_{vft} with ageing. A lower D_{vft} indicates a greater deviation from the Arrhenius form. As shown in Fig. 4.26 (a), there is a non-linear dependency

Table 4.7 Parameters in the Arrhenius and VFT equations utilized to describe the dependence of viscosity at 2.09 rad/s on temperature. Samples without C_{vft} and D_{vft} values indicate that only the Arrhenius equation is used due to minimal fragility of those samples.

Samples	A_{arr}	E_{arr}	A_{vft}	C_{vft}	D_{vft}	Samples	A_{arr}	E_{arr}	A_{vft}	C_{vft}	D_{vft}
Q460_F	-31.3	104.7	-14.9	177.1	19.1	VPMB_F	-26.7	92.4	-12.5	175.5	17.5
Q460_O	-29.1	99.4	-12.8	189.8	15.2	VPMB_O	-30.5	87.6	-21.3	147.9	25.9
Q460_1P	-31.6	109.2	-17.6	146.0	32.9	VPMB_1P	-26.6	95.8	-13.2	126.7	36.4
Q460_2P	-32.4	113.3	-19.7	132.5	43.1	VPMB_2P	-32.0	113.5	/	/	/
Q460_4P	-32.5	115.0	-21.5	116.5	57.4	VPMB_4P	-32.5	118.4	/	/	/
Q710_F	-31.0	100.7	-14.1	191.1	14.7	T710_F	-28.4	93.6	-12.7	190.6	13.8
Q710_O	-27.5	92.8	-11.3	200.2	11.8	T710_O	-26.0	88.9	-10.8	195.1	12.2
Q710_1P	-33.2	113.4	-21.2	122.4	50.3	T710_1P	-30.4	105.4	-16.8	147.1	31.3
Q710_2P	-34.7	119.8	/	/	/	T710_2P	-30.0	105.4	-18.5	125.6	44.2
Q710_4P	-37.7	132.3	-55.5	/	/	T710_4P	-32.3	115.7	/	/	/
QPMB_F	-26.7	92.0	-11.5	190.6	13.7	T1015_F	-27.1	88.3	-11.5	196.2	11.5
QPMB_1P	-28.7	101.0	-15.9	146.9	30.3	T1015_O	-23.4	79.3	-8.6	219.1	7.4
QPMB_2P	-31.9	113.0	/	/	/	T1015_1P	-28.1	96.8	-13.3	174.9	18.5
QPMB_4P	-34.8	123.0	/	/	/	T1015_2P	-30.6	105.9	-18.6	130.7	41.0
V710_F	-30.0	97.7	-13.6	190.0	14.4	T1015_4P	-33.5	111.6	/	/	/
V710_O	-27.1	91.4	-11.8	195.8	12.7	T1622_F	-26.2	84.4	-11.8	197.1	11.3
V710_1P	-32.5	112.2	-20.2	127.3	46.1	T1622_O	-21.2	71.5	-7.4	227.6	5.8
V710_2P	-33.9	118.3	/	/	/	T1622_1P	-26.4	90.4	-12.4	178.5	16.4
V710_4P	-39.1	136.3	/	/	/	T1622_2P	-28.5	98.7	-15.2	154.0	26.3
						T1622_4P	-29.4	105.1	-20.5	102.6	65.6

of logarithmic viscosity on the inverse of temperature. A downward convex curve towards the lower right of the graph is observed for binders at fresh state. This deviation of viscosity to the Arrhenius form can be described as the fragility of viscosity (Zhai & Salomon, 2005). According to Angell (Angell, 1991), materials with strong intermolecular interactions exhibit stable microstructure and consistent properties during glass transition process, while fragile materials undergo significant variations when transitioning from liquid to glassy state. Therefore fragile liquids are likely to have larger configurational heat capacities. With increasing ageing, this curve gradually shifts upwards to a linear relationship. This shift is a consequence of the increased polarity and stiffness in bitumen, leading to a lower fragility.

4.5.5 Correlations among rheological properties

To study the correlations between various rheological indices, the Pearson correlation coefficients were calculated and the results are listed in Table 4.8.

Among the parameters determined based on frequency sweep (FS) tests, the two constants in the WLF equation, namely, C_1 and C_2, have a high correlation of 0.99. The WLF equation is derived based on the free volume theory. This theory assumes that free space/volume is required for all types of molecular motions beyond simple vibrational and rotational states. Molecules with more freedom of motion compared with solids can be shifted over a distance of macroscopic scale through holes or interstitial space, known as free volume. The temperature dependence of viscoelastic properties, characterized by the shift factor α_T, is related to the variation of fractional free volume (f^{free}) with temperature (Williams et al., 1955) as

$$\log\alpha_T = \frac{B}{2.303}\left(\frac{1}{f^{\text{free}}} - \frac{1}{f_g^{\text{free}}}\right) \tag{4.29}$$

where B is a constant and f_g^{free} is the fractional free volume at glass transition temperature. The f^{free} is linearly related to temperature as

$$f^{\text{free}} = f_g^{\text{free}} + \alpha_f(T - T_g) \tag{4.30}$$

where α_f is the thermal expansion coefficient. Combining Equations 4.29, 4.30, and 4.7 (the WLF equation), it can be seen that the ratio of C_1 to C_2 is proportional to the thermal expansion coefficient of the free volume. The strong correlation between C_1 and C_2 corroborates the linear relationship between them. The crossover frequency (f_c) is highly related to the Glover-Rowe parameter ($G-R$) (r=-0.97), C_1 (r=-0.90), and C_2 (r=-0.86). These high negative correlations suggest that f_c and $G-R$ depend on the thermodynamic properties of f_g^{free} and α_f. The r between crossover modulus (G_c^*) and rheological index (R_{rhe}) is -0.95, denoting an inverse relationship between them. The R_{rhe} has been shown to describe the shape of relaxation spectrum and its skewness (Christensen et al., 2017).

Parameters obtained from the LAS tests and the S-VECD model exhibit good correlations. The r between the peak shear stress during LAS tests ($\tau_{\max}$) and the complex modulus within the linear viscoelastic (LVE) range (G_{LVE}^*) is 0.99, implying that the maximum shear stress depends on the complex modulus within LVE range. The r of -0.98 between the two constants in the damage equation ($C(D)$), i.e., C_{D1} and C_{D2}, denotes a

Table 4.8 Pearson correlation between rheological indices. This table only lists the correlation coefficients < -0.7 or > 0.7 and p < 0.05. Indices with a superscript of 'L' denote that the values in the logarithmic scale were used to conduct the correlation analysis.

r	f_c^L	G_g^L	C_1	C_2	G_c^{*L}	GR^L	R_{rhe}	τ_{max}^L	G_{LVE}^{*L}	C_{D1}	C_{D2}	C_f	D_f	k_D	A_D^L	B_D	N_{f25}^L	N_{f50}^L	G_0^L	G_1^L	G_2^L	G_3^L	G_4^L	γ_1^L	γ_2^L	γ_3^L	γ_4^L	m_η	k_η	ZSV^L	A_{arr}	B_{arr}	A_{vft}	B_{vft}	C_{vft}
f_c	1.00																																		
G_g		1.00																																	
C_1	-0.90		1.00																																
C_2	-0.86		0.99	1.00																															
G_c^*	0.83				1.00																														
GR	-0.97		0.85	0.82	-0.77	1.00																													
R_{rhe}	-0.77	0.79			-0.95	0.73	1.00																												
τ_{max}	-0.79					0.84		1.00																											
G_{LVE}^*	-0.84		0.74	0.70		0.89		0.99	1.00																										
C_{D1}	-0.87		0.79	0.78	-0.72	0.89	0.70		0.77	1.00																									
C_{D2}	0.86		-0.76	-0.73	0.76	-0.90	-0.73		-0.75	-0.98	1.00																								
C_f												1.00																							
D_f	0.77					-0.79		-0.87	-0.89				1.00																						
k_D	-0.98		0.91	0.89	-0.84	0.95	0.78	0.72	0.79	0.92	-0.90		-0.73	1.00																					
A_D	-0.72				-0.87		0.79				-0.75			0.76	1.00																				
B_D	0.98		-0.92	-0.89	0.83	-0.95	-0.76	-0.74	-0.80	-0.86	0.84		0.76	-0.99	-0.73	1.00																			
N_{f25}												0.79					1.00																		
N_{f50}								-0.77	-0.76				0.91				0.78	1.00																	
G_0	-0.92		0.84	0.80		0.94		0.92	0.96	0.84	-0.83		-0.87	0.89		-0.90		-0.71	1.00																
G_1																				1.00															
G_2								0.82	0.83				-0.74						0.81		1.00														
G_3						0.71		0.88	0.89				-0.80					-0.72	0.88		0.97	1.00													
G_4	-0.83		0.77	0.73		0.86		0.94	0.96	0.77	-0.74		-0.87	0.79		-0.79		-0.74	0.98		0.90	0.95	1.00												
γ_1																								1.00											
γ_2								0.76	0.74														0.71	0.79	1.00										
γ_3						0.73		0.82	0.82										0.78				0.79		0.97	1.00									
γ_4	-0.81					0.86		0.88	0.89	0.71	-0.74			0.77		-0.78			0.88			0.74	0.85		0.85	0.94	1.00								
m_η																												1.00							
k_η	-0.96		0.82	0.79	-0.76	0.99	0.73	0.84	0.89	0.89	-0.89		-0.78	0.94		-0.93			0.93			0.71	0.86			0.74	0.85	1.00						
ZSV	-0.98		0.85	0.82	-0.79	0.98	0.77	0.81	0.86	0.90	-0.89		-0.79	0.96		-0.95			0.92				0.84				0.82	0.99	1.00						
A_{arr}	0.78		-0.76	-0.72		-0.72		-0.74	-0.75				0.77	-0.72		0.74			-0.79			-0.72	-0.79					-0.73	-0.75	1.00					
B_{arr}	-0.88		0.82	0.78		0.84		0.81	0.83	0.73			-0.82	0.83		-0.84			0.88			0.75	0.85				0.74	0.85	0.87	-0.98	1.00			
A_{vft}	0.89		-0.84	-0.82	0.72	-0.80				-0.74				-0.87		0.87			-0.78				-0.71					-0.82	-0.87	0.87	-0.92	1.00		
B_{vft}	-0.88		0.82	0.80	-0.75	0.78	0.72			0.73				0.86		-0.86			0.74									0.80	0.86	-0.80	0.86	-0.99	1.00	
C_{vft}	0.91		-0.82	-0.81	0.78	-0.83	-0.76			-0.76	0.73			-0.88		0.88			-0.78									-0.85	-0.90	0.81	-0.88	0.99	-0.99	1.00

linear relationship between them. The fatigue-related parameter k_D is related to the exponential fatigue constant (B_D) by a r value of -0.99. The strong correlations between the LAS-related parameters of k_D and B_D and the FS-based parameters of f_c, C_1, and $G-R$ indicate that these fatigue-related parameters are highly related to the undamaged (LVE) viscoelastic parameters. These undamaged properties are linked to the thermodynamic properties of bituminous binders, including f_g^{free} and α_f.

However, damage intensity at failure point (D_f) is not closely linked to the parameters obtained from the FS tests. Therefore, the pre-factor fatigue constant (A_D), as a function of C_{D1}, C_{D2}, k_D, and D_f, is associated with both LVE performance and damage accumulation process. The r between D_f and fatigue life at 5% strain (N_{f50}) is 0.91, revealing that damage intensity at the defined failure point reflects more the fatigue life at a higher strain level of 5%. The correlation between B_D and f_c is 0.98. This high correlation offers an approach to use the inverse of the slope of the storage modulus versus frequency at a log-log plot measured within the LVE range to calculate the crossover frequency of bituminous binders.

Table 4.8 also presents the Pearson correlation coefficients between various relaxation parameters. Highest correlation is revealed between relaxation strengths or relaxation times next to each other. As an example, G_0 (corresponding to the relaxation strength for the relaxation mode with pseudo infinite relaxation time) is related to G_4 (for the fourth relaxation mode), G_3 (for the third relaxation mode), and G_2 (for the second relaxation mode) with the r of 0.98, 0.88, and 0.81, respectively. This can be explained through the bitumen composition and its microstructure. Bitumen components with similar molecular structures tend to be placed more closely to each other and have more interactions, and thus their responses to loading depend on each other. Molecules situated at longer distances essentially interact less with the central structure, leading to a lower correlation.

The parameter G_0 is related to f_c and $G-R$ with r values of -0.92 and 0.94, respectively. γ_4 (relaxation time for the fourth mode) also shows correlations with f_c and $G-R$, denoted by r values of -0.81 and 0.86, respectively. It can be derived that f_c and $G-R$ are mainly linked to the relaxation strength with the longest relaxation time. The longest relaxation time or the relaxation strength corresponding to longest relaxation time captures the fundamental physicochemical properties and the morphological changes of asphaltene microstructure (F. Li et al., 2022). Furthermore, G_0, G_4, and γ_4 exhibit the strongest correlations with τ_{max}, G^*_{LVE}, C_{D1}, C_{D2}, and k_D obtained from LAS test. This is consistent with the aforementioned discussion since these LAS-based parameters are also linked to f_c and $G-R$, which correlates well with G_0, G_4, and γ_4.

The zero shear viscosity at 60 °C (ZSV) is strongly related to the constant k_η in the Cross model describing the dependence of viscosity on shear frequency. According to this model, the k_η can be regarded as the longest rotational relaxation time (Lemarchand et al., 2015). The Pearson analysis supports this explanation with a r value of 0.93 between k_η and G_0 and a value of 0.85 between k_η and γ_4. Many parameters derived from the FS and LAS tests are associated with the ZSV value. This value is related to f_c, $G-R$, C_{D1}, and B_D with respective r values of -0.98, 0.98, 0.90, and 0.95. Parameters in the Arrhenius equation and the VFT model that describe the dependence of viscosity on temperature are highly related to each other, indicating their linear relationship with each other. The correlation coefficients between parameters A_{arr}, B_{arr}, A_{vft}, B_{vft}, and C_{vft} based on the

viscosity and most of the parameters obtained from FS and LAS tests are larger than 0.7–0.8 but smaller than 0.9. This suggests that these parameters are largely linearly related to each other while other factors may also contribute to the correlation.

Parameters exhibiting weaker correlations with the other parameters include glassy modulus (G_g), material integrity at failure point (C_f), fatigue life at 2.5% strain level (N_{f25}), relaxation strength for the first relaxation mode (G_1), relaxation time for the first relaxation mode (γ_1), and viscosity-based parameter m_η, as indicated in Table 4.8. The G_g denotes the complex modulus at extremely high frequencies or low temperatures. According to the CAM model, the value of G_g is directly proportional to the overall magnitude of the relaxation spectrum (Christensen et al., 2017). Among all the calculated parameters, only R_{rhe} is related to G_g with a coefficient of 0.79. R_{rhe} is considered to be linked to the shape of relaxation spectrum. Other calculated parameters mostly describe the rheological properties at higher temperatures, therefore exhibit much lower correlation (<0.7). The C_f and N_{f25} are fatigue-related parameters. The G_1 and γ_1 are the highest relaxation strength and shortest relaxation time. These two relaxation parameters are not representative of the whole relaxation spectrum and are not correlated to the longest relaxation time, which is found to characterize the fundamental properties of bitumen. Therefore, less correlation is observed. It should be noted that the correlation can be affected by the repeatability of the rheological tests and fitting quality of the applied models.

As shown in Table 4.8, most of the parameters obtained from the rheological tests are correlated to each other with coefficients higher than 0.7 but less than 0.9. This means that part of the information within these parameters is linearly correlated with other rheological properties. To gain a full understanding of these rheological phenomena, it is essential to consider multiple factors together. In this context, the canonical correlation analysis (CCA) is utilized to further analyze the relationship between different rheological tests.

To perform the canonical correlation analysis, for each variable set, several parameters are specifically selected to prevent the presence of parameters with high correlation (r>0.9). This is to avoid multicollinearity, which can significantly affect the reliability and interpretation of the results. Specifically, for the FS test, G_g, R_{rhe}, $G-R$, and C_1 were selected. The τ_{max}, C_{D1}, A_D, and D_f were used as the variable sets of LAS test. As for relaxation test, G_1, G_2, G_3, and G_4 were used. The selected parameters representative of viscosity are m_η, k_η, B_{arr}, and B_{vft}.

Table 4.9 exhibits the canonical correlations of the first two canonical variables between different variable sets. As explained in Section 4.3.6, CCA results help identify the linear combinations from each variable set that exhibit the strongest correlations with one another. Notably, Table 4.9 illustrates robust correlations exceeding 0.97 among various rheological variable sets. These high correlations mean that the variable sets derived from different rheological tests share a robust linear relationship through optimized canonical variables. In other words, two variable sets share substantial common information. Consequently, one variable set can be accurately explained or predicted by the other variable set. In contrast to the Pearson correlations among all variables listed in Table 4.8, the correlations among diverse rheological variable sets are significantly higher. This highlights the notion that a single parameter cannot fully enclose the comprehensive information from the test. Instead, a combination of all parameters obtained from this test

provides a more holistic comprehension of the bitumen samples. The strong correlations between all the rheological variable sets corroborate with the initial assumption proposed in the introduction section this chapter, i.e., although various tests measure the bitumen samples from distinct perspectives, they are essentially characterizing the same samples. This concept is better elucidated in the upcoming discussion on the chemical-rheological relationships.

Table 4.9 Canonical correlations of the first two canonical functions (CC_1, CC_2) for different variable sets.

	CC_1						CC_2							
Tests	FTIR	GPC	DSC	FS	LAS	Re	Vis	FTIR	GPC	DSC	FS	LAS	Re	Vis
FTIR	1.00							1.00						
GPC	0.98	1.00						0.97	1.00					
DSC	0.96	0.93	1.00					0.95	0.87	1.00				
FS	0.99	0.91	0.93	1.00				0.96	0.85	0.76	1.00			
LAS	0.99	0.89	0.93	1.00	1.00			0.93	0.74	0.77	0.90	1.00		
Re	0.98	0.85	0.90	0.98	0.99	1.00		0.87	0.64	0.63	0.92	0.90	1.00	
Vis	0.99	0.91	0.93	0.99	0.97	0.98	1.00	0.95	0.81	0.81	0.84	0.87	0.81	1.00

4.6 Relationship between physico-chemical and rheological properties

To characterize the relationships between physicochemical and rheological properties, the Pearson correlation analysis was performed among parameters derived from FTIR and DSR test results. Table 4.10 presents the Pearson correlations between the ageing index at 1700 cm^{-1} (carbonyl index) and all the rheological properties. These values demonstrate the extent to which the rheological indices of binders are linearly influenced by their long-term ageing. The B_D and f_c have strongest correlations with the carbonyl index, followed by k_D, ZSV, and $G-R$. The high correlation of these indices highlights their efficacy in evaluating the degree of bitumen ageing. Most rheological parameters are related to the carbonyl index by r values of 0.7–0.9, suggesting that these parameters are largely affected by the carbonyl index, while other factors also play a role. The r between the relaxation strength with the longest relaxation time (G_0) and the carbonyl index is 0.85. The carbonyl index is also related to G_4 and γ_4 with r values of 0.76 and 0.75, respectively. All other parameters derived from relaxation tests show a weaker link to the carbonyl index, with $r < 0.7$. The decreased r value suggests a reduced correlation between the carbonyl-generated ageing process and the parameters associated with faster relaxation modes. This observation indicates that long-term oxidative ageing mainly occurs in the stiffer molecular structures such as aromatic rings (Petersen, 2009) that relax much slower. The correlations between other peak indices obtained from FTIR tests and rheological properties are less than 0.7, except for G_g. This parameter is related to peaks indices at 3014, 2850, 724, and 695 cm^{-1} by r values of -0.75, -0.79, -0.76, and 0.71. The first three peaks are indicative of aliphatic structures while the last one describes the styrene in SBS modifiers.

The Pearson correlation coefficients between parameters derived from GPC and rheological tests were calculated. The r between G_g and M_p (peak molecular size) is -0.72,

Table 4.10 Pearson correlation coefficients between ageing index of 1700 cm^{-1} and all the rheological properties. Indices with a superscript of 'L' refers to the values in the logarithmic scale.

Indices	f_c^L	G_g^L	C_1	C_2	G_c^{*L}	$G-R^L$	R_{rhe}	τ_{max}^L	G_{LVE}^{*L}	C_{D1}	C_{D2}	C_f
r	-0.95	<0.7	0.88	0.84	-0.80	0.90	0.72	0.71	0.75	0.76	-0.75	<0.7
Indices	D_f	k_D	A_D	B_D	N_{f25}^L	N_{f50}^L	G_0^L	G_1^L	G_2^L	G_3^L	G_4^L	γ_1^L
r	-0.72	0.93	<0.7	-0.96	<0.7	<0.7	0.85	<0.7	<0.7	<0.7	0.76	<0.7
Indices	γ_2^L	γ_3^L	γ_4^L	m_η	k_η	ZSV^L	A_{arr}	B_{arr}	A_{vft}	B_{vft}	C_{vft}	
r	<0.7	<0.7	0.75	<0.7	0.88	0.91	-0.80	0.87	-0.89	0.87	-0.89	

and that between R_{rhe} and S_{MMS} (medium molecular size) is -0.71. Beyond these, none of the absolute r values exceed 0.7, suggesting that neither average molecular weight nor fractional areas in chromatograms strongly correlate with specific rheological properties. Additionally, all correlation coefficients between the parameters obtained from DSC tests and the rheological properties are below 0.7. Thermal properties measured by DSC tests are either linked to the glass transition or to the crystalline fractions. Their dependence on the chemical composition and ageing process of bitumen is complex. Therefore, the correlation between two specific parameters is insufficient to comprehensively describe the correlations between thermal and rheological properties. Moreover, there is no standard approach to calculate these thermal properties, as discussed in Section 4.4.3, which may affect the accuracy of the calculated parameters.

The CCA was conducted to further understand the relationship between physico-chemical and rheological properties. As shown in Table 4.9, the r values between the first pair of canonical variables (CCX_1 and CCY_1) derived from FTIR and rheological tests are 0.96 – 0.99. Peak indices calculated based on FTIR spectra are indicative of the aliphatic and aromatic structures, as well as various polar functional groups. These parameters collectively provide a more comprehensive characterization of the chemical composition and microstructure of bitumen. Consequently, they can accurately describe the various thermal and rheological properties, which inherently depend on the chemical composition of bitumen. Table 4.11 lists the structure coefficients for the first two pairs of canonical variables in the CCA results between FTIR and rheological tests.

As shown in Table 4.9, spectral parameters effectively describe a significant amount of variance demonstrated by variables determined based on FS tests. The first canonical function leads to a r of 0.99 between the CCX_1 and CCY_1. The corresponding structure coefficients listed in Table 4.11 show that peak variables 3014 (-0.53), 2910 (-0.71), 2850 (-0.58), and 1700 (0.91) are strongly linked to CCX_1. These peaks are representative of the aliphatic structure and carbonyl functional groups, with the former decreasing and the latter increasing with ageing. For parameters obtained from the FS tests, glassy modulus (G_g), WLF constant (C_1), Glover-Rowe parameter ($G-R$), and rheological index (R_{rhe}) are linked to CCY_1 with coefficients of 0.62, 0.87, 0.93, and 0.91, respectively. These high coefficients suggest that C_1, $G-R$, and R_{rhe} are strongly correlated to the oxidative reactions of functional groups and the dehydrogenation of aliphatic chains. In the second canonical function, peak indices of 3014 (-0.47), 814 (-0.52), and 724 (-0.40) are closely linked to CCX_2. These peaks signify the presence of aromatic C-H groups and long aliphatic

Table 4.11 Structure coefficients for the first two pairs of canonical variables (CCX_1 and CCY_1, CCX_2 and CCY_2) derived from the CCA analysis of FTIR (X) and rheological (Y) datasets, including FS, LAS, Relaxation, and Viscosity.

FTIR	CCX_1	CCX_2	FTIR	CCX_1	CCX_2	FTIR	CCX_1	CCX_2	FTIR	CCX_1	CCX_2
3340 (-OH)	0.43	-0.04	3340	0.32	0.28	3340	0.35	-0.03	3340	-0.34	0.22
3014 (-CH)	-0.53	-0.47	3014	-0.49	0.21	3014	-0.18	0.12	3014	0.57	0.42
2910 (-CH_2)	-0.71	0.13	2910	-0.73	0.16	2910	-0.65	-0.31	2910	0.54	-0.42
2850 (-CH_2)	-0.58	-0.25	2850	-0.50	0.20	2850	-0.32	-0.27	2850	0.46	0.00
1700 (-C=O)	0.91	-0.24	1700	0.84	0.46	1700	0.87	-0.32	1700	-0.85	0.47
1600 (C=C)	0.48	-0.21	1600	0.39	0.37	1600	0.46	0.06	1600	-0.31	0.56
1030 (-S=O)	0.49	-0.28	1030	0.40	0.64	1030	0.61	-0.46	1030	-0.54	0.29
864 (-CH)	-0.34	-0.37	864	-0.14	-0.55	864	-0.09	0.82	864	0.57	0.54
814 (-CH)	-0.34	-0.52	814	-0.06	-0.76	814	0.01	0.89	814	0.56	0.57
743 (-CH)	0.13	0.26	743	0.08	-0.22	743	-0.07	0.38	743	0.00	0.13
724 (-CH_2)	-0.44	-0.40	724	-0.33	0.20	724	-0.12	-0.27	724	0.34	0.12
FS	CCY_1	CCY_2	LAS	CCY_1	CCY_2	Re.	CCY_1	CCY_2	Vis.	CCY_1	CCY_2
G_g	0.62	0.52	τ_{max}	0.78	0.01	G_1	0.22	0.93	B_{arr}	-0.66	0.73
C_1	0.87	-0.36	C_{D1}	0.98	-0.07	G_2	0.77	0.56	B_{vft}	-0.81	0.38
$G-R$	0.93	-0.31	D_f	-0.78	0.02	G_3	0.85	0.38	m_η	-0.09	0.00
R_{rhe}	0.91	0.41	A_D	0.66	0.52	G_4	0.97	0.21	k_η	-0.96	0.14

chains -$(CH_2)_n$. Meanwhile, the G_g, C_1, $G-R$, and R_{rhe} relate to CCY_2 with respective coefficients of 0.52, -0.36, -0.31, and 0.41. This means that $G-R$ and C_1 are positively related to these chemical components while R_{rhe} and G_g exhibit negative relationships. Both $G-R$ and R_{rhe} tend to increase as ageing proceeds. Their contrasting correlations with CCY_2 underscore the varied impact of this chemical information on their respective properties.

In the first canonical function derived from CCA analysis on FTIR- and LAS- based parameters, the spectral indices with relatively high structure coefficients involve 3014 (-0.49), 2910 (-0.73), 2850 (-0.50), 1700 (0.84), and 1030 (-0.40). The structure coefficients for peak shear stress (τ_{max}), constant in damage equation (C_{D1}), damage intensity at failure point (D_f), and pre-factor fatigue constant (A_D) are 0.78, 0.98, -0.78, and 0.66, respectively. Analysis of these structure coefficients suggests that these fatigue-related parameters are dominantly affected by carbonyl index, while the changes in aliphatic chains also reflect the ageing-caused degradation in bitumen. Notably, sulfoxide index shows contrasting effects compared to the carbonyl index, indicating their varied effects on fatigue performance. The second canonical function shows a strong correlation with A_D obtained from LAS tests and spectral indices of 1700 (0.46), 1030 (0.64), 864 (-0.55), and 814 (-0.76). This suggests that A_D are affected by carbonyl and sulfoxide functional groups, as well as the aromatic C-H groups.

The CCA results between FTIR and relaxation parameters show that the correlation between the first canonical variable (CCY_1) and parameters from the relaxation tests are $G_4 > G_3 > G_2 > G_1$. Conversely, for the second canonical variable, the order of the structure coefficients is $G_4 < G_3 < G_2 < G_1$. The first canonical variable for FTIR (CCX_1) depends on indices of 2910 (-0.65), 1700 (0.87), 1600 (0.46), 1030 (0.61), representing functional groups, aromatic rings, and aliphatic chains. The second canonical variable is corre-

Table 4.12 Structure coefficients for the first two pairs of canonical variables, derived from the CCA analysis of GPC (X) and rheological (Y) datasets, i.e., FS, LAS, Relaxation, and Viscosity.

GPC	CCX_1	CCX_2	GPC	CCX_1	CCX_2	GPC	CCX_1	CCX_2	GPC	CCX_1	CCX_2
M_w	-0.05	0.14	M_w	-0.09	-0.41	M_w	-0.10	0.22	M_w	0.18	-0.33
M_n	0.47	-0.21	M_n	0.25	0.53	M_n	0.24	-0.07	M_n	0.67	-0.21
M_p	-0.38	0.75	M_p	-0.02	-0.63	M_p	-0.12	0.95	M_p	-0.45	0.33
PDI	0.50	-0.30	PDI	0.28	0.64	PDI	0.30	-0.20	PDI	0.55	-0.04
S_{LMS}	0.55	0.06	S_{LMS}	0.41	-0.57	S_{LMS}	0.47	0.02	S_{LMS}	0.62	0.02
S_{MMS}	-0.58	0.73	S_{MMS}	-0.11	-0.09	S_{MMS}	-0.24	0.74	S_{MMS}	-0.76	0.41
FS	CCY_1	CCY_2	LAS	CCY_1	CCY_2	Re.	CCY_1	CCY_2	Vis.	CCY_1	CCY_2
G_g	0.67	-0.68	τ_{max}	0.92	-0.32	G_1	0.32	0.92	B_{arr}	0.35	0.88
G_1	0.63	0.37	C_{D1}	0.91	0.40	G_2	0.75	0.55	B_{vft}	0.53	0.57
$G-R$	0.92	0.32	D_f	-0.85	0.18	G_3	0.84	0.47	m_η	-0.19	-0.01
R_{rhe}	0.84	-0.36	A_D	0.56	0.23	G_4	0.93	0.32	k_η	0.91	0.40

lated with indices of 2910 (-0.31), 1030 (-0.46), 864 (0.82), 814 (0.89), 743 (0.38), which represent mainly aromatic C-H groups and polar functional groups. These correlations demonstrate that slower relaxation modes are mostly affected by polar functional groups generated by oxidative reactions, while faster modes are dominated by the changes in aromatic ring structures during the ageing process.

In the context of the relationship between FTIR and viscosity parameters, CCX_1 is influenced by indices of 3014 (0.57), 2910 (0.54), 1700 (-0.95), 1030 (-0.54), 864 (0.57), and 814 (0.56). The CCY_1 correlates with B_{arr}, B_{vft}, and k_η with the coefficients of -0.66, -0.81, and -0.96, respectively. This indicates the significant effects of carbonyl index on the evolution of viscosity with ageing process.

The CCA results between FTIR and all rheological show that, in most cases, the first canonical variable for FTIR is primarily related to the aliphatic chains, carbonyl functional groups, and aromatic rings. Among all the rheological variables used, $G-R$, C_{D1}, G_1, and k_η exhibit the strongest correlations with the first set of canonical variables. Their behavior is essentially dependent on ageing process, which can be more comprehensively described by considering both the formation of polar functional groups and the changes in aliphatic groups. The second canonical variable is mainly associated with the aromatic C-H groups. A higher aromatic C-H content suggests more independent aromatics rings that are not fused with each other. This higher fraction of aromatic C-H groups is positively linked to C_{D1}, $G-R$, and G_1, and is negatively related to G_g and A_D. Therefore, these parameters depend more on the aromatic structures instead of the formation of polar functional groups.

The structure coefficients resulting from the CCA analysis of GPC and rheological datasets are listed in Table 4.12. Among the six selected GPC parameters, PDI, S_{LMS}, and S_{MMS} are the most significant contributors to the linear combination of viscoelastic parameters, especially $G-R$ and R_{rhe}. This verifies that $G-R$ and R_{rhe} are mainly affected by asphaltens, resins, and aromatics, along with the width of molecular size distributions. Parameters obtained from fatigue tests are strongly related to the linear combination of S_{LMS}, PDI, and M_n, highlighting the importance of asphaltene content, molecular weight distribution shape, and presence of smaller molecules in determining fatigue

performance of bitumen. Additionally, the linear combination of PDI, S_{LMS}, and S_{MMS} also shows a robust correlation with the relaxation strengths at longer relaxation times. The lower structure coefficient for the strengths at shorter relaxation times indicates that these GPC parameters cannot reveal effectively the microstructure with short relaxation time. All the utilized GPC parameters are closely linked to viscosity-related parameters, among which the structure coefficients of k_η is the largest (0.91).

The canonical correlations between the first set of canonical variables derived from DSC and rheological tests range between 0.90 and 0.93, slightly lower than that between FTIR and rheological tests. This difference can be attributed to the fewer thermal properties derived from DSC tests, coupled with uncertainties in both calculating and interpreting the underlying mechanisms of these thermal properties. Despite the relatively lower canonical correlations observed for DSC, they remain sufficiently high to indicate the linear correlation between DSC and rheological tests. Consequently, when considering various parameters together, CCA offers a more thorough understanding of the bitumen properties as characterized by specific tests.

4.7 Summary

This chapter investigated the physicochemical and rheological properties of bituminous binders from diverse crude oil sources, with different penetration grades, and subjected to SBS modifications. The effects of ageing on these properties were elucidated. In this chapter, we attempted to answer the following question: Can diverse physico-chemical and rheological tests, although originating from different viewpoints, uncover consistent variations or insights about binders, such that the findings of one test can predict the results of another? In this context, we could provide a comprehensive evaluation of bitumen properties without conducting multiple complex tests. To address this question, the relationships between various physicochemical tests, those between different rheological tests, and the physicochemical-rheological relationships were analyzed using the Pearson correlation and canonical correlation analysis.

The FTIR, GPC, and DSC tests were utilized to characterize the chemical composition, molecular weight distribution, and thermal properties of bitumen. Peak indices describing aliphaticity, aromaticity, heteroatom-based functionality, and oxygenation of bitumen components were derived based on FTIR tests. GPC data reveal the various types of average molecular weight and fractional areas with different molecular weight. Through DSC tests, the glass transition temperature as well as crystallization-related enthalpies and temperatures were obtained. Rheological tests were performed to evaluate the bitumen properties involving the stiffness, crack resistance, fatigue life, relaxation at low temperatures, and viscosity.

Penetration grade significantly affects bitumen properties. A higher T_{g} is observed for bitumen with lower penetration grade. Softer bitumen also presents smaller LMS area and larger SMS area. Bitumen of higher penetration grade is softer with lower complex modulus and higher phase angle. Higher penetration grade leads to an increased crossover frequency, a lower crossover modulus, and a lower $G-R$ value while the R_{rhe} is less varied. Based on the fatigue test, a slower damage evolution and a higher fatigue life are observed from softer bitumen. Relaxation tests show that bitumen with higher penetration grade relaxes faster and has a lower relaxation strength. The viscosity of softer

bitumen, as well as its activation energy, is also lower.

Binders derived from three sources present different chemical, physical, and mechanical performance. Fresh binders from three sources display comparable sulfoxide indices. After long-term ageing, binders from source Q and V demonstrate a smaller sulfoxide index and a larger carbonyl index than T-sourced binders. Similar weight distribution width and shape are obtained for bitumen from the same sources, indicating their similar molecule types. The crystallization enthalpy of bitumen derived from source T is less than that from source V and Q. The fresh T710 and V710 exhibit a reduced complex modulus and an elevated phase angle compared to Q710. A relative lower $G-R$ value is obtained for T710, and other parameters including crossover frequency, crossover modulus, and rheological index are similar for Q710, V710, and T710. Compared to penetration grade, crude oil source exerts more influence on the fatigue performance since bitumen from same source displays similar fatigue-related parameter values. Among three sources, source T reveals the best fatigue resistance. Bitumen from source T also displays a higher fragility as revealed by the dependence of viscosity on temperature.

Ageing causes fundamental changes in the chemical composition of bitumen, which results in the degradation of bitumen properties. The decreased indices for peaks related to -CH_3, -CH_2 and aromatic C-H bonds and the increased indices for polar functional groups and aromatic C=C bonds reveal the aromatic condensation and increase in polar functional groups for bitumen during oxidative ageing process. Ageing also leads to increased LMS fraction, lower MMS fraction, and stable SMS fraction. The higher complex modulus, lower phase angle, lower crossover frequency, lower crossover modulus, higher R_{rhe}, larger A_{D}, smaller B_{D}, and lower fatigue life all indicate the hardening and degradation of bitumen due to the oxidative ageing process. With higher ageing levels, both the relaxation time and viscosity increase, and bitumen becomes less fragile.

The addition of SBS can significantly increase bitumen properties. Z+1 average molecular weight characterizes well the presence of SBS. Compared to base bitumen, the T_{g} of PMB is higher. SBS modification leads to a plateau region in master curves of phase angle at frequencies of 10^{-1} – 10^{-3} Hz due to the presence of the polymeric network structure. Bitumen modified by SBS exhibits a flatter damage characteristic curve, and a higher resistance to damage. Adding SBS to bitumen leads to an increased relaxation time. PMBs present a non-Newtonian shear-thinning viscosity at a wide range of temperatures. The ageing process of bitumen can be slowed down by the added SBS as noted by the slower increase in $G-R$ compared to base bitumen. After short-term ageing, the plateau in the master curves of phase angle disappears. At higher ageing levels, SBS is completely aged. Consequently, the viscosity of SBS-modified bitumen is comparable to that of pure bitumen.

Among all the rheological indices, the f_{c}, C_1, C_2, and $G-R$ derived from the frequency test, the k_{D}, B_{D}, C_{D1}, and C_{D2} based on the LAS test, the G_0, G_4, and γ_4 obtained from the relaxation test, and the k_η, ZSV, A_{vft}, B_{vft} and C_{vft} calculated based on viscosity are well correlated to each other. These parameters are theoretically linked to the fractional free volume, thermal expansion coefficient, and the relaxation strength at the longest relaxation time. They also show highest correlation with carbonyl index. The G_{c}^* is significantly related to R_{rhe}, and has the highest correlation with the A_{D} (the parameter in the fatigue equation). R_{rhe} explains both the shape of master curve and relaxation spectrum, sug-

gesting the fatigue is not only linked to the properties within LVE range, but to the overall properties of bitumen. Other parameters and indices have lower correlations with each other and with carbonyl index, indicating a more complex relationship which requires more comprehensive analysis.

The CCA results shows that the variable sets derived from chemical, physical, and rheological tests are significantly linearly correlated to each other. This implies that they share a substantial amount of common variance, and hence variables in one set can be largely described by the those in the other set. Notably, FTIR provides the most comprehensive characterization of bituminous binders due to the larger number of variables it yields. These variables elucidate the contents of aliphatic groups, aromatic components, and functional groups, as well as their structures. According to the CCA results, the -CH_2, -CH_3, and -CH in partly substituted aromatic rings, as well as alkyl chains, are the main chemical groups informative of the molecular weight distribution. The crystallization primarily depends on the aliphatic groups, especially the content of the methyl group. The $G-R$, R_{rhe}, C_1, C_{D1}, G_4, and k_η depend on the combination of the aliphatic compounds and polar functional groups. This means that other rheological properties highly related to these variables (through Pearson coefficients) are also linked to the aliphatic compounds and polar functional groups, including, f_c, C_2, G_c^*, k_{D}, B_{D}, G_0, γ_4, and ZSV. The dependence of fatigue-related parameters on chemical components are more complex. Basically, they can be affected by both functional groups and aromatic structures. In contrast, the parameters derived from GPC and DSC tests offer less insight into rheological properties. For GPC data, a linear combination of molecular weight distribution shape and fractional areas is required to adequately describe rheological properties, particularly for $G-R$, $\tau_{\max}$, G_4, and k_η.

References

Airey, G. D. (2003). Rheological properties of styrene butadiene styrene polymer modified road bitumens. *Fuel, 82*(14), 1709–1719.

Ameri, M., Nowbakht, S., Molayem, M., & Mirabimoghaddam, M. H. (2016). A study on fatigue modeling of hot mix asphalt mixtures based on the viscoelastic continuum damage properties of asphalt binder. *Construction and Building Materials, 106*, 243–252.

Angell, C. (1991). Relaxation in liquids, polymers and plastic crystals—strong/fragile patterns and problems. *Journal of Non-Crystalline Solids, 131*, 13–31.

Apeagyei, A. K., Grenfell, J. R. A., & Airey, G. D. (2014). Moisture-induced strength degradation of aggregate-asphalt mastic bonds. *Road Materials and Pavement Design, 15*, 239–262.

Apostolidis, P., Elwardany, M., Porot, L., Vansteenkiste, S., & Chailleux, E. (2021). Glass transitions in bituminous binders. *Materials and Structures, 54*(3), 132.

Asemani, M., & Rabbani, A. R. (2020). Detailed FTIR spectroscopy characterization of crude oil extracted asphaltenes: Curve resolve of overlapping bands. *Journal of Petroleum Science and Engineering, 185*, 106618.

Behzadfar, E., & Hatzikiriakos, S. G. (2013). Viscoelastic properties and constitutive modelling of bitumen. *Fuel, 108*, 391–399.

Bird, R. B., Stewart, W. E., & Lightfoot, E. N. (2002). Transport phenomena. *John Wiley and Sons: New York*.

Buenrostro-Gonzalez, E., Andersen, S. I., Garcia-Martinez, J., & Lira-Galeana, C. (2002). Solubility/molecular structure relationships of asphaltenes in polar and nonpolar media. *Energy & Fuels*, *16*(3), 732–741.

Cao, W., Mohammad, L. N., & Barghabany, P. (2018). Use of viscoelastic continuum damage theory to correlate fatigue resistance of asphalt binders and mixtures. *International Journal of Geomechanics*, *18*(11), 04018151.

Cappello, M., Filippi, S., Hung, Y., Losa, M., & Polacco, G. (2021). Apparent molecular weight distributions for investigating aging in polymer-modified bitumen. *Advances in Polymer Technology*, *2021*, 1–14.

Cardone, F., Ferrotti, G., Frigio, F., & Canestrari, F. (2014). Influence of polymer modification on asphalt binder dynamic and steady flow viscosities. *Construction and Building Materials*, *71*, 435–443.

Castro, L. V., & Vazquez, F. (2009). Fractionation and characterization of mexican crude oils. *Energy & Fuels*, *23*(3), 1603–1609.

Christensen, D. W., & Anderson, D. A. (1992). Interpretation of dynamic mechanical test data for paving grade asphalt cements (with discussion). *Journal of the Association of asphalt paving technologists*, *61*.

Christensen, D. W., Anderson, D. A., & Rowe, G. M. (2017). Relaxation spectra of asphalt binders and the Christensen–Anderson rheological model. *Road Materials and Pavement Design*, *18*(sup1), 382–403.

Claudy, P., Letoffe, J. M., King, G. N., Planche, J. P., & Brule, B. (1991). Characterization of paving asphalts by differential scanning calorimetry. *Fuel Science & Technology International*, *9*(1), 71–92.

Corbett, L. W. (1969). Composition of asphalt based on generic fractionation, using solvent deasphaltening, elution-adsorption chromatography, and densimetric characterization. *Analytical Chemistry*, *41*(4), 576–579.

Cox, W., & Merz, E. (1958). Correlation of dynamic and steady flow viscosities. *Journal of Polymer Science*, *28*(118), 619–622.

Creek, J. L. (2005). Freedom of action in the state of asphaltenes: Escape from conventional wisdom. *Energy & fuels*, *19*(4), 1212–1224.

Cross, M. M. (1965). Rheology of non-Newtonian fluids: A new flow equation for pseudoplastic systems. *Journal of Colloid Science*, *20*(5), 417–437.

De Visscher, J., Soenen, H., Vanelstraete, A., & Redelius, P. (2004). A comparison of the zero shear viscosity from oscillation tests and the repeated creep test. *Proceedings of Euroasphalt & Eurobitume Congress*.

Ding, H., & Hesp, S. A. (2021). Another look at the use of modulated differential scanning calorimetry to study thermoreversible aging phenomena in asphalt binders. *Construction and Building Materials*, *267*, 121787.

Dos Santos, S. F., & Brandi, H. S. (2014). A canonical correlation analysis of the relationship between sustainability and competitiveness. *Clean Technologies and Environmental Policy*, *16*, 1735–1746.

dos Santos, S., Partl, M. N., & Poulikakos, L. D. (2015). From virgin to recycled bitumen: A microstructural view. *Composites Part B: Engineering*, *80*, 177–185.

Eberhardsteiner, L., Füssl, J., Hofko, B., Handle, F., Hospodka, M., Blab, R., & Grothe, H. (2015a). Influence of asphaltene content on mechanical bitumen behavior: Experimental investigation and micromechanical modeling. *Materials and Structures*, *48*, 3099–3112.

Eberhardsteiner, L., Füssl, J., Hofko, B., Handle, F., Hospodka, M., Blab, R., & Grothe, H. (2015b). Towards a microstructural model of bitumen ageing behaviour. *International Journal of Pavement Engineering*, *16*(10), 939–949.

Edwards, Y., & Redelius, P. (2003). Rheological effects of waxes in bitumen. *Energy & Fuels*, *17*(3), 511–520.

Elkashef, M., Elwardany, M. D., Liang, Y., Jones, D., Harvey, J., Bolton, N. D., & Planche, J.-P. (2020). Effect of using rejuvenators on the chemical, thermal, and rheological properties of asphalt binders. *Energy & Fuels*, *34*(2), 2152–2159.

Farrar, M. J., Turner, T. F., Planche, J.-P., Schabron, J. F., & Harnsberger, P. M. (2013). Evolution of the crossover modulus with oxidative aging: Method to estimate change in viscoelastic properties of asphalt binder with time and depth on the road. *Transportation research record*, *2370*(1), 76–83.

Ferry, J. D. (1980). *Viscoelastic properties of polymers*. John Wiley & Sons.

Frolov, I. N., Okhotnikova, E. S., Ziganshin, M. A., & Firsin, A. A. (2020). Interpretation of double-peak endotherm on DSC heating curves of bitumen. *Energy & Fuels*, *34*(3), 3960–3968.

Frolov, I. N., Yusupova, T. N., Ziganshin, M. A., Okhotnikova, E. S., & Firsin, A. A. (2018). Formation of phase composition of petroleum bitumen according to data of temperature modulated differential scanning calorimetry. *Journal of Thermal Analysis and Calorimetry*, *131*, 555–560.

Gabrienko, A. A., Morozov, E. V., Subramani, V., Martyanov, O. N., & Kazarian, S. G. (2015). Chemical visualization of asphaltenes aggregation processes studied in situ with ATR-FTIR spectroscopic imaging and NMR imaging. *The Journal of Physical Chemistry C*, *119*(5), 2646–2660.

Garca-Coln, L., Del Castillo, L., & Goldstein, P. (1989). Theoretical basis for the Vogel-Fulcher-Tammann equation. *Physical Review B*, *40*(10), 7040.

Glover, C. J., Davison, R. R., Domke, C. H., Ruan, Y., Juristyarini, P., Knorr, D. B., & Jung, S. H. (2005). Development of a new method for assessing asphalt binder durability with field validation. *Texas Dept Transport*, *1872*, 1–334.

Gundla, A., & Underwood, B. S. (2020). Molecular weight distribution of asphalt binders from Laser Desorption Mass Spectroscopy (LDMS) technique and its relationship to linear viscoelastic relaxation spectra. *Fuel*, *262*, 116444.

Hardoon, D. R., Szedmak, S., & Shawe-Taylor, J. (2004). Canonical correlation analysis: An overview with application to learning methods. *Neural computation*, *16*(12), 2639–2664.

Herrington, P. R. (2012). Diffusion and reaction of oxygen in bitumen films. *Fuel*, *94*, 86–92.

Hintz, C., & Bahia, H. (2013). Simplification of linear amplitude sweep test and specification parameter. *Transportation Research Record*, *2370*(1), 10–16.

Hintz, C., Velasquez, R., Johnson, C., & Bahia, H. (2011). Modification and validation of linear amplitude sweep test for binder fatigue specification. *Transportation Research Record*, *2207*(1), 99–106.

Hofko, B., Alavi, M. Z., Grothe, H., Jones, D., & Harvey, J. (2017). Repeatability and sensitivity of FTIR ATR spectral analysis methods for bituminous binders. *Materials and Structures*, *50*, 1–15.

Hofko, B., Handle, F., Eberhardsteiner, L., Hospodka, M., Blab, R., Füssl, J., & Grothe, H. (2015). Alternative approach toward the aging of asphalt binder. *Transportation Research Record*, *2505*(1), 24–31.

Jennings, P., Pribanic, P., Campbell, W., Dawson, K., Shane, S., & Taylor, R. (1980). *High pressure liquid chromatography as a method of measuring asphalt composition* (tech. rep.).

Johnson, C. M. (2010). *Estimating asphalt binder fatigue resistance using an accelerated test method* (Doctoral dissertation). University of Wisconsin–Madison.

Juristyarini, P., Davison, R., & Glover, C. J. (2011). Development of an asphalt aging procedure to assess long-term binder performance. *Petroleum science and technology*, *29*(21), 2258–2268.

Kaya, D., Topal, A., Gupta, J., & McNally, T. (2020). Aging effects on the composition and thermal properties of styrene-butadiene-styrene (sbs) modified bitumen. *Construction and Building Materials*, *235*, 117450.

Kim, K. W., Kim, K., Doh, Y. S., & Amirkhanian, S. N. (2006). Estimation of RAP's binder viscosity using GPC without binder recovery. *Journal of materials in civil engineering*, *18*(4), 561–567.

Kriz, P., Stastna, J., & Zanzotto, L. (2008). Glass transition and phase stability in asphalt binders. *Road Materials and Pavement Design*, *9*(sup1), 37–65.

Kumar, Y., Singh, S. K., Oberoi, D., Kumar, P., Mohanty, P., & Ravindranath, S. S. (2020). Effect of molecular structure and concentration of styrene-butadiene polymer on upper service temperature rheological properties of modified binders. *Construction and Building Materials*, *249*, 118790.

Lamontagne, J., Dumas, P., Mouillet, V., & Kister, J. (2001). Comparison by Fourier transform infrared (FTIR) spectroscopy of different ageing techniques: Application to road bitumens. *Fuel*, *80*(4), 483–488.

Lau, C., Lunsford, K., Glover, C., Davison, R., & Bullin, J. (1992). Reaction rates and hardening susceptibilities as determined from pressure oxygen vessel aging of asphalts. *Transportation Research Record*, (1342).

Lemarchand, C. A., Bailey, N. P., Todd, B. D., Daivis, P. J., & Hansen, J. S. (2015). Non-Newtonian behavior and molecular structure of Cooee bitumen under shear flow: A non-equilibrium molecular dynamics study. *The Journal of Chemical Physics*, *142*(24), 244501.

Lesueur, D. (2009). The colloidal structure of bitumen: Consequences on the rheology and on the mechanisms of bitumen modification. *Advances in colloid and interface science*, *145*(1-2), 42–82.

Li, D. D., & Greenfield, M. L. (2014). Viscosity, relaxation time, and dynamics within a model asphalt of larger molecules. *The Journal of Chemical Physics*, *140*(3), 034507.

Li, F., Wang, Y., Miljković, M., & Chan, K. M. (2022). Changes in the nanoscale asphaltene particles and relaxation spectra of asphalt binders during aging and rejuvenation. *Materials & Design*, *219*, 110808.

Liu, J., Sun, Y., Wang, W., & Chen, J. (2017). Using the viscoelastic parameters to estimate the glass transition temperature of asphalt binders. *Construction and Building Materials*, *153*, 908–917.

López-Montero, T., & Miró, R. (2016). Differences in cracking resistance of asphalt mixtures due to ageing and moisture damage. *Construction and Building Materials*, *112*, 299–306.

Ma, J., Sun, G., Sun, D., Yu, F., Hu, M., & Lu, T. (2021). Application of gel permeation chromatography technology in asphalt materials: A review. *Construction and Building Materials*, *278*, 122386.

Marasteanu, M., & Anderson, D. (1999). Improved model for bitumen rheological characterization. *Eurobitume workshop on performance related properties for bituminous binders*, *133*.

Melendez, L. V., Lache, A., Orrego-Ruiz, J. A., Pachon, Z., & Mejía-Ospino, E. (2012). Prediction of the SARA analysis of colombian crude oils using ATR–FTIR spectroscopy and chemometric methods. *Journal of Petroleum Science and Engineering*, *90*, 56–60.

Mensching, D. J., Rowe, G. M., Daniel, J. S., & Bennert, T. (2015). Exploring low-temperature performance in Black Space. *Road Materials and Pavement Design*, *16*(sup2), 230–253.

Michon, L. C., Netzel, D. A., Turner, T. F., Martin, D., & Planche, J.-P. (1999). A ^{13}C NMR and DSC study of the amorphous and crystalline phases in asphalts. *Energy & Fuels*, *13*(3), 602–610.

Mirwald, J., Werkovits, S., Camargo, I., Maschauer, D., Hofko, B., & Grothe, H. (2020a). Investigating bitumen long-term-ageing in the laboratory by spectroscopic analysis of the SARA fractions. *Construction and Building Materials*, *258*, 119577.

Mirwald, J., Werkovits, S., Camargo, I., Maschauer, D., Hofko, B., & Grothe, H. (2020b). Understanding bitumen ageing by investigation of its polarity fractions. *Construction and Building Materials*, *250*, 118809.

Morea, F., Agnusdei, J., & Zerbino, R. (2010). Comparison of methods for measuring zero shear viscosity in asphalts. *Materials and structures*, *43*(4), 499–507.

Morian, N., Zhu, C., & Hajj, E. Y. (2015). Rheological indexes: Phenomenological aspects of asphalt binder aging evaluations. *Transportation Research Record*, *2505*(1), 32–40.

Nivitha, M., Prasad, E., & Krishnan, J. (2016). Ageing in modified bitumen using FTIR spectroscopy. *International Journal of Pavement Engineering*, *17*(7), 565–577.

Olard, F., Di Benedetto, H., Eckmann, B., & Triquigneaux, J.-P. (2003). Linear viscoelastic properties of bituminous binders and mixtures at low and intermediate temperatures. *Road materials and pavement design*, *4*(1), 77–107.

Partal, P., Martınez-Boza, F., Conde, B., & Gallegos, C. (1999). Rheological characterisation of synthetic binders and unmodified bitumens. *Fuel*, *78*(1), 1–10.

Petersen, J. C. (2000). Chemical composition of asphalt as related to asphalt durability. In *Developments in petroleum science* (pp. 363–399). Elsevier.

Petersen, J. C. (2009). A review of the fundamentals of asphalt oxidation: Chemical, physicochemical, physical property, and durability relationships. *Transportation Research Circular*, (E-C140).

Pipintakos, G., Lommaert, C., Varveri, A., & Van den Bergh, W. (2022). Do chemistry and rheology follow the same laboratory ageing trends in bitumen? *Materials and Structures*, *55*(5), 146.

Pipintakos, G., Soenen, H., Ching, H. V., Velde, C. V., Van Doorslaer, S., Lemière, F., Varveri, A., et al. (2021). Exploring the oxidative mechanisms of bitumen after laboratory short-and long-term ageing. *Construction and Building Materials*, *289*, 123182.

Polo-Mendoza, R., Martinez-Arguelles, G., Walubita, L. F., Moreno-Navarro, F., Giustozzi, F., Fuentes, L., & Navarro-Donado, T. (2022). Ultraviolet ageing of bituminous materials: A comprehensive literature review from 2011 to 2022. *Construction and Building Materials*, *350*, 128889.

Qin, Q., Schabron, J. F., Boysen, R. B., & Farrar, M. J. (2014). Field aging effect on chemistry and rheology of asphalt binders and rheological predictions for field aging. *Fuel*, *121*, 86–94.

Redelius, P. (2004). Bitumen solubility model using Hansen solubility parameter. *Energy & Fuels*, *18*(4), 1087–1092.

Redelius, P., & Soenen, H. (2015). Relation between bitumen chemistry and performance. *Fuel*, *140*, 34–43.

Rowe, G. M., & Sharrock, M. J. (2016). Cracking of asphalt pavements and the development of specifications with rheological measurements. *6th Eurasphalt & Eurobitume Congress, Prague, Czech Republic*.

Rowe, G., King, G., & Anderson, M. (2014). The influence of binder rheology on the cracking of asphalt mixes in airport and highway projects. *Journal of Testing and Evaluation*, *42*(5), 1063–1072.

Schaur, A., Unterberger, S., & Lackner, R. (2017). Impact of molecular structure of SBS on thermomechanical properties of polymer modified bitumen. *European Polymer Journal*, *96*, 256–265.

Sherry, A., & Henson, R. K. (2005). Conducting and interpreting canonical correlation analysis in personality research: A user-friendly primer. *Journal of Personality Assessment*, *84*(1), 37–48.

Siddiqui, M. N., & Ali, M. F. (1999). Studies on the aging behavior of the Arabian asphalts. *Fuel*, *78*(9), 1005–1015.

Smith, B. C. (2018). *Infrared spectral interpretation: A systematic approach*. CRC press.

Soenen, H., Besamusca, J., Fischer, H. R., Poulikakos, L. D., Planche, J.-P., Das, P. K., Kringos, N., Grenfell, J. R., Lu, X., & Chailleux, E. (2014). Laboratory investigation of bitumen based on round robin DSC and AFM tests. *Materials and Structures*, *47*, 1205–1220.

Tauste, R., Moreno-Navarro, F., Sol-Sánchez, M., & Rubio-Gámez, M. (2018). Understanding the bitumen ageing phenomenon: A review. *Construction and Building Materials*, *192*, 593–609.

Tenenhaus, A., & Tenenhaus, M. (2014). Regularized generalized canonical correlation analysis for multiblock or multigroup data analysis. *European Journal of operational research*, *238*(2), 391–403.

Themeli, A., Chailleux, E., Farcas, F., Chazallon, C., & Migault, B. (2015). Molecular weight distribution of asphaltic paving binders from phase-angle measurements. *Road Materials and Pavement Design*, *16*(sup1), 228–244.

Underwood, B. S., Baek, C., & Kim, Y. R. (2012). Simplified viscoelastic continuum damage model as platform for asphalt concrete fatigue analysis. *Transportation research record*, *2296*(1), 36–45.

Wang, D., Liu, Q., Yang, Q., Tovar, C., Tan, Y., & Oeser, M. (2021). Thermal oxidative and ultraviolet ageing behaviour of nano-montmorillonite modified bitumen. *Road Materials and Pavement Design*, *22*(1), 121–139.

Wang, D., Falchetto, A. C., Riccardi, C., Poulikakos, L., Hofko, B., Porot, L., Wistuba, M. P., Baaj, H., Mikhailenko, P., & Moon, K. H. (2019). Investigation on the combined effect of aging temperatures and cooling medium on rheological properties of asphalt binder based on DSR and BBR. *Road Materials and Pavement Design*, *20*(sup1), S409–S433.

Weigel, S., & Stephan, D. (2017). Modelling of rheological and ageing properties of bitumen based on its chemical structure. *Materials and Structures*, *50*, 1–15.

Williams, M. L., Landel, R. F., & Ferry, J. D. (1955). The temperature dependence of relaxation mechanisms in amorphous polymers and other glass-forming liquids. *Journal of the American Chemical society*, *77*(14), 3701–3707.

Yan, C., Huang, W., Lin, P., Zhang, Y., & Lv, Q. (2019). Chemical and rheological evaluation of aging properties of high content sbs polymer modified asphalt. *Fuel*, *252*, 417–426.

Yang, K., Li, R., Castorena, C., & Underwood, B. S. (2022). Correlation of asphalt binder linear viscoelasticity (LVE) parameters and the ranking consistency related to fatigue cracking resistance. *Construction and Building Materials*, *322*, 126450.

Yu, X., Burnham, N. A., Granados-Focil, S., & Tao, M. (2019). Bitumen's microstructures are correlated with its bulk thermal and rheological properties. *Fuel*, *254*, 115509.

Yut, I., & Zofka, A. (2014). Correlation between rheology and chemical composition of aged polymer-modified asphalts. *Construction and Building Materials*, *62*, 109–117.

Zeiada, W., Liu, H., Al-Khateeb, G. G., Shanableh, A., & Samarai, M. (2022). Evaluation of test methods for measurement of zero shear viscosity (ZSV) of asphalt binders. *Construction and Building Materials*, *325*, 126794.

Zhai, H., & Salomon, D. (2005). Evaluation of low-temperature properties and the fragility of asphalt binders with non-Arrhenius viscosity–temperature dependence. *Transportation Research Record*, *1901*(1), 44–51.

Zhang, H., Xu, G., Chen, X., Wang, R., & Shen, K. (2019). Effect of long-term laboratory aging on rheological properties and cracking resistance of polymer-modified asphalt binders at intermediate and low temperature range. *Construction and Building Materials*, *226*, 767–777.

Zojaji, I., Esfandiarian, A., & Taheri-Shakib, J. (2021). Toward molecular characterization of asphaltene from different origins under different conditions by means of FT-IR spectroscopy. *Advances in Colloid and Interface Science*, *289*, 102314.

5

Interplay between moisture and ageing behavior in bituminous binders

Based on the insights on moisture diffusion and oxidative ageing behavior of bitumen obtained from Chapter 2 to Chapter 4, this chapter delves deeper into how moisture diffusion influences oxidative ageing and vice versa.

Within this framework, Section 5.1 offers a comprehensive review on the effects of moisture on ageing and that of ageing on moisture behavior. In Section 5.2, the effects of ageing on moisture diffusion are explored through dynamic vapor sorption tests. This section specifically elucidates the variations in the diffusion coefficient and solubility due to ageing, highlighting key bitumen properties affecting moisture diffusion. Moisture damage caused by diffused water in various types of bitumen at different ageing states is evaluated in Section 5.3. Meanwhile, Section 5.4 interprets the ageing kinetics of bitumen in the presence of moisture. By separately investigating the effects of ageing on moisture and vice versa, a more profound understanding of moisture and ageing behavior is achieved, providing insights that can explain their coupling performance. Section 5.5 summarizes the main findings of this chapter.

5.1 Introduction

Ageing- and moisture-caused damage play a crucial role in pavement durability. Accurate prediction of long-term pavement performance necessitates not only studying the effects of moisture and oxygen on bitumen properties, but also understanding their mutual influence and coupled mechanisms. The ubiquitous presence of oxygen and moisture in the ambient environment also underscores the need to evaluate bitumen properties while taking both factors into account concurrently.

The presence of moisture has been shown to affect the ageing kinetics and oxidative products of bituminous binders. During PAV (pressure aging vessel) ageing at elevated pressure (2.1 MPa) and temperatures of 60 and 80 °C, bitumen conditioned with both oxygen and water vapor revealed faster ageing kinetics and higher concentrations of carbonyl-related compounds compared to samples without moisture (Thomas, 2002). However, the effects of moisture on the ageing process appeared to be minimal when conducting PAV ageing at atmospheric pressure and a testing temperature of 60 °C (Huang et al., 2012). Noguera et al. (2014) performed one-year water immersion tests for bitumen and showed that bitumen was stiffer in the presence of water due to the solution of oxygen in water. Furthermore, the cycled sorption and desorption of moisture in bitumen can leave history traces (open voids), leading to changes in microstructure (Vasconcelos et al., 2011). This may also facilitate the direct diffusion of oxygen into the bulk of bitumen, thereby accelerating oxidative reaction.

UV-Visible radiation can accelerate the oxidation process of bitumen. This accelerating effect was shown to reduce under moist conditions in accelerated weathering tests because water vapor absorbed some of the UV-Visible radiation, effectively reducing the intensity of the UV radiation that reached bitumen components (He et al., 2018). However, Alamdary et al. (2019) reported an increased ageing of bitumen under five days of solar radiation and daily water spray for 5 min, and attributed this to the dissolution of oxidized products into water. Some oxidative products formed during the ageing process can be soluble in water (Das et al., 2015), especially the components containing elements such as oxygen, nitrogen, and sulfur. When no moisture is present, these elements continuously increase on the surface of bitumen film with ageing time. In the presence of moisture, these elements may initially increase and then keep constant or even decrease as time progresses due to the dissolution and removal by flowing water on the surface, namely water leaching effect (Menapace et al., 2017). The dissolved bitumen surface components also expose the underlying less oxidized bitumen to age conditioning. Furthermore, under moisture conditions, polar groups tend to migrate from the bulk to bitumen surface, resulting in increased concentration of polar groups on the surface (Hung et al., 2017; Z. Liu et al., 2020). This migration may accelerate water leaching. Menapace and Masad (2020) revealed inconsistent evolution of surface microstructure during ageing process with the presence of moisture and also explained that part of aged chemicals were soluble and were taken away from bitumen, resulting in more severe cracking for the remaining bitumen. In general, moisture may increase oxidative reaction rate by dissolving oxygen in water. Moisture diffusion also creates micro-voids within bitumen and dissolves some of the aged products, both resulting in more reactive bitumen components being exposed to oxygen. On the other hand, moisture may inhibit UV-caused oxidation by absorbing UV radiation.

Moisture diffusion or absorption in bitumen depends on its chemical composition and microstructure, both of which undergo significant changes during ageing process. Distinct moisture diffusion coefficients have been observed for different types of bitumen (Apeagyei et al., 2014; Chen et al., 2022; X. Chen et al., 2022; Herrington et al., 2021). Based on this, it may be deduced that moisture diffusion coefficient is also likely to vary with aging, although studies on this specific aspect remain limited. The correlation between ageing and moisture diffusion in bitumen is still unclear. Cheng et al. (2021) reported a positive relationship between water absorption and asphaltene fraction, and Cheng et al. (2003) demonstrated that bitumen with a higher moisture diffusion coefficient tended to present a lower amount of moisture absorption. Oxidation of bitumen increases the concentration of polar functional groups such as carbonyl and sulfoxide groups (Petersen, 2009). Based on this, we could hypothesize that the moisture diffusion coefficient decreases and moisture absorption increases for aged bitumen.

Moisture damage in bitumen is affected by its ageing levels. Bituminous mixtures after short-term aging exhibit enhanced moisture resistance. This is attributed to the strong interactions between bitumen and aggregates caused by increased bitumen polarity. As a result of long-term ageing, bitumen becomes stiffer and more brittle, resulting in significant reduction in moisture resistance (Xiao & Huang, 2022). Bituminous mixtures, in general, are more susceptible to moisture-induced damage after long-term ageing (Ali et al., 2022). Bitumen ageing leads to increased polar functional groups. These groups can result in increased agglomeration of water molecules, as demonstrated in Chapter 3, which may damage its structure and impair its mechanical properties. Ageing also leads to phase separation and changes in microstructure of bitumen that affects moisture behavior.

The mutual interactions between moisture and oxygen behavior are complicated, as is the degradation in bitumen caused by ageing and moisture. These complex mechanisms and interactions are the main contributors to the variability in the findings of previous studies, and thus a consensus concerning ageing and moisture behavior has not been reached. Factors adding to this complexity involve the diverse evaluation indices and methods and varying bitumen composition and microstructure. Moisture damage and ageing originate from the diffusion and reaction of moisture and oxygen in bitumen. Hence it is of critical importance to study the diffusion and reaction behavior in bitumen through effective tests and modeling methods.

Direct measurements of moisture diffusion and oxidative ageing in bitumen can be time-consuming. Establishing a correlation between the bitumen properties that can be easily determined and the parameters that directly characterize the diffusion and reaction process can save time and effort for the analysis of these phenomena. Examples of such parameters include viscosity (Herrington, 2012) and free volume (Ding et al., 2022). Viscosity is a critical indicator of the fluid properties of bitumen, exhibiting substantial variations during ageing process. Oxidative reaction increases the content of polar groups with larger molecular weights, resulting in higher viscosity of bitumen. Viscosity has been linked to many bitumen properties such as ageing index and rheological properties (Liang et al., 2019; Redelius & Soenen, 2015; Weigel & Stephan, 2017). Viscosity can also be correlated with the oxygen and moisture diffusion in bitumen (Bird et al., 2002; Han et al., 2013; Herrington, 2012; Nguyen & Ali, 1998). Most proposed relationships are structured

in the format of

$$\frac{D}{T} = A\eta^{-B} \tag{5.1}$$

where D is diffusion coefficient, T represents temperature, η denotes the viscosity, and A and B are fitting constants. The free volume theory has been widely used to evaluate the diffusion behavior of a solvent-polymer system (Sharma et al., 2017). The free volume refers to the spaces required for all types of molecular motions beyond simple vibrational and rotational states, such as the diffusion of moisture or oxygen in bitumen (Vrentas & Duda, 1977b). A higher fractional free volume is related to increased water diffusion rates due to more available space for water molecules to diffuse through (Broudin et al., 2015).

Other parameters potentially related to the diffusion and reaction of moisture and oxygen in bitumen include the glass transition temperature, crystallinity, solubility parameter, density, and polarity. In polymers, apart from fractional free volume, the diffusion of penetrants is also influenced by two critical factors: the rigidity of molecular chains, which can be characterized by the glass transition temperature, and the compatibility between polymer and penetrants, as determined by the solubility parameter (George & Thomas, 2001). Moreover, a higher degree of crystallinity and a lower fraction of amorphous phase reduce the diffusion coefficient since the crystalline phase is generally considered as impermeable or to absorb significantly less water (Broudin et al., 2015; Jou & Huang, 1992). The density of a polymer is indicative of its fraction of free volume, and thus is also related to the diffusivity and solubility of penetrants in it (Vrentas & Duda, 1977b). Yiu et al. (2006) indicated that higher hydrophilicity led to decreased activation energy required for water diffusion, facilitating water molecules to overcome the attractive forces among themselves, indicating the influence of polarity on the diffusion behavior in polymers. All of these parameters are likely to also influence oxygen and moisture diffusion in bitumen given its similarities to polymers, both of which are organic materials with high average molecular weights.

The objective of this chapter is to unravel the intricate moisture-ageing interactions by investigating separately the moisture behavior in aged bitumen and the ageing kinetics in the presence of moisture. To this end, the moisture diffusion in various bituminous binders at different ageing states is explored using dynamic vapor sorption tests. Specifically, the diffusion coefficient and solubility of water, as well as their dependence on temperature are discussed. Additionally, the relationship between water diffusion behavior and specific bitumen properties is examined, with the goal of developing predictive models for moisture behavior based on these properties. Furthermore, this chapter explores the performance degradation of aged bitumen caused by diffused water. It also investigates the ageing kinetics of fresh bitumen in moist conditions, again utilizing dynamic vapor sorption tests. Through this comprehensive analysis, the chapter aims to elucidate the mutual influence of moisture and ageing in bitumen, paving the way for a deeper understanding of their coupled effects.

5.2 Moisture diffusion in aged bitumen utilizing sorption tests

5.2.1 Materials and methods

To evaluate the effects of ageing on moisture diffusion in bitumen, samples of V710 bitumen were tested at unaged state (V710_F), after oven ageing (V710_O), and after PAV

ageing for 20 (V710_1P), 40 (V710_2P), and 80 (V710_4P) hours. To assess the influence of bitumen sources, Q460 bitumen was also measured in its unaged (Q460_F) and 20-hour PAV (Q460_1P) states. For each of these samples, water sorption tests were conducted at 25, 40, and 55 °C instead of the 10, 25, and 40 °C used in Chapter 2, due to the small amount of moisture absorption at 10 °C, which approached the systematic error margin and resulted in reduced accuracy. Additionally, the impact of penetration grade was explored by performing sorption tests on T-sourced bitumen with different penetration grades at 25 °C, including both unaged and 20-hour PAV samples, namely, T710_F, T1015_F, T1622_F, T710_1P, T1015_1P and T1622_1P. Sample preparation followed similar steps as described in Chapter 2. However, the sample mass was increased from 40±1 mg to 60±1 mg. This was to increase the absolute moisture sorption, thus mitigating the effects of systematic error caused by the balance drift (±0.002 mg/4 days) on the accuracy of testing results. More sample mass in the aluminum pan also leads to a lower surface curvature (h_e=1.0 mm and h_c=0.83 mm, as illustrated in Fig. 2.2). The dynamic moisture transport behavior was studied using the constant relative humidity (RH) method consisting of a two-day drying at 60 °C, a following two-day drying at testing temperature, and a four-day RH loading at 80%.

The S-Cluster model proposed in Section 2.3 in Chapter 2 was used to interpret the moisture diffusion in aged bitumen, which describes the dynamic process of surface adsorption and bulk absorption. The absorption process consists of free water that diffuses at a constant rate, and clustered water that is considered to be immobile. As discussed in Section 3.4 of Chapter 3, when the moisture concentration is within the range of 0.11 – 0.22 wt%, water molecules tend to either diffuse freely without forming hydrogen bonds or bind to polar functional groups, which can be regarded as completely immobile. Such water diffusion behavior conforms to the assumptions of the absorption dynamics involved in the S-Cluster model. Considering that the moisture absorption amount for most bitumen samples was lower than 0.2 wt%, as shown in Fig. 5.1 and Fig. 5.2, the S-Cluster model was thus utilized here. To solve the unknown parameters in the S-Cluster model and to simulate the moisture diffusion process, integrated Monte Carlo and the bound Optimization by Quadratic Approximation (BOBYQA) methods were applied. The details about sample preparation, testing procedure, moisture diffusion model, and model optimization procedures are provided in Section 2.2 to Section 2.5 of Chapter 2.

5.2.2 Models for characterizing diffusion coefficient

For the diffusion behavior in liquids, hydrodynamic theory and activated-state theory have been used to calculate the diffusion coefficient by relating it to thermodynamic and physical parameters (Bird et al., 2002). The Stokes-Einstein equation relates the diffusion coefficient to the viscosity of diffusing medium:

$$D = \frac{k_B T}{6\pi R_A \eta} \tag{5.2}$$

where R_A is the mean molecule radius of the diffusing species, k_B denotes the Boltzmann constant, and η is the viscosity of the diffusing medium. More studies have found that the dependence of diffusion coefficient on temperature is weaker than that of viscosity, revealing a D linked to $1/\eta^{\epsilon}$ with $\epsilon < 1$ (Han et al., 2013; Mansuri et al., 2023; Nguyen & Ali, 1998).

Compared to the results obtained from the classical Stokes-Einstein equation, the free volume theory (FVT) proposed by Vrentas and Duda (Vrentas & Duda, 1977a, 1977b) has been stated to be more accurate for describing the diffusion of small molecules in amorphous polymers (Sharma et al., 2017). The FVT classifies the total volume of a polymer into three parts, i.e., occupied volume, interstitial free volume, and hole free volume. The interstitial free volume requires substantial redistribution energy and is not adaptable to diffusion behavior. The remaining hole free volume is presumed to be responsible for molecular diffusion. In polymers, the self-diffusion coefficient of a diffusing species (D_1) is correlated to the fractional free volume of the polymer as

$$D_1 = D_{01}\exp\left(\frac{-E_{\text{in}}}{RT}\right)\exp\left(-\frac{\omega_1\hat{V}_1^* + \omega_2\xi\hat{V}_2^*}{\hat{V}_{\text{FH1}}/\gamma_1 + \hat{V}_{\text{FH2}}/\gamma_2}\right) \tag{5.3}$$

where ω_i is the weight fraction of component i, $\hat{V}_i^*$ denotes the specific hole free volume needed for a diffusional step of component i, ξ is the ratio of the molar volume of the jumping unit of the diffusing species (component 1) to that of the polymer (component 2), $\hat{V}_{\text{FH},i}$ represents the specific hole free volume of component i, γ_i is the overlap factor for the free volume of component i, D_{01} is a constant pre-exponential factor, T is the temperature of the system, R is the gas constant, and E_{in} indicates specifically the energy per mole that a molecule needs to overcome the intermolecular interactions. The mutual diffusion coefficient can then be approximated by the equation

$$D = \frac{D_1\omega_1\omega_2}{RT}\left(\frac{\partial\mu_1}{\partial\ln\omega_1}\right)_{T,P} \tag{5.4}$$

where μ_1 is the chemical potential of the diffusing species. Assuming that the system thermodynamics can be described by the Flory-Huggins model, Equation 5.4 is derived as

$$D = D_1(1-\phi_1)^2(1-2\chi\phi_1) \tag{5.5}$$

where ϕ_1 is the volume fraction of the diffusing species and χ represents the Flory-Huggins interaction parameter.

The hole free volume can be directly determined utilizing the lattice-based equation of state (EOS) theories (Wang et al., 2007; White & Lipson, 2014). Moreover, the hole free volume in Equation 5.3 can be described by

$$\frac{\hat{V}_{\text{FH},i}}{\gamma_i} = \frac{K_{1,i}(K_{2,i} + T - T_{\text{g},i})}{\gamma_i} \tag{5.6}$$

where $T_{\text{g},i}$ represents the glass transition temperature of component i. The $K_{1,i}$ and $K_{2,i}$ are free-volume parameters and can be evaluated based on the dependence of dynamic properties, such as viscosity, on temperature, which conforms to the Williams–Landel–Ferry (WLF) model (Vrentas & Duda, 1977a; Williams et al., 1955):

$$\log\alpha_{\text{T}} = \frac{-C_1(T-T_{\text{r}})}{C_2 + T - T_{\text{r}}} = \frac{B}{2.303}\left(\frac{1}{f^{\text{free}}} - \frac{1}{f_{\text{g}}^{\text{free}}}\right) \tag{5.7}$$

$$\frac{K_{1,i}}{\gamma_i} = \frac{\hat{V}_i^*}{2.303C_{1,i}C_{2,i}} \tag{5.8}$$

$$K_{2,i} = C_{2,i} = T_r - T_{V,i} \tag{5.9}$$

where T_r denotes the reference temperature, C_1 and C_2 are WLF constants, T_v is the Vogel temperature, as described by the VFT equation in Chapter 4, f_g^{free} is the fraction free volume at glass transition temperature, and f^{free} is fractional free volume. The f^{free} is linked to f_g^{free} via thermal expansion coefficient α_f as

$$f^{free} = f_g^{free} + \alpha_f(T - T_g) \tag{5.10}$$

For bitumen, it is more challenging to determine the required parameters in the expressions for diffusion coefficient due to limited references. Nevertheless, these theories can help to understand the mechanisms of oxygen and moisture diffusion in bitumen and the construct a correlation between diffusion behavior and physicochemical and mechanical parameters. The diffusion coefficient is a physical constant dependent on molecule weight, molecule size and other properties of diffusing gases, as well as matrix type, temperature, and pressure. Preliminary conclusions based on the molecular models and the free volume theory can be reached, suggesting a nuanced understanding of diffusion in bitumen.

5.2.3 Kinetics and thermodynamics of diffusion in aged binders

Moisture transport behavior

Fig. 5.1 depicts the water sorption dynamics for V710 at various ageing states. At 25 °C, the increase in sample mass over time for V710 at various ageing states is comparable, indicating their analogous moisture diffusion behavior. After 5760 min of moisture exposure, all samples are approaching the equilibrium moisture sorption amount. Among these samples, V710_4P is relatively less equilibrated than the others. At 40 °C, the moisture sorption amount of V710_O is larger than that of V710_F. After PAV ageing, the amount of sorbed moisture declines again. Three samples subjected to 20, 40, and 80 hours of PAV ageing present approximately equivalent moisture sorption dynamics. For bitumen samples at 55 °C, as ageing level increases from F, O, to 1P, the total sorbed

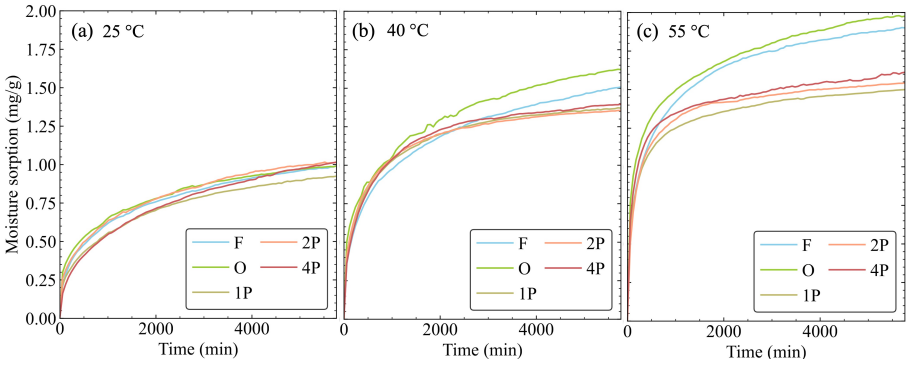

Figure 5.1 Moisture sorption in V710 at different ageing states for temperatures of (a) 25 °C, (b) 40 °C, and (c) 55 °C.

moisture amount initially increases and then decreases, similar to the observations at 40 °C. V710_1P, V710_2P, and V710_4P again exhibit similar overall sorption amount, with V710_4P being slightly higher than V710_2P and V710_1P.

The dependence of moisture sorption on ageing level varies with testing temperatures. For example, at 25 °C, V710_4P shows the slowest initial sorption while it manifests the fastest initial sorption at 55 °C. The differences in the sorption dynamics among the three samples subjected to PAV ageing (1P, 2P, and 3P) are less pronounced compared to the differences observed among unaged (F), oven-aged (O) and 20-hour PAV-aged (1P) states. This indicates that the impact of ageing on moisture behavior becomes less significant after 20 hours of PAV ageing.

Fig. 5.2 displays the moisture sorption for different bitumen types and penetration grades. All these sub-figures show that the overall moisture sorption increases for higher penetration grade. Same penetration grade also leads to different transport behaviors. Compared to V710, T710 experiences a faster sorption rate but a lower maximum sorption amount, agreeing with their diffusion dynamics revealed in Chapter 2, which were measured with a lower sample mass. A large difference in the sorption amount is observed for fresh T710, T1015, and T1622, whereas after 20 hours of PAV ageing, they show similar sorption behavior. This demonstrates that the impact of penetration grade on moisture transport in bitumen diminishes as more ageing occurs. Fig. 5.2 (c) shows that for both V710 and Q460, moisture sorption increases with temperature. Compared to V710, the overall sorption of Q460 is lower at three temperatures, indicating that the trend of decreased sorption associated with a lower penetration grade holds across a wide range of temperatures.

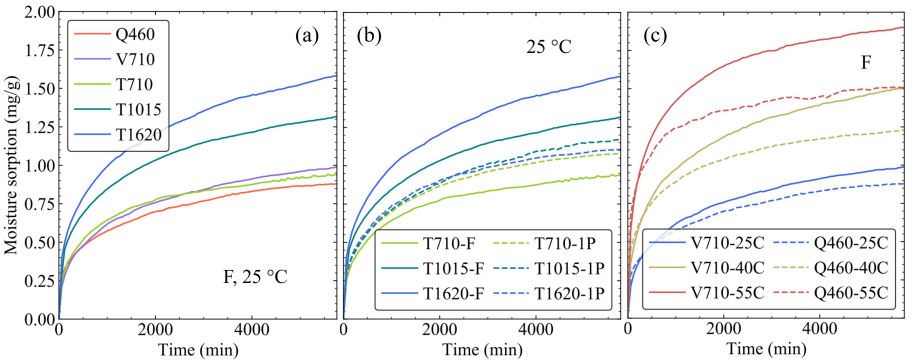

Figure 5.2 Effects of (a) bitumen source and penetration grade, (b) penetration grade, and (c) temperature on moisture diffusion in bituminous binders.

To further analyze the effects of temperature, ageing level, bitumen type, and penetration grade on moisture sorption behavior, the diffusion parameters in the S-Cluster model were optimized utilizing the combined Monte Carlo and BOBYQA methods. The derived parameter values are listed in Table 5.1.

Table 5.1 Parameters of the S-Cluster model for various binders at different ageing states.

Sample	T (°C)	α_{sc} (1/s)	$S_{m,sc}$ (mg)	D_{sc} (m^2/s)	n_{sc} /	β_{sc} /	c_H^0 (mol/m^3)	$c_{sat,sc}$ (mol/m^3)	$c_{clu,sc}$ (mol/m^3)	$c_{bulk,sc}$ (mol/m^3)
V710_F	25	0.013	0.010	5.20E-12	1.63	1.11	42.2	49.4	27.8	77.3
	40	0.012	0.017	6.30E-12	1.40	0.80	59.2	68.1	17.2	85.2
	55	0.013	0.033	8.61E-12	1.25	0.90	67.5	73.7	8.8	82.5
V710_O	25	0.034	0.013	4.86E-12	1.72	0.89	40.8	47.0	20.4	67.5
	40	0.025	0.024	9.46E-12	1.29	0.71	46.0	58.4	18.3	76.7
	55	0.026	0.039	1.78E-11	1.53	1.10	50.5	58.1	24.6	82.8
V710_1P	25	0.019	0.008	4.48E-12	1.47	0.80	41.4	48.1	13.0	61.0
	40	0.028	0.021	9.49E-12	1.25	0.51	53.6	58.8	4.0	62.8
	55	0.019	0.031	1.73E-11	2.24	0.54	45.5	49.3	10.7	60.0
V710_2P	25	0.026	0.011	3.93E-12	1.26	0.76	47.6	52.7	6.0	58.7
	40	0.012	0.024	8.64E-12	1.74	0.93	50.3	53.5	7.0	60.5
	55	0.019	0.039	1.51E-11	2.13	0.61	46.2	49.8	9.2	59.0
V710_4P	25	0.007	0.006	2.80E-12	1.62	0.51	55.8	61.7	9.0	70.7
	40	0.009	0.017	9.05E-12	2.04	0.57	57.7	61.5	8.7	70.2
	55	0.011	0.035	2.72E-11	1.48	0.61	54.7	62.9	13.8	76.6
T710_F	25	0.022	0.009	8.78E-12	2.11	0.41	37.3	42.2	11.9	54.1
T1015_F	25	0.013	0.018	5.27E-12	1.45	0.49	49.1	58.7	13.1	71.8
T1622_F	25	0.026	0.016	5.58E-12	1.75	0.79	64.8	76.8	61.9	138.7
T710_1P	25	0.034	0.012	5.00E-12	1.70	0.61	48.2	52.5	7.3	59.8
T1015_1P	25	0.018	0.012	3.76E-12	1.04	0.40	54.7	60.0	2.3	62.3
T1622_1P	25	0.018	0.013	5.38E-12	1.50	0.57	48.6	52.7	4.8	57.5
Q460_F	25	0.032	0.013	3.96E-12	1.88	0.86	37.4	42.5	18.6	61.1
	40	0.029	0.022	7.38E-12	1.99	0.67	43.8	48.9	16.7	65.5
	55	0.038	0.031	1.58E-11	2.01	0.72	45.6	49.7	11.8	61.5
Q460_1P	25	0.024	0.009	6.55E-12	1.89	0.99	34.1	36.3	4.5	40.7
	40	0.025	0.019	1.09E-11	1.87	1.25	37.3	39.6	5.8	45.5

Moisture diffusion coefficient in aged binders

Table 5.1 shows that the moisture diffusion coefficient increases with temperature for all samples. This dependence of diffusion coefficient on temperature can be described by the Arrhenius equation 2.18. The fitted results are shown in Fig. 5.3 and Table 5.2. The activation energy E_A for water diffusion varies substantially with ageing level. After short-term ageing, the E_A of V710 increases from 13.77 to 35.69 kJ/mol. This energy then reaches values of 36.55 and 37.04 kJ/mol after 20 and 40 hours of PAV ageing, respectively. With ageing level increasing further from 2P to 4P, the E_A significantly increases.

A relatively high E_A implies a substantial barrier to water absorption. This diffusion barrier depends on the microstructure of bitumen which is a function of molecular structure, molecular weight, and polarity, and can be affected by polymer modifiers and additives. During short- and long-term ageing processes, the evaporation of light components and the oxidative ageing occur in bitumen, leading to increased polarity, density, and molecular weight. According to the FVT, the presence of vacancies or holes, known as free volume, is essential for the diffusion process (Bird et al., 2002). Increased ageing level essentially leads to a lower free volume fraction (Qu et al., 2018). This decreased free volume makes it more difficult for water molecules to find a diffusing path. Therefore, a larger E_A is expected for bitumen with a higher ageing level. According to the Equation

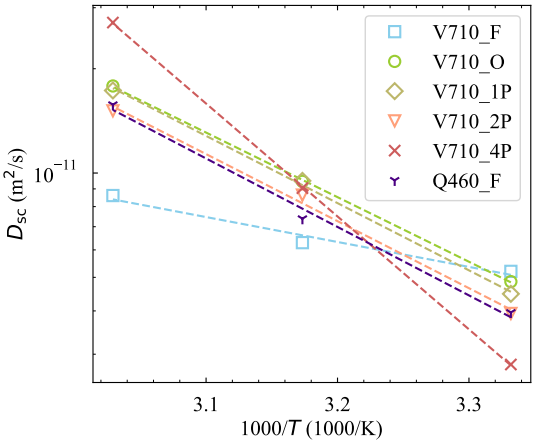

Figure 5.3 Temperature dependence of diffusion coefficients based on the S-Cluster model, where dashed lines are the fitting of the Arrhenius equation.

Table 5.2 Fitted parameters in the Arrhenius equation and the fitting accuracy.

Parameter	V710_F	V710_O	V710_1P	V710_2P	V710_4P	Q460_F
D_0	1.27E-09	7.87E-06	1.05E-05	1.13E-05	2.00E-01	1.47E-05
E_A (kJ/mol)	13.77	35.69	36.55	37.04	62.38	37.83
R^2	0.97	1.00	1.00	1.00	1.00	0.99

5.7 – 5.10, the fractional free volume f_g^{free} at T_g is inversely proportional to WLF constant C_1. Given T_r as 25 °C and T_g as -25 °C (as shown in Fig. 4.14), the f^{free} is linked to $(C_2+50)/(C_1C_2)$.

Apart from free volume fraction, the polarity of bitumen may also affect the E_A for moisture diffusion (Bouvet et al., 2016; Seo & Han, 2001). As ageing proceeds, bitumen tends to develop a higher polarity, primarily due to an increase in carbonyl and sulfoxide functional groups. This change in the chemical composition and the resulting increase in polarity, as detailed in 4, can impact the diffusion dynamics of moisture within the bitumen matrix. According to the Eyring's absolute reaction rate theory (Eyring, 1936; Gusev et al., 1994), the pre-exponential factor in the Arrhenius equation is associated with the exponent of entropy, i.e.,

$$D = D_0 \exp\left(-\frac{E_A}{RT}\right) = \hat{D}_0 \exp\left(\frac{\Delta S}{R}\right)\exp\left(-\frac{\Delta H}{RT}\right) \tag{5.11}$$

where ΔH and ΔS are the enthalpy- and entropy-related energy barrier for diffusion, respectively. The ΔH depends on the interaction energy between the diffusing species and the medium, as well as the energy required for local structural rearrangements that facilitate the diffusion of water molecules. The ΔS, the entropy-related energy barrier, relates

to the number of available diffusive paths (Bouvet et al., 2016). As discussed in Chapter 3, at low water concentrations, water molecules mainly stay as free or form hydrogen bonds with bitumen. According to Bouvet et al. (2016), water molecules in a polymer diffuse from one polar site to another with a residence time of ca. 1 ns. This process depends on the concentration and distribution of polar groups. More polar groups in bitumen create more diffusion paths, resulting in a higher entropy and consequently a higher pre-exponential factor D_0. Nevertheless, a higher concentration of polar groups also indicates stronger interactions between water and bitumen, which further increases ΔH.

Table 5.2 presents a higher pre-exponential factor D_0 as the E_A increases. This phenomenon is defined as the compensation effect (L. Liu & Guo, 2001; Zheng et al., 2007), which describes the relationship between D_0 and E_A as

$$\ln D_0 = \alpha + \beta E_A \tag{5.12}$$

where α and β are fitting constants. Fig. 5.4 illustrates the fitting results based on Equation 5.12, demonstrating a strong linear correlation between D_0 and E_A. This equation applies not only to V710 at various ageing states, but also extends to Q460_F, signifying its broader relevance to different types of bitumen. The compensation effect has been observed in many diffusion phenomena, particularly for the diffusion of small molecules in polymers (Zheng et al., 2007). This effect implies that factors causing a higher enthalpy for diffusion simultaneously result in a higher entropy. While the precise mechanisms causing the compensation effect remain debatable, the robust linear correlation between D_0 and the E_A provides a promising approach for estimating the diffusion coefficient in specific bitumen samples. Providing that E_A can be determined based on the free volume and polarity of the bitumen, and D_0 can be calculated according to Equation 5.12, the diffusion coefficient can then be effectively predicted. A similar approach was also used in the prediction of oxidative ageing kinetics in bitumen where the pre-exponential factor and activation energy for reaction in accordance with the compensation effect (Jin et al., 2011).

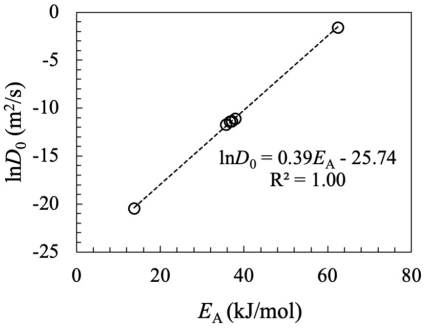

Figure 5.4 Relationship between pre-exponential factor and activation energy of moisture diffusion for V710 at all ageing states and fresh Q460.

To examine the relationship between the E_A for water diffusion and its properties, the correlations between E_A and factors including viscosity, polarity (carbonyl index + sulfoxide index), and fractional free volume were analyzed. These correlations were fitted using

linear and power models, with the fitting accuracies listed in Table 5.3. The power model shows a better performance, indicating the non-linearity of these relationships. A high correlation between E_A and free volume is observed, aligning with the FVT. Viscosity and polarity also present significant correlations with E_A. Overall, a higher ageing level leads to a lower fractional free volume, a higher viscosity, and a higher polarity, all of which contribute to a higher E_A. However, it is important to note that these findings are based only on V710 at various ageing states. Introducing bitumen from other sources complicates the prediction of E_A. This complexity results from the fact that the activation energy for diffusion depends on the chemical composition and microstructure of bitumen, which can vary significantly among different sources. To obtain better prediction of E_A on a broader scale, dynamic vapor sorption tests on more binder types are required.

Table 5.3 Fitting accuracy (R^2) of activation energy as a function of various bitumen properties for V710 at various ageing levels.

Fitting model	Viscosity	Polarity	1/C1	C1/C2	(C2+50)/(C1C2)
Linear	0.78	0.69	0.88	0.63	0.86
Power	0.79	0.70	0.95	0.70	0.95

Furthermore, the synchronous increase in E_A and D_0 with increasing ageing level is informative of the relationship between moisture diffusion coefficient and bitumen ageing level as specific temperatures. As depicted in Fig. 5.3, at 25 °C, the diffusion coefficient decreases as bitumen ages, with the V710_4P displaying the lowest value. However, at 55 °C, it is the most aged bitumen that exhibits the highest diffusion coefficient. Similar to the E_A, the moisture diffusion coefficient is affected by free volume and polarity, as indicated by the Equation 5.3 – 5.5. At all examined temperatures, the decreasing free volume for bitumen at higher ageing level always reduces diffusion rate as revealed by Equation 5.3. However, the role of polarity is more complex for the moisture diffusion at different temperatures. On one hand, a higher polarity increases the interactions between bitumen and water, while on the other, it creates more possible diffusing pathways. At low temperatures, increased interaction energy dominates the effects of polarity. With increasing temperature, once the energy required for overcoming these interactions is met, the increased polarity leads to additional diffusing pathways. This contributes to a higher diffusion coefficient.

Moreover, the solubility parameter of water is 47.8 $MPa^{0.5}$ (Hansen, 2007), significantly higher than that of bitumen (ca. 19.2 $MPa^{0.5}$) (Redelius, 2004), indicating a low compatibility between moisture and bitumen. The increased polarity of bitumen caused by the ageing process results in higher chemical affinity to water. According to the Equation 5.5, assuming a constant D_1, the D increases with decreasing solubility parameter χ, indicating faster water diffusion within aged bitumen (Bouvet et al., 2016; Seo & Han, 2001).

The diffusion coefficient of moisture in bitumen is also influenced by its penetration grade. As shown in Table 5.1, the moisture diffusion coefficient of fresh T710 at 25 °C is higher than that of fresh T1015 and T1622. After 20 hours of PAV ageing, the moisture diffusion coefficient of all three samples from source T decreases, with T1622 displaying a less pronounced decrease than T1015 and T710. The greater variation in the diffu-

sion coefficient after PAV ageing for lower penetration grade indicates its more substantial changes in chemical and microstructure.

Thermodynamics of moisture absorption in aged binders

The saturated moisture concentration in Henry's mode ($c_{sat,sc}$) as a function of temperature is shown in Fig. 5.5. Here $c_{sat,sc}$ rather than $c_{bulk,sc}$ is used to avoid complicating the analysis by introducing the clustering effect. For fresh bitumen, the solubility in Henry's mode increases with temperature while a decreasing trend occurs as ageing proceeds.

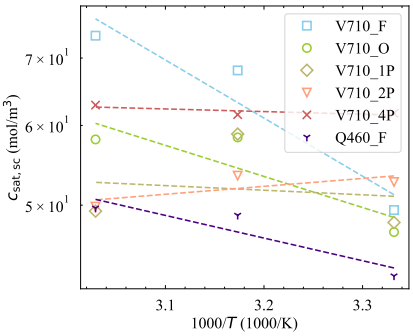

Figure 5.5 Saturated moisture concentration in Henry's mode as a function of temperature. The dotted lines denote the fitting based on Equation 5.13.

The temperature dependence of water absorption in bitumen is characterized by the enthalpy of sorption, which can be effectively described through the van't Hoff relationship (Petropoulos, 1994):

$$S = S_0 \exp\left(-\frac{\Delta H_s}{RT}\right) \tag{5.13}$$

where S_0 is a pre-exponential constant and ΔH_s is the enthalpy of sorption. The fitted results are displayed in Fig. 5.5. A noticeable reduction in ΔH_s is observed with increasing ageing level as reflected by the slope of the fitting curves in Fig. 5.5. For V710 at higher ageing levels, the ΔH_s is even negative in some cases. This decreased ΔH_s results from the complex physicochemical changes in bitumen due to the ageing process.

The absorption of water in bitumen involves the condensation of water vapor followed by the mixing of the condensed vapor with the bitumen segments. Based on this, the enthalpy of sorption can be separated into parts, i.e., the enthalpy related to the condensation (ΔH_{cond}) and that linked to the mixing process (ΔH_{mix}) (Petropoulos, 1994):

$$\Delta H_s = \Delta H_{cond} + \Delta H_{mix} \tag{5.14}$$

According to the Flory-Huggins theory (Rubinsten & Colby, 2003), the $\Delta H_{mix} = RT\chi\phi_1(1-\phi_1)$, where ϕ_1 represents the volume fraction of water. Here, the interaction parameter χ between bitumen (V710) and water is positive and high, as indicated in Chapter 2, suggesting a low compatibility between them. More energy is thus required for water and

bitumen to mix properly, leading to an endothermic and energetically unfavorable mixing process, as reflected by a generally positive ΔH_{mix}. As ageing proceeds, the polarity of bitumen increases, resulting in a decrease in χ due to enhanced affinity between water and aged bitumen. Consequently, a lower ΔH_{mix} is obtained. Conversely, the ΔH_{cond} for water vapor is negative, which corresponds to the exothermic nature of the vapor condensation process. Since the ΔH_{cond} depends on water and does not vary for different bitumen samples, the decreased ΔH_{mix} with ageing results in a lower ΔH_s.

A linear model was applied to fit the correlation between ΔH_s and polarity of binders including V710 at various ageing level and Q460_F. A R^2 of 0.73 was obtained, suggesting a fair correlation between ΔH_s and polarity.

Ageing affects not only the dependence of moisture absorption on temperature, but also moisture absorption at specific temperatures. Fig. 5.6 (a) depicts the saturated moisture solution in Henry's mode ($c_{sat,sc}$), the clustered moisture concentration ($c_{clu,sc}$), and the overall maximum moisture concentration $c_{bulk,sc}$ of V710 at various ageing levels for three testing temperatures. At all temperatures, the $c_{sat,sc}$ of V710 exhibits an initial decrease and then a slight increase as ageing advances. In most cases, the $c_{clu,sc}$ and the $c_{bulk,sc}$ of V710 also initially decrease with ageing and show a slight increase when the ageing level increases from 2P to 4P.

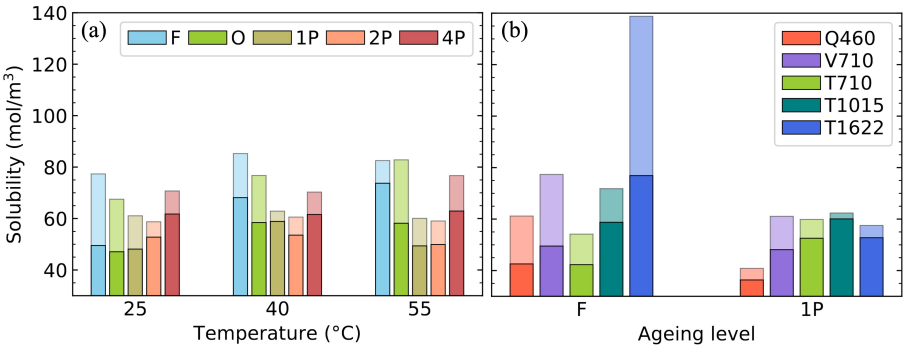

Figure 5.6 Moisture concentration (a) in V710 at various ageing levels and (b) in various types of bitumen at 25 °C. For each column, the lower section denotes the saturated moisture solution in Henry's mode and the upper section with higher transparency describes the clustered moisture concentration. The sum of them reveals the overall moisture concentration in bitumen.

Several factors might contribute to the observed decrease in $c_{sat,sc}$ and $c_{clu,sc}$ with ageing from fresh to 40-hour PAV condition, and the subsequent increase with further ageing from 40 to 60 hours of PAV treatment. One primary factor is the fractional free volume of bitumen, which decreases as ageing level increases, reducing the microspaces available for water molecules to diffuse and form clusters. Simultaneously, ageing enhances the number of polar functional groups, which act as nuclei for water clusters, benefiting the absorption of moisture in bitumen. The moisture absorption in bitumen is affected by these two concurrent but conflicting factors. The prevailing decreasing trend of $c_{sat,sc}$ and $c_{clu,sc}$ when ageing level increases fresh to 2P indicates that the reduction in the fractional free volume dominates the moisture diffusion behavior in bitumen. The higher $c_{clu,sc}$ of

V710_4P compared to V710_2P may be more attributed to the increase in bitumen polarity rather than the reduction in free volume. Furthermore, phase incompatibility may occur in severely oxidized binders (Kriz et al., 2008), which provides accessible volumes for water dissolution and clustering. Other ageing-related changes in bitumen properties could also contribute significantly to the moisture absorption behavior.

The moisture concentration in various bitumen types is shown in Fig. 5.6 (b). For unaged binders, the $c_{sat,sc}$ and $c_{clu,sc}$ exhibit an increasing trend with higher penetration grade, particularly in the case of T-sourced binders. After 20 hours of PAV ageing, less difference in the moisture concentration between different penetration grades is observed. The substantial reduction in the $c_{clu,sc}$ of T1622 with ageing is linked to its ageing process. As shown in Fig. 4.9, the initial sulfoxide index of T1622 is lower compared to T710 and T1015. After 1P ageing, the sulfoxide and carbonyl indices of T1622 approach those of T710 and T1015, indicating their comparable degree of ageing. This results in similar maximum moisture absorption among the three binders.

5.3 Hydrothermal degradation of aged binders

5.3.1 Sample preparation and hydrothermal degradation protocols

To study the moisture damage of aged bitumen, several types of binders were utilized, i.e., Q460, Q710, T1622, V710, V710_1P, V710_2P, V710_4P, and VPMB. These binders varied in ageing states, crude oil sources, and SBS modification. For each binder, bitumen weighing 5.62 g was placed into a glass Petri dish with a diameter of 5 cm and a height of 1.6 cm. It was then heated in oven at 140 °C for 5 min to obtain a homogeneous bitumen film with a thickness of 1mm. Fourteen identical samples were prepared for each type of binder. These samples were separated into four groups. The first group, labelled as "W", consisted of four samples that were immersed in deionized water for 15, 30, 60, and 90 days. This was achieved by adding 10 ml of water into the glass Petri dish, ensuring that the bitumen film was fully covered by the water, which was then sealed by plastic package to prevent water from evaporation. The second group, referred to as "CY", had three samples subjected to one, two, and three cycles of wetting (15d) and drying (15d) over 30, 60, and 90 days, respectively. In each cycle, the wetting phase was achieved by adding water to the sample container, followed by a drying phase where the water was removed. The three samples in the third group ("RH") were placed in weather chamber with a relative humidity of 80% for 15, 30, and 60 days, respectively. The remaining four samples were put in an oven (assuming zero humidity) for 0, 30, 60, and 90 days, collectively known as Group "C". All theses tests were performed at 40 °C. Details about sample preparation and testing protocols are illustrated in Fig. 5.7.

Rheological tests were performed on all the samples, including frequency sweep tests at temperatures of 0–40 °C, linear amplitude sweep (LAS) at 20 °C, and relaxation tests at 0 °C. The detailed test procedures, along with the analysis of the results, are presented in Section 4.5 of Chapter 4.

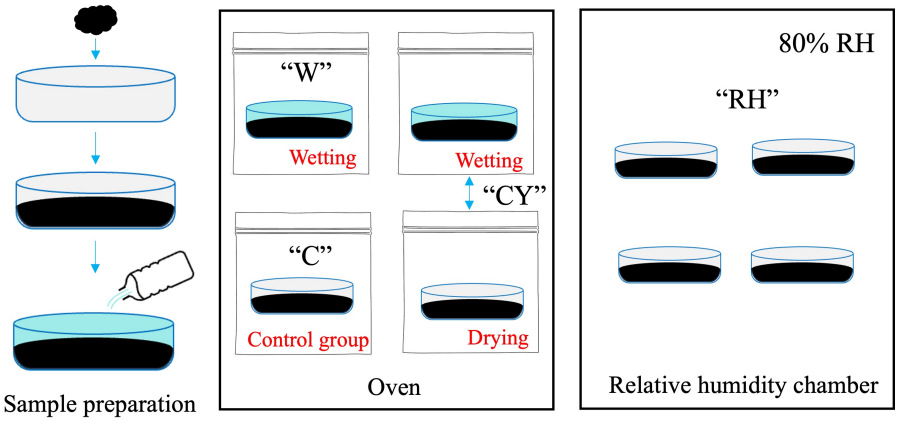

Figure 5.7 Sample preparation and hydrothermal ageing protocols.

5.3.2 Rheological properties of aged binders under moisture conditions

Fig. 5.8 presents the master curves of V710 and its various ageing states when subjected to water immersion, wetting-drying cycles, and relative humidity at 40 °C. Different extents of moisture-caused degradation in bitumen properties are observed from these hydrothermal tests. This may be related to the variations in chemical composition and microstructure of bituminous binders at various ageing levels. For the four sample groups, namely, C, CY, W, and RH, the complex modulus increases and phase angle decreases over time, demonstrating an increased stiffness for V710_F, V710_1P, V710_2P, and V710_4P. Among these ageing states, V710_F shows the largest changes in the master curves of complex modulus and phase angle, with most changes in stiffness occurring within the first 30 days. This is likely due to a higher content of reactive components in the fresh bitumen compared to its more aged states. Compared to the samples exposed to oven ageing at 40 °C (Group C), bitumen samples immersed in water exhibit overall larger increase in stiffness.

Based on the master curves depicted in Fig. 5.8, the crossover frequency (f_c), crossover modulus (G_c^*), rheological index (R_{rhe}), and Glove-Rowe parameter ($G-R$) for V710_F, V710_1P, V710_2P, and V710_4P under various water conditions were calculated and are summarized in Fig. 5.9. Lower f_c and G_c^* are linked to stiffer and more brittle bituminous binders. Generally, among four testing groups, Group CY exhibits the lowest crossover frequency and crossover modulus, followed by Group W, Group RH, and the control group. This indicates that bitumen subjected wetting-drying cycles experiences the most significant degradation. However, for R_{rhe} and $G-R$, Group W mostly exhibits the highest values, exceeding those of groups CY, RH, and C. Therefore, in terms of R_{rhe} and $G-R$, water immersion causes the largest moisture-related degradation in bitumen.

As indicated in Chapter 4, the f_c and G_c^* describe the viscoelatic behavior of bitumen. The R_{rhe} reflects the shape of master curves and stress relaxation spectra, while G-R can be used to evaluate the crack resistance of binders. The varied changes in these rheological properties caused by different water conditions (CY, W, and RH) indicate that these

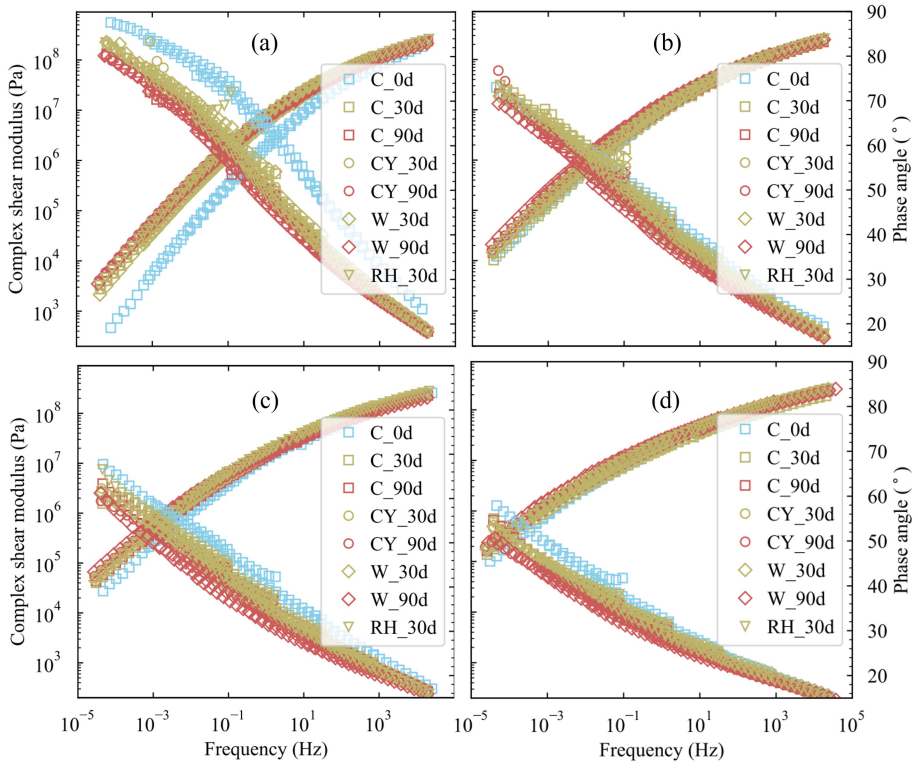

Figure 5.8 Master curves of (a) V710-F, (b) V710-1P, (c) V710-2P, (d) V710-4P conditioned by oven ageing without moisture (C), water immersion (W), wetting-drying cycles (CY), and relative humidity (RH) at 40 °C.

properties are affected by different mechanisms. The presence of water or moisture may slow down or accelerate the oxidative ageing process (Huang et al., 2012; Thomas, 2002), and water can leach specific chemicals from bitumen (Menapace et al., 2017). Among the three water conditions, compared to water immersion (W), the wetting-drying cycles may lead to more structural changes and water vapor may not leach oxidative product. These differences lead to distinct chemical and structural changes in bitumen samples, contributing differently to the four rheological parameters. Additionally, when comparing Group RH with Group C, assuming that relative humidity cannot leach chemicals from bitumen, the small increase in R_{rhe} and $G-R$, along with the decrease in f_{c} and G_{c}^{*}, indicates that the presence of moisture accelerates slightly the ageing kinetics and lead to more degradation. Other bitumen types, including Q460_F, Q710_F, Q710_2P, T1622, and VPMB exhibit similar changes in rheological properties as V710 at various ageing states.

To evaluate the leaching effect, the water samples above the bitumen in glass Petri dishes were collected after 60 days of bitumen immersion. The total organic carbon (TOC) dissolved in these water samples was measured through a TOC analyzer. This analyzer measures the total amount of carbon from organic compounds in a sample. For

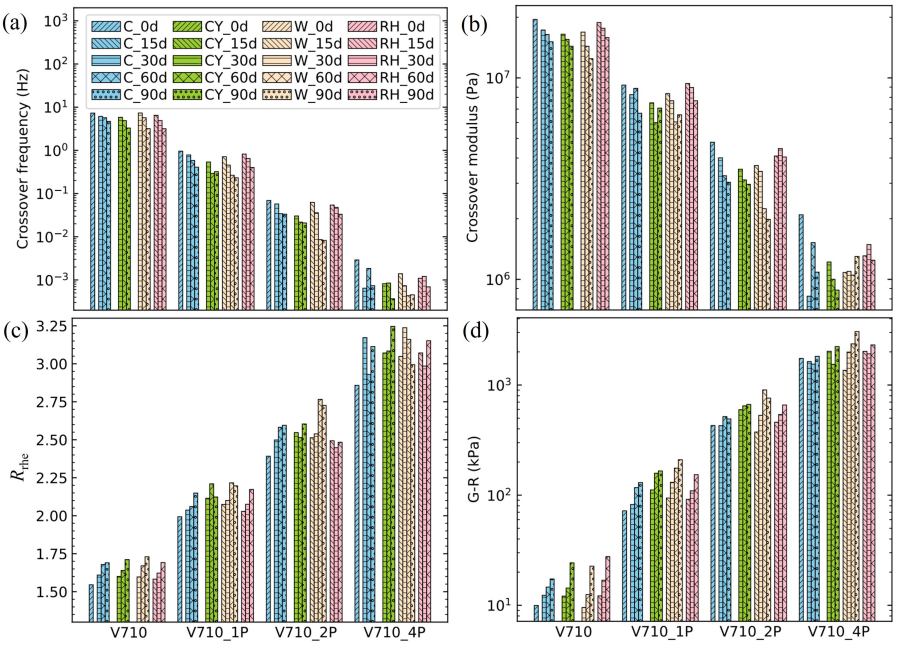

Figure 5.9 Effects of water immersion, wetting-drying cycle, and relative humidity on the rheological properties of V710 at various ageing states including (a) Crossover frequency, (a) crossover modulus, (c) Glove-Rowe parameter, and (d) R_{rhe}.

V710_F, V710_1P, V710_2P, and V710_4P, the concentrations of organic carbon measured are 3.4, 5.1, 4.9, and 8.5 mg/L, respectively. The higher concentration of dissolved organics in more aged samples indicates that water-soluble components in bitumen increases with level of oxidative ageing.

5.4 Ageing kinetics of bitumen in the presence of moisture

5.4.1 Sample preparation and testing conditions

To investigate the ageing kinetics of bitumen in the presence of moisture or water, dynamic vapor sorption tests were conducted at elevated temperatures under four conditions: dry air, air with 80% relative humidity (RH), dry nitrogen, and nitrogen with 80% RH. It was assumed that the bitumen does not react with nitrogen gas, and thus the impact of moisture on ageing kinetics can be evaluated by comparing the sorption results under the four conditions. Initial tests were conducted at several temperatures ranging from 25 to 80 °C. For fresh bitumen at temperatures below 50 °C, the mass increase over a four-day period in dry air was too minor to be accurately determined, considering factors like balance drift and resolution of the equipment. Therefore, the testing temperature was set as higher than 50 °C. The original idea was to measure both fresh bitumen and bitumen subjected to 20 hours of PAV ageing. In this case, the effects of moisture on both short-term and long-term ageing kinetics could be obtained. However, preliminary tests

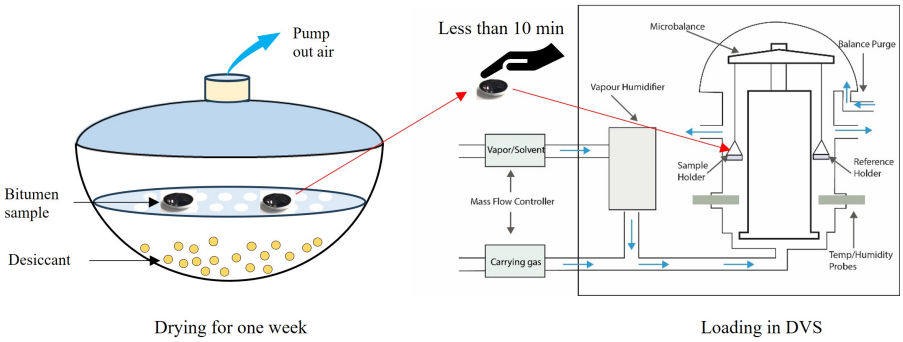

Figure 5.10 Sample drying in desiccator and loading in dynamic vapor sorption

exhibited a negligible mass increase in PAV-aged bitumen after four days in dry air. As a result, only two fresh bitumens were analyzed, namely, V710 and T710.

Prior to testing, prepared samples weighing 60±1 mg were placed in a container for one week. This container was filled with desiccant to remove moisture and equipped with a pump to extract air. To conduct the moisture sorption test, the DVS equipment was first set up with designed parameters. Subsequently, the bitumen sample was quickly transferred from the drying container to the hang-down sample pan in DVS chamber, as illustrated in Fig. 5.10. The sorption test started immediately upon placing the sample in the DVS, with each test running for 6400 min. Considering the quick operation, it was hypothesized that only surface adsorption of moisture occurred during the sample transfer. Therefore, a short initial stabilization (desorption) in a dry condition within the DVS was implemented to remove any adsorbed moisture from the sample. This stabilization phase was determined to be complete after 150 min, marked by the termination of rapid change in mass due to surface moisture desorption. The sample mass recorded at the end of this stabilization period was then taken as the reference mass. Following this period, the observed changes in sample mass became more stable and were attributed solely to the testing conditions. For the tests involving relative humidity, this parameter was introduced at 400 min and then removed at 3600 min.

5.4.2 Effects of moisture on ageing kinetics of bitumen

The sorption results for fresh T710 under the four different conditions are presented in Fig. 5.11. T710 exposed to dry air condition exhibits an increase in sample mass with time, while a decreasing trend is observed for bitumen in a dry nitrogen environment (Fig. 5.11 (a)). At high temperatures, fresh bitumen in dry air undergoes accelerated oxidative ageing, leading to a rapid increase in sample mass. This increased mass primarily results from the oxygen captured through chemical reaction process (Siddiqui & Ali, 1999). The decreased mass for the sample exposed to nitrogen condition may be attributed to several factors. At 75 °C, above the softening point of bitumen, T710 is in a highly viscous state, The high flow rate of nitrogen at 200 sccm (cm^2/min) may facilitate the removal of volatile components from bitumen, resulting in a decrease in sample mass. This vaporization is also expected in dry air; however, the decrease in mass due to vaporization is masked by

the more significant mass increase resulting from oxidative ageing. Furthermore, the molar mass of nitrogen gas is 28.02 g/mol, lower than that of air, whose molar mass is 28.97 g/mol. Therefore, when conditioned by nitrogen, replacing air originally in the bitumen with nitrogen through diffusion may also result in decreased sample mass. Based on published data (Herrington, 2012; Kretschmer et al., 1946), the solubility of air or nitrogen in bitumen is probably lower than 0.01 mol/L at 75 °C. Hence, the mass change caused by the complete substitution of air with nitrogen should be less than 0.001 wt%, significantly lower than the up to 0.1 wt% mass loss observed in bitumen under the dry nitrogen condition. Consequently, the decreased mass observed when bitumen is exposed to nitrogen is primarily due to the vaporization of volatile components within the bitumen samples, as explained in Fig. 5.12.

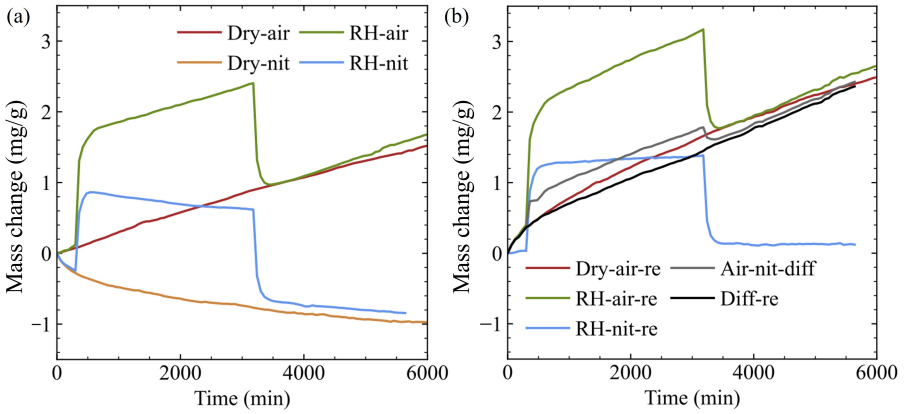

Figure 5.11 (a) Mass changes in T710_F at 75 °C under conditions of dry air, air with 80% relative humidity, dry nitrogen, and nitrogen with 80% relative humidity and (b) calibrated mass changes, where "Dry-air-re" = "Dry-air" – "Dry-nit", "RH-air-re" = "RH-air" – "Dry-nit", "RH-nit-re" = "RH-nit" – "Dry-nit", "Air-nit-diff" = "RH-air-re" – "RH-nit-re", as illustrated in Fig. 5.12. "Diff-re" is the amended results of "Air-nit-diff", where sharp jumps around RH loading and unloading time points are removed.

Upon loading 80% RH, the mass of bitumen samples immediately increases no matter using air or nitrogen as the carrying gas. Under the condition of air-based RH, the sample mass continues to increase until the unloading of RH. This increase is attributed to the combined effects of moisture absorption, oxidative ageing, and vaporization. In contrast, for the sorption with nitrogen and RH, after initial increase, the sample mass decreases again. This pattern suggests that the loss of volatile components from the bitumen sample outweighs the dynamic absorption of moisture. Once the RH is removed, the sample mass in the air environment continues to increase due to further ageing and that under nitrogen condition decreases again resulting from the continued vaporization.

During the air-based drying period following the loading and unloading of relative humidity, a faster mass increase rate is observed compared to that in the constant dry condition. To further analyze the impact of moisture on ageing kinetics, the mass changes under air conditions were calibrated and are depicted in Fig. 5.11 (b). Given that the

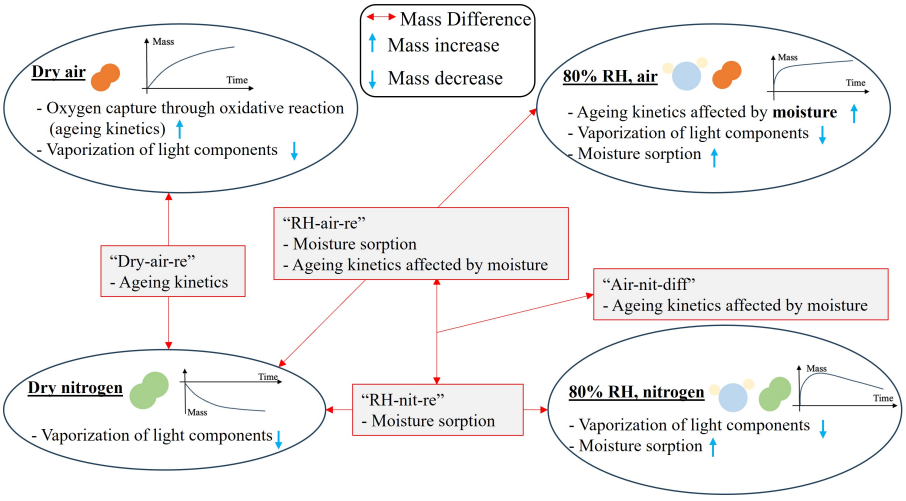

Figure 5.12 Illustration of sorption and reaction mechanisms for bitumen under four conditions, namely, dry air, dry nitrogen, 80% RH with air, and 80% RH with nitrogen.

mass decrease in dry nitrogen is ascribed to the loss of volatile components in bitumen, which applies similarly to bitumen in dry air, the net mass increase due to oxidative ageing can be calculated by subtracting the mass changes in dry nitrogen from that in dry air, denoted as "Dry-air-re" in Fig. 5.11 (b). This calculation yields a greater mass increase, indicative of the actual amount of oxygen captured during the ageing process.

The weight loss of volatile components, as determined from the sorption test under dry nitrogen condition, is also used to calibrate the mass changes under both wet air and wet nitrogen conditions, as shown as the "RH-air-re" and "RH-nit-re" in the figure. After removing the impact of vaporization, the "RH-nit-re" describes only the mass change caused by moisture sorption process, which initially increases significantly and then gradually approaches equilibrium during the RH loading period. A faster convergence to equilibrium is observed compared to the moisture sorption at lower temperatures (Fig. 5.1). However, in the case of "RH-nit-re", the overall mass change still encompasses both moisture sorption and ageing kinetics affected by moisture.

The difference in the sample mass between "RH-air-re" and "RH-nit-re" was calculated and is denoted as "Air-nit-diff" in Fig. 5.11 (b), representing the actual mass change due to oxidative ageing in the presence of moisture. As elucidated in Chapter 2, in DVS, moisture sorption of bitumen consists of surface adsorption and bulk absorption. Any contaminants, such as dust attached to the sample pan, can induce noticeable mass variations, especially during the initial testing state. In light of this, the abrupt jumps in "Air-nit-diff" near the beginning points of loading and unloading may be caused by different amounts of contaminants attached to the two samples. For a better visualization of the dynamic ageing process, these abrupt jumps were smoothed under the assumption of the same moisture sorption in different bitumen samples (of the same mass and under identical relative humidity), as represented by the "Diff-re". By comparing the mass changes

of "Dry-air-re" and "Diff-re", a slower oxidative reaction is observed in the presence of moisture, while a faster reaction is revealed once the moisture is removed, compared to the reactions occurring in the dry air condition.

Fig. 5.13 depicts the mass changes of fresh V710 under the four conditions at 80 °C. Analogous to the results obtained from the fresh T710, V710 also exhibits an increasing mass over time in dry air and a decreasing mass in dry nitrogen. The introduction of RH leads to similar initial mass increases for samples in air and nitrogen, with distinct mass changes during the subsequent loading period, as illustrated in Fig. 5.13 (a). The calibrated mass changes are shown in Fig. 5.13 (b). According to the calibrated results, the oxidative ageing of V710 is faster in the presence of moisture and slower after the removal of moisture, aligning with the observations for T710.

In the presence of moisture, the direct interaction between oxygen and the surface of bitumen sample is inhibited by the adsorbed moisture layers. Within the bitumen film, there is also a competition between the diffusion of oxygen and moisture. The reaction efficiency depends on the fraction of active components exposed to oxygen. In this case, it is plausible that in dry air, more oxygen interacts with bitumen compared to that in wet air. As a result, a slower reaction is revealed in the presence of moisture. The faster oxidative reaction after the removal of moisture could be attributed to the open diffusion pathways formed during moisture diffusion process, especially through the clustering of water molecules. These pathways not only facilitate faster oxygen diffusion and higher solubility but also potentially expose more active bitumen component to oxygen, thereby accelerating the reaction process, as illustrated in Fig. 5.14.

5.5 Summary

The mutual effects of moisture and ageing are indispensable for a comprehensive understanding of moisture- and ageing-caused degradation of pavement performance. In this chapter, to provide a deep insight into these mutual effects, we evaluated the effects of

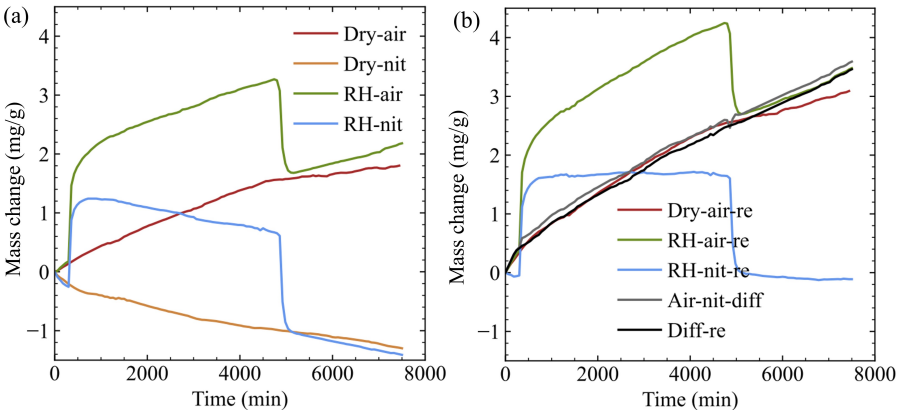

Figure 5.13 (a) Mass changes in V710_F at 80 °C under conditions of dry air, air with 80% relative humidity, dry nitrogen, and nitrogen with 80% relative humidity and (b) calibrated mass changes. The legends denote the same meaning as explained in Fig. 5.11.

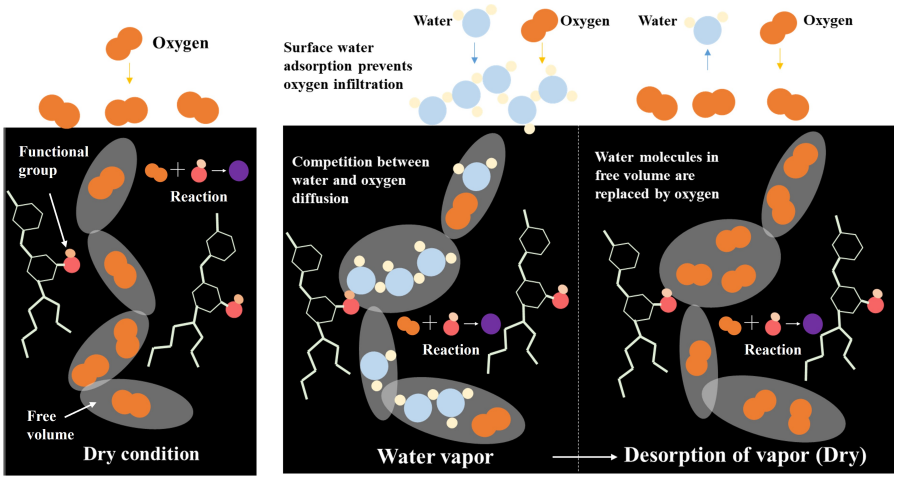

Mechanisms of oxygen diffusion in dry condition

Interplay between moisture and oxygen diffusion

Figure 5.14 Effects of water on the oxygen diffusion in bitumen.

ageing on the moisture diffusion behavior and moisture-caused damage within bitumen, as well as the ageing kinetics of fresh bitumen in the presence of moisture.

Results show that moisture diffusion in bitumen depends on testing temperature, ageing level, bitumen type, and penetration grade. The activation energy for diffusion demonstrates an increasing trend for bitumen at higher ageing level, signifying a higher energy barrier for diffusion. The free volume theory and the Eyring's absolute reaction rate theory indicate that both free volume and polarity contribute to the increased activation energy, with the former decreasing and the latter increasing as ageing proceeds. A linear relationship between the pre-exponential factor and activation energy in the Arrhenius equation is observed. By integrating this linear relationship with how the activation energy varies with free volume and polarity (determined by chemical or rheological tests), the diffusion coefficient for different bitumen types can thus be predicted.

Saturated moisture concentration initially decreases and then increases with increasing ageing level. Two concurrent but conflicting factors are associated with this behavior, i.e., free volume and polarity. As ageing goes on, the decreased free volume restrains the solution of moisture in bitumen while the increased polarity provides more available nuclei for water clusters, thereby increasing the moisture concentration. The van't Hoff relationship reveals that sorption enthalpy consists of the enthalpy of vapor condensation and that of energy required for the mixing of water and bitumen. The former keeps invariant while the latter decreases with increasing polarity, which avails the chemical affinity between water and bitumen.

Rheological properties of aged bitumen vary at different moisture conditions. Bitumen conditioned by water immersion exhibits the highest rheological index and Glove-Rowe paramter, whereas wetting-drying cycles lead to the lowest crossover frequency and crossover modulus. These differences are attributed to the different applications of leach-

ing in immersion, wet-dry cycle, and humidity conditions. This leaching refers to the removal of oxidized products on bitumen surface, which depends on the ageing level of bitumen. More aged bitumen provides more leachable products and therefore presents more serious leaching effects.

Dynamic vapor sorption results demonstrate that a slower oxidation reaction is obtained in the presence of moisture. Upon removing moisture, the oxidative reaction occurs at a faster rate than the one at constant drying condition. Moisture adsorbed on the surface of bitumen and diffused within bitumen prevents the direct contact between oxygen and bitumen, thus reducing reaction rate. After the removal of moisture, the left open pathways created by moisture diffusion expose more bitumen to oxygen, leading to an accelerated oxidation.

References

Ali, S. A., Zaman, M., Ghabchi, R., Rahman, M. A., Ghos, S., & Rani, S. (2022). Effect of additives and aging on moisture-induced damage potential of asphalt mixes using surface free energy and laboratory-based performance tests. *International Journal of Pavement Engineering*, *23*(2), 285–296.

Apeagyei, A. K., Grenfell, J. R. A., & Airey, G. D. (2014). Moisture-induced strength degradation of aggregate-asphalt mastic bonds. *Road Materials and Pavement Design*, *15*, 239–262.

Azimi Alamdary, Y., Singh, S., & Baaj, H. (2019). Laboratory simulation of the impact of solar radiation and moisture on long-term age conditioning of asphalt mixes. *Road Materials and Pavement Design*, *20*(sup1), S521–S532.

Bird, R. B., Stewart, W. E., & Lightfoot, E. N. (2002). Transport phenomena. *John Wiley and Sons: New York*.

Bouvet, G., Dang, N., Cohendoz, S., Feaugas, X., Mallarino, S., & Touzain, S. (2016). Impact of polar groups concentration and free volume on water sorption in model epoxy free films and coatings. *Progress in Organic Coatings*, *96*, 32–41.

Broudin, M., Le Gac, P.-Y., Le Saux, V., Champy, C., Robert, G., Charrier, P., & Marco, Y. (2015). Water diffusivity in PA66: Experimental characterization and modeling based on free volume theory. *European Polymer Journal*, *67*, 326–334.

Chen, Geng, J., Chen, H., Niu, Y., Wang, R., Wu, W., Zhao, S., & Zhong, Z. (2022). Diffusion of moisture and oxygen in bitumens using electrochemical impedance spectroscopy. *Fuel*, *315*, 123212.

Chen, X., Xiao, H., Cao, C., Yan, C., Ren, D., & Ai, C. (2022). Study on moisture diffusion behavior in asphalt binder based on static and dynamic pore water conditions. *Journal of Materials in Civil Engineering*, *34*(8), 04022183.

Cheng, Kong, F., & Zhang, X. (2021). Application of the Langmuir-type diffusion model to study moisture diffusion into asphalt films. *Construction and Building Materials*, *268*, 121192.

Cheng, Little, D. N., Lytton, R. L., & Holste, J. C. (2003). Moisture damage evaluation of asphalt mixtures by considering both moisture diffusion and repeated-load conditions. *Transportation Research Record*, *1832*(1), 42–49.

Das, P. K., Balieu, R., Kringos, N., & Birgisson, B. (2015). On the oxidative ageing mechanism and its effect on asphalt mixtures morphology. *Materials and Structures*, *48*, 3113–3127.

Ding, Y., Li, D., Wang, Y., & Wei, W. (2022). Prediction of the rejuvenator diffusion coefficient in aged asphalt based on free volume theory. *ACS Sustainable Chemistry & Engineering*, *11*(1), 407–415.

Eyring, H. (1936). Viscosity, plasticity, and diffusion as examples of absolute reaction rates. *The Journal of chemical physics*, *4*(4), 283–291.

George, S. C., & Thomas, S. (2001). Transport phenomena through polymeric systems. *Progress in Polymer science*, *26*(6), 985–1017.

Gusev, A., Müller-Plathe, F., Van Gunsteren, W., & Suter, U. (1994). Dynamics of small molecules in bulk polymers. *Atomistic modeling of physical properties*, 207–247.

Han, R., Jin, X., & Glover, C. (2013). Oxygen diffusivity in asphalts and mastics. *Petroleum Science and Technology*, *31*(15), 1563–1573.

Hansen, C. M. (2007). *Hansen solubility parameters: A user's handbook*. Taylor & Francis.

He, X., Hochstein, D., Ge, Q., Ali, A. W., Chen, F., & Yin, H. (2018). Accelerated aging of asphalt by UV photo-oxidation considering moisture and condensation effects. *Journal of Materials in Civil Engineering*, *30*(1), 04017261.

Herrington, P. R. (2012). Diffusion and reaction of oxygen in bitumen films. *Fuel*, *94*, 86–92.

Herrington, P. R., Wu, J. P., van den Kerkhof, L. C., & Bagshaw, S. A. (2021). Water diffusion in bitumen films. *Construction and Building Materials*, *294*, 123530.

Huang, S.-C., Glaser, R., & Turner, F. (2012). Impact of water on asphalt aging: Chemical aging kinetic study. *Transportation research record*, *2293*(1), 63–72.

Hung, A. M., Goodwin, A., & Fini, E. H. (2017). Effects of water exposure on bitumen surface microstructure. *Construction and Building Materials*, *135*, 682–688.

Jin, X., Han, R., Cui, Y., & Glover, C. J. (2011). Fast-rate–constant-rate oxidation kinetics model for asphalt binders. *Industrial & Engineering Chemistry Research*, *50*(23), 13373–13379.

Jou, J.-H., & Huang, P.-T. (1992). Compatibility effect on moisture diffusion in polyimide blends. *Polymer*, *33*(6), 1218–1222.

Kretschmer, C. B., Nowakowska, J., & Wiebe, R. (1946). Solubility of oxygen and nitrogen in organic solvents from —25° to 50° C. *Industrial & Engineering Chemistry*, *38*(5), 506–509.

Kriz, P., Stastna, J., & Zanzotto, L. (2008). Glass transition and phase stability in asphalt binders. *Road Materials and Pavement Design*, *9*(sup1), 37–65.

Liang, Y., Wu, R., Harvey, J. T., Jones, D., & Alavi, M. Z. (2019). Investigation into the oxidative aging of asphalt binders. *Transportation Research Record*, *2673*(6), 368–378.

Liu, L., & Guo, Q.-X. (2001). Isokinetic relationship, isoequilibrium relationship, and enthalpy-entropy compensation. *Chemical Reviews*, *101*(3), 673–696.

Liu, Z., Cao, L., Zhou, T., & Dong, Z. (2020). Multiscale investigation of moisture-induced structural evolution in asphalt–aggregate interfaces and analysis of the relevant chemical relationship using atomic force microscopy and molecular dynamics. *Energy & Fuels*, *34*(4), 4006–4016.

Mansuri, A., Völkel, M., Feuerbach, T., Winck, J., Vermeer, A. W., Hoheisel, W., & Thommes, M. (2023). Modified free volume theory for self-diffusion of small molecules in amorphous polymers. *Macromolecules*, *56*(8), 3224–3237.

Menapace, I., & Masad, E. (2020). The influence of moisture on the evolution of the microstructure of asphalt binders with aging. *Road Materials and Pavement Design*, *21*(2), 331–346.

Menapace, I., Yiming, W., & Masad, E. (2017). Chemical analysis of surface and bulk of asphalt binders aged with accelerated weathering tester and standard aging methods. *Fuel*, *202*, 366–379.

Nguyen, T., & Ali, S. F. (1998). Effect of nitrogen on the solubility and diffusivity of carbon dioxide into oil and oil recovery by the immiscible WAG process. *Journal of Canadian Petroleum Technology*, *37*(02).

Noguera, J. A. H., Quintana, H. A. R., & Gómez, W. D. F. (2014). The influence of water on the oxidation of asphalt cements. *Construction and building materials*, *71*, 451–455.

Petersen, J. C. (2009). A review of the fundamentals of asphalt oxidation: Chemical, physicochemical, physical property, and durability relationships. *Transportation Research Circular*, (E-C140).

Petropoulos, J. (1994). Mechanisms and theories for sorption and diffusion of gases in polymers. In *Polymeric gas separation membranes* (pp. 17–81). CRC Press.

Qu, X., Liu, Q., Guo, M., Wang, D., & Oeser, M. (2018). Study on the effect of aging on physical properties of asphalt binder from a microscale perspective. *Construction and Building Materials*, *187*, 718–729.

Redelius, P. (2004). Bitumen solubility model using Hansen solubility parameter. *Energy & Fuels*, *18*(4), 1087–1092.

Redelius, P., & Soenen, H. (2015). Relation between bitumen chemistry and performance. *Fuel*, *140*, 34–43.

Rubinsten, M., & Colby, R. (2003). *Polymer physics*. United States of America.

Seo, J., & Han, H. (2001). Water diffusion studies in polyimide thin films. *Journal of applied polymer science*, *82*(3), 731–737.

Sharma, J., Tewari, K., & Arya, R. K. (2017). Diffusion in polymeric systems–a review on free volume theory. *Progress in Organic Coatings*, *111*, 83–92.

Siddiqui, M. N., & Ali, M. F. (1999). Studies on the aging behavior of the Arabian asphalts. *Fuel*, *78*(9), 1005–1015.

Thomas, K. P. (2002). Impact of water during the laboratory aging of asphalt. *Road Materials and Pavement Design*, *3*(3), 299–315.

Vasconcelos, K. L., Bhasin, A., & Little, D. N. (2011). History dependence of water diffusion in asphalt binders. *International Journal of Pavement Engineering*, *12*(5), 497–506.

Vrentas, J., & Duda, J. (1977a). Diffusion in polymer–solvent systems. ii. A predictive theory for the dependence of diffusion coefficients on temperature, concentration, and molecular weight. *Journal of Polymer Science: Polymer Physics Edition*, *15*(3), 417–439.

Vrentas, J., & Duda, J. (1977b). Diffusion in polymer—solvent systems. I. Reexamination of the free-volume theory. *Journal of Polymer Science: Polymer Physics Edition*, *15*(3), 403–416.

Wang, B.-g., Lv, H.-l., & Yang, J.-c. (2007). Estimation of solvent diffusion coefficient in amorphous polymers using the Sanchez–Lacombe equation-of-state. *Chemical engineering science*, *62*(3), 775–782.

Weigel, S., & Stephan, D. (2017). Modelling of rheological and ageing properties of bitumen based on its chemical structure. *Materials and Structures*, *50*, 1–15.

White, R. P., & Lipson, J. E. (2014). Free volume, cohesive energy density, and internal pressure as predictors of polymer miscibility. *Macromolecules*, *47*(12), 3959–3968.

Williams, M. L., Landel, R. F., & Ferry, J. D. (1955). The temperature dependence of relaxation mechanisms in amorphous polymers and other glass-forming liquids. *Journal of the American Chemical society*, *77*(14), 3701–3707.

Xiao, R., & Huang, B. (2022). Moisture damage mechanism and thermodynamic properties of hot-mix asphalt under aging conditions. *ACS Sustainable Chemistry & Engineering*, *10*(45), 14865–14887.

Yiu, C. K., King, N. M., Carrilho, M. R., Sauro, S., Rueggeberg, F. A., Prati, C., Carvalho, R. M., Pashley, D. H., & Tay, F. R. (2006). Effect of resin hydrophilicity and temperature on water sorption of dental adhesive resins. *Biomaterials*, *27*(9), 1695–1703.

Zheng, J.-M., Qiu, J., Madeira, L. M., & Mendes, A. (2007). Polymer structure and the compensation effect of the diffusion pre-exponential factor and activation energy of a permeating solute. *The Journal of Physical Chemistry B*, *111*(11), 2828–2835.

6

Chemometric analysis of chemo-mechanical relationship of binders

Previous chapters have delved into the moisture behavior in bitumen, the effects of ageing on its properties, and their interplay. This chapter revisits the physicochemical-rheological relationship of various types of bituminous binders under different moisture and ageing conditions using multivariate data analysis, aiming at providing new insights into the evaluation and prediction of bitumen properties and pavement performance, along with the understanding of underlying mechanisms. To achieve this, the classification of bitumen types, ageing states, and testing conditions is conducted through classification methods, aided by variable selection methods. Subsequently, the prediction of rheological properties of bitumen based on its physicochemical variables is achieved using linear and non-linear regression models. Four distinct variable selection methods are employed to increase the predictive performance and the interpretability and reliability of predicted results.

To begin, Section 6.1 introduces the application of chemometric analysis in bitumen area. Section 6.2 details the preprocessing of multivariate data, classification models, regression models, four variable selection methods, evaluation metrics, specific procedures for classification and prediction analysis. The classification performances based on three datasets are discussed in Section 6.3. It also elaborates the characteristic chemical, structural, and thermal variables indicative of different sources, ageing states, and the effects of moisture and field ageing. Section 6.4 presents the prediction performance for various combinations of regression models and variable selection methods. Finally, Section 6.5 summarizes the key findings derived from this chapter.

Parts of this chapter have been published in Ma L., Varveri A., Jing R., Erkens S. (2023). Chemical characterization of bitumen type and ageing state based on FTIR spectroscopy and discriminant analysis integrated with variable selection methods. *Road Materials and Pavement Design*, 24 (sup1), 506-520

6.1 Introduction

Many studies have focused on the evaluation of moisture diffusion and oxidative ageing in bitumen, along with their effects on both bitumen properties and the long-term performance of asphalt pavement. A variety of test protocols, parameters, and indices are proposed to describe the chemical and structural changes caused by moisture and ageing conditions, as well as the resultant degradations in the physical, rheological, and mechanical properties of bitumen. Both ageing and moisture behavior can be integrated into the modeling of pavement asphalt to provide more accurate evaluation, modeling, and prediction of its field performance. This requires correlating the oxygen/moisture-affected chemical and structural changes to the mechanical properties of bitumen, and further to the deterioration of pavement performance (Das et al., 2015; Nobakht et al., 2020; Qian et al., 2021; Redelius & Soenen, 2015).

A single evaluation index has been demonstrated to be insufficient for evaluating the chemical and mechanical properties of bitumen (Pipintakos et al., 2022), as well as for understanding the chemo-mechanical relationship, especially when targeting the generalization of all types of bitumen. To obtain a more accurate evaluation of the chemical and mechanical properties of bitumen and the relationship between them, multiple parameters were derived from different tests as discussed in Chapter 4. However, significant challenges arose, particularly the substantial overlaps for characteristic chemical, structural, and thermal properties in the curves obtained from FTIR, DSC, and GPC tests. These include the peak overlap in FTIR spectra, the overlap of different thermal behaviors in thermograms, and the continuous weight distributions in chromatograms, which are difficult to distinguish or separate through preliminary analysis. Taking FTIR spectra as an example, apart from sulfoxide- and carbonyl-related peaks, some other peaks and spectral regions are also informative of the chemical changes in bitumen due to ageing. However, the overlap of different functional groups in these spectral regions (Asemani & Rabbani, 2020) and the shift of the fingerprint area caused by increased polarity (Mirwald et al., 2020a) make it rather difficult to monitor the change of functional groups during the ageing process.

To address the overlap problem, for FTIR, peak decomposition based on the second derivative of the spectra can be utilized to distinguish distinct overlapping peaks within original spectra. For DSC, modulated DSC is capable of separating thermokinetic (glass transition) and thermodynamic (crystallization) processes. However, as discussed in Frigio et al. (2013), even modulated DSC cannot differentiate recrystallization and dissolution peaks during the heating process. Rather than focusing on decomposing experimental curves and isolate specific properties, it may be an effective alternative approach to consider more comprehensive sets of variables derived from the entire curves. Furthermore, for bitumen samples with varying sources or ageing states, the chemical, structural, and thermal differences are encompassed in the whole curves. The consideration of specific regions may not be sufficient in characterizing the complex properties of bitumen.

Chemometric approaches such as principal component analysis (PCA), hierarchical cluster analysis (HCA), linear discriminant analysis (LDA), partial least squares (PLS) analysis, and support vector regression (SVR) (Gómez-Caravaca et al., 2016; Khanmohammadi et al., 2012) are increasingly employed to extract useful chemical information from the spectroscopic tests. Recent studies have used FTIR spectra integrated with chemo-

metrics to precisely identify bitumen sources (Weigel & Stephan, 2018) and ageing states (Primerano et al., 2022), determine bitumen SARA fractions (Melendez et al., 2012; Mohammadi et al., 2021), and predict the physical and mechanical properties of bitumen (Siroma et al., 2021; Sun et al., 2020). Wilt and Welch (1998) predicted the asphaltene content in crude oil using a PLS model with an R^2 value of 0.95. Aske et al. (2001) reported a high accuracy of PCA and PLS in determining bitumen SARA fractions based on FTIR spectra. Weigel and Stephan (2018) accurately differentiated bitumen types and ageing states using PCA and LDA models and predicted the rheological properties based on PLS analysis.

Despite the effective predictions achieved through multivariate analysis on high-dimensional datasets, the latent variables derived from full curves are often less interpretable than the original variables (Xiaobo et al., 2010). Moreover, a large number of input variables inevitably contain more irrelevant and noisy variables, which can have harmful effects on prediction accuracy. To this end, variable selection has been used to identify and select a smaller and more informative subset from the original variable sets for enhanced interpretation and prediction. Common variable selection techniques include coefficient-based filter (CF), genetic algorithm (GA), simulated annealing (SA), moving windows (MW), and competitive adaptive re-weighted sampling (CARS) methods. Li et al. (2019) discussed different variable selection methods in the context of determining the penetration grade of bitumen. It was reported that the support vector machine (SVM), when combined with CARS, showed the best performance. Mohammadi et al. (2021) applied a hybrid GA and SVM regression (GA-SVM-R) model to predict the SARA fractions of bitumen. This model exhibited better performance in the quantitative determination of SARA fractions compared to GA-PLS-R. The application of variable selection approaches has enhanced the predictive ability of discriminant and regression models.

This chapter focuses on the physicochemical-rheological characterization of various types of bituminous binders at different moisture and ageing conditions. To overcome the limitations of individual indices, full spectra, chromatograms, and thermograms obtained from FTIR, GPC, and DSC tests, respectively, are used for the classification of various bitumen samples and the prediction of their rheological properties. Advanced classification and regression techniques are introduced to deal with these multivariate data.

Specifically, the classification of bitumen type, ageing state, and testing conditions is initially performed using the PCA-LDA analysis coupled with the MW and SA variable selection methods. The classification analysis facilitates the understanding of varying chemical and structural properties originating from bitumen sources and different testing conditions and exemplifies a classification technique that can quickly and efficiently identify bitumen in terms of specific characteristics such as sources or ageing states based on various efficient chemical and physical tests. Subsequently, the prediction of different rheological properties is achieved based on PLS and SVR models. Four variable selection methods, namely, CF, MW, SA, and GA, are utilized to improve the prediction accuracy and to capture chemical and physical variables critical to various bitumen properties.

6.2 Chemometric analysis

6.2.1 Preprocessing methods

The datasets obtained from FTIR, GPC, and DSC tests are complex, high-dimensional, and often subject to noise originating from instrument limitations or operational procedures (Mishra et al., 2020). Therefore, data preprocessing (DP) is essential for accurate multivariate differentiation of various binders at different conditions and prediction of rheological properties affected by moisture and ageing behavior. Preprocessing methods utilized in this chapter involve standard normal variate (SNV) transformation, Savitzky-Golay (SG) smoothing, and outlier detection (Rinnan et al., 2009).

The SNV is utilized to mitigate baseline shifts and scattering effects within datasets. For each individual sample, the SNV initially calculates the mean and standard deviation of all pooled variables. Each variable is then centered by subtracting the obtained mean value and subsequently normalized by dividing it by the standard deviation. The resulting variables have a zero mean and a standard deviation of one.

The Savitzky-Golay (SG) method consists of two primary functions, namely, curve smoothing and derivative calculation (Rinnan et al., 2009). The smoothing is obtained by fitting polynomials of specified degree to the target curves within a defined window range, using least squares regression. The window size and the degree of polynomial, along with the order of the derivative are critical parameters affecting the subsequent multivariate analysis. A large window size coupled with a low-degree polynomial may inadvertently remove part of important information, whereas a converse setting might not effectively filter out noise (Zimmermann & Kohler, 2013). The selection of appropriate order of derivatives helps to accentuate small structural differences between similar spectra or signals and to extract useful features (Melendez et al., 2012).

The presence of outliers, namely the observations that deviate significantly from the majority of the dataset, influences the outcomes of chemometric analysis. To identify these outliers, Q-residuals and Hotelling's T2 (Mohammadi et al., 2021; Morais et al., 2020) were used in this chapter. The Q-residuals represent the sum of squares of residuals and describe how well the fitted results conform to the model. Outliers typically exhibit larger Q-residuals than other samples. Hotelling's T2 is essentially an F-distribution of Mahalanobis distances from the center of a data cluster. The outliers were determined based on Q-residuals and Hotelling's T2 with a confidence level of 95%.

An optimal DP method can significantly enhance the accuracy of chemometric analysis (Lee et al., 2017; Rinnan et al., 2009). There is no universally superior DP method or definitive combination of multiple DP methods. The selection of DP methods should be customized for each dataset based on its characteristics and objectives of chemometric analysis. For different datasets utilized, the optimization of DP methods was conducted individually, focusing on the accuracy of classifying bitumen type using the PCA-LDA model (as will be explained in the following section) and on the prediction performance of crossover modulus using the PLS model. The optimization of DP methods involves decisions on whether to use the SNV method and selecting appropriate window length (among 10, 15, and 20), polynomial degree (among 4, 5, and 6), and order of derivative (among 0, 1, and 2) for SG smoothing.

6.2.2 Classification models

Chemometric methods such as PCA, PLS, and LDA are powerful for sample classification and pattern recognition. They establish mathematical relationships between a set of descriptive variables (e.g., chemical spectral information) and qualitative variables (e.g., defined class). PCA, in particular, is primarily used to transform datasets with numerous variables into uncorrelated principal components, thereby reducing dimensionality. The scores of target samples are calculated as

$$\boldsymbol{P} = \boldsymbol{X} \times \boldsymbol{W} \tag{6.1}$$

where $\boldsymbol{X}$ denotes the dataset composed of m samples (categorized into l groups) and n variables, $\boldsymbol{W}$ is an $n \times p$ loading matrix where p is the number of selected principal components, and $\boldsymbol{P}$ represents an $m \times p$ score matrix that describes the projection of X onto a p-dimensional feature subspace. To obtain W, the eigenvectors and eigenvalues of the covariance matrix of the variables in a dataset are calculated. The eigenvalues are then sorted in descending order and p eigenvectors corresponding to the largest eigenvalues are selected to construct $\boldsymbol{W}$ (Westerhuis et al., 1998).

LDA is a linear discriminant analysis technique that achieves supervised dimensionality reduction by selecting directions in space that maximize separation among the different classes based on Euclidean distance. Therefore, the loading matrix $\boldsymbol{W}$ of LDA minimizes the scatter within each class and maximizes the scatter between classes. LDA can only project a dataset onto a subspace with a dimension lower than the number of classes l.

In the PCA-LDA approach, PCA is initially performed to reduce the dimensionality of a dataset while retaining as much variance of the original data as possible. The PCA scores are then used to perform LDA modeling. In this combined PCA-LDA model, the loading matrix $\boldsymbol{W}$ is formed by transforming the PCA scores using the LDA loadings, resulting in a matrix of dimension $n \times q$. Here q represents the number of components chosen for the LDA. The PCA-LDA model performs classification on streamlined variables, offering improved differentiation quality.

6.2.3 Regression models

PLS regression is a powerful technique for modeling and analyzing large, multivariate, and collinear datasets. In this method, a data matrix of predictors $\boldsymbol{X}$ and a data matrix of responses $\boldsymbol{Y}$ are decomposed into their respective scores $\boldsymbol{T}$ and $\boldsymbol{U}$, and loadings $\boldsymbol{P}$ and $\boldsymbol{Q}$, such that $\boldsymbol{X} = \boldsymbol{T} \times \boldsymbol{P}^{\mathrm{T}}$ and $\boldsymbol{Y} = \boldsymbol{U} \times \boldsymbol{Q}^{\mathrm{T}}$. The covariance between the scores of the predictors and the responses is maximized by adjusting the decomposition directions (i.e., loadings) using algorithms such as the non-linear iterative partial least squares (NIPALS) (Manne, 1987; Westerhuis et al., 1998). This allows the transformed $\boldsymbol{Y}$ to be predicted as a function of transformed $\boldsymbol{X}$. As a result, through back transforming, the original $\boldsymbol{Y}$ can be described as

$$\boldsymbol{Y} = \beta \boldsymbol{X} \tag{6.2}$$

where β is the regression coefficient matrix.

Support vector regression (SVR) is developed based on the support vector machine (SVM), which is originally formulated for classification. The SVR aims to find a hyperplane in a high-dimensional space that best fits the target values within a specified margin

with a width of ϵ (namely the deviation from actual values no larger than ϵ). Additionally, slack variables ξ_i and ξ_i^* are introduced to account for the deviations beyond this margin. SVR tries to minimize the coefficients of the hyperplane (to ensure the flatness of the hyperplane) and the sum of the slack variables (to reduce the errors) at the same time:

$$\begin{aligned} &\text{minimize} \quad \frac{1}{2}||w||^2 + C\sum_{i=1}^{\ell}(\xi_i + \xi_i^*) \\ &\text{subject to} \quad \begin{cases} y_i - w^{\mathrm{T}}x_i - b \le \epsilon + \xi_i \\ w^{\mathrm{T}}x_i + b - y_i \le \epsilon + \xi_i^* \\ \xi_i, \xi_i^* \ge 0 \end{cases} \end{aligned} \tag{6.3}$$

where w is the feature vector, b is a constant, x_i and y_i are independent and dependent variables respectively in $\boldsymbol{X}$ and $\boldsymbol{Y}$. The constant $C > 0$ balances the trade-off between the flatness of the hyperplane and the amount of deviations from the marginal range (Smola & Schölkopf, 2004). A high value of C emphasizes the correct prediction of all training examples correctly, which is not recommended for a dataset with many noisy observations. Kernel functions, such as polynomial, radial basis function (RBF), and sigmoid, can be introduced to preprocess $\boldsymbol{X}$, facilitating an effective description of non-linear relationships between predictors and responses. When using kernel functions, the kernel coefficient γ must be determined, which defines the influence of a training sample on the regression process. A high γ indicates a better fitting of the training data despite with a risk of overfitting.

6.2.4 Variable selection methods

Coefficient-based filter

Feature selection through filtering is one of the simplest techniques for variable selection. The coefficient-based filter (CF) method uses the regression coefficients as the filtering criterion (Mehmood et al., 2012). This approach starts with conducting the PLS regression on the complete dataset. The obtained regression coefficients quantify the correlation between each variable and the response. The variable revealing the lowest correlation (i.e., the smallest absolute value of the regression coefficient) is removed, and the left variables are used to perform PLS again. This procedure is iterated until removing additional variables results in decreased accuracy according to predefined evaluation metrics.

Moving windows

The MW selection method allows the identification of a more informative region within the full curve, enhancing the differentiation of observations or the prediction of responses. To achieve this, two variables are to be optimized, namely, the window size and the window region. For FTIR, considering that most peak areas span more than 50 cm^{-1}, a spectral width ranging from 50 cm^{-1} to 500 cm^{-1} was utilized, with a wavenumber moving step of 50 cm^{-1}. This corresponds to a window size containing 10 to 100 variables and a moving step of 10 variables. For each window size, a series of sub-windows were generated by moving the window through the whole spectrum with the specified moving step. The optimal window size and window region were assessed based on the classification

accuracy for discriminant analysis and the root mean square error of cross-validation for regression analysis. The same window size and moving step were also applied to the multivariate analysis of GPC and DSC results.

Simulated annealing

Simulated annealing (SA) is a probabilistic global optimization technique that is particularly effective in the presence of large numbers of local optima (Kirkpatrick et al., 1983). This method simulates the annealing of crystals, where materials,after heated to a high temperature, are gradually cooled to minimize their internal energy. Unlike material annealing, simulated annealing focuses on the objective function of an optimization problem. The SA starts with a random selection of a subset of variables from a dataset,. The prediction accuracy is then calculated. Subsequently, some variables within this subset are swapped with variables outside of the subset, followed by a reevaluation of the prediction accuracy. The new variable set is accepted if it leads to increased accuracy. However, if the new set has a lower accuracy, the exchange process can still be accepted with a probability (po) that is quantified by

$$po(\Delta S) = \frac{-\Delta S}{T} \tag{6.4}$$

where ΔS is the difference in the prediction accuracy between the current and previous rounds, and T is a predefined cooling factor. This factor must be carefully determined to ensure a fair probability. Setting this factor too high may hinder convergence while setting it too low may restrict occasional fluctuation for escaping local optima. The acceptance of steps that do not immediately enhance accuracy is to avoid being frozen at a local optimum. The maximum iteration time is also needed to designate the end of the selection procedure. For FTIR, GPC, and DSC datasets, the number of variables ranging from 10 to 120 was utilized for multivariate analysis. The maximum iteration time was defined as 150. Trials of discriminant analysis with regard to bitumen type and ageing state showed that the prediction accuracy had limited improvement after 150 iterations.

Genetic algorithm

Genetic algorithm (GA) is an optimization technique that performs stochastic and global searches across a high-dimensional dataset. Inspired by the principles of biological evolution theory and natural selection, the GA allows variables that yield better fitting performance to have a higher probability to be included in the variable subset for next round of optimization. Moreover, a mutation step is incorporated to introduce a certain degree of randomness in selecting the variable subset. The GA starts with the selection of an initial population of variable subsets with a predefined size. The fitting performance of these variable subsets is then evaluated through a cross-validation procedure. Variables with higher performance are preserved for the next generation. Subsequently, crossover and mutation are applied to generate a new population of variable subsets. The crossover process refers to creating offspring by combining parent chromosomes, and mutation indicates the random alteration in variables to create genetic diversity in the population. For the GA incorporated in the PLS regression, the GA was executed with a threshold of variable selection 0.5, a population size of 100, generations of 150, a crossover probability of 0.5, and a mutation rate of 0.5 (Leardi & Gonzalez, 1998).

6.2.5 Evaluation metrics

The prediction of regression models can be evaluated by the root mean square errors of calibration ($RMSEC$), cross validation ($RMSECV$), and prediction ($RMSEP$), the determination coefficients of calibration (R^2_c), cross-validation (R^2_{cv}) and prediction (R^2_p), the relative percent difference (RPD), and the average bias:

$$RMSE = \sqrt{\frac{1}{N}\sum_{i=1}^{N}\left(\hat{y}_i - y_i\right)^2} \tag{6.5}$$

$$R^2 = 1 - \frac{\sum_{i=1}^{N}\left(\hat{y}_i - y_i\right)^2}{\sum_{i=1}^{N}\left(y_i - \bar{y}_i\right)^2} \tag{6.6}$$

$$RPD = \frac{SD}{RMSE} \tag{6.7}$$

$$bias = \frac{1}{N}\sum_{i=1}^{N}\left(\hat{y}_i - y_i\right) \tag{6.8}$$

where y_i and $\hat{y}_i$ represent the measured and predicted values for sample i, $\bar{y}_i$ is the mean value of y_i, N denotes the number of samples for calibration, cross-validation or prediction, and SD is the standard deviation of measured values for N samples. An RPD value higher than 2 implies a good model accuracy, and models with an RPD larger than 3 are considered to have excellent performance (Douglas et al., 2018). The R^2 and the bias indicate the linearity of regression models, i.e., the deviations from random distribution of residuals and the existence of systematic errors.

6.2.6 Methodology for classification of binders

For the classification of bitumen type and ageing state, the FTIR, GPC, and DSC test results of eight bituminous binders were utilized. These binders were obtained from three different suppliers: Q460, Q710, QPMB from source Q; V710 and VPMB from source V; and T710, T1015, and T1620 from source T. Each binder type at its fresh state (F) was subjected to four different laboratory ageing conditions, namely, oven ageing (O), 20 hours (1P), 40 hours (2P), and 80 (4P) hours of pressure aging vessel (PAV) ageing. Details on the preparation of bitumen samples at different ageing conditions, the methodologies employed for the FTIR, GPC, and DSC tests, and the discussions of the test results are provided in Chapter 4. For the FTIR tests, three replicates were conducted for each sample, while for the GPC and DSC tests, two replicates were performed for each sample, leading to a total of 117, 78, and 78 observations within FTIR, GPC, and DSC datasets, respectively, as shown in Fig. 6.1.

The classification of samples subjected to different conditions, namely, laboratory ageing, laboratory hydrothermal condition, and field condition, was conducted based on the FTIR spectra data. For laboratory ageing, the same set of samples as those used in the classification of bitumen type and ageing state was employed. Samples exposed to relative humidity, namely those belonging to the "RH" group as described in Section 5.3, were utilized for the laboratory moisture condition, including Q460, Q710, T1622, V710, V710_1P, V710_2P, V710_4P, and VPMB. At least two replicates were conducted for each

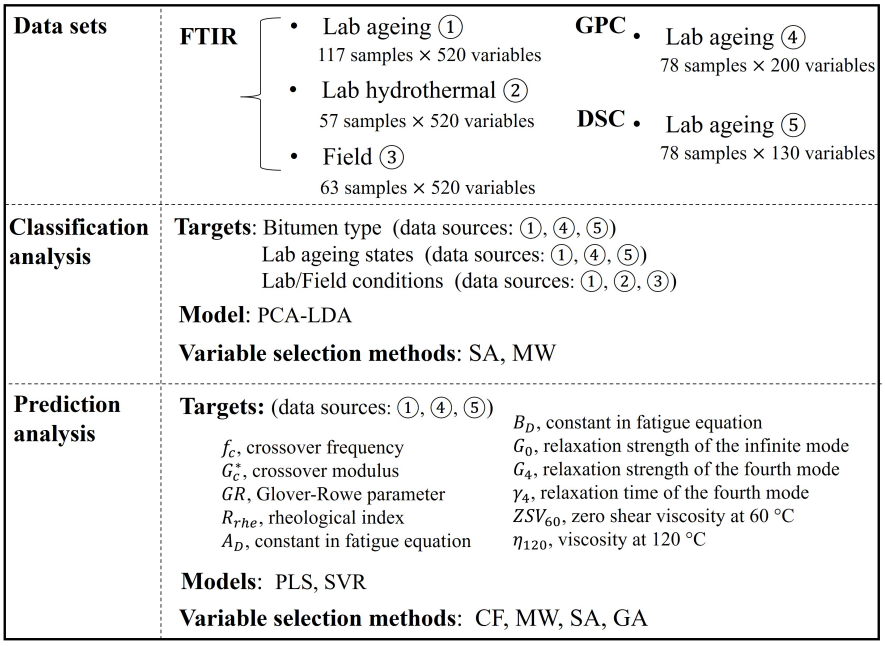

Figure 6.1 Overview of chemometric analysis of bituminous binders

sample, resulting in 57 observations in total. For field conditions, two binder types, V710 and VPMB, were subjected to the atmospheric conditions in Delft, Netherlands, from March 6, 2020 to March 6, 2021. They were exposed either without any shields for durations of 3, 4, 5, 6, 8, 10, and 12 months or with protection by UV-blocking panels for periods of 3, 4, 5, and 8 months. Each sample was prepared by placing a specific amount of bitumen into a glass container, which was then heated in an oven at 120 °C to form a homogeneous binder film with a thickness of 2 mm. These samples were then collected and their chemical composition was measured using FTIR. In sum, 63 FTIR spectra were obtained with at least two replicates for each field sample.

These datasets were then preprocessed to improve data quality. For the FTIR datasets used in this chapter, the initial variables consisted of a wavenumber range of 4000–600 cm^{-1} with a resolution of 1 cm^{-1}. Within this range, the spectral regions of 2400–1900 cm^{-1} and 4000–3700 cm^{-1} were manually excluded from further chemometric analysis because of their limited chemical information (Weigel & Stephan, 2017). Subsequently, the SNV method was applied to correct wavenumber scaling and background effects (Rinnan et al., 2009). This was followed by the SG method with a window size of 10, a 5-degree polynomial, and a 2^{nd} derivative to smooth the FTIR spectra. Each spectrum with a resolution of 1 cm^{-1} was then merged into a resolution of 5 cm^{-1}. Consequently, 520 spectral variables were ultimately selected for further multivariate analysis. For the GPC datasets, the GPC chromatograms within the elution time range of 5.0 – 24.9 min were sampled at an interval of 0.1 min, resulting in a total of 200 variables. The selected GPC variables were initially processed by the SNV method. The normalized dataset was then subjected

to the SG preprocessing with a window size of 10, a 5-degree polynomial, and a 1st derivative. The DSC datasets comprised 130 variables obtained from the thermograms within the temperatures ranging from -28 to 97 °C with an interval of 1 °C. The heat flow results at higher temperatures were excluded due to the absence of informative peaks. The SNV method was then applied on these 130 variables. To smooth the thermograms, the SG with a window size of 20, a 6-degree polynomial, and a 0th derivative was employed, followed by an additional SG process with a window size of 10, a 5-degree polynomial, and a 2nd derivative.

Subsequently, the PCA-LDA modeling was applied to the preprocessed FTIR, GPC, and DSC datasets to differentiate among bitumen types, laboratory ageing states, and lab/field conditions. Preliminary trial analysis using the PCA, LDA, and PCA-LDA models has been conducted, and results showed that the PCA-LDA model presents the best performance in classifying bitumen type and ageing states. As a result, the PCA-LDA model was used for further analysis. To increase the model's performance, the MW and SA variable selection methods were utilized to extract subsets from the original datasets. The classification performance of the PCA-LDA model on these subsets was compared, and the subset with the best performance was adopted as the ultimate input for the classification of bitumen type, ageing states, or lab/field conditions.

To quantify the robustness of the PCA-LDA model and mitigate the risk of overfitting, a 5-fold cross-validation was applied. This method divides the entire dataset into five subsets. Each subset is used exactly once as the validation set while the remaining subsets are combined to form the training set, leading to five different combinations of training and validation datasets. The classification accuracy was defined as the average of the proportion of samples correctly classified in each fold of the cross-validation results.

6.2.7 Methodology for prediction of rheological properties

Regression analysis was conducted on the FTIR, GPC, and DSC results for the laboratory-aged samples comprising eight binder types, each subjected to five distinct ageing levels, as summarized in Fig. 6.1. The same preprocessing procedures employed in the classification analysis were also applied to the FTIR, GPC, and DSC datasets utilized for predicting rheological properties. Additionally, the outlier detection was conducted to identify and remove abnormal observations. Of all the rheological properties calculated in Chapter 4, f_c, G_c^*, GR, R_{rhe}, A_D, B_D, G_0, G_4, γ_4, ZSV_{60}, and η_{120} were selected as the targets for prediction, where f_c indicates the crossover frequency, G_c^* is the crossover modulus, GR represents the Glover-Rowe parameter, R_{rhe} is the rheological index, A_D and B_D are two constants in the equation describing strain-based fatigue life of bitumen, G_0, G_4, and γ_4 are the relaxation moduli and relaxation time derived from relaxation tests, ZSV_{60} denotes the zero shear viscosity at 60 °C, and η_{120} represents the viscosity measured by Viscometer at 20 rpm and 120 °C. Details about these properties are elucidated in Chapter 4. For parameters that show significantly nonlinear changes with ageing level, logarithmic transformations were used in the prediction to mitigate the effects of the nonlinear relationships on the prediction accuracy, especially for the PLS model, which is primarily designed to model linear relationships. This logarithmic scale was implemented for all the selected parameters except R_{rhe}, A_D, B_D, which were used in their original scales.

Prior to regression analysis, all observations in a dataset were randomly divided into

calibration and validation/prediction groups at the ratio of 7:3. The calibration samples were used to train regression models, namely PLS and SVR. For the SVR analysis, the optimal configuration was determined by exploring variations in the kernels and the values for C, γ, and ϵ. The kernels used included linear, RBF, and poly functions. The tested values for C were 0.1, 1, 10, 50, 100, and 150, and γ was tested at 0.1, 0.5, and 1.0. ϵ was evaluated across 0.005, 0.01, 0.1, and 0.3. To identify important features contributing to the accurate prediction of rheological properties, four variable selection methods were integrated into the regression analysis: the CF, MW, SA, and GA. Compared to SVR, PLS holds better interpretability and was therefore used in combination with these variable selection methods. A variety of variable subsets were generated from the original datasets based on the variable selection methods. The optimal subset was determined based on the root mean square error of the 5-fold cross-validation results. In the case of PLS regression, the trained model, along with the optimized variable subsets, was then applied to the validation sample group to evaluate its prediction performance. For SVR modeling, the trained model was applied to the full set of variables.

6.3 Discriminant analysis of bituminous binders

6.3.1 Classification of bitumen types

To classify bitumen types and identify important chemical information essential for the differentiation of bitumen type, PCA-LDA analyses integrated with MW and SA variable selections methods were conducted on FTIR, GPC, and DSC datasets. Different subsets containing variable counts ranging from 10 to 100 were created through the MW and SA methods, which were then utilized in the classification analysis. The optimized classification accuracies for each number of variables are presented in Table 6.1. All three datasets yield high classification accuracies with both selection methods. The FTIR, GPC, and DSC datasets consist of 520, 200, and 130 variables, respectively. Notably, the PCA-LDA model achieves high classification accuracy using only 10 to 20 variables, indicating that FTIR, GPC, and DSC datasets contain distinctive information for the effective differentiation of bitumen types. Applying variable selection is instrumental in accurately identifying the critical variables for the classification results.

Table 6.1 Classification accuracy of bitumen type using PCA-LDA model.

No. of	Optimized accuracy for MW			Selected range for MW			Optimized accuracy for SA		
variables	FTIR	GPC	DSC	FTIR (cm^{-1})	GPC (min)	DSC (°C)	FTIR	GPC	DSC
10	0.928	/	0.816	1450-1400	/	68-77	0.976	0.975	0.951
20	0.968	0.975	0.903	1400-1300	14.0-15.9	58-77	0.976	0.975	0.976
30	0.976	0.975	0.964	1400-1250	13.0-15.9	48-77	0.976	0.975	0.976
40	0.976	0.975	0.976	1400-1200	13.0-16.9	38-77	0.976	0.975	0.976
50	0.976	0.975	0.976	1400-1150	12.0-16.9	28-77	0.976	0.975	0.976
60	0.976	0.975	0.965	1400-1100	11.0-16.9	28-87	0.976	0.975	0.976
80	0.976	0.975	0.976	1350-950	10.0-17.9	8-87	0.976	0.975	0.976
100	0.976	0.975	/	1350-850	10.0-19.9	/	0.976	0.975	0.976

According to Table 6.1, the PCA-LDA analysis, when integrated with the MW method, initially demonstrates the highest prediction accuracy utilizing 30, 20, and 40 variables

selected from FTIR, GPC, and DSC datasets, respectively. For SA method, the highest accuracy is achieved with only 20 variables for all the three datasets. The scores and loading plots obtained from the classification of bitumen types using different datasets are presented in Fig. 6.2 – Fig. 6.4.

Fig. 6.2 (a) and (b) show the score and loading plots derived from the PCA-LDA analysis of bitumen types based on the optimized spectral range generated by the MW method. The score plot describes the transformation of original variables into a new space with reduced dimension, where transformed variables (namely, scores) are arranged in a descending order according to the variance they hold. The variable with the highest variance is defined as principal component 1 (PC1), followed by PC2, and so on. As depicted in Fig. 6.2 (a), eight bitumen types are clearly distinguished in the score plot when using the MW-aided PCA-LDA model. Specifically, most binders can be effectively distinguished by PC1, with the exception of QPMB, V710, and VPMB, which can only be differentiated by PC2. The loading plot describes the contribution of each original variable to the principal components. According to the loading plot shown in Fig. 6.2 (b), among the optimized wavenumber range of 1400 – 1250 cm^{-1}, the peak of 1378 cm^{-1}, which is related to symmetric -CH_3, markedly contributes to PC1. Spectral variables near 1350 cm^{-1} are identified as influential for both PC1 and PC2. The decomposition of the FTIR spectrum reveals distinct peaks at around 1365 and 1347 cm^{-1}, which represent O-H in phenols and C-O-H in saturate alcohols, respectively (Asemani & Rabbani, 2020). The bending vibration of symmetric CH_3 also appears in this region. Therefore, the bands around 1350 cm^{-1} are attributed to the combined presence of CH_3 and oxygen-based functional groups. Based on the analysis of PC1 and PC2, it can be seen that the aliphatic chain with -CH_3 groups and the minor polar functional groups are key features for distinguishing different bitumen types regardless of their ageing states.

To further identify the critical bands over the entire FTIR spectrum that are indicative of different bitumen types, the score and loading plots obtained from the PCA-LDA analysis combined with the SA method are presented in Fig. 6.2 (c) and (d), respectively. The score plot shows that PC1 accurately distinguishes bitumen types from three sources (i.e., Q, V, and T), while PC2 further separates binders originating from the same sources. According to the loading plot, PC1 depends on bands near 3145, 2970, and 1400, which correspond to the -OH or -NH stretching, asymmetric C-H stretching in CH_3, and symmetric C-H bending in CH_3. Important bands related to PC2 are observed near 1120 cm^{-1}, which relates to sulfones and alcohols (Asemani & Rabbani, 2020; Mirwald et al., 2020b). Additionally, bands close to 1345 cm^{-1} are identified as important for both PC1 and PC2, which denotes the combined effects of CH_3 and oxygen-based polar functional groups as have been discussed.

Fig. 6.2 (d) also presents the classification accuracy for each band interval with a width of 50 cm^{-1}. These intervals were obtained by dividing the entire selected spectrum into segments, with each containing 10 variables. This approach is a special case of the MW method, where window size equals moving step. The PCA-LDA modeling results show that most band intervals achieve good accuracy up to 0.93 in differentiating bitumen types, indicating that these band intervals exhibit distinct chemical differences among all bitumen types. Notably, the peaks corresponding to aliphatic C-H stretching and bending vibrations in CH_2 and CH_3, the aromatic C-H bending, the aromatic C=C stretching,

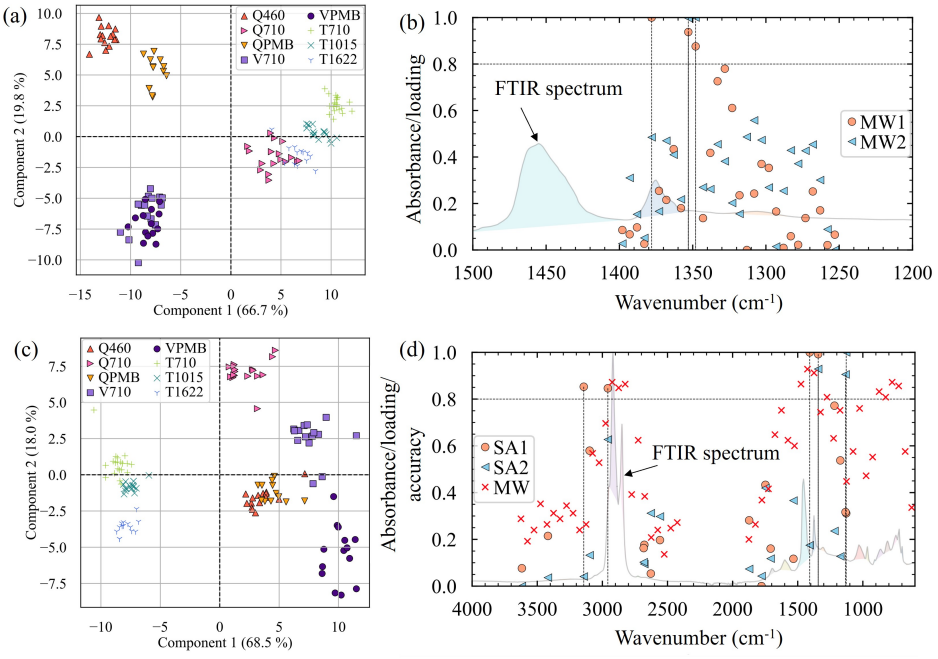

Figure 6.2 Classification of bitumen types based on FTIR dataset using PCA-LDA model coupled with MW and SA variable selection methods: (a) score and (b) normalized loading plots using variables within the optimized range created by the MW method; (c) score and (d) normalized loading plots based on the SA method. In subfigures (a) and (c), the numbers in the brackets of the axis titles represent the variance captured by each principal component. In subfigures (b) and (d), vertical dashed lines highlight the variables with normalized loadings greater than 0.8. The "MW1" and "MW2" in (b) correspond to transformed principal components 1 and 2, respectively, as displayed in (a). Similarly, the "SA1" and "SA2" in (d) represent transformed principal components 1 and 2, respectively, as depicted in (c). The "MW" in (d) refers to the classification accuracy for each band interval with a size of 50 cm^{-1}, which was obtained by dividing the entire FTIR spectrum, comprising 520 variables, into 52 intervals, each containing 10 variables.

and regions of 1750 – 1500 and 1350 – 900 cm^{-1} associated with polar functional groups (Asemani & Rabbani, 2020) are the most informative for classifying bitumen type.

Combining the results in Fig. 6.2 and Table 6.1, it can be seen that spectral variables denoting aliphatic chain structure are essential for the differentiation of bitumen type. Taking into consideration aromatic and polar functional groups further enhances the classification accuracy. Consequently, the highest accuracy is typically obtained in the spectral region predominantly indicative of aliphatic groups, along with some polar functional groups, particularly in the range of approximately 1400 to 1000 cm^{-1}. However, Fig. 4.7 reveals that this spectral region exhibits limited differences for various bitumen types. It suggests that distinguishing between binders may depend not only on the peak intensities but also on their positions, shapes, and the relative intensities of these peaks, which may guide the development of new indices for more effectively classification of bitumen

types.

According to Table 6.1, for various numbers of variables, the region ranging from ca. 14 to 16 min is consistently selected as critical to the classification of bitumen type, highlighting its distinctive patterns across various bitumen types. Specifically, the narrowest variable subset displaying the highest classification accuracy is revealed within the range of 14.0-15.9 min of the GPC chromatograms. The score and loading results for the PCA-LDA analysis of bitumen type using this variable range are displayed in Fig. 6.3 (a) and (b), respectively. Eight binders are well distinguished by the score plot. The loading plot identifies the region around 15.6 min as highly correlated with the classification of bitumen type. Large differences are observed in this region of GPC chromatograms for different bitumen types, and this region mostly remains unchanged with ageing (Fig. 4.10).

The PCA-LDA analyses based on the SA method demonstrate comparable accuracies in classifying bitumen types, as shown in Table 6.1. The score and loading plots derived from the analysis with the highest accuracy are presented in Fig. 6.3 (c) and (d). The score plot shows a good classification of eight bitumen types by PC1 and PC2. As revealed by the loading plot, the PC1 and PC2 are substantially related to the elution times of 18.6, 16.5, 16.1 and 13.9 min. These elution times span regions related to small molecular size

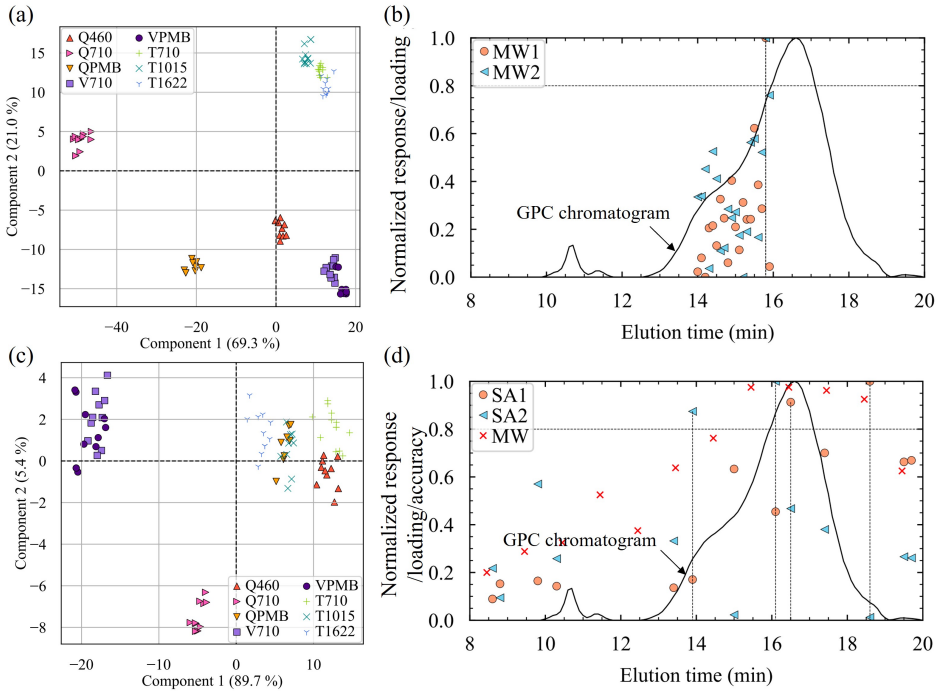

Figure 6.3 Classification of bitumen types based on GPC dataset using PCA-LDA model coupled with MW and SA variable selection methods: (a) score and (b) normalized loading plots based on MW; (c) score and (d) normalized loading plots using SA. Legends correspond to the same meaning as described in Fig. 6.2.

(SMS), medium molecular size (MMS), and large molecular size (LMS). Furthermore, the classification accuracy for each interval with a width of 1 min was calculated and is shown in Fig. 6.3 (d) as "MW". The intervals between 13 and 19 min provide good classification accuracies of 0.60 – 0.98, particularly in the region of 15 – 18 min, which shows the highest intensity in the chromatograms.

The results in Fig. 6.3 and Table 6.1 concerning the GPC dataset collectively highlight the key importance of the molecular weight distribution related to resins and aromatics in classifying bitumen types. The combined molecular weights of specific molecules from the SARA fractions also provide valuable insights for the effective bitumen type classification.

When using the MW method, the thermogram between 38 – 77 °C is recognized as the subset with the smallest size but highest classification accuracy, as indicated in Table 6.1. The corresponding score and loading plots are presented in Fig. 6.4. As shown in the score plot, PC1 mainly distinguishes the three penetration grades obtained from source T, and PC2 effectively differentiates three Q-sourced binders. According to the loading plot, PC1 and PC2 are related to heat flow peaks at about 38, 64, and 70 °C. These positions are

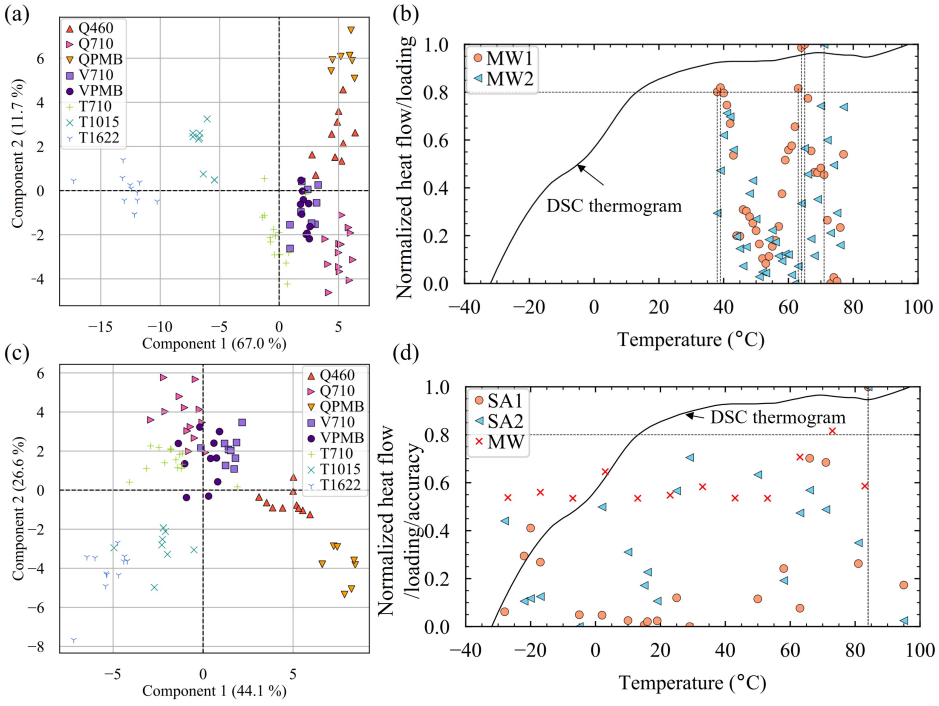

Figure 6.4 Classification of bitumen types based on DSC dataset using PCA-LDA model coupled with MW and SA variable selection methods: (a) score and (b) normalized loading plots based on MW; (c) score and (d) normalized loading plots using SA. Legends correspond to the same meaning as described in Fig. 6.2.

associated with the exothermic behavior of the crystalline phase in bitumen, as discussed in Chapter 4. Re-examining the original heat flow curves of various binders (Fig. 4.12), different changes in heat flow are observed at these specific temperatures identified by the PCA-LDA analysis.

Fig. 6.4 (c) and (d) display the score and loading plots obtained from the PCA-LDA analysis integrated with the SA method. The classification among eight bitumen types is not as clear as that revealed by GPC and FTIR datasets. This is due to the lower cumulative variance of 70.7 % for PC1 and PC2. The combined PC1 and PC2 lead to good classification of T1015, T1622, Q460, and QPMB. A more accurate separation of T710, Q710, V710, and VPMB can be achieved by more principal components. The PC1 and PC2 are substantially linked to the heat flow at around 84 °C, where a small peak is revealed for most bitumen types as indicated by Fig. 4.12. Among all intervals with a width of 10 °C, the interval between 65 and 75 °C achieves the highest classification accuracy. Table 6.1 also indicates that, regardless of the number of variables used, the range between 68 and 77 °C is consistently identified as correlating strongly with the classification of bitumen type.

6.3.2 Classification of ageing states

The classification of ageing states was conducted utilizing PCA-LDA analysis combined with the MW and SA methods, and results are presented in Table 6.2. This table indicates that the classification accuracy varies with the number of selected variables. As this number grows from 10 to 100, the accuracy of the PCA-LDA analysis using all three datasets initially increases and then decreases. This suggests that a specific number of variables is adequate to distinguish all the bitumen samples. Including additional variables can introduce noise and irrelevant information, potentially leading to decreased prediction accuracy. In contrast, for the classification of bitumen types, the accuracy remains consistent regardless of the number of variables used, as indicated in Table 6.1. This implies that the variance accounting for distinguishing bitumen type is more differentiable and less susceptible to noise. Consequently, introducing more variables does not significantly affect the classification accuracy.

Table 6.2 reveals that for the classification using the MW method, when fewer than 20 variables are utilized, the carbonyl-related region is selected, whose intensity increases significantly with ageing. As the number of variables used in the PCA-LDA analysis in-

Table 6.2 Accuracy for the classification of ageing states using PCA-LDA model.

No. of	Optimized accuracy for MW			Selected range for MW			Optimized accuracy for SA		
variables	FTIR	GPC	DSC	FTIR (cm^{-1})	GPC (min)	DSC (°C)	FTIR	GPC	DSC
10	0.832	/	0.34	1700-1650	/	8-17	0.912	0.862	0.462
20	0.832	0.812	0.366	1700-1600	15.0-16.9	48-67	0.944	0.825	0.452
30	0.872	0.812	0.402	1000-850	13.0-15.9	-2-27	0.968	0.912	0.476
40	0.872	0.85	0.378	1550-1350	12.0-15.9	-12-27	0.968	0.875	0.452
50	0.872	0.812	0.44	1050-800	15.0-19.9	-12-37	0.952	0.888	0.464
60	0.92	0.838	0.366	1050-750	11.0-16.9	-22-37	0.992	0.888	0.464
80	0.912	0.888	0.392	1650-1250	10.0-17.9	-2-77	0.960	0.838	0.476
100	0.888	0.875	/	1400-900	9.0-18.9	/	0.920	0.838	0.451

creases, the selected spectral regions involve mostly a combination of polar functional groups, aromatic structure, and aliphatic chains, providing a more comprehensive characterization of the ageing process.

The classification results of ageing states using variables within the optimized widow range are depicted in Fig. 6.5 (a) and (b). The score plot reveals that fresh and oven-aged binders are less distinctly separated compared to other ageing states, indicating smaller chemical differences between these two conditions. The PC1 effectively distinguishes all ageing states. Meanwhile, PC2 reveals closer distributions of fresh and 4P-aged binders, setting them apart from 1P- and 2P-aged binders. The cumulative variance captured by PC1 and PC2 is larger than 99 %, indicating that the primary chemical information relevant to the ageing process is effectively extracted by the first two principal components. Compared to PC2, significantly larger variance is captured by PC1, indicating that PC1 contains most chemical information related to the classification of ageing state. According to the corresponding loading plot, PC1 is mostly associated with the spectral region around 900 cm^{-1} due to the presence of aromatic C-H bonds and SBS modifiers, while PC2 relates more to the peaks indicative of sulfur-based functional groups and C-H bonds in aromatic rings.

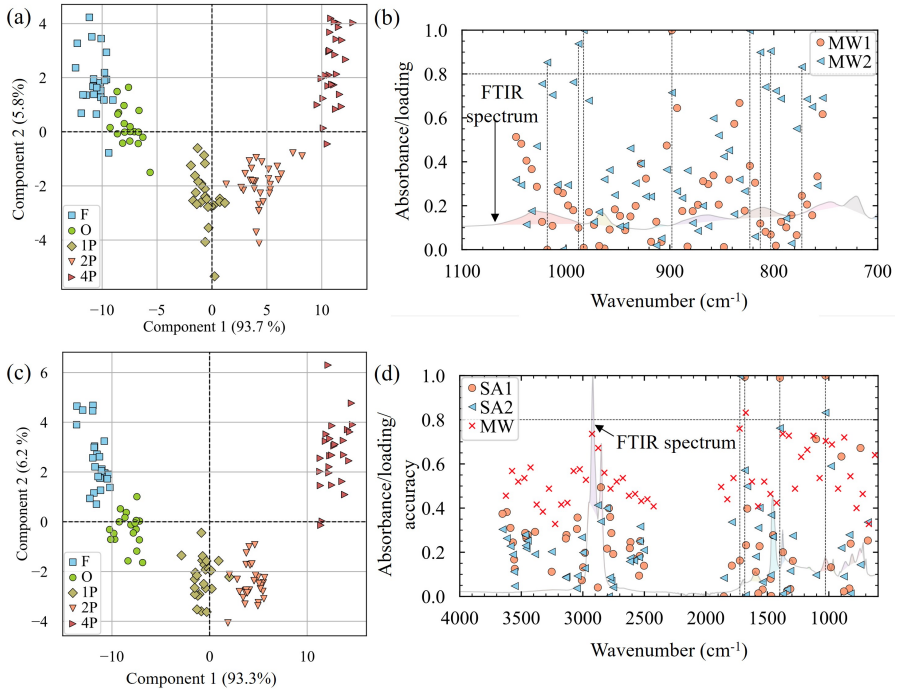

Figure 6.5 Classification of ageing states based on FTIR dataset using PCA-LDA model coupled with MW and SA variable selection methods: (a) score and (b) normalized loading plots based on MW; (c) score and (d) normalized loading plots using SA. Legends describe the same context as described in Fig. 6.2.

Fig. 6.5 (c) and (d) display the score and loading plots derived from the SA-based PCA-LDA analysis using 60 spectral variables. The score plot reveals a distribution of various ageing levels similar to that obtained from the MW-aided classification. The loading plot of PC1 underscores the significance of the combination of sulfoxide, carbonyl, and aliphatic groups in accurate determination of ageing state. PC2 is mainly related to peaks indicative of carbonyl functional groups.

Additionally, Fig. 6.5 (d) presents the classification accuracy of PCA-LDA modeling across all band intervals with a width of 50 cm^{-1}. Fair classification accuracies are observed for regions relating to aliphatic chains, aromatic structure, and carbonyl and sulfoxide functional groups, as well as other polar functional groups with much lower concentration.

In summary, spectral peaks corresponding to polar functional groups involved in the oxidative reactions of bitumen are recognized as critical contributors to the classification of ageing state. These peaks predominantly fall within the spectral regions of approximately 1800 – 900 cm^{-1}, including carbon-related functional groups such as esters, ketones, aldehydes, and carboxylic acids (Asemani & Rabbani, 2020), sulfur-containing groups such as sulfoxides, sulfones and sulfate esters (Mirwald et al., 2020b), and nitrogen-based amides. Among these functional groups, carbonyls and sulfoxides are commonly used as indicators of bitumen ageing. Other carbon-, sulfur-, and nitrogen-associated functional groups receive less attention due to peak overlap and their weaker intensity, but they still reveal important chemical changes during ageing. Furthermore, the variations in aliphatic- and aromatic-related peaks provide additional insights into the ageing process, and should be integrated into the evaluation of bitumen ageing.

According to Table 6.2, the classification of ageing states based on GPC dataset achieves a high accuracy up to 0.912 when employing the MW and SA variable selection methods. This accuracy is slightly lower than that obtained from the analysis on the FTIR data. The score and loading plots for the classification analyses based on the optimized variables are displayed in Fig. 6.6. The score plots for the two variable selection methods consistently classify different ageing states along PC1, which accounts for up 99% variance. This sequential distribution of different ageing states from F to 4P along PC1 implies a stepwise variation in chemical composition as ageing proceeds. The loading plot derived from the MW-based discriminant analysis shows that PC1 depends predominantly on the chromatograms within the elution time of 14 – 15 min. A similar elution time range is revealed by the SA-based discriminant analysis. The classification accuracy for each interval with a width of 1 min is also plotted in Fig. 6.6 (d), with the highest value obtained in the region of 15 – 16 min. This critical region between 14 and 16 min lies at the intersection of LMS and MMS, highlighting the changes in the molecular weight of asphaltenes and resins during the ageing process.

Table 6.2 shows a diminished performance when using the DSC dataset for classifying the ageing state of bitumen. This demonstrates that thermal behavior of bitumen is less affected by its ageing process. The corresponding scores and loadings for DSC dataset are not elaborated here. In general, different optimal window ranges are identified for the classification of bitumen types and ageing states, which is around 65 – 75 °C for type classification and -10 – 30 °C for ageing classification.

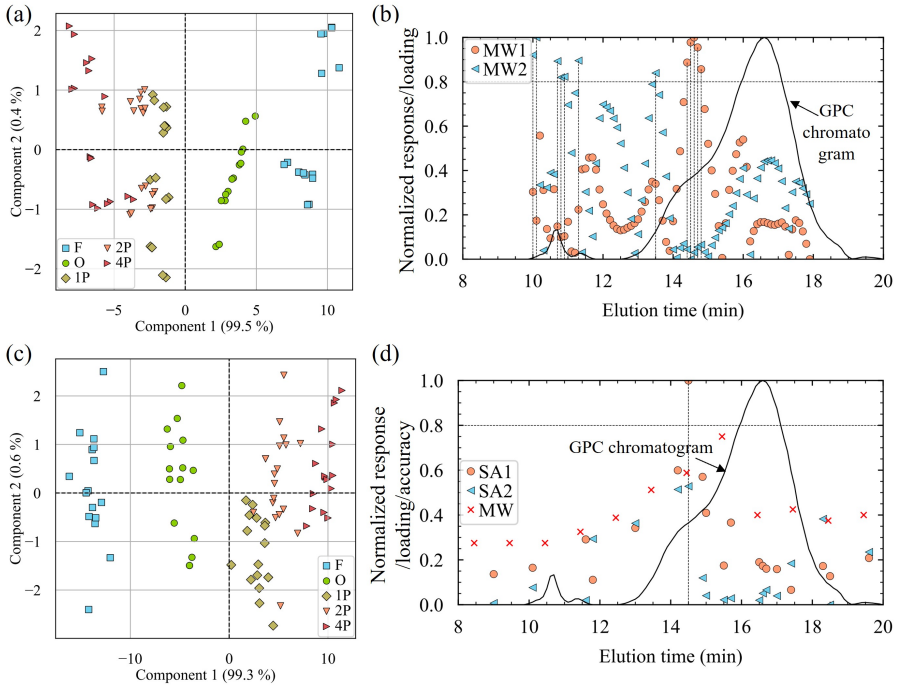

Figure 6.6 Classification of ageing states based on GPC dataset using PCA-LDA model coupled with MW and SA variable selection methods: (a) score and (b) normalized loading plots based on MW; (c) score and (d) normalized loading plots using SA. Legends describe the same context as described in Fig. 6.2.

6.3.3 Classification of binders aged in laboratory and field conditions

To investigate the chemical changes in bitumen caused by different ageing conditions, classification analysis was conducted on samples subjected to PAV ageing, hydrothermal ageing, and field ageing. The classification accuracies are detailed in Table 6.3. A high accuracy of up to 0.878 is obtained, suggesting the presence of distinct chemical components resulting from these varied laboratory and field conditions.

Table 6.3 indicates that the spectral region from 1250 to 950 cm^{-1} is particularly significant in differentiating samples subjected to the three ageing conditions. The score and loading plots for the PCA-LDA analysis using the spectral variables within this spectral range are presented in Fig. 6.7 (a) and (b). The score plot shows a clear separation of field samples from those under laboratory conditions along PC1. The loading plot shows that PC1 primarily relates to the spectral range of 1000-950 cm^{-1}, which is linked to S=O stretching in sulfoxides, C-O-C stretching in ethers, in-plane C-H bending in aromatics, and alkenes of SBS (Asemani & Rabbani, 2020; Kumar et al., 2020; Mirwald et al., 2020a). The differentiation between PAV and hydrothermal ageing conditions is largely characterized by PC2, relating mostly to sulfoxides, as indicated by the spectral region between 1100 and 1000 cm^{-1}.

Table 6.3 Accuracy for the classification of binders subjected different ageing conditions using FTIR data.

No. of variables	Optimized accuracy for MW	Selected range for MW	Optimized accuracy for SA
10	0.780	2900-2850	0.824
20	0.808	1450-1350	0.796
30	0.824	1150-1000	0.841
40	0.808	1150-950	0.829
50	0.857	1200-950	0.853
60	0.878	1250-950	0.837
80	0.824	1500-1100	0.824
100	0.824	1500-1000	0.853

Fig. 6.7 (c) and (d) display the SA-aided classification of ageing conditions with the optimized variable number of 50. In the score plot, PC1 identifies field samples, and PC2 differentiates between laboratory ageing and moisture conditions. The variables related to PC1 span the spectral ranges of 3000 – 2800 cm^{-1} and 1100 – 1000 cm^{-1}. Specifically, peaks at 2900, 2945, and 1080 cm^{-1} exhibit high correlation, corresponding to the asymmetric C-H stretching in CH_2 and CH_3 and S=O in sulfoxides. PC2 is primarily related to the regions of 3000 – 2800 cm^{-1}, informative of the aliphatic C-H stretching in CH_2 and CH_3. The polar functional groups at 1680 and 1150 cm^{-1} also contribute to PC2. Furthermore, classification analysis of individual spectral intervals, each with a width of 50 cm^{-1}, yields relatively high accuracies (around 0.75) near 2875, 1400, and 750 cm^{-1}. These regions are associated with aliphatic and aromatic structures in bitumen.

The score plots based on both the MW and SA methods show closer clusters of samples under laboratory PAV and hydrothermal ageing conditions compared to field samples, reflecting the more unique field conditions including high temperature, UV light, moisture, and other contaminants. Fig. 6.7 (b) and (d) suggest that the primary chemical differences between laboratory and field ageing involve the aliphatic CH_2 and CH_3 structures, along with sulfur-based functional groups. The different aliphatic structures could result from the different reaction processes or the vaporization of light components. The observed variations in polar functional groups might be attributed to distinct oxidative reactions that occur during field and laboratory ageing processes (Feng et al., 2016; Hosseinnezhad et al., 2019; Petersen, 2009). For distinguishing hydrothermal and ageing conditions, identified key factors also include aliphatic CH_2 and CH_3 structures. The relative ratio of CH_2 and CH_3 associated with PC2 differs from that linked to PC1, suggesting variations in the asymmetric/symmetric CH_2 and CH_3 structures between field/lab and PAV/hydrothermal conditions. Furthermore, the functional groups related to PC2, namely, carbonyls and polar function group of sulfones or alcohols, are also different from those associated with PC1.

6.4 Prediction of rheological behavior

6.4.1 Comparison among variable selection methods and datasets

To characterize the chemo-rheological relationship of bituminous binders and predict their rheological properties, PLS regression was conducted utilizing chemical, structural,

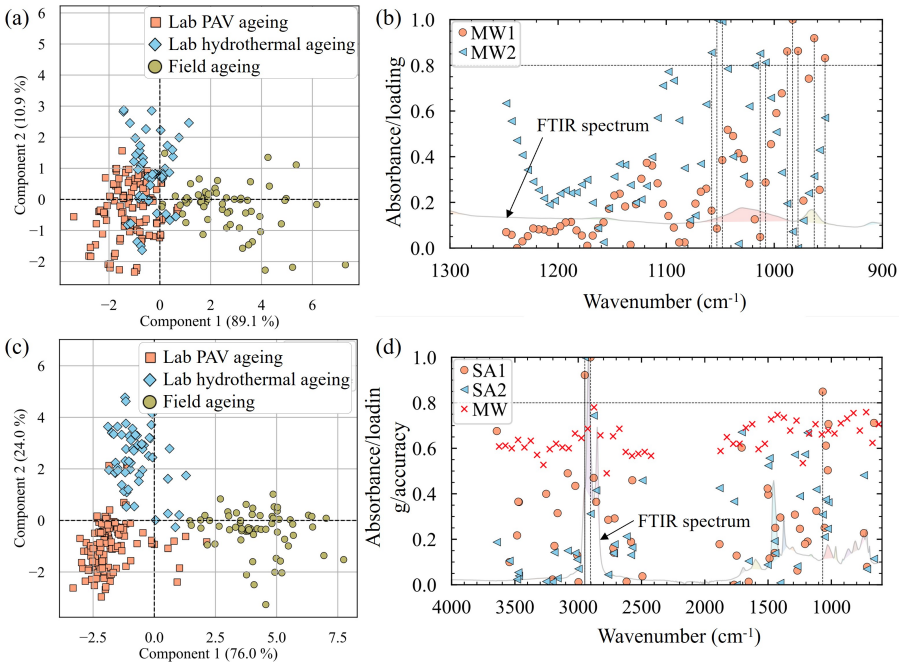

Figure 6.7 Classification of different ageing conditions based on FTIR dataset using PCA-LDA model coupled with MW and SA variable selection methods: (a) score and (b) normalized loading plots based on MW; (c) score and (d) normalized loading plots using SA. Legends describe the same parameters as described in Fig. 6.2.

and thermal data obtained from FTIR, GPC, and DSC tests. Table 6.4 summarizes the performance of these datasets in predicting rheological parameters through PLS regression without any variable selection. For most rheological properties, the FTIR dataset reveals a slightly better prediction performance compared to GPC. Both datasets yield R^2_{cv} and R^2_p mostly higher than 0.9 and RPD larger than 3 for f_c, G^*_c, GR, R_{rhe}, B_D, G_0, ZSV_{60}, and η_{120}. For the remaining parameters listed in Table 6.4, their R^2_{cv} and R^2_p are generally higher than 0.8. Two factors that might contribute to this lower prediction accuracy include the lower repeatability of these parameters and the degree of nonlinear relationship between them and chemical and structural properties.

The lowest R^2 and highest $RMSE$ values are obtained when conducting PLS regression on the DSC dataset. As discussed in Chapter 4, large variances are observed among the thermograms of duplicate samples. The measured thermal behaviors of binders are sensitive to a variety of factors including instrument stability, sample homogeneity, and measuring operations, as well as data processing such as baseline correction. Particularly, the observed lateral shift of characteristic peaks with temperature in the thermograms is difficult to mitigate through data preprocessing. The heat flow of bitumen samples at temperatures of approximately -50 – 100 °C involves information about glass transition temperature, crystalline phases, and volatilization of low molecular weight components

(Frolov et al., 2020). The former presents a complex correlation with the SARA fractions (Kriz et al., 2008) in bitumen, and the latter two offer only partial insights into the bitumen components. Consequently, the thermal properties measured by DSC may not represent the full complexity of bitumen as comprehensively as the chemical and structural data provided by FTIR and GPC tests.

The performance of PLS regression combined with different variable selection (VS) methods in predicting rheological parameters is listed in Table 6.5. Applying VS generally leads to increased prediction accuracy of the regression model, with the R^2 mostly above 0.9 for f_c and R_{rhe}, and higher than 0.8 for G_4. For most rheological properties, the regres-

Table 6.4 Comparing the performance of different test results in predicting rheological properties of bitumen utilizing PLS regression, where LV represents the number of latent variables.

Parameter	Dataset	LV	R_c^2	*RMSEC*	R_{cv}^2	*RMSECV*	R_p^2	*RMSEP*	*RPD*	bias
f_c	FTIR	9	0.975	0.179	0.896	0.366	0.970	0.214	5.911	0.038
	GPC	9	0.973	0.184	0.875	0.398	0.890	0.466	3.069	0.090
	DSC	5	0.817	0.517	0.656	0.709	0.741	0.552	2.110	-0.201
G_c^*	FTIR	9	0.959	0.066	0.924	0.091	0.945	0.066	4.279	0.005
	GPC	7	0.942	0.072	0.820	0.126	0.883	0.128	2.924	0.003
	DSC	5	0.840	0.126	0.602	0.198	0.694	0.190	1.810	-0.009
GR	FTIR	10	0.977	0.160	0.918	0.301	0.972	0.161	6.037	-0.019
	GPC	12	0.991	0.102	0.933	0.286	0.968	0.248	5.928	-0.082
	DSC	4	0.830	0.450	0.579	0.708	0.724	0.452	1.903	0.000
R_{rhe}	FTIR	9	0.970	0.074	0.916	0.123	0.959	0.091	4.937	0.004
	GPC	6	0.915	0.110	0.728	0.197	0.904	0.141	3.380	-0.042
	DSC	4	0.798	0.206	0.570	0.300	0.702	0.209	1.871	0.042
A_D	FTIR	4	0.804	0.237	0.718	0.285	0.815	0.251	2.329	-0.020
	GPC	7	0.914	0.158	0.701	0.295	0.882	0.188	3.326	0.090
	DSC	4	0.818	0.208	0.675	0.278	0.709	0.341	1.865	-0.037
B_D	FTIR	10	0.987	0.108	0.950	0.212	0.971	0.181	6.033	0.044
	GPC	5	0.938	0.217	0.845	0.343	0.902	0.382	3.384	0.127
	DSC	4	0.737	0.488	0.514	0.664	0.814	0.480	2.348	0.073
G_0	FTIR	10	0.967	0.083	0.944	0.109	0.921	0.113	3.660	-0.028
	GPC	6	0.950	0.108	0.825	0.202	0.891	0.217	3.042	-0.015
	DSC	5	0.859	0.167	0.677	0.253	0.691	0.284	1.799	0.000
G_4	FTIR	10	0.963	0.072	0.939	0.094	0.827	0.115	2.406	0.001
	GPC	11	0.962	0.069	0.763	0.173	0.861	0.150	2.906	-0.058
	DSC	3	0.806	0.136	0.581	0.200	0.753	0.158	2.018	-0.013
γ_4	FTIR	9	0.812	0.038	0.701	0.048	0.585	0.045	1.638	-0.014
	GPC	4	0.852	0.047	0.686	0.068	0.666	0.052	1.731	-0.001
	DSC	2	0.498	0.065	0.188	0.083	0.490	0.062	1.402	-0.003
ZSV_{60}	FTIR	10	0.978	0.105	0.929	0.189	0.906	0.214	3.356	0.048
	GPC	12	0.988	0.080	0.904	0.228	0.950	0.169	4.498	-0.019
	DSC	3	0.766	0.344	0.539	0.482	0.897	0.210	3.136	0.026
η_{120}	FTIR	10	0.966	0.070	0.927	0.103	0.940	0.093	4.152	-0.017
	GPC	14	0.995	0.027	0.955	0.086	0.952	0.091	4.839	-0.030
	DSC	5	0.768	0.177	0.451	0.273	0.634	0.203	1.702	-0.048

sion without any variable selection presents comparable prediction accuracy for the calibration/training and prediction/validation samples, as indicated by the values of $RMSE$ and R^2. Sometimes, the R^2_p is even higher than R^2_{cv}. The application of VS typically leads to a notable increase in R^2 for the calibration samples, while only a slight improvement in R^2 is obtained for the validation samples. In certain cases, the application of VS significantly enhances the R^2 for calibration at the cost of reducing it for validation samples, indicating that better calibration performance may come with a trade-off in validation accuracy. This observation suggests that applying VS to PLS regression may increase the risk of overfitting, which refers to a model that is excessively complex and fits the training data very well, but fails to generalize effectively to new data. In such cases, while the model may demonstrate excellent performance on the training samples, its applicability and accuracy diminish when applied to data not included in the training process.

Among the four variable selection methods, i.e., CF, MW, SA and GA, the MW and GA methods overall exhibit better performance for all three datasets, which can be attributed to the specific attributes of each dataset and the unique characteristics of different VS methods. The FTIR dataset, for instance, is characterized by high collinearity. The bands ranging from 2965 to 2864 cm^{-1} are informative of the asymmetric and

Table 6.5 Comparing performance of regression models integrated with different variable selection methods in predicting rheological properties of bitumen using FTIR and GPC datasets, where LV represents number of latent variables.

Dataset	Parameter	VS	LV	R^2_c	$RMSEC$	R^2_{cv}	$RMSECV$	R^2_p	$RMSEP$	RPD	bias
FTIR	f_c	CF	15	0.996	0.081	0.979	0.186	0.964	0.169	5.306	0.014
		MW	8	0.992	0.107	0.957	0.247	0.969	0.213	5.780	0.044
		SA	10	0.998	0.059	0.992	0.107	0.936	0.305	3.954	0.004
		GA	7	0.998	0.058	0.984	0.153	0.937	0.303	4.017	0.046
	R_{rhe}	CF	15	0.994	0.034	0.976	0.069	0.883	0.135	2.942	0.014
		MW	9	0.990	0.033	0.955	0.071	0.951	0.095	4.528	-0.010
		SA	8	0.991	0.032	0.977	0.051	0.928	0.115	3.733	-0.009
		GA	10	0.978	0.062	0.957	0.088	0.963	0.087	5.239	-0.006
	G_4	CF	15	0.993	0.032	0.975	0.060	0.715	0.148	1.911	0.029
		MW	10	0.994	0.029	0.959	0.075	0.821	0.130	2.384	0.018
		SA	10	0.975	0.060	0.962	0.073	0.832	0.116	2.538	-0.032
		GA	10	0.999	0.011	0.968	0.058	0.829	0.169	2.427	0.016
GPC	f_c	CF	15	0.992	0.097	0.931	0.294	0.900	0.417	3.194	0.056
		MW	9	0.950	0.250	0.914	0.327	0.953	0.286	4.648	0.038
		SA	10	0.991	0.120	0.971	0.211	0.904	0.331	3.245	-0.034
		GA	10	0.983	0.145	0.945	0.261	0.926	0.360	3.681	-0.033
	R_{rhe}	CF	13	0.976	0.056	0.912	0.106	0.871	0.170	2.824	-0.028
		MW	8	0.940	0.105	0.886	0.144	0.915	0.096	3.427	-0.004
		SA	10	0.952	0.083	0.912	0.111	0.888	0.146	3.128	-0.044
		GA	8	0.955	0.076	0.887	0.120	0.873	0.169	2.956	-0.054
	G_4	CF	13	0.939	0.091	0.872	0.131	0.738	0.191	2.042	-0.056
		MW	9	0.955	0.083	0.922	0.110	0.774	0.147	2.128	0.023
		SA	10	0.978	0.058	0.952	0.086	0.748	0.155	2.073	0.043
		GA	7	0.960	0.074	0.907	0.112	0.758	0.183	2.155	-0.061

symmetric C-H stretching vibration of CH_2 and CH_3 groups, while the spectral regions of 1485 – 1357 cm^{-1} are linked to the bending vibration of these groups (Castro & Vazquez, 2009). Both regions contribute to understanding the aliphatic structure of bitumen. Selecting these regions simultaneously results in redundancy of information provided. An increased number of variables also enhances the risk of introducing unnecessary noise into the analysis. The MW approach mitigates this issue by identifying a narrower spectral region with essential and non-redundant chemical information. Compared to the full spectrum, this selected region involves fewer variables, thereby reducing the potential for noise introduction. The high prediction accuracy achieved with this region further confirms that the chemical information it offers is sufficient and relevant for accurately predicting rheological properties.

Both SA and GA methods focus on selecting variables based on their contributions to target prediction. However, GA, while inheriting the most effective variables like SA, further incorporates crossover and mutation, facilitating a complex and effective variable selection process. Therefore, better regression performance is achieved when using GA method. The predictions of crossover modulus obtained through the integrated GA-PLS modeling on FTIR, GPC, and DSC datasets are shown in Fig. 6.8. High precision is observed for both calibration and validation samples when using GA-PLS regression on FTIR and GPC datasets, while DSC dataset shows a relatively lower performance.

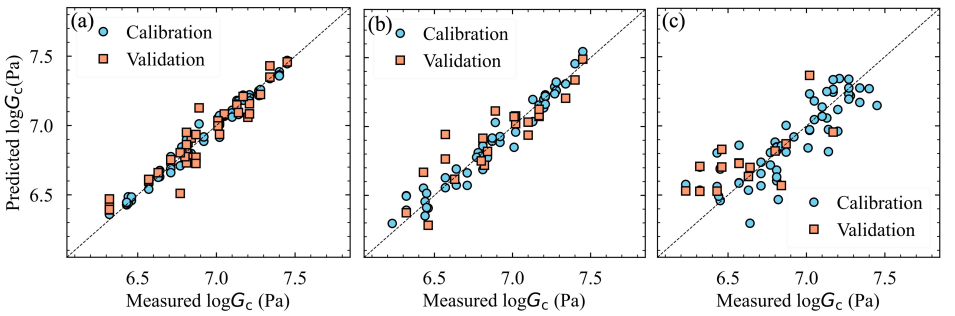

Figure 6.8 Prediction of crossover modulus through GA-PLS modeling on (a) FTIR, (b) GPC, and (c) DSC datasets.

Compared to PLS, SVR overall presents better performance in predicting rheological properties of bitumen regardless of input datasets, as indicated by the values of R^2, $RMSE$, and RPD listed in Table 6.6. The SVR results for FTIR and GPC datasets are comparable. For the DSC dataset, compared to the outcomes from PLS regression, the prediction accuracy for the calibration samples is significantly increased when utilizing SVR modelling, and a slight increase is observed for the validation samples. This increased performance by the SVR analysis may be due to its ability to better capture the inherent nonlinear thermal-rheological relationship of bituminous binders, which can be achieved through the use various kernel functions. Furthermore, SVR is robust against outliers due to the ϵ-insensitive loss function and the incorporation of a regularization parameter C, along with the use of non-linear kernel (Awad et al., 2015).

To optimize the performance of SVR in predicting the rheological properties of bitu-

men using FTIR, GPC, and DSC datasets, various combinations of kernel functions, regularization parameters (C), kernel coefficients (γ), and margin widths (ϵ) were compared. The combination yielding the best performance was ultimately selected for the prediction analysis. For the FTIR and GPC datasets, a mix of linear, poly, and RBF kernel functions is selected. In most scenarios involving DSC dataset, the RBF kernel function is utilized, which is one of the most popular kernels with wide application. The effective application of RBF kernel in SVR analysis indicates the complex and non-linear relationship between the predictors and the responses (Awad et al., 2015; Üstün et al., 2007). This kernel is exclusively selected for the prediction of R_{rhe}, A_{D}, G_4, and γ_4 based on FTIR, GPC, and

Table 6.6 Comparing the performance of different test results in predicting rheological properties of bitumen through the SVR model.

Para.	Dataset	R^2_{c}	$RMSEC$	R^2_{cv}	$RMSECV$	R^2_{p}	$RMSEP$	RPD	bias	kernel	C	γ	ϵ
f_{c}	FTIR	1.000	0.005	0.949	0.258	0.993	0.107	11.66	-0.011	rbf	10	0.1	0.005
	GPC	0.996	0.085	0.891	0.423	0.956	0.205	4.86	-0.045	poly	1	0.5	0.1
	DSC	0.963	0.245	0.749	0.640	0.823	0.456	2.38	-0.029	rbf	150	0.1	0.005
G^*_{c}	FTIR	0.981	0.042	0.929	0.082	0.903	0.107	3.48	0.041	linear	1	0.1	0.005
	GPC	0.941	0.080	0.903	0.102	0.773	0.137	2.13	0.024	poly	1	0.5	0.1
	DSC	1.000	0.005	0.815	0.134	0.656	0.216	1.71	-0.009	rbf	100	0.5	0.005
GR	FTIR	1.000	0.010	0.968	0.187	0.986	0.120	8.59	0.026	poly	1	0.5	0.01
	GPC	1.000	0.005	0.987	0.134	0.995	0.074	14.42	0.006	poly	1	0.5	0.005
	DSC	0.943	0.259	0.804	0.480	0.740	0.474	2.11	-0.177	poly	10	0.1	0.3
R_{rhe}	FTIR	1.000	0.005	0.937	0.106	0.980	0.064	7.01	0.005	rbf	10	0.1	0.005
	GPC	1.000	0.005	0.959	0.092	0.997	0.020	17.12	0.003	rbf	50	0.1	0.005
	DSC	0.805	0.189	0.571	0.280	0.789	0.239	2.30	-0.078	rbf	10	0.1	0.01
A_{D}	FTIR	1.000	0.005	0.886	0.182	0.987	0.066	8.65	0.006	rbf	10	0.1	0.005
	GPC	0.999	0.016	0.917	0.153	0.867	0.224	2.99	0.090	rbf	10	0.1	0.005
	DSC	0.975	0.086	0.851	0.208	0.395	0.357	1.51	0.187	rbf	50	0.5	0.1
B_{D}	FTIR	1.000	0.010	0.977	0.142	0.956	0.222	5.14	0.082	poly	1	0.1	0.01
	GPC	0.993	0.082	0.971	0.170	0.920	0.272	3.62	0.062	poly	1	0.1	0.1
	DSC	0.987	0.119	0.846	0.409	0.797	0.361	2.35	0.120	rbf	10	0.5	0.1
G_0	FTIR	0.971	0.077	0.921	0.128	0.605	0.259	1.66	0.072	poly	1	0.5	0.1
	GPC	0.999	0.016	0.959	0.103	0.964	0.117	5.40	0.029	rbf	10	0.1	0.01
	DSC	0.915	0.138	0.724	0.247	0.589	0.277	1.91	0.160	rbf	1	0.5	0.005
G_4	FTIR	1.000	0.005	0.937	0.088	0.943	0.085	4.20	-0.010	rbf	10	0.1	0.005
	GPC	0.999	0.009	0.982	0.051	0.929	0.085	3.81	0.014	rbf	50	0.1	0.01
	DSC	0.933	0.086	0.763	0.162	0.570	0.181	1.53	-0.004	rbf	10	0.5	0.1
γ_4	FTIR	0.997	0.005	0.687	0.045	0.947	0.020	4.45	-0.004	rbf	10	0.1	0.005
	GPC	0.990	0.011	0.829	0.045	0.817	0.050	2.42	0.013	rbf	1	0.1	0.01
	DSC	0.837	0.035	0.522	0.060	0.501	0.078	1.44	-0.014	rbf	10	0.1	0.01
ZSV_{60}	FTIR	0.994	0.055	0.975	0.110	0.922	0.202	4.05	0.094	linear	1	0.1	0.005
	GPC	1.000	0.005	0.988	0.092	0.918	0.161	3.77	-0.061	poly	1	0.1	0.005
	DSC	0.981	0.105	0.841	0.306	0.912	0.232	3.39	0.024	rbf	150	0.1	0.1
η_{120}	FTIR	1.000	0.005	0.934	0.097	0.972	0.064	5.96	0.007	rbf	10	0.1	0.005
	GPC	0.997	0.023	0.973	0.069	0.975	0.063	6.87	-0.025	linear	100	0.1	0.01
	DSC	0.932	0.103	0.731	0.203	0.857	0.140	2.68	-0.021	rbf	50	0.1	0.1

DSC datasets, indicating their complex dependence on bitumen properties. This is consistent with the observed weaker correlations between these properties and carbonyl and sulfoxide groups, as detailed in Table 4.10, and their intricate dependence on the relative aliphatic-aromatic structure, as shown in Fig. 6.9, which will be discussed in the following sections. Furthermore, the selection of optimal combinations for the C, γ, and ϵ varies across different rheological properties and different datasets due to the distinct characteristics of each rheological property and unique nature of the datasets involved. Such parameter tuning is essential to ensure the high prediction accuracy in the SVR analysis.

6.4.2 Prediction of rheological properties

To identify the key parameters that are closely associated with specific rheological properties, the corresponding regression coefficients were analyzed. Fig. 6.9 shows the regression coefficients derived from the PLS regression of various rheological properties using FTIR dataset. The results based on the four variable selection methods are presented collectively for cross-verification and increased reliability. As illustrated in Fig. 6.9 (a), the MW, SA, and GA methods consistently report similar spectral peaks within the range of 1800 – 900 cm^{-1} that are strongly associated with the prediction of crossover frequency (f_c). These peaks are predominantly related to carbonyl functional groups, aromatic C=C bonds, and various polar function groups that distribute with low intensity in the region between 1400 and 1000 cm^{-1}. Notably, the CF method shows a distinct distribution of regression coefficients compared to the other three methods. The peak at 3200 cm^{-1}, identified only by the CF method, is considered to have relatively lower reliability since other VS methods do not identify this variable as significant.

For the rheological index (R_{rhe}), the four variable selection methods recognize different wavenumber variables that are critical to the determination of R_{rhe}. The majority of these variables are observed within the wavenumber range of 1500 – 900 cm^{-1}, with the most critical ones appearing near 1410, 1200, and 950 cm^{-1}. The peak near 1410 cm^{-1} is linked to aliphatic -CH_2 and -CH_3, and the region between 1250 and 1200 cm^{-1} is attributed to oxygen- or sulfur-based functional groups. According to the spectra of binders at different ageing levels (Fig. 4.8), for bitumen without SBS, the intensity of the spectral region around 950 cm^{-1} decreases with increasing ageing level. Given that peak overlap occurs for FTIR spectra, this decreased intensity may be caused by the peaks around it, including S=O stretching in sulfoxides, C-O-C stretching in ethers, and in-plane C-H bending in aromatics, which vary with ageing or sources. In SBS-modified binders, besides the effects of aforementioned chemical groups, the peak at 950 cm^{-1} is also linked to the alkenes in SBS. Applying spectral decomposition to FTIR spectra may help determine the precise contribution of these chemical groups to the variations near 950 cm^{-1}.

Comparing Fig. 6.9 (a) and (b), different spectral regions have varying contributions to f_c and R_{rhe}. Except for f_c and R_{rhe}, PLS regression was also performed on the other two parameters obtained from frequency sweep tests, namely, crossover modulus (G_c^*) and Glover-Rowe (GR). The optimized wavenumber ranges (through MW method) for f_c, G_c^*, GR and R_{rhe}, are 1750 – 950 cm^{-1}, 1320 – 880 cm^{-1}, 1640 – 1150 cm^{-1}, and 1240 – 840 cm^{-1}, respectively. The selected spectral regions for f_c and GR are similar, as are the regions for G_c^* and R_{rhe}. This is in accordance with the high Pearson correlation coefficients (r) between f_c and GR, and between G_c^* and R_{rhe}, as indicated in Table 4.8. The

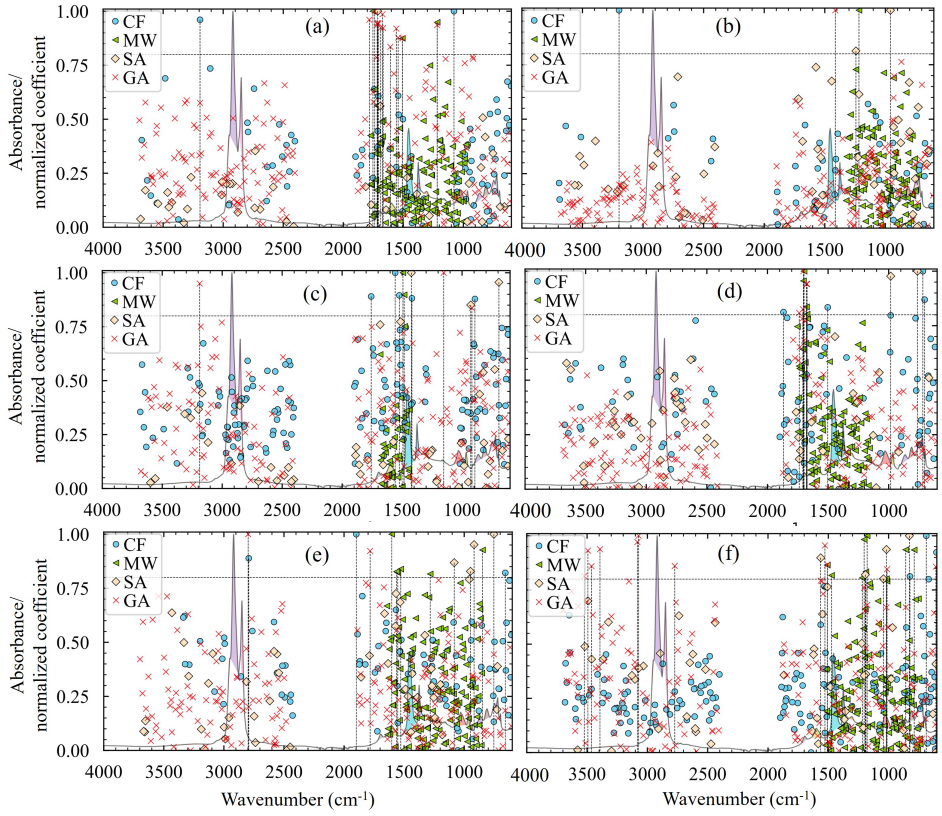

Figure 6.9 Regression coefficients for the prediction of (a) f_c, (b) R_{rhe}, (c) A_D, (d) B_D, (e) G_4, and (f) γ_4 using FTIR dataset. Vertical dashed lines highlight the variables with normalized regression coefficient greater than 0.8. Solid lines represent typical FTIR spectra for bituminous binders.

region between 1800 and 1000 cm^{-1} is mainly linked to carbonyl polar functional groups, aliphatic -CH_3 and -CH_2, and aromatic C=C bonds. The spectral region between 1400 – 800 cm^{-1} is more indicative of sulfoxide polar functional groups and aromatic -CH group. These differences imply that the four rheological parameters are partially influenced by different chemical components and how they change during the ageing process.

The contributions of variables derived from FTIR tests to the prediction of A_D and B_D are exhibited in Fig. 6.9 (c) – (d). As shown in Fig. 6.9 (c), spectral variables highly correlated with the prediction of A_D primarily occur in the regions denoting carbonyls, aromatic C=C, aliphatic CH_2 and CH_3, and SBS-related peaks at around 910 and 700 cm^{-1}. Two peaks at around 3195 cm^{-1} and 1160 cm^{-1} are exclusively underlined by the GA method, which are indicative of the stretching of -OH or -NH and polar function group of sulfones or alcohols, respectively. Among these variables, those related to the aromatic and aliphatic structures within the range between 1600 – 1400 cm^{-1} demonstrate the

strongest correlation. Consequently, the A_D in the equation for strain-controlled fatigue life (4.12) depends on the aromatic and aliphatic structures, modifiers such as SBS, and polar functional groups in bitumen. Regarding B_D, a distribution of regression coefficients similar to that of f_c is observed, with the most informative variables located in the spectral region of 1800 – 1500 cm^{-1}. This similarity results from the strong correlation between B_D and f_c as indicated by their high r of 0.98 (Table 4.8).

Fig. 6.9 (e) and (f) present the regression coefficients derived from the prediction of G_4 and γ_4. Unlike other parameters depicted in Fig. 6.9, the spectral variables that determine G_4 and γ_4 are more scattered across the wavenumber ranges of 3500 – 2600 cm^{-1} and 1800 – 600 cm^{-1}. For G_4, the peaks around 2800, 1900, 1800, 1600, 1550, 1300, 1100, 960, 910, 850, 750, and 620 cm^{-1} are recognized as important variables by the four variable selection methods. These peaks include both aliphatic and aromatic groups, along with various polar functional groups. The key variables for the prediction of γ_4 are revealed at bands around 1500, 1200, 1000, and 800 cm^{-1}, representative of combined effects of aromatic C=C and aliphatic CH_2, sulfur/oxygen-based functional groups, sulfoxide, and aromatic C-H bonds, respectively. Bands identified by only one variable selection method are excluded from the analysis. Although similar variables are identified as important for G_4 and γ_4, the specific peaks with the highest regression coefficients are different, reflecting their varying dependence on the chemical composition of bitumen.

It should be noted that, due to the collinearity inherent in FTIR spectra, certain peaks that represent similar chemical information to those with high coefficients may not be recognized. In general, the spectral region between 1800 and 800 cm^{-1} is highly related to the prediction of f_c, R_{rhe}, A_D, B_D, G_4, and γ_4. Each of these six parameters is characterized by different peaks with high correlations. The f_c and B_D primarily depend on the carbonyl index. The A_D is significantly affected by the balance between aromatic and aliphatic structures, as well as the presence of polymer modifiers. For R_{rhe}, G_4, and γ_4, the aromatics, aliphatics, and polar functional groups collectively determine their values.

The PLS regressions on the six rheological parameters using the GPC dataset are presented in Fig. 6.10. Four variable selection methods exhibit a certain consistency in characterizing the importance of GPC variables to the prediction of f_c and R_{rhe}. Regarding f_c, variables with high regression coefficients are observed around the elution time of 14.5 – 16 min. This region highlights the presence of resins and asphaltenes in bitumen. For R_{rhe}, except for the region near 15 min, the elution time indicative of the presence of SBS is also identified, indicating the more significant impact of SBS on R_{rhe} compared to f_c.

For A_D, several dispersed variables with high regression coefficients are identified by at least two variable selection methods, including the variables at elution times of 8.8, 11.1, 13.3, 15.0, 16.0, and 17.0 min. These variables correlate with asphaltenes, resins, aromatics, and SBS modifiers, denoting that the fatigue life of bitumen depends comprehensively on the interactions between SARA fractions. The prediction of B_D is depicted in Fig. 6.10 (d). A similar distribution of the chromatographic variables as that of f_c is observed for B_D, with the most important variables occurring in the range of 14.5 – 16 min.

As for G_4 and γ_4, most crucial variables are observed around 14.5 min, as shown in Fig. 6.10 (e) and (f), which are mainly related to the asphaltenes in bitumen. For G_4, variables representing lower molecular weights are also underlined, while only the variables near

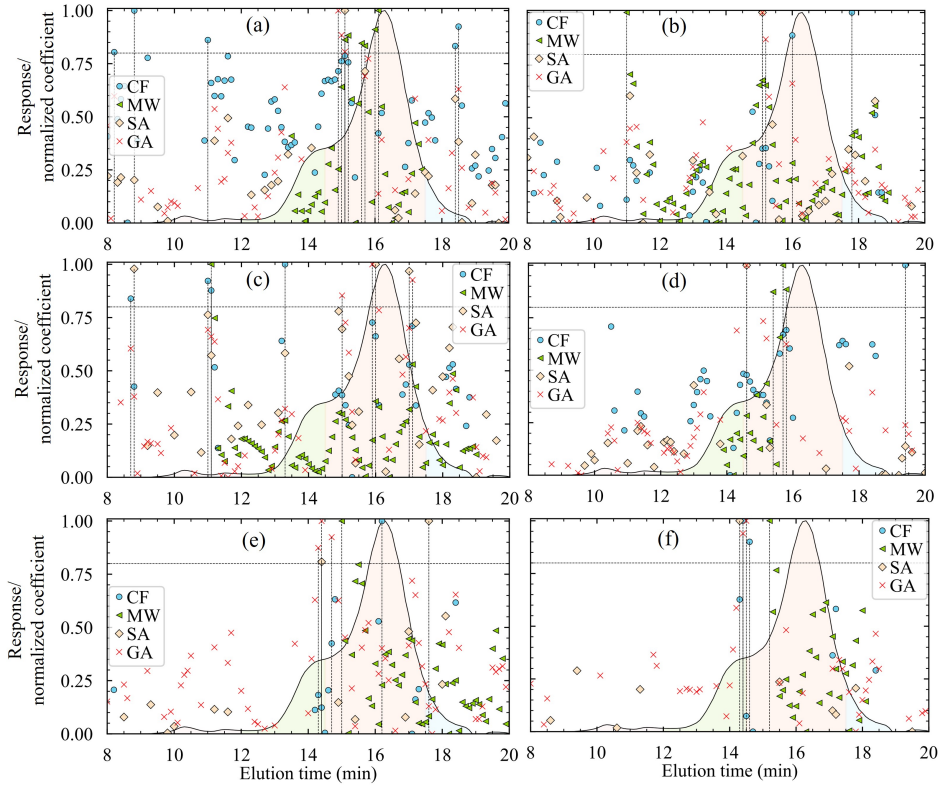

Figure 6.10 Regression coefficients for the prediction of (a) f_c, (b) R_{rhe}, (c) A_D, (d) B_D, (e) G_4, and (f) γ_4 using GPC dataset. Vertical dashed lines highlight the variables with normalized regression coefficient greater than 0.8. Solid lines refer to typical chromatograms for bituminous binders.

14.5 min are revealed by three variable selection methods for γ_4. Considering that the γ_4 and G_4 represent the second longest relaxation time in bitumen and corresponding relaxation strength, respectively, these variable distributions indicate that the second longest relaxation time is essentially associated with the molecular structures eluting at 14.5 min, while the corresponding relaxation strength is dominated by this molecular weight but also affected by other lighter bitumen components.

According to the loading plot obtained from the PLS regression on DSC dataset, as shown in Fig. 6.11, the important variables identified by the four variable selection methods are more scattered across the entire curve compared to the distribution of regression coefficients for FTIR and GPC datasets. This broader distribution could be attributed to the lower prediction performance of DSC dataset, which increases the uncertainty in interpreting the contributions of each variable to the prediction of rheological properties. For f_c, the identified variables mostly occur at temperatures corresponding to observable exothermic or endothermic peaks in thermograms, as shown in Fig. 4.12, with the most dominant ones appearing at around 4 and 16 °C. The significant variables with regards to

R_{rhe}, as displayed in Fig. 6.11 (b), are located at temperatures of 0, 18, 60, and 82 °C. The variables at around 18 and 82 °C, identified by either three or two variable selection methods, are particularly noteworthy. They are related to the thermal behavior of crystalline phases in bitumen.

For A_D, variables recognized by at least two variable selection methods are at temperatures around 3, 21, and 70 °C. The B_D is again derived based on variables similar to those for f_c, including variables at temperatures of -21, -7, 5, 23, and 33 °C. Fig. 6.11 (e) shows that the most influential variables for G_4 are near -23, 10, 35, and 64 °C, covering both the glass transition and crystallization-related regions. A similar pattern is observed for γ_4, with critical variables occurring at temperatures of -15, 7, and 65 °C. Among these parameters, f_c, B_D, G_4, and γ_4 reveal more correlation with the glass transition temperature, while R_{rhe} and A_D depend mainly on the crystalline behavior located around 20 °C.

6.5 Summary

This chapter investigated the physicochemical-rheological characterization of various types of bituminous binders at different moisture and ageing conditions through chemometric

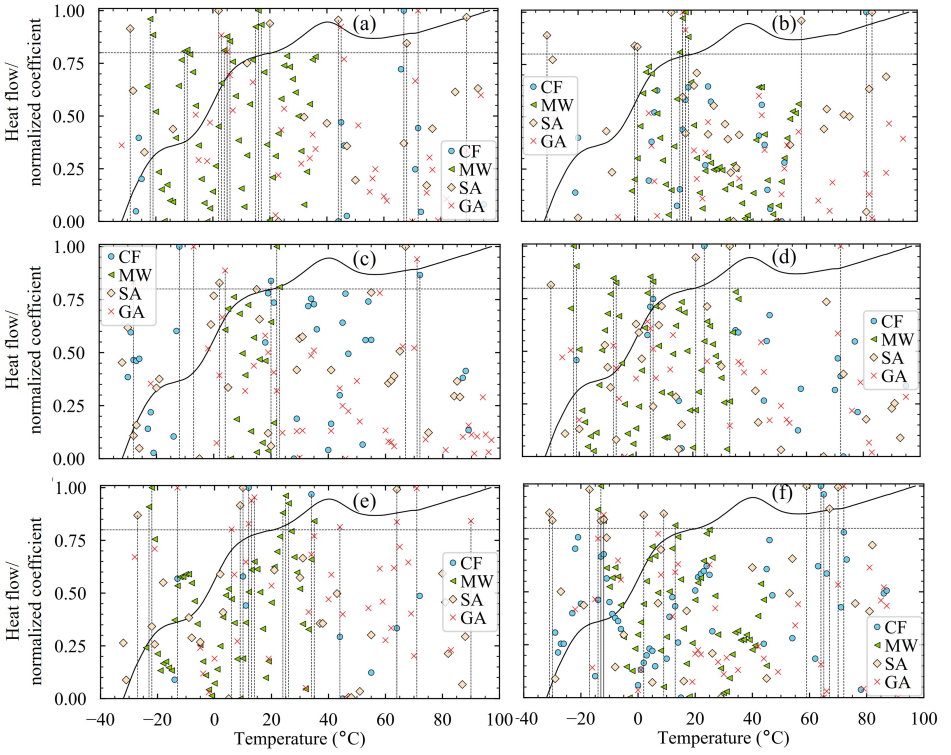

Figure 6.11 Regression coefficients for the prediction of (a) f_c, (b) R_{rhe}, (c) A_D, (d) B_D, (e) G_4, and (f) γ_4 using DSC dataset. Vertical dashed lines highlight the variables with normalized regression coefficient greater than 0.8. Solid lines refer to typical heat flow curves for bituminous binders.

analysis. Chemical, structural, and thermal variables of full curves obtained from FTIR, GPC, and DSC tests, respectively, were utilized. The classification of bitumen type, ageing state, and testing conditions was performed using the PCA-LDA analysis coupled with the MW and SA variable selection methods. The prediction of different rheological properties was achieved based on PLS and SVR models aided by four variable selection methods of CF, MW, SA, and GA.

When applying FTIR, GPC, and DSC datasets to the classification of bitumen type and ageing state, a high classification accuracy of up to 0.99 is obtained through the PCA-LDA model coupled with MW and SA variable selection methods. The three datasets present comparable performance in classifying bitumen type, and the best ageing classification is achieved for the FTIR dataset, followed by the GPC and the DSC datasets. High classification accuracy can be achieved using only 5% to 10 % of the variables within the original datasets. This indicates an increased efficiency in identifying critical variables when applying variable selection methods.

Each of the FTIR spectral regions relating to aliphatic, aromatic, and polar functional groups provides sufficient chemical information for the accurate classification of bitumen. Combining any two of these regions further enhances the classification performance. In particular, the region from approximately 1400 to 1000 cm^{-1}, which contains both aliphatic groups and oxygen-/sulfur-/nitrogen-based minor polar functional groups in bitumen, shows the highest classification accuracy. For the classification of ageing state, oxygen-, sulfur-, and nitrogen-based polar functional groups spanning from 1800 to 900 cm^{-1} are recognized as the most relevant factors. The spectral regions describing aliphatic and aromatic groups provide additional chemical information, leading to a more comprehensive understanding of the oxidative ageing process.

For the GPC dataset, each of the intervals with a width of 1 min within the region between about 15 and 18 min demonstrates high accuracy above 0.9 in classifying bitumen type. This region mainly relates to bitumen components with medium molecular size, indicative of the presence of aromatics and resins. For the classification of ageing state, the region ranging from 14 to 16 min, which locates around the intersection of LMS and MMS, shows the highest correlation with ageing. This region is indicative of the changes in the molecular weights of asphaltenes and resins during the ageing process.

In the thermograms derived from DSC tests, the peaks around 60 – 80 °C, which relate to the exothermic behavior of crystalline phase in bitumen, present the highest correlation with the identification of bitumen type. The classification of ageing state based on DSC dataset is less accurate compared to FTIR and GPC datasets. In general, the region between -10 – 30 °C is more strongly linked to the ageing behavior.

The laboratory PAV and hydrothermal-conditioned samples show a chemical composition more similar to each other than to field samples. The primary chemical components that contribute to differentiation are the aliphatic CH_2 and CH_3 structures, as well as the polar functional groups. The relative importance of these components varies when distinguishing between lab / field conditions and between laboratory PAV / hydrothermal ageing scenarios.

The PLS regression overall shows high performance in predicting rheological properties of bitumen, with R^2 above 0.9 for crossover frequency (f_c), crossover modulus (G_c^*), Glover-Rowe parameter (GR), rheological index (R_{rhe}), fatigue constant (B_D), relaxation

strength of infinite mode (G_0), zero shear viscosity at 60 °C (ZSV_{60}), and viscosity at 120 °C (η_{120}), and higher than 0.8 for fatigue constant (A_D), relaxation time of the fourth mode (G_4), and relaxation strength of the fourth mode (γ_4). For most rheological properties, the FTIR dataset reveals a slightly better prediction performance compared to GPC, and the lowest performance is obtained from the DSC dataset. Utilizing variable selection improves the regression accuracy but also holds the risk of overfitting. Despite that, PLS regression with MW and GA methods presents the best performance for the prediction of rheological properties. Compared to PLS regression, better prediction performance for most rheological properties is obtained through the SVR model, indicating the nonlinear relationship between physicochemical and rheological properties.

According to PLS modeling results, the spectral region between 1800 and 800 cm^{-1} is strongly correlated to the rheological properties of f_c, G_c^*, GR, R_{rhe}, among which the range of 1800-1000 cm^{-1} is mainly linked to f_c and GR while the region at 1400-800 cm^{-1} is related more to G_c^* and R_{rhe}. The similar distribution of regression coefficients between f_c and GR, as well as between G_c^* and R_{rhe}, is in line with their strong correlation as indicated by high Pearson correlation coefficients r. The spectral variables significantly contributing to the determination of A_D associate with carbonyls and SBS structures, as well as aromatic and aliphatic groups, which demonstrate the strongest correlation. The dependence of B_D on FTIR variables is similar to that of f_c, consistent with the high r value between them. The variables crucial for the prediction of G_4 and γ_4 are dispersed over the whole FTIR spectrum, relating to both aliphatic and aromatic groups, along with various polar functional groups.

The GPC variables related to f_c and R_{rhe} are near the elution time of 15 min, denoting mostly the molecular weights of resins. For A_D, several dispersed variables corresponding to asphaltenes, resins, aromatics, and SBS modifiers are identified, suggesting the complex dependence of fatigue on SARA fractions and polymer modifiers. A variable distribution similar to that of f_c is obtained for B_D. Key factors linking to G_4 and γ_4 are observed near 14.5 min, which are mainly related to the asphaltenes in bitumen, where longer relaxation time and higher relaxation modulus are obtained.

References

Asemani, M., & Rabbani, A. R. (2020). Detailed FTIR spectroscopy characterization of crude oil extracted asphaltenes: Curve resolve of overlapping bands. *Journal of Petroleum Science and Engineering, 185*, 106618.

Aske, N., Kallevik, H., & Sjöblom, J. (2001). Determination of saturate, aromatic, resin, and asphaltenic (sara) components in crude oils by means of infrared and near-infrared spectroscopy. *Energy & Fuels, 15*(5), 1304–1312.

Awad, M., Khanna, R., Awad, M., & Khanna, R. (2015). Support vector regression. *Efficient learning machines: Theories, concepts, and applications for engineers and system designers*, 67–80.

Castro, L. V., & Vazquez, F. (2009). Fractionation and characterization of mexican crude oils. *Energy & Fuels, 23*(3), 1603–1609.

Das, P. K., Baaj, H., Kringos, N., & Tighe, S. (2015). Coupling of oxidative ageing and moisture damage in asphalt mixtures. *Road Materials and Pavement Design, 16*(sup1), 265–279.

Douglas, R. K., Nawar, S., Alamar, M. C., Mouazen, A., & Coulon, F. (2018). Rapid prediction of total petroleum hydrocarbons concentration in contaminated soil using vis-nir spectroscopy and regression techniques. *Science of the Total Environment*, *616*, 147–155.

Feng, Z.-g., Bian, H.-j., Li, X.-j., & Yu, J.-y. (2016). Ftir analysis of uv aging on bitumen and its fractions. *Materials and Structures*, *49*, 1381–1389.

Frigio, F., Pasquini, E., Ferrotti, G., & Canestrari, F. (2013). Improved durability of recycled porous asphalt. *Construction and Building Materials*, *48*, 755–763.

Frolov, I. N., Okhotnikova, E. S., Ziganshin, M. A., & Firsin, A. A. (2020). Interpretation of double-peak endotherm on DSC heating curves of bitumen. *Energy & Fuels*, *34*(3), 3960–3968.

Gómez-Caravaca, A. M., Maggio, R. M., & Cerretani, L. (2016). Chemometric applications to assess quality and critical parameters of virgin and extra-virgin olive oil. a review. *Analytica Chimica Acta*, *913*, 1–21.

Hosseinnezhad, S., Zadshir, M., Yu, X., Yin, H., Sharma, B. K., & Fini, E. (2019). Differential effects of ultraviolet radiation and oxidative aging on bio-modified binders. *Fuel*, *251*, 45–56.

Khanmohammadi, M., Garmarudi, A. B., & de la Guardia, M. (2012). Characterization of petroleum-based products by infrared spectroscopy and chemometrics. *TrAC Trends in Analytical Chemistry*, *35*, 135–149.

Kirkpatrick, S., Gelatt Jr, C. D., & Vecchi, M. P. (1983). Optimization by simulated annealing. *science*, *220*(4598), 671–680.

Kriz, P., Stastna, J., & Zanzotto, L. (2008). Glass transition and phase stability in asphalt binders. *Road Materials and Pavement Design*, *9*(sup1), 37–65.

Kumar, Y., Singh, S. K., Oberoi, D., Kumar, P., Mohanty, P., & Ravindranath, S. S. (2020). Effect of molecular structure and concentration of styrene-butadiene polymer on upper service temperature rheological properties of modified binders. *Construction and Building Materials*, *249*, 118790.

Leardi, R., & Gonzalez, A. L. (1998). Genetic algorithms applied to feature selection in pls regression: How and when to use them. *Chemometrics and intelligent laboratory systems*, *41*(2), 195–207.

Lee, L. C., Liong, C.-Y., & Jemain, A. A. (2017). A contemporary review on data preprocessing (dp) practice strategy in atr-ftir spectrum. *Chemometrics and Intelligent Laboratory Systems*, *163*, 64–75.

Manne, R. (1987). Analysis of two partial-least-squares algorithms for multivariate calibration. *Chemometrics and Intelligent Laboratory Systems*, *2*(1-3), 187–197.

Mehmood, T., Liland, K. H., Snipen, L., & Sæbø, S. (2012). A review of variable selection methods in partial least squares regression. *Chemometrics and intelligent laboratory systems*, *118*, 62–69.

Melendez, L. V., Lache, A., Orrego-Ruiz, J. A., Pachon, Z., & Mejía-Ospino, E. (2012). Prediction of the SARA analysis of colombian crude oils using ATR–FTIR spectroscopy and chemometric methods. *Journal of Petroleum Science and Engineering*, *90*, 56–60.

Mirwald, J., Werkovits, S., Camargo, I., Maschauer, D., Hofko, B., & Grothe, H. (2020a). Investigating bitumen long-term-ageing in the laboratory by spectroscopic analysis of the SARA fractions. *Construction and Building Materials*, *258*, 119577.

Mirwald, J., Werkovits, S., Camargo, I., Maschauer, D., Hofko, B., & Grothe, H. (2020b). Understanding bitumen ageing by investigation of its polarity fractions. *Construction and Building Materials*, *250*, 118809.

Mishra, P., Biancolillo, A., Roger, J. M., Marini, F., & Rutledge, D. N. (2020). New data preprocessing trends based on ensemble of multiple preprocessing techniques. *TrAC Trends in Analytical Chemistry*, *132*, 116045.

Mohammadi, M., Khorrami, M. K., Vatani, A., Ghasemzadeh, H., Vatanparast, H., Bahramian, A., & Fallah, A. (2021). Genetic algorithm based support vector machine regression for prediction of sara analysis in crude oil samples using atr-ftir spectroscopy. *Spectrochimica Acta part A: Molecular and biomolecular spectroscopy*, *245*, 118945.

Morais, C. L., Lima, K. M., Singh, M., & Martin, F. L. (2020). Tutorial: Multivariate classification for vibrational spectroscopy in biological samples. *Nature Protocols*, *15*(7), 2143–2162.

Nobakht, M., Zhang, D., Sakhaeifar, M. S., & Lytton, R. L. (2020). Characterization of the adhesive and cohesive moisture damage for asphalt concrete. *Construction and Building Materials*, *247*, 118616.

Petersen, J. C. (2009). A review of the fundamentals of asphalt oxidation: Chemical, physicochemical, physical property, and durability relationships. *Transportation Research Circular*, (E-C140).

Pipintakos, G., Lommaert, C., Varveri, A., & Van den Bergh, W. (2022). Do chemistry and rheology follow the same laboratory ageing trends in bitumen? *Materials and Structures*, *55*(5), 146.

Primerano, K., Mirwald, J., Maschauer, D., Grothe, H., & Hofko, B. (2022). Influence of selected reactive oxygen species on the long-term aging of bitumen. *Materials and Structures*, *55*(5), 133.

Qian, G., Yu, H., Jin, D., Bai, X., & Gong, X. (2021). Different water environment coupled with ultraviolet radiation on ageing of asphalt binder. *Road Materials and Pavement Design*, *22*(10), 2410–2423.

Redelius, P., & Soenen, H. (2015). Relation between bitumen chemistry and performance. *Fuel*, *140*, 34–43.

Rinnan, Å., Van Den Berg, F., & Engelsen, S. B. (2009). Review of the most common preprocessing techniques for near-infrared spectra. *TrAC Trends in Analytical Chemistry*, *28*(10), 1201–1222.

Siroma, R. S., Nguyen, M. L., Hornych, P., Lorino, T., & Chailleux, E. (2021). Clustering aged bitumens through multivariate statistical analyses using phase angle master curve. *Road Materials and Pavement Design*, *22*(sup1), S51–S68.

Smola, A. J., & Schölkopf, B. (2004). A tutorial on support vector regression. *Statistics and computing*, *14*, 199–222.

Sun, X., Yuan, H., Song, C., Deng, X., Lv, G., Li, X., & Hu, A. (2020). Rapid and simultaneous determination of physical and chemical properties of asphalt by ATR-FTIR spectroscopy combined with a novel calibration-free method. *Construction and Building Materials*, *230*, 116950.

Üstün, B., Melssen, W., & Buydens, L. (2007). Visualisation and interpretation of support vector regression models. *Analytica chimica acta*, *595*(1-2), 299–309.

Weigel, S., & Stephan, D. (2017). The prediction of bitumen properties based on FTIR and multivariate analysis methods. *Fuel*, *208*, 655–661.

Weigel, S., & Stephan, D. (2018). Differentiation of bitumen according to the refinery and ageing state based on FTIR spectroscopy and multivariate analysis methods. *Materials and Structures*, *51*, 1–11.

Westerhuis, J. A., Kourti, T., & MacGregor, J. F. (1998). Analysis of multiblock and hierarchical pca and pls models. *Journal of Chemometrics: A Journal of the Chemometrics Society*, *12*(5), 301–321.

Wilt, B. K., Welch, W. T., & Rankin, J. G. (1998). Determination of asphaltenes in petroleum crude oils by fourier transform infrared spectroscopy. *Energy & fuels*, *12*(5), 1008–1012.

Xiaobo, Z., Jiewen, Z., Povey, M. J., Holmes, M., & Hanpin, M. (2010). Variables selection methods in near-infrared spectroscopy. *Analytica chimica acta*, *667*(1-2), 14–32.

Zhihui, L., Rui, Z., Yonghua, Z., Qian, C., & Weijun, Q. (2019). Discriminating wavenumbers selection of atr-ftir spectra for identifying graded asphalt. *Construction and Building Materials*, *214*, 565–573.

Zimmermann, B., & Kohler, A. (2013). Optimizing savitzky–golay parameters for improving spectral resolution and quantification in infrared spectroscopy. *Applied spectroscopy*, *67*(8), 892–902.

7

Closing remarks and insights

This chapter summarizes the main findings of this thesis, highlighting the insights into the coupling of moisture and ageing in bitumen. Additionally, further recommendations are offered concerning a feasible course towards addressing fully coupled effects of moisture and ageing on bituminous binders and asphalt pavements.

7.1 Conclusions

This research was motivated by the goal of increasing the durability and sustainability of the porous asphalt pavements that is extensively applied in the Netherlands. Such durability is primarily affected by traffic load and climate changes. This thesis concentrates on the latter, with a specific focus on the key issues of moisture damage and oxidative ageing caused by climate factors. While these two aspects are commonly assessed separately, the fact that one is also affected by the other factor complicates the accurate evaluation of these factors in bituminous materials. The objectives of this thesis were to gain a thorough understanding of the mechanisms underlying moisture and ageing effects on bitumen and explore their interdependent relationship, aiming for a comprehensive evaluation of the coupled moisture and ageing behavior in bitumen and its implications for bituminous materials. In particular, this study employed a multi-scale approach involving both experimental tests and simulations coupled with a multi-faceted analysis of specific parameters and complete curve datasets. The methodology was utilized to enhance the accuracy and reliability of the research findings.

The study of moisture damage in bitumen focused on its diffusion behavior, in order to address the **first objective** stated in Section 1.3. Both experiments and molecular dynamics simulations were utilized to evaluate the moisture diffusion coefficient and water solubility in bitumen and to elucidate the underlying mechanisms, as discussed in Chapters 2 and 3, respectively. Results at nano- and macro-scales serve to mutually interpret and corroborate the key findings regarding the water behavior. The S-Cluster model proposed for the interpretation of experimental results classifies absorbed water into free (Henry) and clustering groups, the latter including water bonded both to polar sites of bitumen and to other water molecules through hydrogen bonding (Section 2.3). The molecular dynamics simulations revealed similar water states according to their types of hydrogen bonds, i.e., free water, water hydrogen bonded to bitumen, and water hydrogen bonded to water, as discussed in Section 3.4. Water clusters mostly form near specific functional groups in bitumen that have a high propensity for forming hydrogen bonds with water molecules. At a specific temperature, bitumen can hold a maximum amount of free and bitumen-bonded water, dependent on its chemical composition and microstructure. Beyond this limit, additional water molecules predominantly form clusters. Increasing temperature leads to a higher fraction of free water and a reduced fraction of hydrogen-bonded water, indicating an increased solubility of water in bitumen.

In the S-Cluster model, the free water group is assumed as diffusing at a constant rate while the clustering group remains immobile in bitumen (Section 2.3). The diffusion coefficient of free water (with an order of approximately 10^{-12} m^2/s) determined through molecular dynamics simulations (Section 3.3) is comparable to the experimental value determined by the S-Cluster model. However, simulation results indicate a minimal to negligible diffusion rate for water hydrogen-bonded to bitumen components and a decreasing diffusion coefficient of water clusters with their increasing cluster size, which typically ranges from 10^{-15} to 10^{-13} m^2/s or even lower (Section 3.4). To conclude, an accurate model for water diffusion in bitumen should incorporate three essential components: one term describing free water characterized by a constant diffusion coefficient and a saturated concentration, a second term for immobile water bonded to polar functional groups with a maximum concentration dependent on the number of these avail-

able groups, and water clusters, whose diffusion coefficient is significantly lower compared to free water, varies with cluster size. At low water concentrations (with limited water clusters), the third term can be omitted, and the diffusion model is reduced to the S-Cluster model. For extremely high water concentrations, the concentration of free and hydrogen-bonded water is too low to be recognized, and the diffusion model can be simplified into the third term as:

$$\gamma_d c_{cu} D_{cu,0} \frac{\partial^2 c_{cu}}{\partial x^2} = \frac{\partial c_{cu}}{\partial t} \tag{7.1}$$

where γ_d represents the dependence of clustering diffusion coefficient (D_{cu}) on the concentration of clusters (c_{cu}).

Furthermore, moisture can cause degradation of bitumen, such as loss of cohesion in bitumen and adhesion failure at the bitumen-aggregate interface. The molecular dynamics simulation results reported in Section 3.3 reveal a reduction in density, viscosity, and cohesive energy as water content increases. This phenomenon is mainly associated with the formation of water clusters, highlighting the influence of water on bitumen, particularly when water remains in the bitumen film.

To evaluate the physicochemical and rheological properties of aged binders and explore the physicochemical-rheological relationship, in relation to the **second objective** in Section 1.3, FTIR, GPC, DSC, and DSR tests were performed in Chapter 4. FTIR results presented in Section 4.4 reveal high correlations between peaks representing different vibration modes of the same molecular structures. The chemical changes caused by the oxidative ageing process are revealed not only by carbonyl and sulfoxide indices but by other peaks representing aliphatic and aromatic chains, as well as minor polar functional groups. In the same section, the fractions with large and medium molecular size were obtained from GPC tests, which also vary with ageing, indicative of the ageing process. However, parameters obtained from DSC tests reveal less correlation with ageing. The correlation analysis between specific parameters obtained from FTIR, GPC, and DSC tests is informative of the relationship between chemical composition, microstructure, and thermal properties.

In order to assess the effect of ageing on the physical properties of bitumen, rheological tests were conducted in Chapter 4. Various rheological parameters were then determined including the crossover frequency, crossover modulus, Glove-Rowe parameter, and rheological index obtained from frequency sweep tests, the maximum shear stress and fatigue life derived from linear amplitude tests, the various relaxation modes and corresponding relaxation moduli based on the relaxation tests at 0 °C, and the complex and apparent viscosity determined using DSR and Viscometer tests, as discussed in Section 4.5. All of these properties indicate the hardening and degradation of bitumen resulting from oxidative ageing. Based on the Pearson correlation between these rheological properties, they can be broadly classified into two categories; parameters in each category exhibit a strong correlation. The parameters in the first category, including crossover frequency and Glove-Rowe parameter, are related to the fractional free volume, thermal expansion coefficient, and the relaxation strength with the longest relaxation time. The high Pearson correlation between these parameters and the carbonyl index indicates their significant dependence on oxidative reactions related to the generation of car-

bonyl groups. The other category, including rheological index and pre-exponential constant in the strain-based fatigue equation, is largely associated with the shape of master curves and relaxation spectrum and reveals a more complex correlation with the chemical changes in functional groups and aromatics due to ageing. The canonical correlation analysis presented in Section 4.6, which evaluates the overall correlation between two sets of variables, demonstrates the high capability of comprehensive information embedded in FTIR spectra for characterizing various rheological properties.

The chemometric analysis of physicochemical and rheological properties based on the full curves obtained from FTIR, GPC, and DSC tests was further conducted in Chapter 6 to evaluate the physicochemical-rheological relationship of bituminous binders and advance the understanding of the ageing mechanisms. Results revealed in Section 6.3 show that the oxygen-, sulfur-, and nitrogen-based polar functional groups reveal the strongest correlation with the bitumen ageing process. The spectral regions concerning aromatic and aliphatic structures add additional information for a complete description of the ageing process. The molecular weights indicative of the structural changes in asphaltenes and resins show the highest correlation with ageing. Consistent with the analysis of thermal parameters, the thermograms obtained from DSC tests show a weaker correlation with ageing. In general, the heat flow at temperatures of -10 – 30 °C is more strongly linked to the ageing behavior.

The prediction of rheological properties utilizing chemical and structural properties was presented in Section 6.4. Results demonstrates high prediction accuracy, with R^2 values predominantly exceeding 0.9, and those based on thermal data above 0.8. According to partial least squares (PLS) modeling results, the spectral region between 1800 and 800 cm^{-1} is strongly correlated to the viscoelastic properties, with slightly different regions recognized for crossover frequency and crossover modulus, as well as parameters highly correlated to them. The fatigue-based pre-exponential constant is associated with carbonyls and SBS structures, as well as aromatic and aliphatic groups, which demonstrate the strongest correlation. The variables crucial for the prediction of relaxation parameters are distributed over the whole FTIR spectrum, relating to both aliphatic and aromatic groups, along with various polar functional groups. The GPC variables related to crossover frequency and rheological index mostly fall within the elution time corresponding to medium molecular size. For the fatigue-based pre-exponential constant, several variables corresponding to asphaltenes, resins, aromatics, and SBS modifiers are identified, suggesting the complex dependence of fatigue on SARA fractions and polymer modifiers. Key factors linking to the slow relaxation mode are observed to be related to molecular sizes corresponding to the asphaltenes in bitumen, where longer relaxation time and higher relaxation modulus occur. The chemometric analysis is demonstrated to be an efficient approach for the accurate prediction of rheological properties, provides new insights into the chemo-mechanical relationship of bitumen, and guides the selection of key physicochemical and rheological parameters for evaluating bitumen degradation.

Irrespective of water concentrations, parameters related to water behavior in bitumen, such as the saturated free water content, the maximum content of water clusters, and water diffusion coefficient, all depend on the chemical composition and microstructure of bitumen, which vary substantially with its type and ageing level. To study the effects of ageing on the moisture diffusion, as a response to the **third objective** described in

Section 1.3, dynamic vapor sorption tests of aged bitumen at 80% relative humidity were conducted in Chapter 5. Results in Section 5.2 demonstrate that ageing leads to increased activation energy for the diffusion of free water and reduced enthalpy of its adsorption. Both parameters, as well as the diffusion coefficient and absorption at specific temperatures, primarily rely on the integrated mechanisms of fractional free volume and polarity of bitumen; the former decreases and the latter increases as ageing proceeds. In terms of water diffusion in bitumen, a lower fractional free volume indicates reduced micro-space available for water molecules to pass and a larger hindrance for the bitumen molecular chains to rearrange and accommodate water diffusion, both leading to enhanced activation energy. The increased polarity, on the other hand, indicates more possible diffusing paths (i.e., increased entropy), which corresponds to a higher pre-exponential factor in the Arrhenius equation for diffusion. Under the combined influences of free volume and polarity, the water diffusion coefficient in aged bitumen is lower at low temperatures and higher at high temperatures compared to fresh bitumen. For the water solubility in bitumen, increased polarity results in better compatibility between water and bitumen and thereby decreases the enthalpy of free water absorption. As ageing progresses, the reduction in free volume dominates the decreased maximum water concentration in bitumen, while exceptions may occur due to an increase in polarity.

The degradation in bitumen varies with its ageing level, as indicated in Section 5.3. After a long-term exposure to water conditions, the rheological properties of aged bitumen after re-drying show only slight changes compared to the continuous dry conditions. This change may be related to the leaching effects of water, namely, water flow can dissolve and remove some of the ageing products, with increased ageing leading to a higher amount of these products being leached away. The experimental and simulated results indicate that water can affect the cohesion of bitumen, while this effect is mostly recoverable when water is removed. However, under field conditions, more damage can be caused when water exists within asphalt pavements, especially when accompanied by pore pressure. When water cannot (easily) move out and traffic adds pressure, aged bitumen provides more available nuclei for increased number of water clusters, suggesting more clusters distributed inside bitumen and at the bitumen-aggregate interface. Therefore, more serious degradation can be expected. As a summary, moisture primarily leads to more damage when the asphalt pavement is functioning under moisture conditions. Ageing may accelerate this degradation by providing more polar groups for water clustering nearby.

The **fourth objective** in Section 1.3 focuses on the the ageing kinetics in the presence of moisture. It can be seen from thesis that the presence of moisture influences the ageing kinetics, as well as the evolution of physicochemical and rheological properties during bitumen ageing. As discussed in Section 5.4, in conditions with moisture, particularly in the dynamic vapor sorption tests, adsorption of moisture on bitumen surface and absorption within bitumen films compete with the diffusion of oxygen. This competition interferes with the diffusion of oxygen, resulting in reduced contact of oxygen with the reactive components in bitumen. As a consequence, the rate of oxidative reaction is reduced. During the wetting period, the diffusing pathways are generated by water molecules, especially by water clusters. These pathways facilitate oxygen diffusion into the bitumen film in the subsequent drying period, resulting in a faster oxidative reaction

in bitumen compared to the continuous drying air condition (approximately 0% relative humidity). In real-world scenarios, the impact of water on the ageing kinetics of bitumen can be ambivalent. Water may accelerate ageing during frequent water sorption and desorption cycles, especially under conditions of high water concentration or pore pressure, both favoring the formation of large water clusters. This process creates additional micro-spaces for oxygen diffusion. Conversely, the continuous presence of water within the bitumen film, while potentially causing more serious degradation, may inhibit further oxygen diffusion into the bitumen, thus decelerating the ageing process.

Overall, these findings provide in-depth insights into the understanding and evaluation of moisture diffusion and oxidative reaction in bitumen, as well as their respective effects on bitumen properties. The effects of moisture on the ageing process and that of ageing on the moisture behavior elucidated in this thesis establish a robust foundation for the modelling of coupled moisture-ageing effects in bituminous binders, namely the **fifth objective** of this study. In the analyses of the way moisture affects ageing and the other way around, it has become clear that these processes are interrelated and should be coupled in the analyses of pavement degradation since they occur simultaneously in the field.

7.2 Recommendations

In line with the fifth objective of this study, the moisture-ageing interactions and the need to couple the effects of moisture and aging were addressed. However, in order to arrive at concrete models for coupled moisture-ageing behavior in bituminous binders, further research is required to unravel its complex mechanisms and to evaluate the effects of important factors not covered in this thesis, such as UV-Visible radiation, reactive oxygen species and salts. Therefore, based on the obtained results in this work, the following recommendations are made to enhance the comprehensive understanding of moisture and ageing behavior.

The conducted molecular simulations and experiments reveal the significant effects of polar functional groups in bitumen on the formation of water clusters. Other inorganic salts and metals may also act as water clustering sites and thereby affect moisture diffusion and moisture-caused damage in bitumen, which should be taken into consideration when evaluating water behavior. The results obtained from molecular dynamics simulations are indicative of the critical impact of polar functional groups on water clustering behavior, and the experimental results highlight the importance of free volume in accommodating water diffusion. These two factors vary significantly with bitumen types and ageing states. Research on how ageing affects water clusters and cluster sizes is thus recommended, which also facilitates the understanding of the adhesion degradation caused by water clustering at the bitumen-aggregate interface. Moreover, it remains unclear if there is a maximum limit to water absorption in bitumen, or if the nano-scale water clusters formed within bitumen can grow continuously to form connected water pathways, especially under conditions of water immersion and pore pressure. If such connected pathway exists, it could act as a "highway" for the accelerated transport of water and oxygen into bitumen films and at the bitumen-aggregate interface, potentially causing serious damage to asphalt pavement.

The correlation analysis of specific chemical, physical, and rheological parameters

of aged bitumen and the chemometric analysis of rheological properties based on full curves of various physicochemical tests shed new light on the selection of key parameters essential for characterizing bitumen ageing. It is recommended to develop and refine applicable models and indices for the evaluation of bitumen properties and pavement performance based on the physicochemical-rheological relationship uncovered in this work. These models and indices should undergo sufficient verification to ensure their effectiveness and accuracy. Both FTIR and GPC datasets, which characterize bitumen from different aspects, have demonstrated a high capability for predicting rheological properties of bitumen. Identifying similarities and differences between these two datasets and assessing the importance of each dataset in predicting rheological properties would be insightful. An integrated analysis of both datasets could yield a more comprehensive description of the ageing process and enhance the overall prediction performance.

This work provides the first insight into the ageing kinetics with and without moisture and its dependence on the chemical composition and microstructure of bitumen, which should be further explored and understood. Therefore, it is recommended to conduct ageing tests under constant water immersion, wetting-drying cycles, and dry conditions and consider the effect of high pressure on the ageing process under these conditions. Simultaneously, microscopic techniques can be utilized to monitor the microstructure change. Both together enable a quantitative determination of the effects of moisture on ageing kinetics and help in understanding of the underlying mechanisms. Furthermore, UV plays a important role in bitumen ageing. Thus, how moisture affects the UV-based ageing should also be considered.

On the basis of in-depth understanding of the interplay between moisture and ageing behavior in bitumen, as characterized by its chemical and physical properties, and detailed analysis of the physicochemical-rheological relationship, it is feasible to propose specific physical or chemical parameters for directly predicting the bitumen properties under the influence of coupled moisture and ageing behavior. However, this coupled behavior is subject to a variety of factors including environmental conditions, bitumen composition, polymer modification, and rejuvenation processes. This presents significant challenges in selecting parameters that are representative of extensive conditions. Alternatively, physics-informed machine learning could be a promising solution for accurately predicting bitumen properties and asphalt pavements. This alternative approach requires the consideration of the complex mechanisms of the coupling behavior and the utilization of large datasets obtained from both laboratory moisture-ageing tests and field samples, thereby ensuring a more holistic model development.

Regarding recommendations beyond this topic, the experiments, simulations, and models developed in this research can be applied for the evaluation of moisture and ageing behavior in sustainable materials such as bio-based and rejuvenated binders. For example, when bio-based materials are utilized as modifiers or substitutes for bituminous binders, their significantly different chemical composition compared to traditional binders invokes the possibility that common indices for the evaluation of binder performance are not as efficient or accurate for bio-based binders. Therefore, it is essential to redefine critical physicochemical and rheological parameters for evaluating binder properties and pavement performance involving bio-based materials. In this scenario, the chemometric tools proposed in this thesis can be employed to detect key chemical and

rheological parameters for the evaluation of binder properties and to provide a more thorough understanding of ageing or moisture damage mechanisms in bio-based binders. Additionally, the methodologies detailed in this thesis can be used to explore how biomaterials affect moisture transport behaviors and ageing kinetics in binders.

Furthermore, the proposed methodologies, including the measurement of interaction parameters based on dynamic vapor sorption, the optimization methods for solving nonlinear problems with multiple unknown parameters, and the chemometric analysis integrating classification or regression models with variable selection methods, can potentially be applied in a wide range of scientific fields, such as the characterization of polymer materials and the analysis of various spectroscopic and chromatographic data.

Acknowledgements

I appreciate this opportunity to express my sincere gratitude to everyone who has supported, encouraged, and helped me throughout my PhD journey.

I am particularly grateful to my promoter, Prof. Sandra Erkens, for her systematic guidance in my PhD research and for steering the direction of my project. Her valuable input was crucial in keeping my research on track and ensuring the high quality of the research outcomes. I remember the moments when I had any questions, she always had her distinctive and memorable perspectives.

My deep appreciation goes to my co-promoter Dr. Aikaterini Varveri. She welcomed me with open arms and trust from the beginning. Her dedicated, insightful, and professional guidance significantly shaped my research and my academic philosophy. During times when my work lagged behind, she showed full understanding and patience, and provided key enlightenment. In moments of despair, confusion, and aimlessness due to encountered research challenges, she helped me with confidence and direction. Her efficient instructions were critical to my writing and presentations. She also assisted me in building an academic network through conferences, workshops, and other activities with thoughtful consideration for my further career in academia. I am so grateful for being in the same office with my co-promoter for the last four and half years, experiencing and sharing both happiness and sadness. I have no doubt she will enjoy a successful career and lead a splendid life.

Special thanks go to Dr. Othonas Moultos (3mE, TU delft) and Dr. Michael Greenfield (College of Engineering, The University of Rhode Island) for their expert supervision in molecular dynamics simulations. Their valuable and patient guidance on journal paper writing and project management has been extremely beneficial. Their rigorous academic attitudes redefined my viewpoint as a researcher. Each meeting with them not only advanced my research but also offered me a new opportunity to acquaint myself with "academically" fun people.

I also would like to thank my daily supervisors, Dr. Ruxin Jing and Dr. Hirad Salehi, for their considerate assistance in my research. Their step-by-step instructions concerning experiments and simulations, particularly at the early stages of my work, laid a solid foundation for the subsequent progress.

I am very grateful for the financial support provided by the Chinese Scholarship Council (CSC) over the past four years.

I would like to thank my colleagues Cor Kasbergen, Dr. Anupam Kumar, Dr. Xueyan Liu, Dr. Peng Lin, Dr. Haopeng Wang, Dr. Panos Apostolidis, and Dr. Yangming Gao for insightful discussions in research, as well as in philosophy of life. I would like to thank our technicians Marco Poot and Michele Aggelen and our secretary Claudia. Their kind help has been important during my PhD journey. Many thanks also go to my colleagues Shisong Ren, Chen Wang, Mohammadjavad Berangi, Dr. Avishreshth Singh, Dr. Ajay Jagadeesh, Sadaf Khalighi, Akinmade Daniel, Eli Martinez-Streignard, Saranga Pre-

marathna, Mahmoud Khadijeh, Zhaojie Sun, Yi Li, and Rui Wu in Delft University of Technology. They have made my PhD life more interesting and surprising. Especially, I would like to thank Dr. Haopeng Wang for his introduction of me into the PhD journey. Many thanks to Cor, Chen, Mohammad, Avi, and Ajay for many fun memories and possibilities in life. Thank my tennis partner Mahmoud for his patient coaching, which has strengthened my confidence as a sporty person. I am thankful to Dr. Xiuli Wang for her detailed instructions on the microscope operation. I also want to thank my colleagues and friends who ever spent time in Delft University of Technology. I would like to acknowledge Dr. Georgios Pipintakos for his support in my research, as well as his introduction to beers to me. Thanks Dr. Dongyu Liu, Yi Zhang and Lu Zou for all the happy experience they have brought to my life. Thanks Junyan Zhang and Bowen Li for their kind help in laboratory.

When I was writing this acknowledgement, the time when I started a new life and met new friends seemed to be yesterday. I was very fortunate to meet these nice friends Li Zou, Qi Shen, Zimu Wei, Fenghua Wang, Zhangyue Wei, Yun Zeng here in the Netherlands, Special thanks go to Li Zou, Qi Shen, and Zimu Wei. We have shared many cherished times in the Netherlands, especially at the beginning when we travelled and cooked food together, which made me feel less lonely during my time here. Moreover, I would like to thank Hong Zhang and Dongbin Cai for leading me to different life experience with bouldering, camping, cats, and dogs. My dear friends back in China, Yuanyuan Ma, Hui Wang, Yue Sun, Han Liu, and Linyi Yao, thank you for the strong support throughout my PhD journey, for the moments, whether happy or sad, that we shared, and for the cherished times we reunited.

My family holds the deepest place in my heart. No words can fully express my love for them. My parents, Dejun Ma and Chunxiang Zhao, have devoted all their lives to my sisters and me. My most heartfelt wish is for their continued health and happiness. My two sisters, Yuanyuan Ma and Fangfang Ma, have always supported in every way they can. I cannot image how my life will go without you.

I have been truly fortunate to find my fiance Yunlong Guo during my PhD time. He always comforts and enlightens me when I am sad, believes in me when I am facing doubt, takes care of me when I feel lost, and cheers me up when I am feeling down. With each challenge we face, our bond grows stronger. Thank you for all the happiness you have brought into my life!

Lili Ma
Delft, 28 February 2024

Curriculum Vitæ

Lili MA

16-06-1994 Born in Huai'an, China.

Education

2012 – 2016 Undergraduate, Bridge and River Crossing Engineering
Southeast University
Nanjing, China

2016 – 2019 Master, Highway and Railway Engineering
Southeast University
Nanjing, China

2019 – 2024 PhD, Civil Engineering and Geosciences
Delft University of Technology
Delft, Netherlands

Thesis:	Interactions of moisture and oxidative ageing mechanisms in paving binders: Towards improving durability of pavements
Promotor:	Prof. dr. S. M. J. G. Erkens
Co-promotor:	Dr. A. Varveri

List of Publications

Publications

1. **L Ma**, HS Salehi, R Jing, S Erkens, TJH Vlugt, OA Moultos, ML Greenfield, and A Varveri, 2023, Water diffusion mechanisms in bitumen studied through molecular dynamics simulations, Construction and Building Materials, 409, 133828.

2. **L Ma**, A Varveri, R Jing, and S Erkens, 2023, Chemical characterization of bitumen type and ageing state based on FTIR spectroscopy and discriminant analysis integrated with variable selection methods, Road Materials and Pavement Design 24 (sup1), 506-520.

3. **L Ma**, A Varveri, R Jing, C Kasbergen, and S Erkens, 2022, Thermodynamics and kinetics of moisture transport in bitumen, Materials & Design 222, 111028.

4. **L Ma**, A Varveri, R Jing, and S Erkens, 2021, Comprehensive review on the transport and reaction of oxygen and moisture towards coupled oxidative ageing and moisture damage of bitumen, Construction and Building Materials, 283, 122632.

5. G Pipintakos, **L Ma**, A Varveri, R Jing, and H Soenen, 2022, Diffusivity and reactivity of oxygen in bitumen and mastics, Advances in Materials and Pavement Performance Prediction - Proceedings of the International AM3P Conference.

Presentations

1. **L Ma**, A Varveri, R Jing, and S Erkens, Thermodynamic sorption and kinetic transport of water in bitumen, the 9th International Conference of the European Asphalt Technology Association, 08/06/2021, Austria.

2. **L Ma**, A Varveri, R Jing, and S Erkens, Chemical characterization of bitumen type and ageing state based on FTIR spectroscopy and discriminant analysis integrated with variable selection methods, the 10th International Conference of the European Asphalt Technology Association, 13/06/2023, Poland.